Bidirectional Reflectance of Snow and Sea Ice: Field, Laboratory and Modeling Studies

Christopher P. Ball M.Sc. B.Sc. (Hons.)

A thesis submitted for the degree of Doctor of Philosophy at the University of London

Department of Earth Sciences
Royal Holloway College
University of London

This thesis was funded by the Natural Environment Research Council (NERC) and the National Physical Laboratory (NPL). The fieldwork was funded by NPL and Royal Holloway Department of Earth Sciences.

Work in this thesis has been published by Ball et al. (2015) and Ball et al. (2013) in the journals: IEEE Transactions on Geoscience and Remote Sensing and OSA Applied Optics, respectively.

Abstract

Field measurements of the Hemispherical-Conical Reflectance Factor (HCRF) of Arctic snow-covered tundra were carried out using the GonioRAdiometric Spectrometer System (GRASS); over the viewing angles 0° to 50°, for the wavelength range 400 nm to 1300 nm. The HCRF measurements agreed well between sites where the snowpack was smooth and snow depth was greater than 40 cm, with a relative standard deviation of less than 10 % for backward and near nadir viewing angles. The site with the largest roughness elements had no forward peak and had a strong asymmetry in the HCRF with respect to the solar principal plane. The Conical-Conical Reflectance Factor (CCRF) of laboratory-generated sea ice was measured for the viewing angles 0° to 60°, for the wavelength range 410 nm to 730 nm. The CCRF of sea ice and the averaged HCRF of snow had forward scattering peaks, and an anisotropy that was strongly wavelength dependent; with the relative strength of the forward peak typically increasing with wavelength. The radiative-transfer model, PlanarRad, was able to reproduce the CCRF of the sea ice with a root-mean-squared-error (RMSE) of less than 9 %, with differences in the reflectance factors of typically less than 0.05. The change in the hemispherical reflectance of Spectralon over the 19 °C phase transition of PTFE was calculated by measuring the change in the output flux from a temperature-controlled Spectralon integrating sphere at 633 nm. The relative change in hemispherical reflectance was calculated as 0.09 ± 0.02 %, and the change in output flux was 1.82 ± 0.21 %. The change in the hemispherical reflectance of Spectralon is small, but the effect is amplified for integrating spheres; thus the influence of the phase transition on PTFE based integrating spheres should be considered for operating temperatures near to the 19 °C PTFE phase transition temperature.

Table of Contents:

List of Figures:

List of Tables

Acknowledgements

Firstly, I would like to acknowledge my supervisors Professor Martin King and Dr Nigel Fox for providing excellent supervision, support and guidance throughout the course of this Ph.D. I would like to acknowledge the Natural Environment Research Council (NERC), the National Physical Laboratory (NPL), and Royal Holloway Department of Earth Sciences for financial support. For the fieldwork in Svalbard, NERC Field Spectroscopy Facility (FSF) for the equipment loan (662.112), the NERC Arctic Office, Kings Bay AS; Dr Amelia Marks for assistance with measurements, and Nick Cox at the British Antarctic Survey (BAS), who provided invaluable support in planning, logistics, and assistance with measurements. In addition, thank you to Dr Alasdair MacArthur, and in particular, Dr Paul Green, for providing pertinent advice and guidance around planning and conducting the field measurements in Svalbard. For the laboratory measurements using the sea ice simulator, thank you to Dr Amelia Marks and Maxim Lamare for assistance with measurements, and in particular, thank you to Jerry Morris for engineering crucial aspects of the sea ice simulator and laboratory goniometer. For the sea ice BRDF modeling study, thank you to Dr John Hedley for providing essential advice and guidance relating to the radiative-transfer model, PlanarRad. For the laboratory PTFE reflectance study, thank you to Dr Emma Woolliams for excellent supervision at NPL, Dr Andrew Levick, and others in the Optical Measurement group for their support and guidance throughout my time at NPL. Last, but certainly not least, a heartfelt thank you to all those family and friends; especially Jen and Grace, who have provided generous support and continuous encouragement to me over the course of this PhD.

Chapter 1

Introduction

1.1 Aims of this study

The thesis aims to investigate the bidirectional reflectance (BRDF) of snow and sea ice through the use of ground-based field and laboratory methods. There are 3 core areas of focus within the thesis; (1) the characterization of the bidirectional reflectance of Arctic snow covered tundra at large solar zenith angles using the GonioRAdiometric Spectrometer System (GRASS) (Ball et al., 2015); (2) the characterization of the bidirectional reflectance of laboratory generated sea ice, using a specially designed laboratory goniometer and the Royal Holloway sea ice simulator; and (3) an investigation into the temperature effects on PTFE reflectors used as reference standards for reflectance (Ball et al., 2013). The overarching aim of the study is to contribute to a better understanding of the bidirectional reflectance of the cryosphere and the methodologies used to determine these properties, through a combination of field, laboratory and modeling studies.

1.2 The cryosphere, solar radiation and climate

The Earth's polar regions experience extreme cold temperatures owing to their distance from the equator, these regions are collectively know as the cryosphere; derived from the greek 'krios', meaning cold. In the Northern Hemisphere, snow covered area varies from approximately 4 million km^2 in August to around 45 million km^2 in January (Warner et al., 2009; Rees, 2006). While sea ice cover varies from around 8 million km^2 in September to around 15 million km^2 in March (Rees, 2006). At its maximum extent, snow and sea ice typically covers about 30 % of the total global land surface area, and 4 % of the total sea surface area respectively. Snow cover area and sea ice extent are highly variable seasonally and annually (Dye, 2002), and both are in long term decline (Stroeve et al., 2007; Comiso et al., 2008; Groisman et al., 1994).

Owing to the spatial extent of the cryosphere and its high reflectivity of short wave incident solar radiation its albedo is an important parameter in Earth energy budget calculations and global climate models (Qu and Hall, 2005; Flanner et al., 2011). The broadband albedo is the proportion of incident energy reflected from a surface integrated over all directions and over the solar spectrum, or more precisely, the hemispherical and wavelength integrated reflectance. The albedo of snow can be in excess of 0.9 at UV and visible wavelengths (Grenfell et al., 1994), which is approximately a factor of ten greater than that for open ocean, and a factor of 5 greater than that of bare ground (Weller and Holmgren, 1974). Mean cryospheric radiative forcing in the Northern Hemisphere was estimated by Flanner et al. (2011) as –4.6 W m^{-2} to –2.2 W m^{-2}, with a peak in May of about –9.0 ± 2.7 W m^{-2}. The presence of light absorbing impurities in snow and sea ice reduces the albedo of the cryosphere (Hansen and Nazarenko, 2004; Warren and Wiscombe, 1985), as does a thinner

snowpack (Wiscombe and Warren, 1980) and the decreasing proportion of multiyear sea ice (Perovich and Polashenski, 2012). Reduction in the albedo of the cryosphere leads to increased absorption of solar radiation and positive radiative forcing, which results in a positive feedback mechanism, whereby warming – as a result of decreased albedo – leads to a further reduction in albedo (Curry and Schramm, 1995; Hall, 2004; Box et al., 2012; Perovich et al., 2008). Cryospheric albedo feedback is likely to have contributed to the dramatic rise in Arctic near-surface air temperatures observed in recent decades (Screen and Simmonds, 2010).

It is becoming increasingly important to accurately monitor the surface radiation balance of the cryosphere to: (a) provide realistic inputs into global climate and snowmelt runoff models, as surface melting and ice discharge rates from glaciers continues to increase (Rignot et al., 2008; Velicogna, 2009); and (b) detect anthropogenic effects and feedback processes on surface albedo given a background of natural variability (Fox et al., 2011).

1.3 Remote sensing of cryospheric albedo

Passive remote sensing by spaceborne radiometers such as the Landsat Enhanced Thematic Mapper (ETM+), the Moderate Resolution Imaging Spectroradiometer (MODIS) and the Visible Infrared Imaging Radiometer Suite (VIIRS) offer the unique ability to monitor the albedo of vast inaccessible regions of the Earth – such as the cryosphere – at unprecedented spatial and temporal resolution. Daily global surface reflectance products are widely available for MODIS, VIIRS and ASTER, at a spatial resolution of 500 m, 375 m and 15 m respectively. Landsat ETM+ provides surface reflectance products with 16-day repeat cycles at 30 m resolution.

1.4 Derivation of albedo from satellite radiometers

A large number of studies have derived cryospheric surface radiation conditions through passive remote sensing by spaceborne radiometers (Hall et al., 1992; Dozier, 1984; Painter et al., 2009; Schaaf et al., 2002b; Zhonghai Jin and Simpson, 2000; Stroeve et al., 1997; Stroeve et al., 2006; Lindsay and Rothrock, 1994; Wright et al., 2014; Wanner et al., 1997; Masek et al., 2006; Box et al., 2012). Early studies of snow reflectance were able to derive the at-satellite, or planetary reflectance, by assuming the reflected radiance was equal in all directions (i.e. the target was a Lambertian reflector) (e.g. Koelemeijer et al., 1993; Hall et al., 1992; Hall et al., 1990; Dozier, 1984). The calculation required knowledge of the at-sensor radiance, and the amount of radiation incident at the top of the atmosphere, which was calculated from the known properties of solar radiation and the distance from the Sun to the Earth; the planetary reflectance is given by (Rees, 2006):

$$\rho_p = \frac{\pi L}{E_s \cos(\theta_s)} \qquad \text{Eq. 1.1}$$

where L is the radiance measured by the sensor, E_s is the solar exoatmospheric irradiance and θ_s is the solar zenith angle. By integrating L and E_s over the solar spectrum (approximately 300 nm to 2500 nm), ρ_p becomes the broadband planetary albedo (König et al., 2001).

The vast majority of satellite sensors measure radiance in narrow spectral bands, thus a variety of approaches have been developed to convert narrowband to broadband radiance (Knap et al., 1999; Li and Leighton, 1992; Hall et al., 1989; Choudhury and C Chang, 1979; Song and Gao, 1999). The at-surface broadband albedo can then be derived by accounting for atmospheric

attenuation, which is achieved through the use of atmospheric radiative-transfer code such as DISORT (Stamnes et al., 1988), 6SV1 (Kotchenova et al., 2006), or MODTRAN (Berk et al., 1999).

The assumption of a Lambertian reflector in Eq. 1.1 is invalid for snow and sea ice, which scatter incident radiation strongly in the forward direction (Perovich, 1996; Arnold et al., 2002; Kuhn, 1985; Warren, 1982). The extent of the reflectance anisotropy is dependent on the wavelength and incidence angle of the incoming solar radiation (Painter, 2004; Bourgeois et al., 2006), and the snow physical properties such as grain size, grain shape, density, liquid water content, impurity content and surface roughness (Peltoniemi et al., 2005; Warren et al., 1998). Solar incidence angles vary according to the time of day, season, latitude and the orbital characteristics of the satellite. Satellite sensor viewing angles vary according to the swath width and for sensors with specialist off-nadir viewing capabilities (e.g. MISR and POLDER). As a result, the radiance recorded by the satellite sensor is a function of the viewing angle and solar incidence angle. It has been shown that invoking the Lambertian assumption (as in Eq. 1.1) can easily result in errors of several percent in the albedo product (Knap and Reijmer, 1998; Zhonghai Jin and Simpson, 2000; Jin and Simpson, 2001; Zhonghai Jin and Simpson, 1999), which is incompatible with uncertainty requirements for Earth climate studies (Fox et al., 2011). High accuracy derivation of the at-surface broadband albedo requires knowledge of the angular distribution of reflected radiation and its wavelength dependence, which is quantified by the Bidirectional Reflectance Distribution Function (BRDF) (Nicodemus et al., 1977).

1.5 BRDF and albedo

The function that describes the angular distribution of reflected radiation is the Bidirectional Reflectance Distribution Function (BRDF). The BRDF describes the intrinsic reflectance properties of a surface, or the irradiance incident from one direction to its contribution to the reflected radiance in another direction (Nicodemus et al., 1977), and is given by,

$$BRDF_{\lambda} = \frac{dL_r(\theta_i,\phi_i;\theta_r,\phi_r;\lambda)}{dE_i(\theta_i,\phi_i;\lambda)}[sr^{-1}] \qquad \text{Eq. 1.2}$$

where L_r is the differential radiance reflected into the azimuth angle ϕ_r, and zenith angle θ_r, for a differential irradiance E_i incident on the surface from the azimuth direction ϕ_i, and zenith direction θ_i, λ is the wavelength. The angles and quantities used to define the BRDF are illustrated in Figure 1.1.

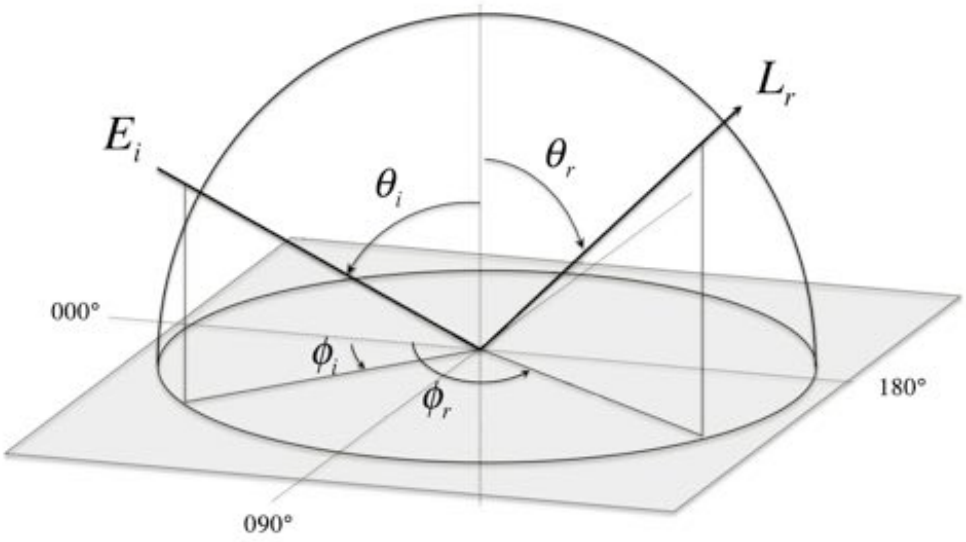

Figure 1.1. Angles and quantities required to define the BRDF: E_i is the irradiance from the azimuth direction θ_i, and the zenith direction ϕ_i, L_r is the measured radiance in the azimuth direction θ_r, and the zenith direction ϕ_r. From Ball et al. (2015).

When integrated over all reflected and incident angles in the upward hemisphere and over a given wavelength range, the BRDF gives the proportion of energy reflected from the surface, or its albedo. Many radiative-transfer computer codes can be used to calculate the BRDF and the albedo of snow or

sea ice (Painter, 2004; Mobley et al. 1998). For example, the discrete-ordinates radiative-transfer model (DISORT) (Stamnes et al. 1988) has been used to calculate the BRDF of snow and applied to correct satellite data for anisotropic reflectance in order to derive the surface albedo (Stroeve et al., 2006; Klein and Stroeve, 2002; Painter, 2004; Nolin et al., 1994). The MODIS BRDF/albedo product is based on a semi-empirical BRDF model and multi-date radiances to provide surface albedo products every 16 days (Schaaf et al., 2002a; Strahler and Muller, 1999). Hence, with knowledge of the angular distribution of reflected radiation – quantified by the BRDF – the albedo can be calculated; but critically, the accuracy of the albedo product is ultimately dependent on the accuracy of the BRDF model used. The characterization of the BRDF of natural surfaces for the validation of BRDF models has thus become a crucial aspect of remote sensing research in recent decades.

1.6 Radiometric concepts and quantities

Given that the BRDF (Eq. 1.2) is a ratio of infinitesimal quantities, it cannot be measured directly. Extension of the BRDF concept to a field or laboratory setup requires consideration of the physical constraints of the experiment setup. A consideration not always adhered to in the literature, which has led to many examples of ambiguous usage of terminology, as identified by Schaepman-Strub et al. (2006). To aid in the comparison between theoretical and measured quantities a brief overview of radiometric concepts and quantities and the nomenclature – as used in this study – is presented here. A detailed theoretical framework for reflectance quantities was first given by Nicodemus et al. (1977), but the terminology has since been updated and adapted for the optical remote sensing case by Martonchik et al. (2000) and Schaepman-Strub et al. (2006).

1.6.1 Geometric concepts in radiometry

Fundamental radiometric quantities are based on geometric concepts. Those most relevant to the measurements made in this study are introduced in this section.

1.6.1.1 Plane and solid angle

The concept of plane angle can be extended to three dimensions in order to describe how much of a given field of view is taken up by an object. Plane angle is defined as the length of an arc l divided by its radius r:

$$\theta = \frac{l}{r} \ [rad] \qquad \text{Eq. 1.3}$$

The angular measure of a full circle is 2π radians. Solid angle ω equals the ratio of the spherical area A on the surface of a sphere to the square of the radius r:

$$\omega = \frac{A}{r^2} \ [sr] \qquad \text{Eq. 1.4}$$

where ω is the solid angle. A hemisphere has a solid angle of 2π steradians given that the area of a sphere is $4\pi r^2$. Figure 1.2 illustrates a patch of differential area dA on the surface of a sphere.

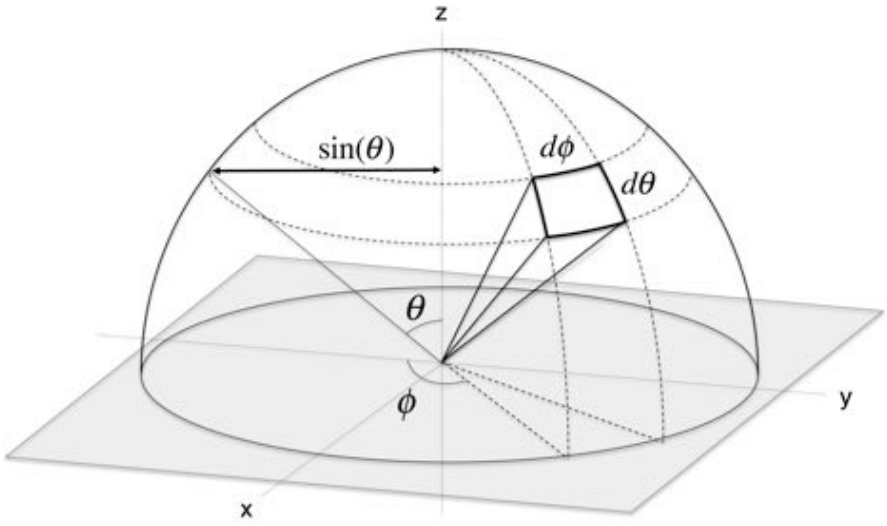

Figure 1.2. Projection of area onto a sphere

The differential spherical area dA on the surface of the sphere is given by:

$$dA = (r\sin(\theta)d\phi)(rd\theta) \qquad \text{Eq. 1.5}$$

where θ is the angle between the surface normal and the area projected on the sphere, $d\theta$ and $d\phi$ are the angular increments in zenith and azimuth respectively, and r is the radius. Combining Eq. 1.4 and Eq. 1.5 gives the differential solid angle $d\omega$:

$$d\omega = \frac{(r\sin(\theta)d\phi)(rd\theta)}{r^2} = \sin\theta d\theta d\phi \qquad \text{Eq. 1.6}$$

The solid angle $d\omega$ is a function of $\sin(\theta)$ as the great circles (lines of constant azimuth) converge at the poles of the sphere as shown in Figure 1.2. Integration of θ and ϕ over the solid angle determines the value of the solid angle:

$$\omega = \int_{\phi}\int_{\theta} \sin\theta\, d\theta\, d\phi \qquad \text{Eq. 1.7}$$

1.6.1.2 Projected area and project solid angle

Projected area is the area observed when the surface is tilted with respect to viewing direction. A surface tilted away from the plane perpendicular to the viewing direction will emit less energy towards the observer, or receive less energy from the observer, than if it were perpendicular to the viewing direction. As a result, the projected area decreases with the cosine of the viewing angle θ as shown by Figure 1.3.

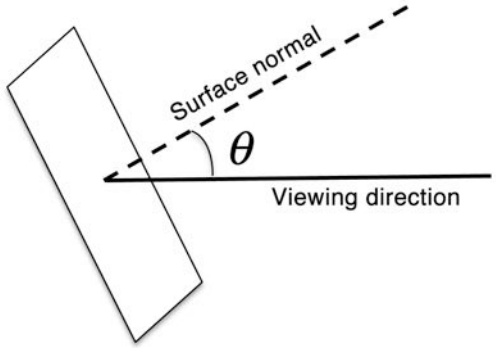

Figure 1.3. Representation of projected area

The projected area A_p is given by the cosine of the angle between the normal and the line of sight, the differential form is:

$$dA_p = \cos(\theta) dA \qquad \text{Eq. 1.8}$$

where A is the true geometric area and θ is the angle of inclination between the surface normal and the viewing direction. Integration over the surface area leads to A_p :

$$A_p = \int_A \cos(\theta) dA \qquad \text{Eq. 1.9}$$

Similar to projected area, the projected solid angle is the solid angle ω weighted by the cosine of the angle between the surface normal and the viewing direction. The projected solid angle is defined as the solid angle projected onto the plane at the base of the hemisphere (Palmer, 2010):

$$d\Omega = d\omega \cos\theta \qquad \text{Eq. 1.10}$$

where ω is the solid angle, and θ is the angle between the surface normal and the viewing direction. The surface area on the unit sphere in Figure 1.2 will have a smaller projected solid angle for regions of solid angle nearer to the equator, as viewed from a flat surface at the base of the hemisphere. A sphere subtends

2π steradians of projected solid angle, and a hemisphere subtends π steradians of projected solid angle.

1.6.2 Radiometric units

Radiometry is the measurement of optical radiation, and the relevant units (given in Table 1.1) relate to power, energy and the geometric characteristics of the measurement.

Symbols	Description	Units
A	Surface area	[m^2]
Φ	Radiant flux (power)	[W]
E	Irradiance	[W m^{-2}]
I	Radiant intensity	[W sr^{-1}]
L	Radiance	[W m^{-2} sr^{-1}]
M	Radiant exitance	[W m^{-2}]
ρ	Reflectance	[dimensionless]
R	Reflectance factor	[dimensionless]
θ	Zenith angle	[rad]
ϕ	Azimuth angle	[rad]
ω	Solid angle	[sr]
Ω	Projected solid angle	[sr]
λ	Wavelength	[nm]

Table 1.1. Units used to define quantities in radiometry and optical remote sensing

Units that relate solely to the optical properties of a medium are known as the inherent optical properties (IOPs) (Mobley, 1994), a list of IOPs relevant to this study is given in Table 1.2.

Symbols	Description	Units
A	Absorptance	[dimensionless]
T	Transmittance	[dimensionless]
S	Scatterance	[dimensionless]
a	Absorption coefficient	[m^{-1}]
b	Scattering coefficient	[m^{-1}]
c	Extinction coefficient	[m^{-1}]

α	Albedo	[dimensionless]
ω_0	Single scattering albedo	[dimensionless]
ψ	Scattering angle	[rad]
β_{vol}	Volume scattering function	[m^{-1} sr^{-1}]
β_{pf}	Scattering phase function	[sr^{-1}]
k	Imaginary index of refraction	[dimensionless]
n	Real index of refraction	[dimensionless]

Table 1.2. Terms, symbols and units used to describe the inherent optical properties of a medium. Adapted from Mobley (1994)

1.6.2.1 Energy and radiant flux

Radiant energy Q is measured in joules (J), whereas radiant flux Φ, or power, is measured in watts, which is energy per unit time. Radiant flux can be thought of as a derivative of energy: dQ/dt, or the rate of increase of energy over an interval of time dt.

1.6.2.2 Radiance

Radiance is the elemental quantity of radiometry; it gives an indication of the spatial distribution of power in terms of area and direction and is defined as the power Φ per unit area A, and per unit projected solid angle Ω (Palmer, 2010):

$$L = \lim_{\Delta A_s, \Delta\omega \to 0} \left(\frac{\Delta \Phi}{\Delta A \cos\theta \Delta\omega} \right) = \frac{d^2\Phi}{dA\cos\theta d\omega} = \frac{d^2\Phi}{dA d\Omega} \qquad \text{Eq. 1.11}$$

where ω is the solid angle and θ is the angle of inclination between the surface normal and the viewing direction. Radiance is a useful quantity because it can be used to calculate how much power will be received by an optical system viewing a surface from a particular angle of view.

1.6.2.3 Irradiance and radiant exitance

Irradiance is the radiant flux (power) arriving at a surface from all directions and radiant exitance is the radiant flux leaving a surface from all directions. As illustrated in Figure 1.4 irradiance E is defined as the power per unit area incident from all directions in a hemisphere onto a surface that coincides with the base of that hemisphere:

$$E = \frac{d\Phi}{dA} \qquad \text{Eq. 1.12}$$

where Φ is the power incident on the surface, and A is the area of the surface. Similarly, the radiant exitance, M, is the power per unit area leaving a surface into the upward hemisphere.

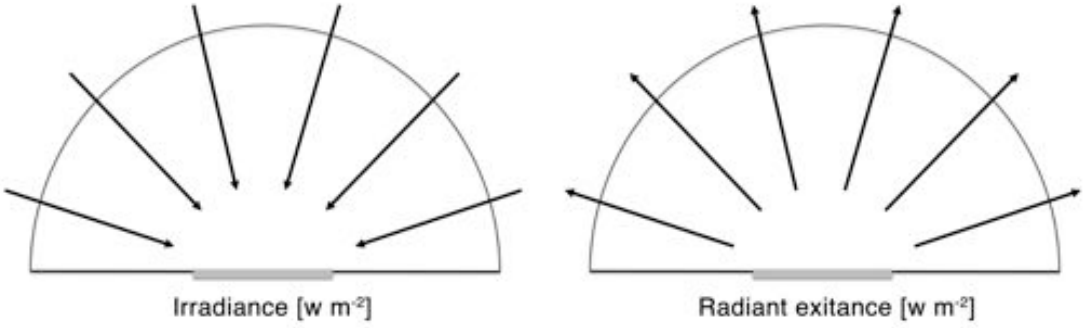

Figure 1.4. Representation of the radiometric quantities irradiance and radiant exitance

1.6.2.4 Relationship between radiance and radiant exitance

Radiant exitance can be calculated from the radiance reflected from a surface by integrating the radiance over the projected solid angle of the upward facing hemisphere. Given that the hemisphere subtends π steradians of projected solid angle, the radiant exitance M is

$$M = \int_{\pi} L \, d\Omega \qquad \text{Eq. 1.13}$$

If the radiance L is constant with direction (i.e. the surface is a Lambertian reflector) then integrating $d\Omega$ over the hemisphere equals π. Thus, the radiant

exitance is the product of the radiance reflected by the surface and π (Palmer, 2010):

$$M = \pi L \quad \text{Eq. 1.14}$$

1.6.2.5 Lambertian BRDF

A Lambertian surface reflects radiance equally into all directions. Its BRDF is simply:

$$BRDF_{lamb}(\theta_i, \phi_i; \theta_r, \phi_r) = \frac{\rho}{\pi} \quad \text{Eq. 1.15}$$

where ρ is the reflectivity of the surface. Lambertian surfaces do not exist in nature, but good approximations are matte paper, except at grazing incidence angles where the specular component becomes much more dominant in the reflected radiance distribution.

1.6.2.6 Radiant intensity

Radiant intensity I, sometimes referred to as intensity, is the power emitted per unit solid angle in a specified direction:

$$I = \frac{d\Phi}{d\omega} \quad \text{Eq. 1.16}$$

where Φ is the radiant flux and ω is the solid angle. Intensity can be derived from the radiance reflected by a surface in a particular direction by integrating over the area of the surface:

$$I = \int_A L \, dA \quad \text{Eq. 1.17}$$

Likewise radiant flux can be found by integrating over the solid angle of the detector:

$$\Phi = \int_{\omega} I \, d\omega \qquad \text{Eq. 1.18}$$

Given that a sphere subtends a solid angle of 4π steradians, an isotropic point source emits a radiant flux a factor of 4π larger than the radiant intensity.

1.6.2.7 Lamberts cosine law

Lambert's cosine law states that the radiant intensity from a flat surface is reduced by the cosine of the observation angle. For the special case of a Lambertian surface, the radiance is independent of view angle because the observed area that the detector samples is increased by the cosine of the observation angle.

1.6.2.8 Reflectance

Reflectance, or reflectivity, is a general term referring to how much radiation is reflected from a surface, given the conservation of energy its value must be between 0 and 1. To add precision to its definition the word "reflectance" should be proceeded by two adjectives, one that describes the position of the light source, and one that describes the detector (Mobley, 2010). For example, *Direction-hemispherical* reflectance describes the proportion of light reflected from a particular direction into the entire hemisphere. Whereas *hemispherical-directional* reflectance describes the proportion of light reflected from the entire hemisphere into a particular direction (Schaepman-Strub et al., 2006). The various reflectance quantities relevant to this study are defined in the following sections.

1.6.2.9 Bihemispherical reflectance (albedo)

The bihemispherical reflectance, generally called albedo, is used to describe the proportion of radiant flux reflected by a surface into the entire hemisphere, to the radiant flux incident on a surface from the entire hemisphere. Bihemispherical reflectance is thus the ratio of radiant exitance to irradiance. Following the law of energy conversation, the bihemispherical reflectance must be between 0 and 1.

1.6.2.10 Reflectance factors

Measuring the directional reflectance properties of a surface usually involves measuring the reflectance factor. A reflectance factor is the ratio of radiant flux reflected by a surface to that reflected into the same beam geometery for a given wavelength range by a lossless Lambertian reflector, irradiated under the same conditions. A Spectralon panel is commonly used to approximate a lossless Lambertain reflector as it exhibits near Lambertian reflectance over the UV-VIS-NIR region of the spectrum (350 nm to 1700 nm) and is chemically inert making it suitable for field use (Springsteen, 1999; Weidner and Hsia, 1981). Reflectance factors can reach values greater than 1, especially for strongly forward scattering surfaces such as snow and sea ice (Painter, 2004; Bourgeois et al., 2006).

The bidirectional reflectance factor (BRF) is commonly used to describe the proportion of reflected radiant flux as a function of illumination and viewing angle (Schaepman-Strub et al., 2006):

$$BRF(\lambda) = \frac{d\Phi_r(\theta_i, \phi_i; \theta_r, \phi_r; \lambda)}{d\Phi_r^{id}(\theta_i, \phi_i; \lambda)} \qquad \text{Eq. 1.19}$$

where Φ_r is the radiant flux reflected in to the zenith angle θ_r and azimuth angle ϕ_r, for the incident zenith angle θ_i and the incident azimuth angle ϕ_i, Φ_r^{id}

is the radiant flux reflected by a lossless Lambertian reflector. Given that a Lambertian surface reflects the same radiance in all directions the view zenith and azimuth angles are omitted from the denominator in Eq. 1.19. The BRDF can be obtained from the BRF by dividing the BRF by π (Schaepman-Strub et al., 2006).

The hemispherical directional reflectance factor (HDRF) is similar in definition to the BRF, but includes illumination from the entire hemisphere:

$$HDRF(\lambda) = \frac{L_r(\theta_i, \phi_i, 2\pi; \theta_r, \phi_r; \lambda)}{L_r^{id}(\theta_i, \phi_i, 2\pi; \lambda)} \qquad \text{Eq. 1.20}$$

where L_r is the radiance reflected into the viewing azimuth ϕ_r, and viewing zenith θ_r, for a given radiance L_r^{id} reflected by a lossless Lambertian reflector into the same beam geometry under ambient illumination conditions with a solar azimuth ϕ_i, and solar zenith θ_i, λ is the wavelength.

1.6.2.11 Measurable directional reflectance factors

From the strict physical point of view, the mathematical concepts of BRDF, BRF and HDRF can only be approximated by measurements as sensors subtend a finite field of view (FOV), which has to be large enough for measurable amounts of radiant flux to be detected (Nicodemus et al., 1977). As a result, measurable quantities of reflectance are either conical or hemispherical in geometrical configuration rather than directional (Schaepman-Strub et al., 2006; Nicodemus et al., 1977). Further, it is not possible to achieve purely directional illumination under field conditions as solar irradiance consists of both a direct term (non-scattered) and a diffuse term (scattered by clouds, aerosols, gases and the surrounding terrain) (Lyapustin and Privette, 1999). As a result, Schaepman Strub et al. (2006) presented measurable quantities applied to the remote

sensing case that describe the angular distribution of reflected radiation from a surface, these quantities are presented in Figure 1.5.

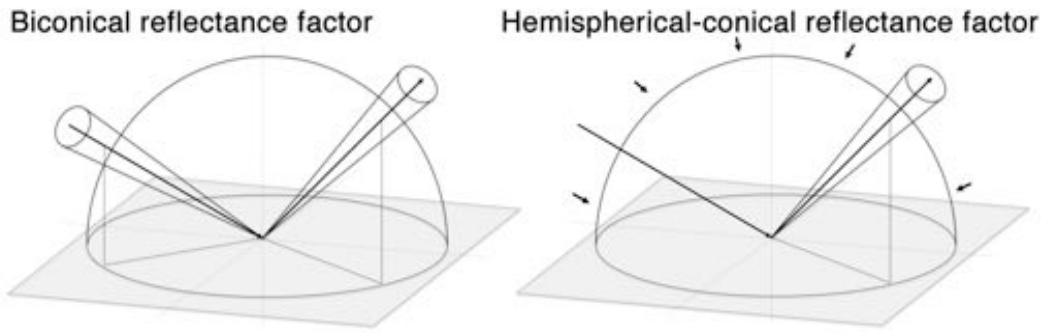

Figure 1.5. Measurable directional reflectance quantities used to approximate the bidirectional reflectance distribution function (BRDF) of a surface

The surface area on the unit sphere taken up by the end of each cone in Figure 1.5 represents the solid angle subtended by the light source and the detector. It is common in the literature to read that the BRDF, BRF or HDRF was 'measured' when an author is describing a physical experiment or measurement, in which case it should be assumed that the actual quantity being referred to is the biconical reflectance factor (CCRF), or the hemispherical-conical reflectance factor (HCRF). The degree to which the CCRF or HCRF measurement resembles the directional quantity (BRDF, BRF, HDRF) will depend on geometrical configuration of the experiment setup, and more specifically, the range of angles the detector and light source integrate over. The CCRF will better approximate the BRDF if: (a) the light source is well collimated and subtends a small solid angle through which the source emits radiation; and (b) the sensor subtends a small solid angle through which it is sensitive to radiation (i.e. the sensor has a small instantaneous field of view (IFOV). In addition, the range of angles the sensor integrates over is also dependent on the ground instantaneous field of view (GIFOV), or the size of the foreoptic footprint on the target surface, as shown in Figure 1.6.

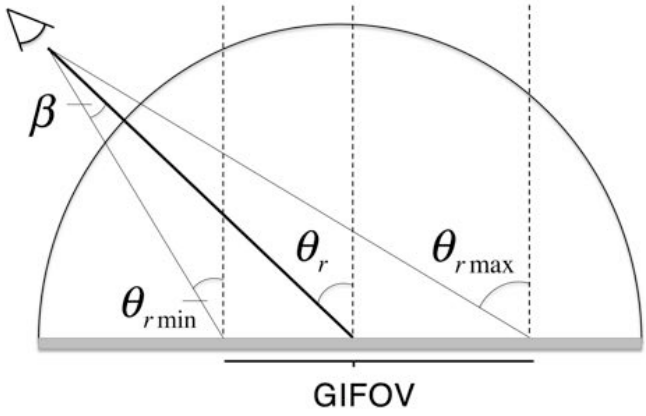

Figure 1.6. Viewing angles associated with the sensors field of view (FOV). β is the sensors half angle FOV, θ_r is the viewing angle central to the sensors FOV, $\theta_{r\max}$ is the maximum viewing angle in the sensors FOV, $\theta_{r\min}$ is the minimum viewing angle in the sensors FOV

The CCRF is usually the measurable quantity obtained through laboratory studies of reflectance, and is defined as (Schaepman-Strub et al., 2006):

$$CCRF_\lambda = \frac{\int_{\omega_r}\int_{\omega_i} f_r(\theta_i,\phi_i;\theta_r,\phi_r;\lambda)L_i(\theta_i,\phi_i;\lambda)d\Omega_i\, d\Omega_r}{(\Omega_r/\pi)\int_{\omega_i} L_i(\theta_i,\phi_i;\lambda)d\Omega_i} \quad \text{Eq. 1.21}$$

where $f_r(\theta_i,\phi_i;\theta_r,\phi_r;\lambda)$ is the spectral BRDF, L is the radiance, ϕ, θ define the azimuth and zenith angles central to the cone respectively, Ω is the projected solid angle of the cone and ω is the solid angle of the cone, λ is the wavelength, while the subscripts i and r define the incident or reflected radiation respectively.

For measurements that are performed under ambient sky illumination the incident irradiance originates from the entire hemisphere, in which case the extent to which the measurement resembles BRDF will also depend on the fraction of diffuse irradiance, which has strong wavelength dependence and causes HCRF measurements to be less representative of the BRDF at shorter wavelengths (Li and Zhou, 2004). For field measurements made under ambient sky illumination the incident cone has a solid angle of 2π, thus the measurable

quantity is most accurately described as the hemispherical-conical reflectance factor (Schaepman-Strub et al., 2006):

$$HCRF_{\lambda} = \frac{\int_{\omega_r}\int_{2\pi} f_r(\theta_i,\phi_i;\theta_r,\phi_r;\lambda)L_i(\theta_i,\phi_i;\lambda)d\Omega_i\, d\Omega_r}{(\Omega_r/\pi)\int_{2\pi} L_i(\theta_i,\phi_i;\lambda)d\Omega_i} \quad \text{Eq. 1.22}$$

The CCRF and HCRF are integrated quantities over a range of angles and can only provide an approximation of BRDF or BRF, thus BRDF and BRF remain the most useful quantities from a modeling perspective. A detailed discussion of reflectance quantities in optical remote sensing – including their mathematical derivation – is given by Schaepman-Strub et al. (2006).

To aid in the comparison of directional reflectance measurements it is often useful to quantify the extent of the reflectance anisotropy in the distribution of reflected radiation using a single value. The extent of the anisotropy can be quantified by the anisotropy index, ANIX (Bourgeois et al., 2006):

$$ANIX(\lambda) = \frac{HCRF_{\max}(\lambda)}{HCRF_{\min}(\lambda)} \quad \text{Eq. 1.23}$$

Note that the HCRF term in Eq. 1.23 can be replaced by any directional reflectance quantity (i.e. CCRF, HDRF, BRDF or BRF).

1.7 Previous field and laboratory studies of snow and sea ice directional reflectance

There has been considerable effort to characterize the angular distribution of light reflected by snow empirically to assist in the development and parameterization of snow BRDF models (Painter, 2004; Bourgeois et al., 2006; Peltoniemi et al., 2005; Kuhn, 1985; Hall et al., 1992; Hudson et al., 2006; Aoki and Aoki, 2000; Li and Zhou, 2004; Dumont et al., 2010). Very a few studies have made ground based measurements of bare sea ice HCRF or CCRF

(Perovich, 1994; Schlosser, 1988). This section summarizes the techniques used in previous field and laboratory studies of snow and sea ice BRDF. A list of previous field and laboratory studies of snow and sea ice BRDF is given in Table 1.3, a review of previous field studies is given in Section 1.7.1 and review of previous laboratory studies is given in Section 1.7.3.

Author	Type of study	Quantity measured	Spectral range (nm)	Spectral resolution (nm)	View zenith angles (°)	View azimuth angles (°)	Incident angles (°)
O'Brien and Munis [1975]	Snow (laboratory)	CCRF	600 – 2500	0.3 – 3.0	5, 30	0	0, 5
Kuhn [1985]	Snow (field)	HCRF	450, 514, 750, 1000	15 – 25	60 – 87 by 10	± 60	61, 67
Steffen [1987]	Snow (field)	HCRF	500 – 600	single band	45, 60, 75	0 – 345 by 15	28 – 76
Schlosser [1988]	Sea ice (laboratory)	CCRF	400 – 1350	broadband	61 – 73	0 – 60 by 10	61 – 68
Dozier et al. [1988]	Snow (field)	HCRF	368 – 1100	5 – 10	0 – 75 by 15	0 – 180 by 45	21 – 58
Perovich [1994]	Sea ice (field)	HCRF	400 – 1000	8	0 – 60 by 30	0 – 330 by 30	60 – 70
Grenfell et al. [1994]	Snow (field) (tower)	HCRF	900		0 – 75 by 15	0 – 360 by 15	75
Leroux et al. [1998a]	Snow (field)	HCRF	450, 650, 850, 1650	100	0 – 80 by 10	0, 90, 180, 270	48 – 63
Warren et al. [1998]	Snow (field) (tower)	HCRF	600, 660, 900	10	22.5 – 82.5 by 15	0 – 210 by 15	67–90
Aoki et al. [2000]	Snow (field)	HCRF	350 – 2500	3 < 1000, 10 > 1000	0 – 80 by 10	0 – 337.5 by 22.5	54 – 57
Painter and Dozier [2004]	Snow (field)	HCRF	350 – 2500	3 < 1000, 10 > 1000	0–80 by 10	0 – 350 by 10	51 – 47
Li and Zhou [2004]	Snow covered sea ice (field)	HCRF	350 – 1050	1.4	10 – 80 by 10	0 – 180 by 10	65, 85
Peltoniemi et al. [2005]	Snow (field)	HCRF, CCRF	390 – 1070	4	0 – 75		55 – 72
Hudson et al. [2006]	Snow, (field) (tower)	HCRF	350 – 2400	3 – 30	22.5 – 82.5 by 15	0 – 345 by 15	51 – 87
Bourgeois et al. [2006]	Snow (field)	HCRF	350 – 1050	3	0 – 85 by 15	0 – 360 by 15	49 – 85
Dumont et al. [2010]	Snow (laboratory)	CCRF	5000 – 2600	0.2 – 0.6	0 – 80	0, 45, 90, 135, 180	0, 30, 60, 70
Kuchiki et al. [2011]	Snow (field)	HCFC	350 – 2500		0 – 60 by 15	0, 45, 180, 225, 90, 270, 135, 315	52.5 – 52.9

Table 1.3. Previous field and laboratory measurements of snow and sea ice BRDF

1.7.1 Review of field studies of snow BRDF

Middleton and Mungall (1952) were among the first to make HCRF measurements of snow using a portable field goniometer, their study showed evidence of a specular reflection that was dependent on the snow type and the angle of incidence. Dirmhirn and Eaton (1975) observed the anisotropic nature of snow reflectance and identified a forward scattering peak using a single broadband measurement spanning the wavelength range 200 nm to 4500 nm. Warren (1982) reviewed previous measurements of snow reflectance and reported that snow reflectance was not isotropic, it was rather a function of 3-angles: the source zenith angle θ_i, the view zenith angle θ_r, and the relative azimuth angle $\phi_i - \phi_r$.

Kuhn (1985) presented the first detailed measurements of snow HCRF for different snow types. A few years later Steffen (1987) recorded the HCRF over a range of solar incident angles for snow with varying snow grain size. Dozier et al. (1988) determined through a combination of radiative-transfer modeling and field measurements that the strength of forward scattering increased with wavelength. Possible effects of longitudinal roughness features (sastrugi) on the BRDF of snow were recognised by Grenfell (1994) who measured the HCRF of snow from a 23 m tower in Antarctica. Four years later, Warren et al. (1998) carried out experiments from the same tower as Grenfell (1994) and specifically investigated the effect of sastrugi on the BRDF of snow, the authors concluded that the effects of the sastrugi were mainly restricted to large viewing angles for wavelengths up to 900 nm.

Leroux et al. (1998) investigated the influence of snow grain shape and size on the HCRF, as well as the polarization of light reflected by snow. In the study by Leroux et al. (1998) model simulations based on the assumption of spherical snow grains were not able to reproduce field measurements of HCRF for all view angles, the authors showed better agreement between the model and field results when hexagonal particles were used in the model (Leroux et al., 1998). Aoki et al. (2000) studied the effect of snow grain size and impurities on the BRDF of snow and compared the results with two radiative-transfer models (Aoki and Aoki, 2000). Li and Zhou (2004) also compared field measurements with radiative-transfer simulations. The field measurements by Li and Zhou (2004) were performed under large solar zenith angles and BRF and HDRF radiative-transfer simulations were made using in-situ snow physical data as inputs to model. The authors found that the HDRF simulations were within ± 10 % of the field HCRF measurements for view angles $< 45°$ and agreed better than the BRF simulations.

Several studies have since reported HCRF measurements investigating the influence of solar zenith angle and various snow properties on the BRDF of snow, the snow properties investigated include grain size and shape, wetness, impurity content, density and depth. Published in 2004, experiments by Painter and Dozier (2004) involved the measurement of HCRF at high spectral resolution using an automated goniometer, the authors compared the field measurements with the radiative-transfer model DISORT (Stamnes et al., 1988). Peltoniemi et al. 2005 measured the HCRF of snow at various locations in Finland and observed a dependence on snow grain shape, snow wetness and density. Bourgeois et al. (2006) collected HCRF measurements over a wide range of solar zenith angles (49° to 85°) on the Greenland ice sheet, the

measurements showed the strongest anisotropy for smooth surfaces and for large solar zenith angles. Hudson et al. (2006) made a comprehensive set of HCRF measurements over a 96 different solar zenith angles from 51° to 87° over a wavelength range 350 nm to 2400 nm at high spectral resolution from a 32 m tower at Dome C in Antarctica (Hudson et al., 2006). The snow surface at Dome C was smoother and the roughness elements were more randomized than for snow surfaces previously measured from other towers in Antarctica. The measurements by Hudson et al. (2006) showed a decrease in anisotropy at shorter wavelengths, the authors indicate that their measurements of HCRF were not representative of the BRDF of snow for wavelengths less than 900 nm because of atmospheric Rayleigh scattering. Kuchiki et al. (2011) studied the effect of sastrugi on snow BRDF in detail by measuring the HCRF over artificial linear ridges of snow (Kuchiki et al., 2011). The study reported differences of up to ± 50 % in the HCRF measurements when compared to the HCRF for a flat snow surface. A Monte Carlo radiative-transfer model was able to reproduce the field measurements using artificial ridges and for previous measurements of natural sastrugi made at the South Pole by Warren et al. (1998).

1.7.2 Review of field studies of sea ice BRDF

To the author's knowledge, very few studies in the literature have reported ground based HCRF measurements of bare sea ice. Perovich (1994) reported HCRF measurements for first year sea ice over a wavelength range of 400 nm to 1000 nm for 3 different viewing zenith angles (0°, 30° and 60°) for 360° of azimuth angles at 30° intervals. The measurements were obtained using a 1° FOV foreoptic at solar zenith angles between 60° and 70° for 5 distinct surface types: (1) ice covered by dry snow, (2) ice covered by dry snow with a glazed surface (3) bare ice (4) blue ice, and (5) melt pond. The measurements

indicated the HCRF was weakly azimuthally dependent at 30° viewing azimuth angles. A strong specular speak was observed at 0° azimuth and 60° zenith for all ice types. The anisotropy in the HCRF was greatest for bare ice and glazed snow surfaces, for bare ice there was a 3-fold increase in the HCRF from the backward to the forward direction at 60° zenith angle in the solar principal plane (Perovich, 1994). Li and Zhou (2004) carried out HCRF measurements on two snow covered second year ice floes in the Ross Sea, Antarctica. The measurements were obtained with a 26 cm and 36 cm thick snowpack under 66° and 85° solar zenith angles respectively. Viewing zenith angles were sampled over the range 10° to 80° degrees at 10° intervals for 0° to 180° in azimuth at 10° intervals, with 15° and 2° FOV foreoptics. The measurements were compared with a multilayered plane-parallel radiative-transfer model. Simulated HDRF agreed to within ±10 % for viewing zenith angles less than 45° for the lateral sides of the viewing hemisphere (Li and Zhou, 2004). Both modeling and measurements revealed the strong forward scattering nature of snow and sea ice, and the dependence of the BRDF on solar zenith angle.

A quantitative comparison of field BRDF studies in Table 3 is difficult because the studies provide measurements of HCRF and CCRF which by definition, are different physical quantities and not directly comparable. For example, HCRF and CCRF are dependent on the sensor IFOV and GIFOV. In addition, HCRF is dependent on the atmospheric conditions and the surrounding terrain at the time of the measurement. Laboratory BRDF studies with a narrow sensor FOV and well collimated source potentially offer a major advantage over field-based studies because the diffuse component of irradiance can almost be completely eliminated.

1.7.3 Review of laboratory studies of snow and sea ice BRDF

A practical way to study sea ice is through laboratory experiments that allow control of environmental conditions, and which reduce the hazards and costs associated with studying sea ice in the field. Several large scale facilities have been created to simulate sea ice in the laboratory, including: the United States Cold Regions Research and Engineering Laboratory (CRREL); the Arctic environment test basin in Germany; the Aalto University ice tank in Finland; and the sea ice environmental research facility in Canada. The majority of large-scale simulators have been designed to study the mechanical behavior, structural interactions and the biology and chemistry of sea ice. Few laboratory facilities have been designed to measure radiation reflected by sea ice. Perovich and Grenfell (1981) studied the optical properties of young sea ice by growing ice at different temperatures and different salinities in a 1 m diameter cylindrical tank, for the wavelength range 400 nm to 1000 nm. Marks (2014) studied the effect of black carbon on light penetration on sea ice generated using the Royal Holloway Sea Ice Simulator.

Fewer studies have reported laboratory CCRF measurements of snow or sea ice. Schlosser (1988) measured a broadband radiance reflected from laboratory-generated sea ice using a photometer and a slide projector as an artificial light source. The results showed a forward scattering peak in the specular direction that was less developed for thicker ice and for colder ice (–27° C). The authors attributed the decrease in anisotropy for colder and thicker ice to an increase in scattering caused by a greater number of air bubbles, brine inclusions and precipitated salts per unit volume.

Combining observed BRDF with polarization measurements may be an effective method for estimating the physically properties of ice, such as air bubbles and brine inclusions, through inverse models of ice radiative-transfer. As such, a number of studies have investigated the polarization of light reflected by sea ice (Perovich and Gow, 1996; Sun et al., 2013; Perovich, 1998; Miller et al., 1997). Sun et al. (2013) conducted a laboratory study that measured the spectral distribution (350 – 2500 nm) of the degree of linear polarization for bubble-free sea ice and lake ice with air bubbles at the nadir and specular directions only. The study found that polarization was greatest at larger incident angles and was inversely, but not linearly, proportional to reflectance, with bubbles and brine pockets also contributing inversely to linear polarization.

Dumont et al. (2010) measured the CCRF of 4 natural snow samples in a cold room at – 10 °C over the wavelength range 500 nm to 2600 nm for a wide range of incident and viewing angles. The measurements by Dumont et al. (2010) are a close approximation of BRDF as the detector has a narrow FOV (2.05° half angle) and the light source is well collimated and subtends a small solid angle.

1.7.4 Comparison of field and laboratory studies

Laboratory experiments are not affected by atmospheric conditions such as aerosols, cloud cover, changing sun angle, or environmental effects such as wind, or changing temperatures. In addition, during a laboratory study the operator has full control over the position of the light source, whereas the angle of the incident radiation during a field campaign is dependent on the time of year and the location of the field study. Control over the angles of incidence makes it easier to take repeated measurements on the same surface, which allows for a better assessment of the measurement precision. Given that it is very difficult to

obtain reliable measurements of radiance from multiple angles simultaneously, it is very useful to have a stable illumination source during the acquisition of HCRF or CCRF. Irradiance in a laboratory study can be stabilized or the output can be monitored, whereas under field conditions irradiance can vary as a result of changes in atmospheric conditions, or due to the movement of the sun in the sky. Ability to control the fraction of diffuse irradiance is a major advantage in a laboratory study, as completely eliminating the diffuse irradiance under natural conditions is not possible. It is also problematic to measure the fraction of diffuse irradiance in the field. Some field studies have estimated the fraction of diffuse irradiance by obscuring the direct portion of irradiance from the target surfacing using a screen (Peltoniemi et al., 2005), however, given that atmospheric aerosols are strongly forward scattering a significant portion of diffuse irradiance follows a path close to the original solar path (Lyapustin and Privette, 1999), meaning that much of diffuse irradiance is also obscured by the screen (Schaepman-Strub et al., 2006). In the laboratory diffuse irradiance can be significantly reduced and almost eliminated through the use of blackout materials that absorb the scattered light.

However, there are several disadvantages to laboratory BRDF studies. Creating an artificial light source that is well collimated, subtends a small solid angle and also provides sufficient intensity to provide acceptable signal to noise levels offers considerable challenges, all of which cannot be fully overcome. Hence laboratory irradiance is usually heterogeneous and not well collimated. In addition, given the proximity of the light source to the target area, temperature changes and heating of the sample may lead to changes in the BRDF characteristics of the sample during the acquisition. During a laboratory study the sample is not in-situ and is limited to relatively small dimensions, which may

result in a CCRF that is unrepresentative of the BRDF of the sample in situ, or under natural irradiance. Sandmeier et al. (1998) and Sandmeier and Strahler (2000) give a detailed discussion of the methodologies used for laboratory BRDF studies and identify common sources of uncertainty.

1.8 Interaction of light with matter

In order to understand how light is reflected from a medium the absorption and scattering properties of that medium need to be considered. The absorption and scattering properties of a medium are described by its inherent optical properties (IOPs), these properties are intrinsic to the medium, and therefore independent of the ambient light field under which any measurement of reflectance is made (Mobley, 1994).

1.8.1 Absorption transmission and scattering

When light interacts with a surface it can be absorbed, transmitted or scattered. Absorptance A is the fraction of incident radiant flux that is absorbed within the medium:

$$A(\lambda) = \frac{\Phi_a(\lambda)}{\Phi_i(\lambda)} \qquad \text{Eq. 1.24}$$

where Φ_α is the radiant flux absorbed, Φ_i is the incident radiant flux, and λ is the wavelength. Transmittance T is the fraction of incident radiant flux that passes through the medium:

$$T(\lambda) = \frac{\Phi_\tau(\lambda)}{\Phi_i(\lambda)} \qquad \text{Eq. 1.25}$$

where Φ_τ is the radiant flux transmitted. Scatterance S is the fraction of incident radiant flux that is scattered out of the unidirectional beam into all directions:

$$S(\lambda) = \frac{\Phi_s(\lambda)}{\Phi_i(\lambda)} \qquad \text{Eq. 1.26}$$

where Φ_s is the radiant flux scattered. Scattered photons may undergo multiple scattering inside the medium before eventually becoming reflected, transmitted or absorbed. If a photon exits through the top layer of the medium it is reflected and contributes to the surface BRDF or albedo, if the photon exits beneath the medium it is transmitted and contributes to the diffuse transmittance. By the conservation of energy the sum of the absorptance, transmittance and scatterance is unity, or

$$A(\lambda) + T(\lambda) + S(\lambda) = 1 \qquad \text{Eq. 1.27}$$

The absorption coefficient a describes the extinction of light per unit distance in the medium due to absorption by the medium and is given by (Mobley, 1994):

$$a(\lambda) = \frac{dA(\lambda)}{dr} \qquad \text{Eq. 1.28}$$

where A is the absorptance and r is the thickness of the medium. Likewise, the scattering coefficient, b, describes the extinction of light per unit distance in the medium due to scattering (Mobley, 1994):

$$b(\lambda) = \frac{dS(\lambda)}{dr} \qquad \text{Eq. 1.29}$$

The extinction coefficient c (often known as the attenuation coefficient) is the sum of the scattering and absorption coefficients:

$$c(\lambda) = a(\lambda) + b(\lambda) \qquad \text{Eq. 1.30}$$

The extinction coefficient can be thought of as the fraction of incident radiation removed from a unidirectional beam per unit length in the medium.

It is useful to quantify the proportion of radiant flux that is initially scattered in the medium, this is given by a quantity known as the single-scattering albedo (ω_0), which is the ratio of the scattering coefficient to the extinction coefficient:

$$\omega_0(\lambda) = \frac{b(\lambda)}{c(\lambda)} \qquad \text{Eq. 1.31}$$

For mediums that are strongly scattering and weakly absorbing, such as snow and sea ice, the single scattering albedo is near unity. The single scattering albedo is also the probability that a photon will be scattered in any given direction, rather than absorbed.

1.8.2 Penetration depth and transmission

The product of the extinction coefficient c and the thickness of the medium z is known as the optical depth:

$$\tau(\lambda) = c(\lambda)\ z \qquad \text{Eq. 1.32}$$

Each nondimensional unit of optical depth τ corresponds to a reduction in irradiance by $1/e$, or ~ 37% of the initial value. The transmittance T is related to optical depth as follows:

$$T = e^{-\tau} \qquad \text{Eq. 1.33}$$

The e-folding depth ε gives a measure of light penetration into the medium, and is the length of the path where the incident irradiance has been reduced to $1/e$ (~ 37 %) of its previous value:

$$\varepsilon(\lambda) = \frac{1}{c(\lambda)} \qquad \text{Eq. 1.34}$$

1.8.3 Complex refractive index

The fundamental optical property of a pure bulk material is its complex refractive index, which describes the interactions of radiation with a homogenous media in a single parameter (Petty, 2006):

$$N = n_r + n_i i \qquad \text{Eq. 1.35}$$

The real part of the complex refractive index, n_r, determines the phase speed of radiation in the medium relative to the speed of light in a vacuum. As radiation enters a medium it is the change in phase speed that gives rise to reflection and refraction, thus n_r controls the scattering properties of the medium. The imaginary part of the index, n_i, determines the absorption properties of the medium, when n_i is nonzero, absorption of radiation occurs within the medium. The absorption coefficient a is related to n_i as follows (Petty, 2006):

$$a(\lambda) = \frac{4\pi n_i(\lambda)}{\lambda} \qquad \text{Eq. 1.36}$$

where λ is the wavelength in a vacuum. The real and imaginary parts of the complex index of refraction for ice, as given by Warren and Brandt (2008), are presented as a function of wavelength in Figure 1.7. The imaginary part of the index of refraction of ice is very small in the visible band, but increases more than 6 orders of magnitude over the wavelength range 400 nm to 1800 nm (Warren and Brandt, 2008). Whereas the real part of the complex index of refraction of ice is near constant over the same wavelength range, varying less than 0.04.

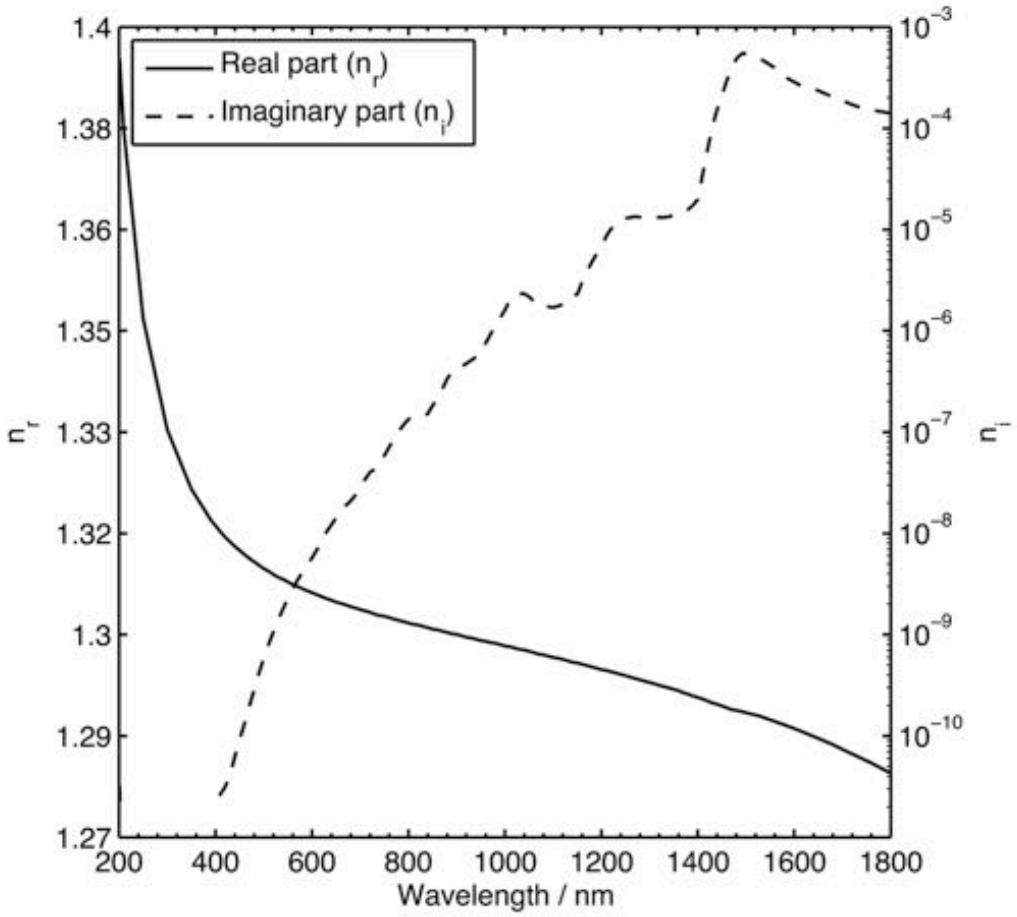

Figure 1.7. Real, n_r, and imaginary, n_i, parts of the complex index of refraction of ice (data from Warren and Brandt, 2008)

Another useful quantity that can be derived from n_i of a medium is the penetration depth D, which is the reciprocal of the absorption coefficient (Petty, 2006), and describes extinction owing to absorption in the medium only:

$$D(\lambda) = \frac{\lambda}{4\pi n_i} \qquad \text{Eq. 1.37}$$

The penetration depth D is a function n_i and thus is strongly wavelength dependent for ice. D has been calculated for bubble-free pure ice using Eq. 1.37 and is presented in Figure 1.8.

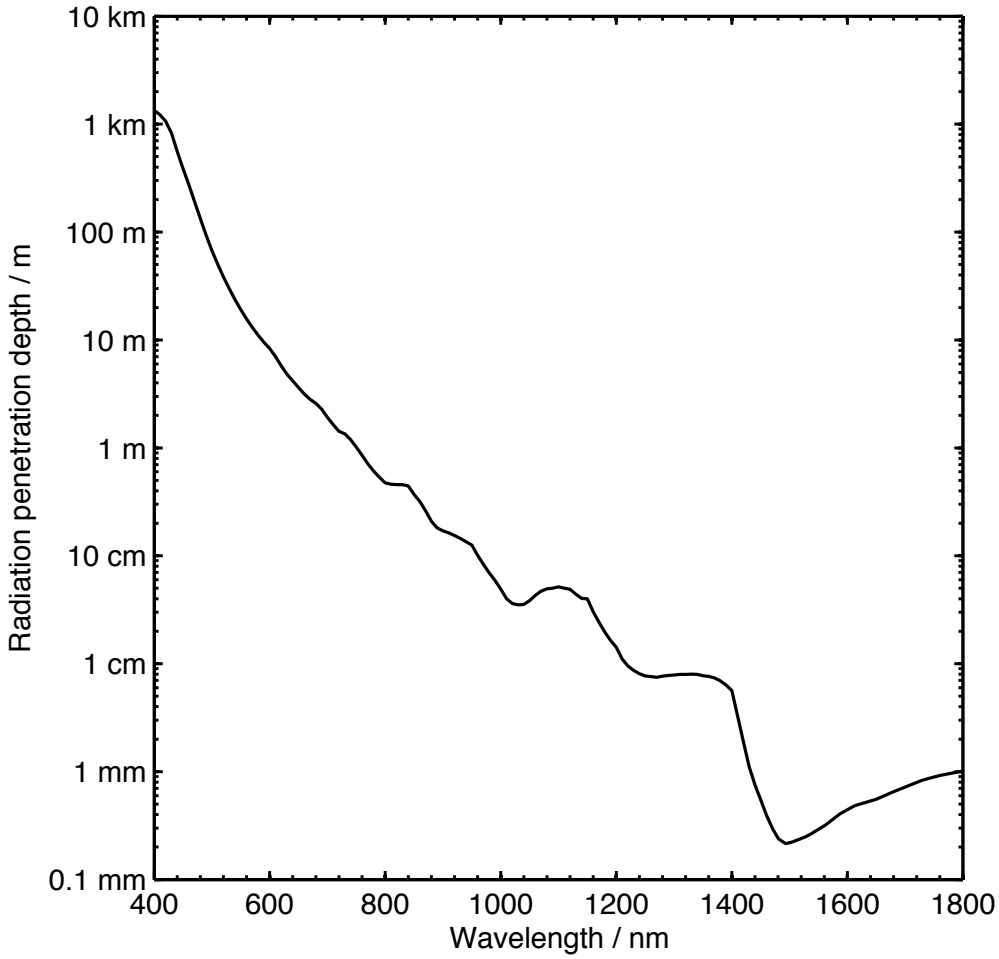

Figure 1.8. Penetration depth of radiation in pure ice with no bubbles

1.8.4 Scattering phase function

Scattered photons may be scattered into a different direction relative to the initial trajectory. The scattering phase function describes the angular distribution of light scattered by particles in a medium, or the probability density of scattering occurring through a specific angle. The scattering angle, ψ, describes the azimuth direction into which light is scattered. If the medium can be considered isotropic (i.e. the influence on light is the same in all directions at a given point) and the light is unpolarized, then the scattering angle is azimuthally symmetric and thus its value – in units of radians – lies within the interval $0 \leq \psi \leq \pi$. The angular scatterance per unit distance and solid angle, is given by (Mobley, 1994):

$$\beta_{vol}(\psi,\lambda) = \frac{\Phi_s(\psi,\lambda)}{\Phi_i(\lambda)\ dr\, d\omega} \qquad \text{Eq. 1.38}$$

where $d\omega$ is the solid angle centered on the scattering angle, ψ, through which the scattered light travels. Given that the scattered radiant flux is equal to the scattered radiant intensity, $I_s(\psi,\lambda)$, multiplied by the solid angle through which the scattered light travels, $\Phi_s(\psi,\lambda) = I_s(\psi,\lambda)\ d\omega$, and the incident radiant flux is equal to the incident irradiance, $E_i(\lambda)$, multiplied by the area that the radiant flux falls onto, $\Phi_i(\lambda) = E_i(\lambda)\ dA$, and noting that $dV = dr\, dA$ (dV is the volume of the medium that is illuminated by the incident beam), then the scattered radiant intensity per unit incident irradiance and volume of the medium (the volume scattering phase function, $\beta_{vol}(\psi,\lambda)$) is (Mobley, 1994):

$$\beta_{vol}(\psi,\lambda) = \frac{I_s(\psi,\lambda)}{E_i(\lambda)\ dV} \qquad \text{Eq. 1.39}$$

Integrating $\beta_{vol}(\psi,\lambda)$ over all directions (solid angles) gives the total scatter radiant flux per unit incident irradiance and unit volume of the medium, or the scattering coefficient b. The scattering phase function is defined as the ratio of the volume scattering phase function to the scattering coefficient (Mobley, 1994):

$$\beta_{pf}(\psi,\lambda) = \frac{\beta_{vol}(\psi,\lambda)}{b(\lambda)} \qquad \text{Eq. 1.40}$$

Averaging over all scattering directions gives the asymmetry parameter, g, a convenient measure of the shape of the phase function (Mobley, 1994):

$$g = 2\pi \int_0^{\pi} \beta_{pf}(\lambda)\cos(\psi)\sin(\psi)d\psi \qquad \text{Eq. 1.41}$$

If the scattering phase function β_{pf} is large for a small scattering angle ψ then g is near 1 (i.e. the particles are strongly forward scattering), g is near -1 if the scattering phase function is large for a large scattering angle (i.e. the particles

are strongly backward scattering). If the scattering phase function is symmetric over the forward and backward scattering directions then g is 0 (i.e. the particles scatter radiation isotropically).

Under the assumption that the scattering particles in the medium are spherical and imbedded in a infinite, uniform, non absorbing media, it is possible to reproduce an observed volume scattering phase function with Mie scattering calculations (Mie, 1908), the methodology for which is described in detail in Petty (2006). It is often convenient to have an analytic formula that approximates the shape of a phase function, such as the Henyey-Greenstein phase function (Mobley, 1994):

$$\beta_{HG}(g;\psi) = \frac{1}{4\pi}\frac{1-g^2}{(1+g^2-2g\cos\psi)^{3/2}} \qquad \text{Eq. 1.42}$$

The g parameter, defined in Eq. 1.40, can be adjusted to control the relative amounts of forward and backward scattering. The Henyey-Greenstein phase function for 3 different values of g has been calculated using equation Eq. 1.42 and has been plotted in Figure 1.9.

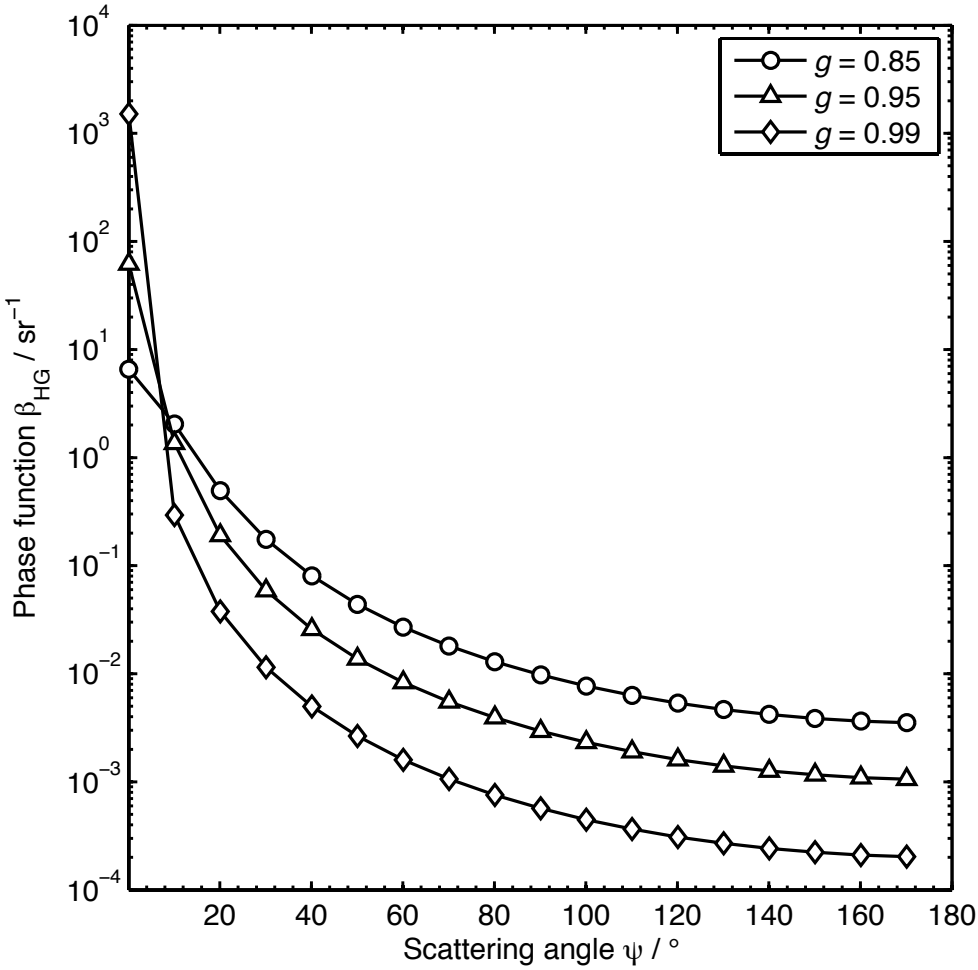

Figure 1.9. Henyey-Greenstein phase function with scattering angle for 3 different values of the asymmetry parameter (*g*)

1.9 Optical properties of snow and sea ice

In order to model the transfer of radiation in a medium a quantitative understanding of the optical properties of the medium are required. An introduction to the inherent physical and optical properties of snow and sea ice is given in this section.

1.9.1 Physical properties of snow

Snow is formed by solid precipitation of ice crystals around condensation nuclei such as dust particles in the atmosphere. Ice crystals grow into snowflakes as water vapor freezes onto the primary crystal. Snow can form as a variety of crystal shapes depending on the temperature and the humidity of the air

(LaChapelle, 1969). After falling snow crystals are broken by the wind and undergo metamorphism causing the crystal to tend to a more spherical shape. Snow on the ground primarily consists of grains of ice with air and sometimes water in the pore spaces. Newly fallen snow has a fine grain size and a low density, metamorphism and sintering tends to increases the grain size and density as the snowpack ages (LaChapelle, 1969). Average grain radii in the top 20 cm of snow is typically in the range 20 μm to 100 μm for new snow; 100 μm to 300 μm for fine grained older snow; and 1000 μm to 1500 μm for older snow near melting point (Wiscombe and Warren, 1980).

1.9.2 Absorption of light by snow

Snow is weakly absorbing of light at visible wavelengths. Snow is mostly composed of ice crystals in a matrix of air, and thus the dominant absorber in a snowpack – with zero impurities – is ice. The absorption coefficient of pure ice can be determined from the imaginary part of the complex index of fraction of ice using Eq. 1.36. The absorption coefficient of pure ice was calculated using the imaginary part of the complex index of fraction for pure ice measured by Warren and Brandt (2008), and is presented in Figure 1.10 for a wavelength range 400 nm to 800 nm. Absorption of visible radiation by ice is small, but has very strong wavelength dependence, spanning nearly 3 orders of magnitude between 400 nm and 750 nm.

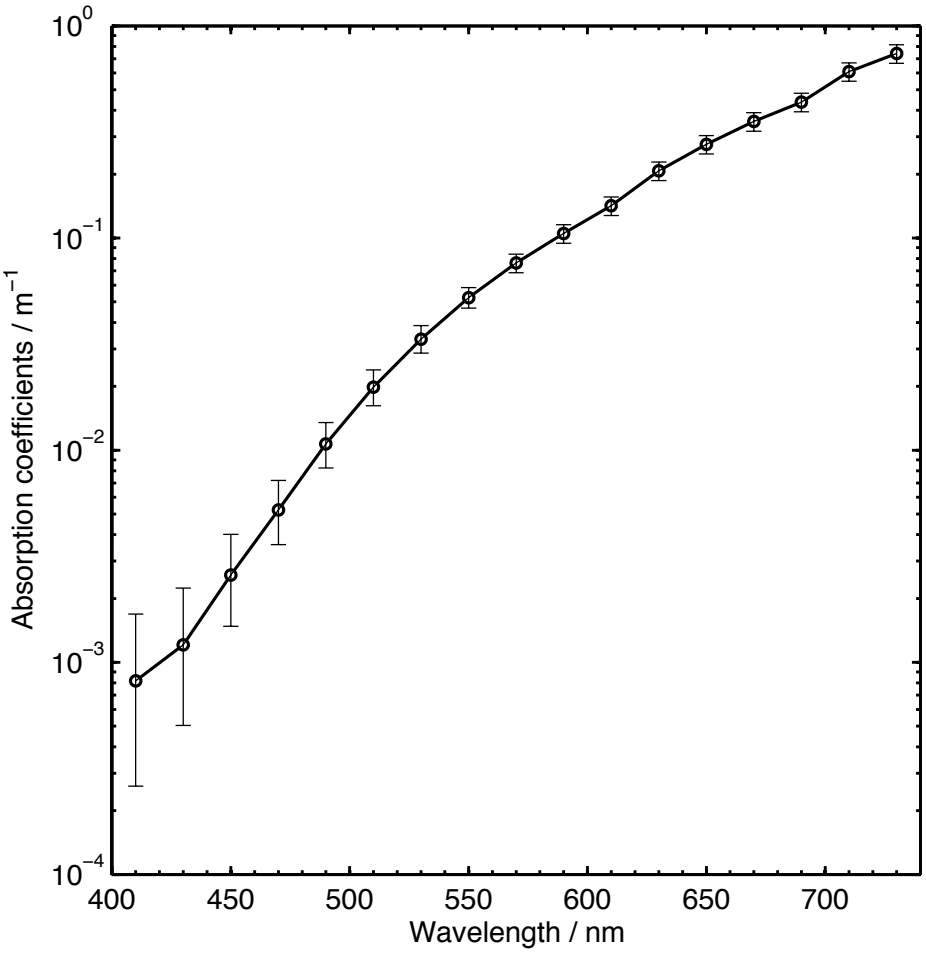

Figure 1.10. Absorption coefficients calculated for pure ice using the imaginary part of the complex index of refraction for pure ice. Data from Warren and Brandt (2008)

1.9.3 Scattering of light by snow

Snow is strongly scattering of radiation at visible wavelengths. A photon that penetrates the surface of the snowpack may undergo multiple scattering events between ice grains, with little absorption in the top layers, particularly at shorter wavelengths. The photons are often scattered back into the atmosphere from the top layers of the snowpack, giving the snow a white appearance to the human eye. Owing to large size of the snow grains compared with the wavelength of light, scattering in snow is usually assumed to be independent of wavelength in the visible range (Wiscombe and Warren, 1980). Snow radiative-transfer models often assume that snow grains are spherical in shape

(Wiscombe and Warren, 1980). Although snow grains are not spherical, Wiscombe and Warren (1980) maintained that the spherical assumption provided good estimates of albedo provided the correct grain size is chosen in the model. More recent studies have shown departure from a spherical shape can strongly affect the single scattering albedo and phase function of snow, which in turn, can strongly influence albedo, light penetration and BRDF (Aoki and Aoki, 2000; Dumont et al., 2010; Grenfell et al., 2005; Picard et al., 2009).

1.9.4 Snow albedo

Wiscombe and Warren (1980) introduced an analytical model for spectral albedo of snow albedo based upon the delta-Eddington approximation and Mie theory for the scattering by individual snow grains. The model covers the solar spectrum (300 nm to 5000 nm) and calculates snow albedo as a function of snow grain size, solar zenith angle, ratio of diffuse to direct irradiance, snow depth and the albedo of the underlying surface. The albedo of snow is shown to be sensitive to snow thickness and impurities at visible wavelengths, and to the effective grain size at near infrared wavelengths. Increased absorption at longer wavelengths occurs because a larger grain size results in a longer path length of light through each grain of ice (Wiscombe and Warren, 1980). Snow albedo as a function of wavelength and snow depth was calculated by Warren (2013) and is presented in Figure 1.11. The snow depth is expressed as the snow water equivalent (SWE) (in units of centimeters) and provides a measure of water contained within the snowpack. A snowpack with density 300 kg m^{-3} and a depth of 30 cm has an SWE of 9 cm.

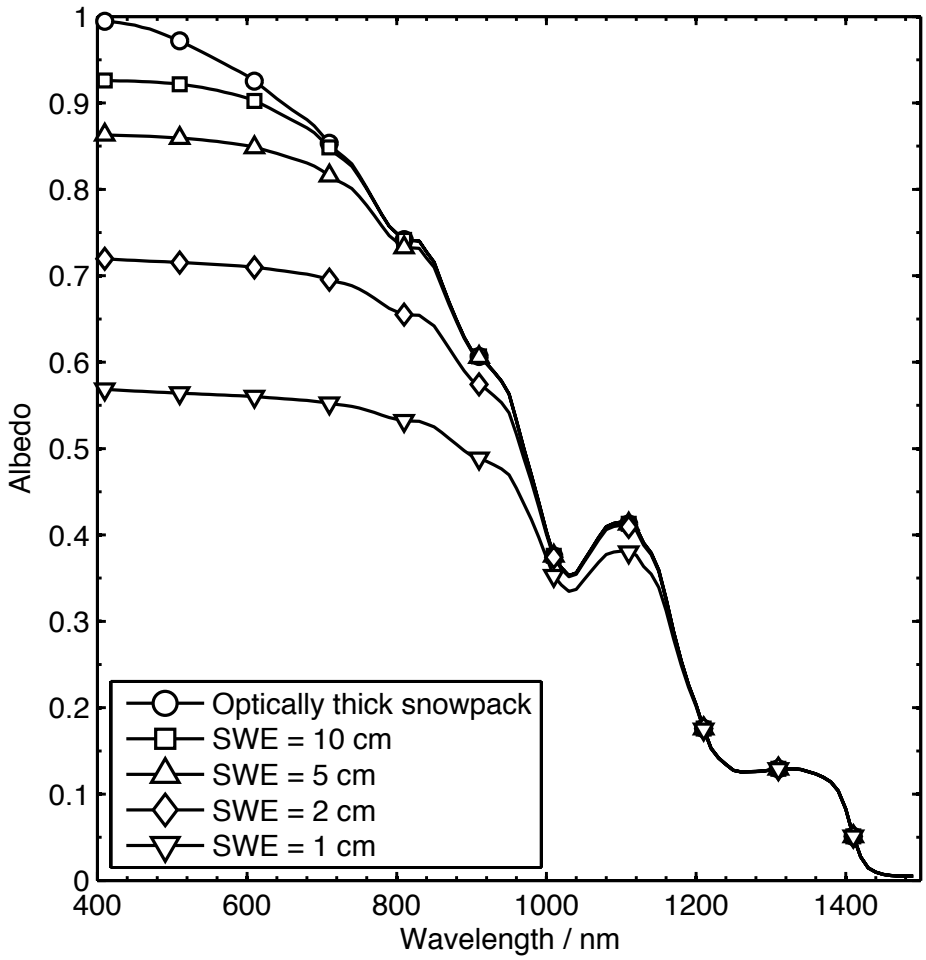

Figure 1.11. Spectral albedo of pure snow over a black surface for a variety of snow depths expressed in snow liquid water equivalent (SWE). Data from Warren (2013)

1.9.5 Physical properties of sea ice

Sea ice is formed from frozen ocean water. At the microscopic scale sea ice consists of an ice matrix with inclusions of brine and air. As seawater freezes the salts are rejected from the ice lattice. As a result, the ice grows as platelets with pockets of brine trapped in between. The size of the ice platelets depends on the growth rate of the ice, and they are typically 1 mm across (Perovich, 2003). The brine pockets have an elongated shape with the major axis usually orientated vertically (Perovich and Gow, 1996). Perovich and Gow (1996) characterized the size distribution of brine and air inclusions in sea ice and found that the size distributions fitted a lognormal distribution with a correlation coefficient greater than 0.99. Brine inclusion dimensions in the study by

Perovich and Gow (1996) were typically 0.1 mm across, and tenths of a millimeter to millimeters long. Air bubbles were found to be more circular, and were much larger than brine pockets, having a major axis length of the order of millimeters. Sea ice can exhibit considerable vertical variability in the physical and optical properties owing to differences in temperature, salinity, brine volume and air volume (Weeks, 2010). In addition, as sea ice ages brine drainage from the upper layers can cause the proportion of air bubbles in the upper layers to increase. The relative proportions of brine and air in sea ice can be calculated with knowledge of the sea ice temperature, salinity and density using empirical relationships derived by Cox and Weeks (1983). The equations are governed by the equilibrium curve of the sea ice phase diagram. The relationship between brine volume v_b, salinity S and temperature T is as follows (Cox and Weeks, 1982):

$$v_b = S\left(0.0532 - \frac{4.919}{T}\right) \qquad \text{Eq. 1.43}$$

As shown in Eq. 1.43 brine volume is sensitive to temperature. Brine volumes for sea ice can vary greatly, from 2 % to 40 % (Perovich and Gow, 1996). As sea ice warms the mean size of brine pockets increases as the individual brine pockets coalesce (Perovich and Gow, 1996). Precipitation of salts occurs in sea ice if temperatures are cold enough. Mirabilite ($Na_2SO_410H_2O$) precipitates in sea ice at –8.2°C and hydrohalite ($NaCl_212H_2O$) precipitates at –22.9°C (Perovich, 2003).

1.9.6 Absorption of light by sea ice

Sea ice is primarily composed of pure ice, brine, air bubbles and precipitated salts. Thus the bulk absorption coefficient a can be described by the volume

weighted sum of the absorption coefficients for each of the constituent components (Light, 2000):

$$a(\lambda) = a_i(\lambda)v_i + a_g(\lambda)v_g + a_s(\lambda)v_s \qquad \text{Eq. 1.44}$$

where the subscripts (i,g,s) correspond to the absorption coefficients for pure ice, air, and precipitated salt crystals respectively. v is the volume fraction of each component in the sea ice. Absorption by brine can be estimated by a spectral absorption coefficient representative of natural Arctic waters (Smith and Baker, 1981). Absorption by air is negligible and absorption by precipitated salts is thought to be small relative to absorption by pure ice or brine (Light, 2000), so it is assumed that $a_g = 0$ and $a_s = 0$. Absorption coefficients for clear Arctic waters were measured by Smith and Baker (1981) and scaled by Light (2000) to correspond with attenuation measurements made at 490 nm beneath Arctic sea ice. The absorption coefficients for natural Arctic seawater given by Light (2000) and pure ice given by Warren and Brandt (2008) are presented in Figure 1.12. Absorption coefficients for clear Arctic water show a very similar spectral shape and magnitude to that of pure ice. Since the primary constituent of sea ice is fresh ice, absorption in sea ice is dominated by pure ice, especially for sea ice at low temperatures or low salinity, with a smaller brine volume fraction.

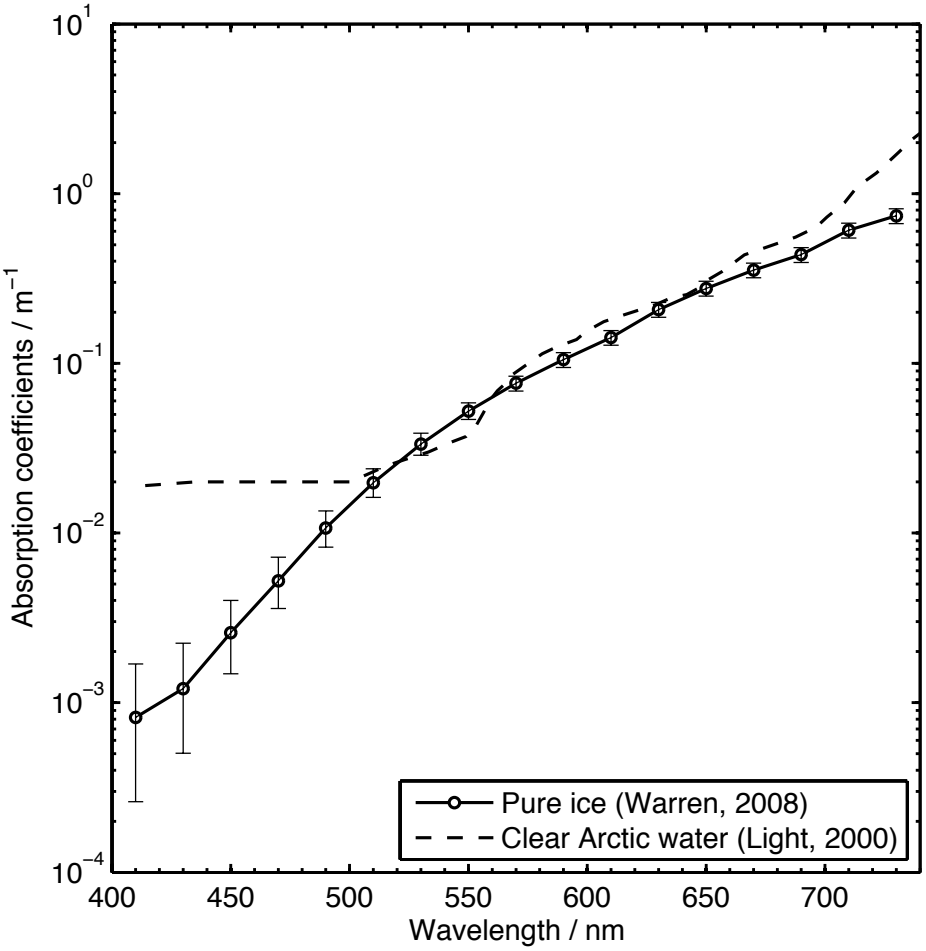

Figure 1.12. Absorption coefficients for pure ice and clear Arctic seawater. Data from Warren and Brandt (2008) and Light (2000)

1.9.7 Scattering of light by sea ice

The intricate internal structure of brine inclusions and air bubbles in an ice matrix makes sea ice a strongly scattering medium. The relative scattering strength of the inclusions depends on the difference in their real indices of refraction n to that of ice. Pure ice has an n of ~ 1.31 at visible wavelengths (Warren and Brandt, 2008), whereas air has an n of ~ 1. The index of refraction of brine was measured by Maykut and Light (1995) over a temperature range – 2 °C to –32 °C, corresponding to a range of salinities from 35 PSU to 240 PSU. The measurements of n made by Maykut and Light (1995) varied between 1.34 and 1.40 over the range of temperatures, and had weak wavelength

dependence at visible wavelengths. Air bubbles have a greater difference (~ 0.31) in n than brine channels (~ 0.03 to ~ 0.09) at visible wavelengths, and thus are stronger scatters of light compared to brine inclusions in sea ice. At lower temperatures precipitation of solid salts can greatly increase scattering (Perovich and Grenfell, 1981).

Owing to the large amount of scattering in sea ice it is difficult to directly and accurately measure scattering coefficients and phase functions. In addition, scattering in sea ice is not simply a function of the brine and air volume fractions, but is also dependent on how the brine is distributed within the ice matrix, for example, 100 small inclusions with the same volume fraction will scatter light different compared to a single large inclusion. Measured scattering coefficients typically have values greater than 10 m^{-1} for warm sea ice, and greater than 200 m^{-1} for sea ice with hydrohalite or abundant air bubbles (Perovich, 1996; Maykut, 1978). Mobley (1998b) calculated scattering coefficients in first year Arctic sea ice for a range of brine pocket and air bubble size distributions as 175 m^{-1} for sea ice with few bubbles, and 250 m^{-1} for sea ice with many bubbles. Observational and modeling studies have shown that the phase function for sea ice is strongly forward peaked (Light, 2000), and at least a factor of 50 greater than sideward or backward scattering (Perovich, 1996). Mobley (1998b) determined the phase function asymmetry parameter g for first year Arctic sea ice from Mie scattering calculations based on size distributions of air bubbles and brine channels. The Mie calculations by Mobley (1998b) yielded values ranging from $g = 0.96$ for sea ice with many bubbles, to $g = 0.99$ for sea ice with few bubbles. Small differences in n combined with the large differences in the size of the inclusions with the wavelength of light results

in scattering that is dominated by diffraction (Mobley 1998b). As the difference in n is smaller for brine channels than for air bubbles, the phase function for brine channels in the Mie calculations by Mobley (1998b) was more strongly forward scattering for brine channels ($g = 0.99$) than for air bubbles ($g = 0.86$), despite air bubbles being larger than brine channels. Given the weak wavelength dependence of the real index of refraction for ice, and owing to the large size of brine and air inclusions compared to the wavelength of incident radiation, the scattering coefficients are often assumed to be constant with wavelength (Grenfell, 1983; Perovich, 2003).

1.9.8 Sea ice albedo

At a spatial scale comparable to a footprint of a satellite sensor sea ice exhibits extensive horizontal variability in albedo as a result of melt ponds and snow cover. Arctic seasonal sea ice was observed by Perovich (2012) to undergo an albedo evolution with seven phases; involving a decrease in albedo with the onset of melting in the summer, and a change in ice cover from snow covered ice to bare ice, or from frozen ponds, to melting ice, to ponded ice. Ponding of water on sea ice reduces the albedo by filling air voids with water, albedos of ponded water are characterized by a maximum in the 400 nm to 500 nm wavelength range owing to the transparency of water at shorter wavelengths (Perovich, 1996). The albedo of multiyear sea ice is typical 0.1 greater than the albedo of seasonal sea ice, owing to a higher bubble fraction in its upper layers making multiyear sea ice a more efficient scatterer of radiation (Perovich and Polashenski, 2012). In addition, multiyear sea ice undergoes a slower transition from snow-covered ice to bare ice, thus maintaining its higher albedo for longer.

In winter multiyear Arctic sea ice is typically covered by few tens of centimeters of snow (Weeks, 2010). Despite the presence snow cover, the albedo of the underlying sea ice remains an important consideration at ultraviolet and visible wavelengths owing to light penetration in snow (Marks and King, 2013). Warren (2013) used updated optical constants for ice (Warren and Brandt, 2008) to show that the albedo of pure snow is sensitive to the underlying surface at ultraviolet and visible wavelengths for a snowpack thinner than ~ 1 m. Observations by Perovich (2012) for Arctic multiyear sea ice indicate that much of the snow cover has melted by late June, with all the snow melting by August resulting in large areas of exposed bare sea ice.

1.9.9 Impurities in snow and sea ice

Scattering in snow and sea ice is generally so strong that absorption has little impact on albedo. However, the presence of impurities such as black carbon can increase absorption and thus greatly reduce albedo. Just 10 ng g^{-1} of black carbon (BC) in snow has been shown to cause a 1 % change in its albedo (Clarke and Noone, 1985; Hansen and Nazarenko, 2004; Warren and Wiscombe, 1985; Marks and King, 2013), which can increase the grain size of snow crystals in the snowpack and trigger an earlier spring melt (Flanner et al., 2007), further enhancing ice-albedo feedback. Flanner et al. (2007) estimated human induced radiative forcing by the deposition of black carbon on snow cover as +0.054 W m^{-2} globally. Predominant sources are the incomplete combustion of fossil fuels and biomass burning (Bond et al., 2013). Median concentrations of black carbon in surface snow in the industrial northeast of China have been measured as 1220 ng g^{-1} of black carbon per gram of snow (Wang et al., 2013), with concentrations up to 88 ng g^{-1} in Scandinavia and up to

14 ng g^{-1} in Svalbard (Forsström et al., 2013). Typical values in the study by Forsström et al. (2013) for Svalbard were in the range 11 ng g^{-1} to 14 ng g^{-1}.

1.10 Radiative-transfer modeling

The radiative-transfer model PlanarRad (Hedley, 2008) was used in this study to calculate the BRDF of laboratory generated sea ice. A brief introduction to radiative-transfer modeling is therefore given in this section, along with an introduction to PlanarRad.

1.10.1 Calculating extinction over a finite path

Extinction of radiation over a finite path in a homogenous absorbing medium can calculated using the exponential decay relationship, or Beer's law (Petty, 2006):

$$E_z(\lambda) = E_i(\lambda)\ e^{-c(\lambda)z} \qquad \text{Eq. 1.45}$$

where E_z is the irradiance at depth z, E_i is the irradiance at the surface and c is the extinction coefficient. Eq. 1.45 assumes that; (1) irradiance is isotropic; (2) the medium has infinite thickness; and (3) there are no contributions to irradiance at depth owing to multiple scattering. A more detailed treatment of radiative transfer in a multiple scattering medium is given by the radiative-transfer equation (RTE).

1.10.2 Deriving the equation of radiative-transfer

With knowledge of the inherent optical properties of a medium and the ambient illumination conditions, the BRDF of a medium can be calculated using radiative-transfer theory. The radiative-transfer equation (RTE) expresses conservation of energy written for a collimated beam of radiance travelling through an absorbing, scattering and emitting medium (Mobley, 1994). The

processes affecting a beam travelling through a medium such as snow or sea ice has been discussed in the preceding sections. These processes are presented formally in the context of radiative-transfer equation, and are illustrated in Figure 1.13.

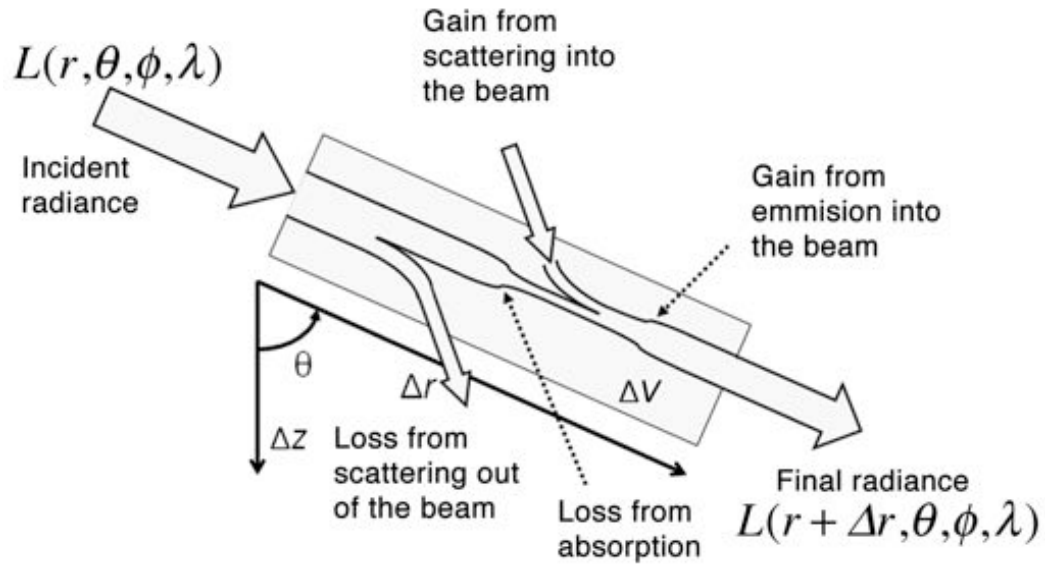

Figure 1.13. Processes that affect a single beam of radiance with wavelength λ as it propagates over a distance Δr within a volume ΔV. Adapted from Mobley (2010)

The change in radiance owing to absorption over a distance Δr can be described as follows (Mobley, 2010):

$$\frac{\Delta L(r+\Delta r,\theta,\phi,\lambda)}{\Delta r} = -a(r,\lambda)L(r,\theta,\phi,\lambda) \qquad \text{Eq. 1.46}$$

where a is the absorption coefficient defined in Eq. 1.28 in Section 1.8.1 rewritten in terms of the change in radiance ΔL rather than the change in absorptance ΔA. Similarly, the change in radiance owing to scattering is given by:

$$\frac{\Delta L(r+\Delta r,\theta,\phi,\lambda)}{\Delta r} = -b(r,\lambda)L(r,\theta,\phi,\lambda) \qquad \text{Eq. 1.47}$$

where b is the scattering coefficient defined in Eq. 1.29 in Section 1.8.1. The right hand sides of Eq. 1.45 and Eq. 1.46 require a negative sign because radiance decreases along the path Δr.

Gain of photons into the beam direction (θ,ϕ) from another direction can be calculated with knowledge of the incident radiance $L(\theta',\phi',\lambda)$, the solid angle of the incident beam $\Delta\omega(\theta',\phi')$, and the volume scattering phase function β_{vol} defined in Section 1.8.4:

$$\frac{\Delta L(r+\Delta r,\theta,\phi,\lambda)}{\Delta r} = L(\theta',\phi',\lambda)\beta_{vol}(\theta',\phi' \rightarrow \theta,\phi,\lambda)\Delta\omega(\theta',\phi') \quad \text{Eq. 1.48}$$

The sum of scattering from all directions into the beam direction (θ,ϕ) is given by integrating the right hand side of the Eq. 1.47 over all directions:

$$\frac{\Delta L(r+\Delta r,\theta,\phi,\lambda)}{\Delta r} = \int_0^{2\pi}\int_0^{\pi} L(\theta',\phi',\lambda)\beta_{vol}(\theta',\phi' \rightarrow \theta,\phi;\lambda)\Delta\omega(\theta',\phi') \quad \text{Eq. 1.49}$$

Radiance created along the path Δr in direction (θ,ϕ) at wavelength λ by emission or inelastic scattering (absorbed photons that are emitted at a different wavelength) is given by the source function:

$$\frac{\Delta L(r+\Delta r,\theta,\phi,\lambda)}{\Delta r} = S(r,\theta,\phi,\lambda) \quad \text{Eq. 1.50}$$

Summing the various contributions to changes in L over the path Δr (right hand sides of Eq. 1.46 Eq. 1.47 Eq. 1.49 and Eq. 1.50) and taking the conceptual limit of $\Delta r \rightarrow 0$ gives the time-independent, monochromatic radiative-transfer equation written as the change in radiance with distance along a given beam direction (Mobley, 2010):

$$\frac{dL(r,\theta,\phi,\lambda)}{dr} = -[a(r,\lambda)+b(r,\lambda)]L(r,\theta,\phi,\lambda) + \int_0^{2\pi}\int_0^{\pi} L(\theta',\phi',\lambda)\beta_{vol}(\theta',\phi' \rightarrow \theta,\phi;\lambda)\Delta\omega(\theta',\phi') + S(r,\theta,\phi,\lambda) \qquad [W\,m^{-3}sr^{-1}nm^{-1}] \quad \text{Eq. 1.51}$$

Eq. 1.51 considers only unpolarized light, which gives sufficiently accurate solutions for most applications (Mobley, 2010). Particularly when multiple

scattering in the medium is significant and the scattering particles are much larger than the wavelength of light. Scattering by larger particles induces less polarization, and multiple scattering tends to depolarize radiance (Mobley, 2010).

1.10.3 Solution methods

The radiative-transfer equation (RTE) defined in Eq. 1.51 is a linear integrodifferential equation – containing an integral and a derivative of a unknown radiance – and is difficult to solve for given IOPs and boundary conditions (Mobley, 2010). An exact analytical solution to the RTE can only be achieved under simplifying assumptions such as with no scattering. For situations where scattering is a dominant process – such as during the transfer of visible radiation in snow or sea ice – approximate analytical or numerical solutions must be used to obtain sufficiently accurate solutions. Three common methods for solving radiative-transfer with multiple scattering are: (1) the invariant embedding method; (2) the discrete ordinates method; and (3) Monte Carlo methods.

1.10.3.1 Quad averaging

Radiative-transfer models often compute a quad-averaged radiance by directionally discretizes the RTE into a grid of quadrilateral regions. Each region is bounded by lines of constant θ and ϕ, plus two polar caps (Mobley et al., 1993). The quad averaged radiance L_Q can be defined as (Mobley et al., 1993):

$$L_Q = \frac{1}{\omega_Q} \int\int_{\theta,\phi} L(\theta,\phi)\, d\theta\, d\phi \qquad \text{Eq. 1.52}$$

where (θ,ϕ) are the zenith angle azimuth angles respectively within each quad Q, and ω_Q is the solid angle of each quad. Quad averaged radiances can be

physically interpreted as the average radiance over a set of directions (θ,ϕ) constrained within the quadrilateral region. Figure 1.14 shows the partitioning of quads over a hemisphere – as used in the radiative transfer model PlanarRad – projected onto a 2-D grid.

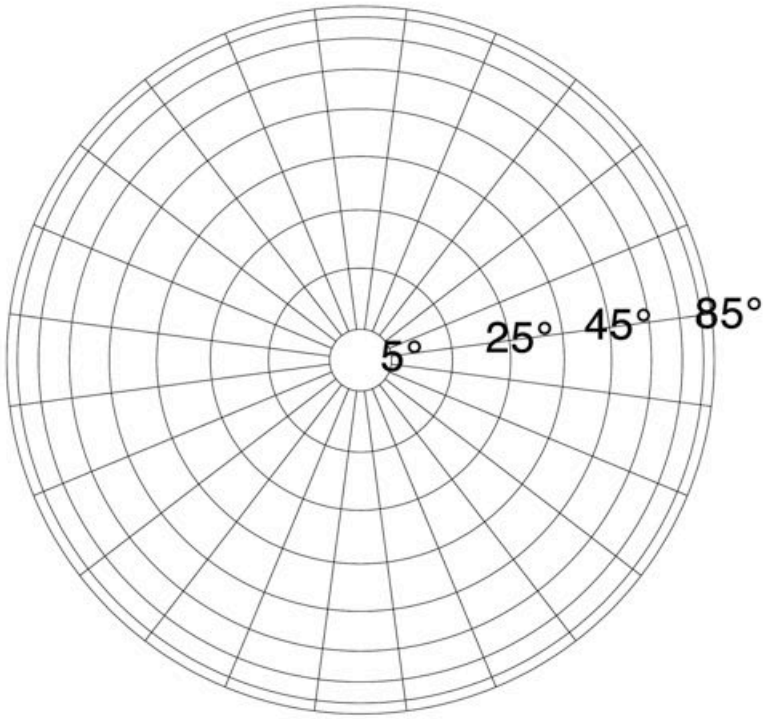

Figure 1.14. Partition of the hemisphere into a grid of quadrilateral regions as used in the radiative transfer model PlanarRad. The regions are separated by 15° degree intervals in azimuth angle and 10° intervals in zenith angle. Quads that extend over the equator (between 85° 95° zenith angle) are not shown

1.10.3.2 Invariant imbedded method

The invariant imbedded method applies integration of radiance over a set of directions defined by a grid of quadrilateral regions called quads, defined in Section 1.10.3.1. Integration over all directions is replaced by summation over all quads and the phase function is replaced by a quad averaged quantity. The equations for the RTE are transformed into a set of Riccati differential equations for which finding a solution for the radiance distribution is an analytical process (Mobley, 1989). The model is therefore computationally efficient and the computation time is a linear function of depth. The IOPs of the medium can be

varied arbitrarily with depth, and the bottom boundary can be either an infinitely thick homogenous layer, or an opaque boundary with a specified BRDF.

1.10.3.3 Discrete ordinates method

The Discrete-Ordinates method for calculating Radiative-Transfer (DISORT) solves the RTE directly without applying the quad averaging method defined in Section 1.10.3.1. The radiance is expanded into a Fourier cosine series and the phase function is expanded into a series of 2N Legendre polynomials (Stamnes et al., 1988;Chandrasekhar, 1960). The method models the medium as a stack of homogenous layers; hence the method is slow if many layers are needed to resolve depth-dependent IOPs. The 'discrete ordinates' refers to the discrete angles at which the radiation is computed, which can be specified arbitrarily. BRDF at the lower boundary can be specified, and intensities can be returned for any angle and optical depth.

1.10.3.4 Monte Carlo methods

Probabilistic or Monte Carlo methods mimic how nature absorbs and scatters photons and can solve time-dependent 3-D problems with arbitrary geometry. Monte Carlo techniques use probability theory and random number generators to simulate the fate of large numbers of photons propagating through a medium. Averages of large numbers of simulated photons called 'ensembles' give statistical estimates for the radiance distribution with for a medium with given IOPs. Although Monte Carlo methods are generally computationally inefficient, they are very widely used because they are conceptually simple, easy to program and can be used to solve complex geometric problems. The output from a 2-D Monte Carlo radiative-transfer model – based on a method outlined by Mobley (1994) – was used to generate random paths for 100 photons with

varying values of the asymmetry parameter (*g*). The random paths of each photon given a medium with an optical depth of 60 and a single scattering albedo of 0.99 are plotted in Figure 1.15.

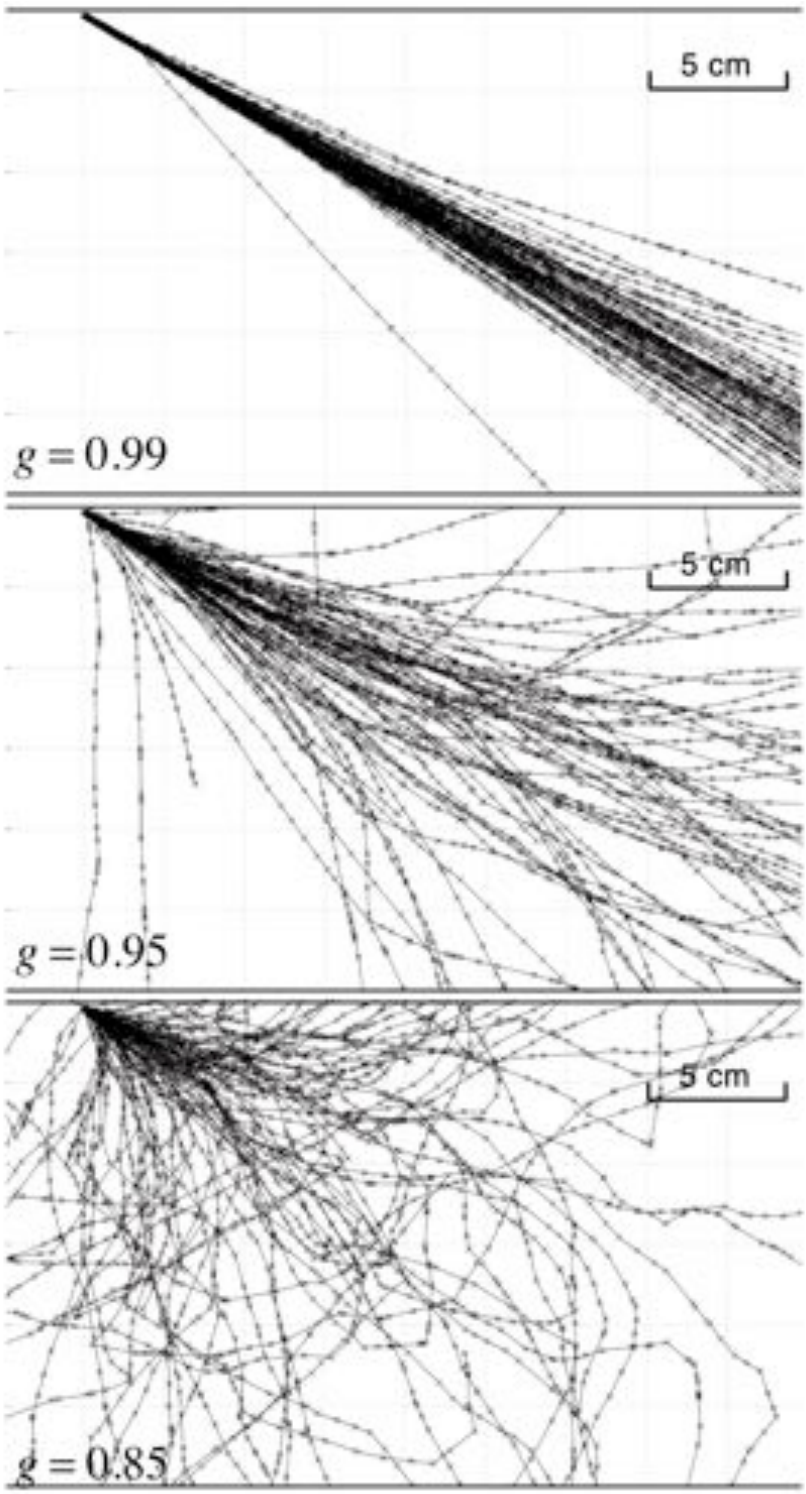

Figure 1.15. Example random paths of 100 photons in a plane parallel scattering and absorbing medium for 3-different values of the asymmetry parameter (*g*). In each simulation the single scattering albedo was 0.99 and the optical depth was 60

The MATLAB code for the 2-D Monte Carlo radiative-transfer model used to produce the output in Figure 1.15 is given in Appendix 1.

1.10.3.5 Plane parallel approximation

The radiative-transfer models discussed in the preceding section assume that the medium is infinite in horizontal extent, and that there are no horizontal variations of IOPs or boundary conditions. The assumption drastically simplifies the geometry, allowing powerful analytical techniques to be implemented, while still representing a usefully realistic model of nature (Mobley, 1994).

1.10.4 Overview of PlanarRad radiative transfer model

PlanarRad was designed to model radiation in homogenous scattering and absorbing media and is based on an algorithm described by Mobley (1994) and adapted by Hedley (2008). PlanarRad computes quad averaged radiances for a homogenous slab of media, hence there is no horizontal or vertical variation in the IOPs. PlanarRad uses the invariant imbedded method – described in Section 1.10.2.2 – to solve the radiative-transfer equation, so is computationally efficient. The model accepts arbitrary incident radiances, phase functions, extinction and absorption coefficients, refractive indices for inside and outside the medium, finite depth bottom boundaries with variable properties, and rough surfaces. The directional discretization used by PlanarRad splits each hemisphere into 9 by 24 quads of constant zenith and azimuth angle, plus an end cap, as is illustrated in Figure 15. Output from the model includes the radiance distribution leaving the medium as a function of depth and direction. PlanarRad is similar to the commercial radiative-transfer software Hydrolight (Mobley, 1998) and has been validated against it (Hedley, 2008). A schematic

representation of the variables considered by the PlanarRad program are given in Figure 1.16.

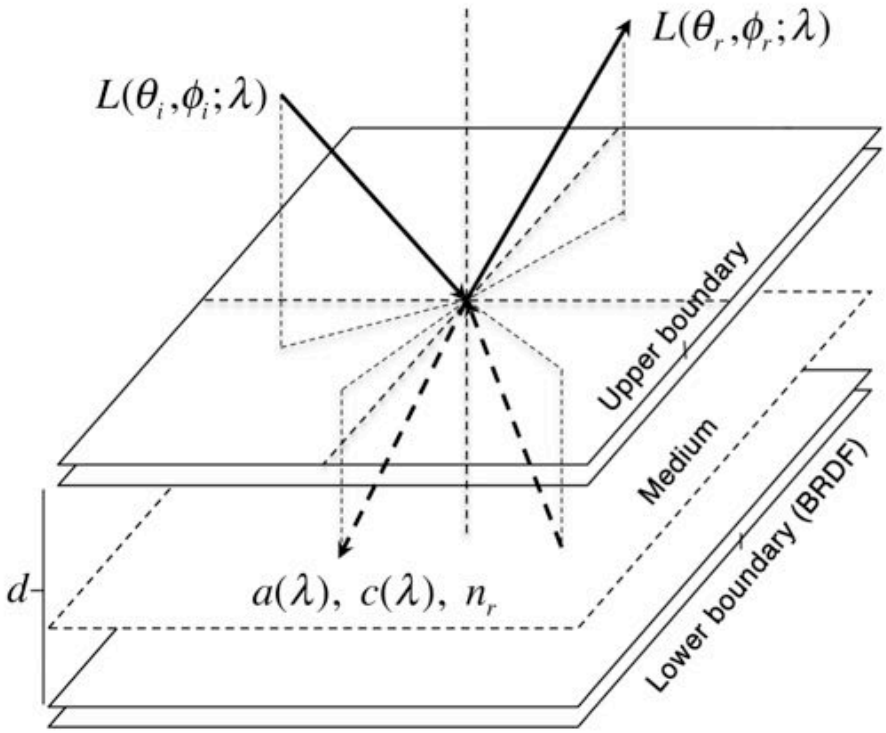

Figure 1.16. Schematic of PlanarRad input variables. Arrows represent the direction of incident and reflected rays on the upper boundary

1.11 Outline of this study

The thesis incorporates field, laboratory and modeling studies of the directional reflectance of snow and sea ice, and investigates the validity of the methodologies used to obtain these measurements.

Chapter 2 focuses on the spring 2013 field campaign to Ny-Alesund, Svalbard, to investigate the bidirectional reflectance of windblown snow covered tundra at large solar zenith angles. The study involved 3-weeks of fieldwork culminating in the BRDF characterization of 6-sites under clear skies with different scales of surface roughness elements. The HCRF measurements were supported with

ancillary snow measurements including: snow grain size, density, depth, temperature, maximum black carbon, and surface roughness; with ancillary sky measurements including: diffuse to direct irradiance, aerosol optical thickness, and all-sky camera imagery. The fieldwork involved the use of the GonioRAdiometric Spectrometer System (GRASS) and the HCRF was sampled over the viewing zenith angles 0° to 50° at 10° intervals, and over 360° in azimuth angles at 30° intervals. The study reports the observations and explores the impact of large solar zenith angles and surface roughness on the HCRF measurements.

Chapter 3 investigates the bidirectional reflectance of laboratory generated sea ice using a specially design laboratory goniometer and the Royal Holloway sea ice simulator. The study reports the first CCRF measurements of laboratory generated sea ice and the associated methodology and instrumentation that were developed in order to undertake the measurements. The chapter reports two laboratory measurements of simulated sea ice CCRF for different ice thicknesses under the same illumination conditions. The BRDF of the laboratory generated sea ice was compared to the results from a plane-parallel radiative transfer model PlanarRad. Input parameters such as absorption coefficients, phase functions and surface roughness were obtained from the physical properties of the laboratory generated sea ice where possible.

Chapter 4 involves an investigation into the temperature effects on the reflectance of Spectralon: a commonly used reference standard for reflectance in field and laboratory BRDF studies. Spectralon reference panels are calibrated for their inherent non-Lambertian and non-lossless reflectance at room temperature. The study addresses concerns over the presence of a material

phase transition at 19 °C in polytetrafluroethylene (PTFE) (Ylianttila and Schreder, 2005; McKenzie et al., 2005), PTFE is the most widely used material used to produce reference standards for reflectance. The work assesses the potential impact of the phase transition on field and laboratory studies of reflectance.

Chapter 5 summarises the key findings from each of the 3 core areas of research, provides concluding remarks relevant to the complete thesis, and makes recommendations for future research.

1.12 References

Aoki, T., and Aoki, T., 2000, Effects of snow physical parameters on spectral albedo and: Journal of Geophysical Research, v. 105, p. 10219–10236.

Arnold, G.T., Tsay, S.C., King, M.D., Li, J.Y., and Soulen, P.F., 2002, Airborne spectral measurements of surface-atmosphere anisotropy for arctic sea ice and tundra: International Journal of Remote Sensing, v. 23, no. 18, p. 3763–3781.

Ball, C.P., Levick, A.P., Woolliams, E.R., Green, P.D., Dury, M.R., Winkler, R., Deadman, A.J., Fox, N.P., and King, M.D., 2013, Effect of polytetrafluoroethylene (PTFE) phase transition at 19°C on the use of Spectralon as a reference standard for reflectance: Applied Optics, v. 52, p. 4806–4812.

Berk, A., Anderson, G.P., Bernstein, L.S., Acharya, P.K., Dothe, H., Matthew, M.W., Adler-Golden, S.M., Chetwynd, J.H., Jr, Richtsmeier, S.C., Pukall, B., Allred, C.L., Jeong, L.S., and Hoke, M.L., 1999, MODTRAN4 radiative transfer modeling for atmospheric correction: Proceedings SPIE 3756, v. 3756, p. 348–353.

Bond, T.C., Doherty, S.J., Fahey, D.W., Forster, P.M., Berntsen, T., DeAngelo, B.J., Flanner, M.G., Ghan, S., Kärcher, B., Koch, D., Kinne, S., Kondo, Y., Quinn, P.K., Sarofim, M.C., et al., 2013, Bounding the role of black carbon in the climate system: A scientific assessment: Journal of Geophysical Research: Atmospheres, v. 118, p. 5380–5552.

Bourgeois, C.S., Calanca, P., and Ohmura, A., 2006, A field study of the hemispherical directional reflectance factor and spectral albedo of dry snow: Journal of Geophysical Research, v. 111, p. D20108.

Box, J.E., Fettweis, X., Stroeve, J.C., Tedesco, M., Hall, D.K., and Steffen, K., 2012, Greenland ice sheet albedo feedback: thermodynamics and atmospheric drivers: The Cryosphere, v. 6, p. 821–839.

Brandt, R.E., and Warren, S.G., 1993, Albedo, thickness distribution, and snow cover: Journal of Geophysical Research, v. 98, p. 417–429.

Chandrasekhar, S., 1960, Radiative transfer: Dover Publications.

Choudhury, B., and C Chang, A., 1979, Two-stream theory of reflectance of snow: IEEE Transactions on Geoscience Electronics, v. 17, p. 63–68.

Clarke, A.D., and Noone, K.J., 1985, Soot in the Arctic snowpack: a cause for perturbations in radiative transfer: Atmospheric Environment, v. 19, p. 2045–2053.

Comiso, J.C., Parkinson, C.L., Gersten, R., and Stock, L., 2008, Accelerated decline in the Arctic sea ice cover: Geophysical Research Letters, v. 35, p. L01703.

Cox, G.F., and Weeks, W.F., 1982, Equations for determining the gas and brine

volumes in sea ice samples: Journal of Glaciology, v. 29, p. 306–316.

Curry, J.A., and Schramm, J.L., 1995, Sea ice-albedo climate feedback mechanism: Journal of Climate, v. 8, p. 1–8.

Dozier, J., 1984, Snow reflectance from Landsat-4 thematic mapper: Geoscience and Remote Sensing, IEEE Transactions on, v. GE-22, p. 323–328.

Dumont, M., Brissaud, O., Picard, G., Schmitt, B., Gallet, J.C., and Arnaud, Y., 2010, High-accuracy measurements of snow Bidirectional Reflectance Distribution Function at visible and NIR wavelengths – comparison with modelling results: Atmospheric Chemistry and Physics, v. 10, p. 2507–2520.

Dye, D.G., 2002, Variability and trends in the annual snow-cover cycle in Northern Hemisphere land areas, 1972-2000: Hydrological Processes, v. 16, p. 3065–3077.

Flanner, M.G., Shell, K.M., Barlage, M., Perovich, D.K., and Tschudi, M.A., 2011, Radiative forcing and albedo feedback from the Northern Hemisphere cryosphere between 1979 and 2008: Nature Geoscience, v. 4, no. 3, p. 151–155.

Flanner, M.G., Zender, C.S., Randerson, J.T., and Rasch, P.J., 2007, Present-day climate forcing and response from black carbon in snow: Journal of Geophysical Research, v. 112 p. D11202.

Forsström, S., Isaksson, E., Skeie, R.B., Ström, J., Pedersen, C.A., Hudson, S.R., Berntsen, T.K., Lihavainen, H., Godtliebsen, F., and Gerland, S., 2013, Elemental carbon measurements in European Arctic snow packs: Journal of Geophysical Research: Atmospheres, v. 118, p. 1–14.

Fox, N., Kaiser-Weiss, A., Schmutz, W., Thome, K., Young, D., Wielicki, B., Winkler, R., and Woolliams, E., 2011, Accurate radiometry from space: an essential tool for climate studies: Philosophical Transactions of the Royal Society A: Mathematical, Physical and Engineering Sciences, v. 369, p. 4028–4063.

Grenfell, T.C., 1983, A theoretical model of the optical properties of sea ice in the visible and near infrared: Journal of Geophysical Research, v. 88, p. 9723.

Grenfell, T.C., Neshyba, S.P., and Warren, S.G., 2005, Representation of a nonspherical ice particle by a collection of independent spheres for scattering and absorption of radiation: Hollow columns and plates: Journal of Geophysical Research: Atmospheres, v. 110, p. D17203.

Grenfell, T.C., Warren, S.G., and Mullen, P.C., 1994, Reflection of solar radiation by the Antarctic snow surface at ultraviolet, visible, and near-infrared wavelengths: Journal of Geophysical Research, v. 99, p. 18669.

Groisman, P.Y., Karl, T.R., Knight, R.W., and Stenchikov, G.L., 1994, Changes of snow cover, temperature, and radiative heat balance over the Northern

Hemisphere: Journal of Climate, v. 7, p. 1633–1656.

Hall, A., 2004, The role of surface albedo feedback in climate: Journal of Climate, v. 17, p. 1550–1568.

Hall, D.K., Chang, A.T.C., Foster, J.L., Benson, C.S., and Kovalick, W.M., 1989, Comparison of in situ and landsat derived reflectance of Alaskan Glaciers: Remote Sensing of Environment, v. 28, p. 23–31.

Hall, D.K., Foster, J.L., and Chang, A.T.C., 1992, Reflectance of snow measured in situ and from space in sub-Arctic areas in Canada and Alaska: IEEE Transactions on Geoscience and Remote Sensing, v. 30, p. 634–637.

Hall, D.K., Kovalick, W.M., and Chang, A., 1990, Satellite-derived reflectance of snow-covered surfaces in Northern Minnesota: Remote Sensing of Environment, v. 33, p. 87–96.

Hansen, J., and Nazarenko, L., 2004, Soot climate forcing via snow and ice albedos: Proceedings of the National Academy of Sciences, v. 101, p. 423–428.

Hedley, J., 2008, A three-dimensional radiative transfer model for shallow water environments: Optics Express, v. 16, p. 21887–21902.

Hudson, S.R., Warren, S.G., Brandt, R.E., Grenfell, T.C., and Six, D., 2006, Spectral bidirectional reflectance of Antarctic snow: Measurements and parameterization: Journal of Geophysical Research, v. 111, p. D18106.

Jin, Z., and Simpson, J., 2001, Anisotropic reflectance of snow observed from space over the Arctic and its effect on solar energy balance: Remote Sensing of Environment, v. 75, p. 63–75.

Klein, A.G., and Stroeve, J., 2002, Development and validation of a snow albedo algorithm for the MODIS instrument: Annals of Glaciology, v. 34, p. 45–52.

Knap, W.H., and Reijmer, C.H., 1998, Anisotropy of the reflected radiation field over melting glacier ice: Remote Sensing of Environment, v. 65, p. 93–104.

Knap, W.H., Reijmer, C.H., and Oerlemans, J., 1999, Narrowband to broadband conversion of Landsat TM glacier albedos: International Journal of Remote Sensing, v. 20, p. 2091–2110.

Koelemeijer, R., Oerlemans, J., and Tjemkes, S., 1993, Surface reflectance of Hintereisferner, Austria, from Landsat 5 TM imagery: Annals of Glaciology, v. 17, p. 17–17.

Kotchenova, S.Y., Vermote, E.F., and Matarrese, R., 2006, Validation of a vector version of the 6S radiative transfer code for atmospheric correction of satellite data. Part I: Path radiance: Applied Optics, v. 45, p. 6762–6774.

König, M., Winther, J.G., and Isaksson, E., 2001, Measuring snow and glacier ice properties from satellite: Reviews of Geophysics, v. 39, p. 1–27.

Kuchiki, K., Aoki, T., Niwano, M., Motoyoshi, H., and Iwabuchi, H., 2011, Effect

of sastrugi on snow bidirectional reflectance and its application to MODIS data: Journal of Geophysical Research, v. 116, p. D18110.

Kuhn, M., 1985, Bidirectional reflectance of polar and alpine snow surfaces: Annals Glaciology, v. 6, p. 164–167.

LaChapelle, R.E., 1969. Field guide to snow crystals. University of Washington Press, International Glaciology Society.

Leroux, C., Deuz, J.L., Goloub, P., Sergent, C., and Fily, M., 1998, Ground measurements of the polarized bidirectional reflectance of snow in the near-infrared spectral domain: Comparisons with model results: Journal of Geophysical Research, v. 103, p. 19–721.

Li, S., and Zhou, X., 2004, Modelling and measuring the spectral bidirectional reflectance factor of snow-covered sea ice: an intercomparison study: Hydrological Processes, v. 18, p. 3559–3581.

Li, Z., and Leighton, H.G., 1992, Narrowband to broadband conversion with spatially autocorrelated reflectance measurements: Journal of Applied Meteorology, v. 31, p. 421–432.

Light, B., 2000, PhD Thesis: University of Washington.

Lindsay, R.W., and Rothrock, D.A., 1994, Arctic sea ice albedo from AVHRR: Journal of Climate, v. 7, p. 1737–1749.

Lyapustin, A.I., and Privette, J.L., 1999, A new method of retrieving surface bidirectional reflectance from ground measurements: Atmospheric sensitivity study: Journal of Geophysical Research, v. 104, p. 6257–6268.

Marks, A.A., and King, M.D., 2013, The effects of additional black carbon on the albedo of Arctic sea ice: variation with sea ice type and snow cover: The Cryosphere, v. 7, p. 1193–1204.

Marks, A.A, 2014. Sea ice response to anthrapogenic pollution: an experiment and modeling study: PhD thesis, Royal Holloway University of London.

Martonchik, J.V., Bruegge, C.J., and Strahler, A.H., 2000, A review of reflectance nomenclature used in remote sensing: Remote Sensing Reviews, v. 19, p. 9–20.

Masek, J.G., Vermote, E.F., Saleous, N.E., Wolfe, R., Hall, F.G., Huemmrich, K.F., Gao, F., Kutler, J., and Lim, T.K., 2006, A Landsat surface reflectance dataset for North America: IEEE Geoscience and Remote Sensing Letters, v. 3, p. 68–72.

Maykut, G.A., 1978, Energy exchange over young sea ice in the central Arctic: Journal of Geophysical Research: Atmospheres, v. 83, p. 3646–3658.

McKenzie, R., Badosa, J., Kotkamp, M., and Johnston, P., 2005, Effects of the temperature dependence in PTFE diffusers on observed UV irradiances: Geophysical Research Letters, v. 32, p. L06808.

Mie, G., 1908, Beiträge zur Optik trüber Medien, speziell kolloidaler Metallösungen: Annalen der Physik, v. 330, p. 377–445.

Miller, D., Quinby-Hunt, M.S., and Hunt, A.J., 1997, Laboratory studies of angle- and polarization-dependent light scattering in sea ice: Applied Optics, v. 36, p. 1278–1288.

Mobley, C., 1994, Light and water, radiative transfer in natural waters: Academic Press Inc.

Mobley, C., 2010, Ocean optics web book, http://www.oceanopticsbook.info.

Mobley, C.D., 1989, A numerical model for the computation of radiance distributions in natural waters with wind-roughened surfaces: Limnology and Oceanography, v. 34, p. 1473–1483.

Mobley, C.D., 1998a, Hydrolight 4.0 Users Guide: Sequoia Scientific Inc Mercer Island WA.

Mobley, C.D., Cota, G.F., Grenfell, T.C., Maffione, R.A., Pegau, W.S., and Perovich, D.K., 1998b, Modeling light propagation in sea ice: Geoscience and Remote Sensing, IEEE Transactions on, v. 36, p. 1743–1749.

Mobley, C.D., Gentili, B., Gordon, H.R., Jin, Z., Kattawar, G.W., Morel, A., Reinersman, P., Stamnes, K., and Stavn, R.H., 1993, Comparison of numerical models for computing underwater light fields: Applied Optics, v. 32, p. 7484–7504.

Nicodemus, F.E., Richmond, J.C., Hsia, J.J., Ginsberg, I.W., and Limperis, T., 1977, Geometrical considerations and nomenclature for reflectance: United States National Bureau of Standards.

Nolin, A.W., Steffen, K., and Dozier, J., 1994, Measurement and modeling of the bidirectional reflectance of snow: Geoscience and Remote Sensing, IEEE Transactions on, p. 1919–1921.

Painter, T.H., 2004, Measurements of the hemispherical-directional reflectance of snow at fine spectral and angular resolution: Journal of Geophysical Research, v. 109, p. D18115.

Painter, T.H., Rittger, K., McKenzie, C., Slaughter, P., Davis, R.E., and Dozier, J., 2009, Retrieval of subpixel snow covered area, grain size, and albedo from MODIS: Remote Sensing of Environment, v. 113, p. 868–879.

Pegrum, H., Fox, N., Chapman, M., and Milton, E., 2006, Design and testing a new instrument to measure the angular reflectance of terrestrial surfaces, IEEE Geoscience and Remote Sensing Symposium, 2006. p. 1119–1122.

Peltoniemi, J.I., Kaasalainen, S., Naranen, J., Matikainen, L., and Piironen, J., 2005, Measurement of directional and spectral signatures of light reflectance by snow: Geoscience and Remote Sensing, IEEE Transactions on, v. 43, p. 2294–2304.

Perovich, D.K., 2003, Complex yet translucent: the optical properties of sea ice:

Physica B, v. 338, p. 107–114.

Perovich, D.K., 1994, Light reflected from sea ice during the onset of melt: Journal of Geophysical, v. 99, p. 3351–3359.

Perovich, D.K., 1998, Observations of the polarization of light reflected from sea ice, Journal of Geophysical Research: Oceans, v. 103, p. 5563–5575.

Perovich, D.K., 1996, The optical properties of sea ice: US Army Corps of Engineers CRREL, p. 1–24.

Perovich, D.K., and Gow, A.J., 1996, A quantitative description of sea ice inclusions: Journal of Geophysical Research, v. 101, p. 18327.

Perovich, D.K., and Grenfell, T.C., 1981, Laboratory studies of the optical properties of young sea ice: Journal of Galciology, v. 27, p. 331–346.

Perovich, D.K., and Polashenski, C., 2012, Albedo evolution of seasonal Arctic sea ice: Geophysical Research Letters, v. 39, p. L08501.

Perovich, D.K., Richter Menge, J.A., Jones, K.F., and Light, B., 2008, Sunlight, water, and ice: Extreme Arctic sea ice melt during the summer of 2007: Geophysical Research Letters, v. 35, p. L11501.

Petty, G.W., 2006, A First Course In Atmospheric Radiation: Sundog Publishing.

Picard, G., Arnaud, L., Domine, F., and Fily, M., 2009, Determining snow specific surface area from near-infrared reflectance measurements: Numerical study of the influence of grain shape: Cold Regions Science and Technology, v. 56, p. 10–17.

Qu, X., and Hall, A., 2005, Surface contribution to planetary albedo variability in cryosphere regions: Journal of Climate, v. 18, p. 5239–5252.

Rees, W.G., 2006, Remote sensing of snow and ice: CRC Press.

Rignot, E., Box, J.E., Burgess, E., and Hanna, E., 2008, Mass balance of the Greenland ice sheet from 1958 to 2007: Geophysical Research Letters, v. 35, p. L20502.

Schaaf, C., Gao, F., Strahler, A., Lucht, W., Li, X., Tsang, T., Strugnell, N., Zhang, X., Jin, Y., Muller, J., Lewis, P., Barnsley, M., Hobson, P., Disney, M., et al., 2002a, First operational BRDF, albedo nadir reflectance products from MODIS: Remote Sensing of Environment, v. 83, p. 135–148.

Schaaf, C.B., Gao, F., Strahler, A.H., Lucht, W., Li, X., Tsang, T., Strugnell, N.C., Zhang, X., Jin, Y., Muller, J.-P., Lewis, P., Barnsley, M., Hobson, P., Disney, M., et al., 2002b, First operational BRDF, albedo nadir reflectance products from MODIS: Remote Sensing of Environment, v. 83, p. 135–148.

Schaepman-Strub, G., Schaepman, M.E., Painter, T.H., Dangel, S., and Martonchik, J.V., 2006, Reflectance quantities in optical remote sensing—definitions and case studies: Remote Sensing of Environment, v. 103, p. 27–42.

Schlosser, E., 1988, Optical studies of Antarctic sea ice: Cold Regions Science and Technology, v. 15, p. 289–293.

Screen, J.A., and Simmonds, I., 2010, The central role of diminishing sea ice in recent Arctic temperature amplification: Nature, v. 464, p. 1334–1337.

Smith, R., and Baker, K., 1981, Optical properties of the clearest natural waters (200–800 nm): Applied Optics, v. 20, p. 177–184.

Song, J., and Gao, W., 1999, An improved method to derive surface albedo from narrowband AVHRR satellite data: Narrowband to broadband conversion: Journal of Applied Meteorology, v. 38, p. 239–249.

Springsteen, A., 1999, Standards for the measurement of diffuse reflectance – an overview of available materials and measurement laboratories: Analytica Chimica Acta, v. 380, p. 379–390.

Stamnes, K., Tsay, S.C., Wiscombe, W., and Jayaweera, K., 1988, Numerically stable algorithm for discrete-ordinate-method radiative transfer in multiple scattering and emitting layered media: Applied Optics, v. 27, p. 2502–2509.

Strahler, A.H., and Muller, J., 1999, MODIS BRDF/albedo product: Algorithm theoretical basis document version 5.0: MODIS BRDF, p. 1–53.

Stroeve, J., Holland, M.M., Meier, W., Scambos, T., and Serreze, M., 2007, Arctic sea ice decline: Faster than forecast: Geophysical Research Letters, v. 34, p. L09501.

Stroeve, J., Nolin, A., and Steffen, K., 1997, Comparison of AVHRR-derived and in situ surface albedo over the greenland ice sheet: Remote Sensing of Environment, v. 62, p. 262–276.

Stroeve, J.C., Box, J.E., and Haran, T., 2006, Evaluation of the MODIS (MOD10A1) daily snow albedo product over the Greenland ice sheet: Remote Sensing of Environment, v. 62, p. 262–276.

Sun, Z., Zhang, J., and Zhao, Y., 2013, Laboratory studies of polarized light reflection from sea ice and lake ice in visible and near infrared: IEEE Geoscience and Remote Sensing Letters, v. 10, p. 170–173.

Velicogna, I., 2009, Increasing rates of ice mass loss from the Greenland and Antarctic ice sheets revealed by GRACE: Geophysical Research Letters, v. 36, p. L19503.

Wang, X., Doherty, S.J., and Huang, J., 2013, Black carbon and other light-absorbing impurities in snow across Northern China: Journal of Geophysical Research: Atmospheres, v. 118, p. 1471–1492.

Wanner, W., Strahler, A.H., Hu, B., Lewis, P., Muller, J.P., Li, X., Schaaf, C.L.B., and Barnsley, M.J., 1997, Global retrieval of bidirectional reflectance and albedo over land from EOS MODIS and MISR data: Theory and algorithm: Journal of Geophysical Research, v. 102, p. 17143.

Warner, T.A., Foody, G.M., and Nellis, M.D., 2009, The SAGE Handbook of

Remote Sensing: SAGE publications.

Warren, S.G., 1982, Optical properties of snow: Reviews of Geophysics, v. 20, p. 67–89.

Warren, S.G., and Brandt, R.E., 2008, Optical constants of ice from the ultraviolet to the microwave: A revised compilation: Journal of Geophysical Research, v. 113, p. D14220.

Warren, S.G., and Wiscombe, W.J., 1985, Dirty snow after nuclear war: Nature Geoscience, v. 313, p. 467–470.

Warren, S.G., Brandt, R.E., and Hinton, P., 1998, Effect of surface roughness on bidirectional reflectance of Antarctic snow: Journal of Geophysical Research, v. 103, p. 25.

Weeks, W.F., 2010, On sea ice: University of Alaska Press.

Weidner, V.R., and Hsia, J.J., 1981, Reflection properties of pressed polytetrafluoroethylene powder: JOSA, v. 71, p. 856–861.

Weller, G., and Holmgren, B., 1974, The microclimates of the Arctic tundra: Journal of Applied Meteorology, v. 13, p.854–862.

Wiscombe, W.J., and Warren, S.G., 1980, A model for the spectral albedo of snow. I: Pure snow: Journal of the Atmospheric Sciences, v. 37, p. 2712–2733.

Wright, P., Bergin, M., Dibb, J., Lefer, B., Domine, F., Carman, T., Carmagnola, C., Dumont, M., Courville, Z., Schaaf, C., and Wang, Z., 2014, Comparing MODIS daily snow albedo to spectral albedo field measurements in Central Greenland: Remote Sensing of Environment, v. 140, p. 118–129.

Ylianttila, L., and Schreder, J., 2005, Temperature effects of PTFE diffusers: Optical Materials, v. 27, p. 1811–1814.

Zhonghai Jin, and Simpson, J.J., 1999, Bidirectional anisotropic reflectance of snow and sea ice in AVHRR Channel 1 and 2 spectral regions. I. Theoretical analysis: IEEE Transactions on Geoscience and Remote Sensing, v. 37, p. 543–554.

Zhonghai Jin, and Simpson, J.J., 2000, Bidirectional anisotropic reflectance of snow and sea ice in AVHRR channel 1 and channel 2 spectral regions. II. Correction applied to imagery of snow on sea ice: IEEE Transactions on Geoscience and Remote Sensing, v. 38, p. 999–1015.

Chapter 2

Bidirectional reflectance of windblown Arctic snow

2.1 Abstract

Measurements of the hemispherical-conical reflectance factor (HCRF) of windblown Arctic snow were made for six sites near to the international research base in Ny-Ålesund, Svalbard. The measurements were carried out under large solar zenith angles (79° to 85°) using the GonioRAdiometric Spectrometer System (GRASS). Reflected radiance was measured over the viewing angles 0° to 50°, and azimuth angles 0° to 360°, for the wavelength range 400 nm to 1700 nm. The HCRF measurements generally agreed well between different sites for viewing angles near nadir and in backward direction for sites where the snowpack was smooth and snow depth was greater than 40 cm, with a relative standard deviation of less than 10 %. The averaged HCRF showed good symmetry with respect to the solar principal plane and exhibited a forward scattering peak that was strongly wavelength dependent, with greater than a

factor of 2 increase in the anisotropy index over the wavelength range 400 nm to 1300 nm. The angular dependence to the reflected distribution had minimal influence for viewing angles less than 15° in the backward viewing direction for the averaged sites, and agreed well with another study of snow HCRF for infrared wavelengths, but showed differences of up to 0.24 in the HCRF for visible wavelengths, which was attributed to large mass ratios of black carbon measured in the snowpack. Maximum mass ratios of the black carbon were measured for each field site in the top 10 cm of the snow pack and were found to be large compared to background levels for Svalbard, with values in the range 90 ng g^{-1} to 299 ng g^{-1}. The site that had the largest roughness elements showed the strongest anisotropy in the HCRF, a large reduction in forward scattering, and a strong asymmetry with respect to the solar principal plane. An improved pointing accuracy, a larger footprint area, and improved characterization of grain size in the surface layer was required to fully understand the effects of macroscale surface roughness.

2.2 Aims of the study

The study aims to provide systematic hyperspectral HCRF measurements of Arctic snow-covered tundra for a range of snow surface types at large solar zenith angles. Previous studies have characterized the HCRF of snow (e.g. Painter, 2004; Bourgeois et al., 2006; Kuhn, 1985; Hall et al., 1992; Hudson et al., 2006; Warren et al., 1998; Peltoniemi et al., 2005; Marks et al., 2015; Hakala et al., 2014), but few studies have obtained systematic measurements of snow HCRF at large solar zenith angles for a variety of snow surface types. In order to explain the differences in the HCRF measurements between sites, this study also aims to acquire ancillary sky and snow measurements including: light absorbing impurities in the snowpack, snow density, snow grain size, snow

surface roughness; and atmospheric properties such as the ratio of the direct to diffuse irradiance for each field site.

2.3 Introduction

Surface albedo is the bihemispherical reflectance, or the ratio of reflected radiant flux to the incident radiant flux of hemispherical angular extent (Schaepman-Strub et al., 2006). As a critical component in the Earth's radiation budget, the albedo defines the proportion of solar radiation absorbed, and reflected, over a large part of the Earth's surface (Qu and Hall, 2005; Flanner et al., 2011). The albedo of snow is dependent on its absorption and scattering properties and is strongly influenced by light absorbing impurities in the snowpack such as black carbon (Clarke and Noone, 1985; Hansen and Nazarenko, 2004; Doherty et al., 2010; Grenfell et al., 2002). Snow is primarily composed of ice crystals in a matrix of air, and as a result, has a strong wavelength dependence to its albedo, which can be in excess of 0.9 for UV and visible wavelengths (Grenfell et al., 1994). Earth observing satellite sensors have the ability to monitor the albedo of snow over remote and inaccessible regions such as the Arctic at high spatial and temporal resolution (Stroeve et al., 2005; Painter et al., 2009; Schaaf et al., 2002). However, space-borne sensors subtend only a discrete angle to the target surface and the directional reflectance of snow is not isotropic (Kuhn, 1985; Hall et al., 1992). Furthermore, the reflectance of snow depends on the wavelength of the reflected radiation, and the majority of satellite sensors measure radiance over a limited number of spectral bands. Consequently, satellite sensors require knowledge of the spectrally-resolved bidirectional reflectance (BRDF) of the target surface to accurately derive surface properties such as surface albedo through the use of albedo/BRDF retrieval algorithms for snow (Jin and Simpson, 2001; Strahler and

Muller, 1999). The accuracy to which satellite sensors are able to derive snow properties is dependent on the accuracy of the BRDF model. To better build, test and validate these models, hyperspectral, ground-based, bidirectional reflectance data are required. Several previous field studies have measured the Hemispherical-Conical Reflectance Factor (HCRF) of snow (e.g. Painter, 2004; Bourgeois et al., 2006; Kuhn, 1985; Hall et al., 1992; Hudson et al., 2006; Warren et al., 1998; Peltoniemi et al., 2005; Marks et al., 2015; Hakala et al., 2014). However, few studies have obtained measurements over rough windblown snow, or at very large solar zenith angles (greater than 80°); where satellite albedo retrieval algorithms are least reliable (Stroeve et al., 2005; Liu et al., 2009), and where snow surface roughness has the greatest effect on the bidirectional reflectance (Warren et al., 1998; Miesch et al., 2002). In addition, it has been shown that failure to account for snow surface roughness at large solar zenith angles in BRDF models can lead to order of magnitude errors in the derivation of snow surface properties (Kuchiki et al., 2011). Hence more systematic measurements of snow bidirectional reflectance for large solar zenith angles, and for a wider variety of snow surface types are required (Peltoniemi et al., 2005).

The bidirectional reflectance distribution function (BRDF) describes intrinsic reflectance properties of a surface, or the relationship between the incident light from a particular direction to the light reflected by the surface into a particular direction (Nicodemus et al., 1977). By definition, the BRDF is a ratio of infinitesimal quantities and cannot be measured directly as all field spectrometers have a finite field-of-view (FOV) (Milton et al., 2009; Schaepman-Strub et al., 2006). In addition, solar irradiance consists of both a direct term (non-scattered), and a diffuse term (scattered by clouds, aerosols, gases and

the surrounding terrain), the relative proportion of which, is wavelength dependent (Lyapustin and Privette, 1999; Grenfell et al., 1994). As a result, the measurable quantity in the field is the hemispherical-conical reflectance factor (HCRF) (Schaepman-Strub et al., 2006).

The investigation described here measured the HCRF of windblown Arctic snow covered tundra at 6 sites under relatively clear sky conditions with minimal cirrus cloud cover. The HCRF measurements were made using the GonioRAdiometric Spectrometer System (GRASS) (Pegrum-Browning et al., 2008) during a three-week field campaign in Ny-Ålesund, Svalbard in Spring 2013. The goniometer's configuration allowed for an angular resolution of 10° in viewing angle and approximately 30° in azimuth angle, covering the angular range of 0° to 50° in zenith angles, and 0° to 360° in azimuth angles.

The work carried out in this thesis chapter has been published in the peer-reviewed journal: IEEE Transaction on Geoscience and Remote Sensing (TGRS), by Ball et al. (2015). The coauthors (A.A. Marks, P.D. Green, A. MacArthur, M. Maturilli, N.P. Fox and M.D. King) provided advice and guidance to the first author of the publication (C.P. Ball) on various aspects of the work in a supervisory fashion. A.A. Marks provided assistance with field measurements in Svalbard.

2.4 Methodology

The methodology will be divided into separate descriptions of the site, the goniometer, laboratory testing of the goniometer, the field measurements, and the data reduction and processing procedures.

2.4.1 Experiment site

Measurements of HCRF were carried out along two transects near to the international research base in Ny-Ålesund (78° 55′N, 11° 56′ E) in Svalbard between the 19th of March and the 1st of April 2013. The transects were 100 m in length and were located on two areas of undisturbed snow covered tundra approximately 0.25 km east, and 2.90 km northwest of the Ny-Ålesund research base. The individual sites were systematically located at approximately 10 m intervals along each transect. The number of field measurements acquired was dependent on the number of clear sky days over the 3-week period. In total, 9 HCRF acquisitions were carried out along the eastern transect, and 2 HCRF acquisitions were carried out along the western transect, although 5 of these acquisitions were later omitted owing to instability in downwelling irradiance. A photograph of the Ny-Ålesund research base is given in Figure 2.1.

Figure 2.1. Photograph of the Ny-Ålesund research base in March 2013

2.4.2 Instrumentation: GonioRAdiometric Spectrometer System (GRASS)

The GonioRAdiometric Spectrometer System (GRASS) was used to measure the HCRF of the snow at each site during the field campaign.

2.4.2.1 Goniometer background

GRASS was first developed at the UK National Physical Laboratory (NPL) by Pegrum-Browning et al. (2008) in collaboration with the UK Natural Environment Research Council Field Spectroscopy Facility (NERC FSF) to measure the hemispherical conical reflectance (HCRF) of natural surfaces. The instrument was field-tested during the international comparison carried out in Tuz Gölü, Turkey, in August 2010, by the Committee on Earth Observing Satellites (CEOS). Since the field campaign in Turkey the instrument has undergone modifications undertaken by NERC FSF, which enabled the GRASS system to operate with just 16-foreoptics located on 3-arms. The instrument has since been used to measure the HCRF of snow at Dome C, Antarctica in 2011 (Marks et al., 2015).

2.4.2.2 Goniometer design

The goniometer was designed to be lightweight, quickly assembled in remote situations, robust, and easily transportable (Pegrum-Browning et al., 2008; Pegrum et al., 2006). The goniometer consists of a series of vertical arms that form a hemispherical structure above the target surface. A schematic of the goniometer's frame is given in Figure 2.2.

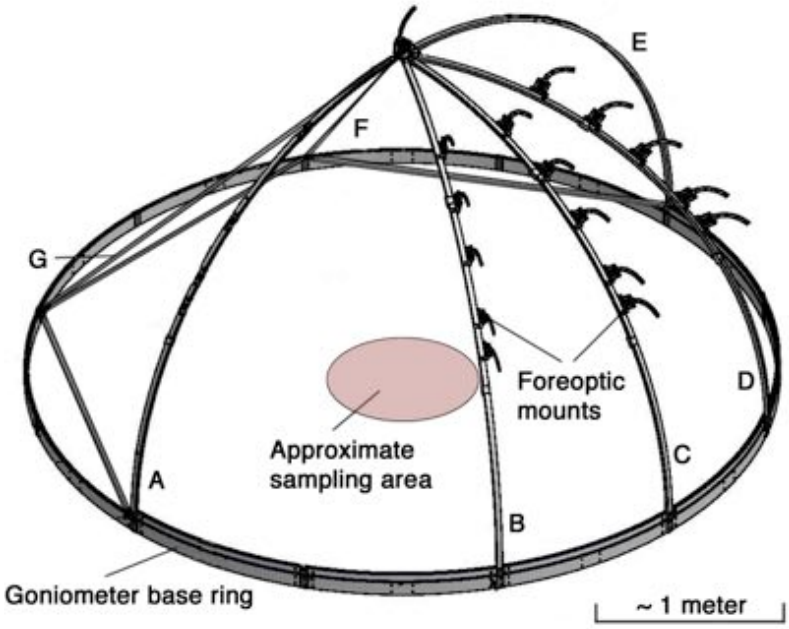

Figure 2.2. Schematic of the goniometer's frame showing the relative position of each of the goniometer's arms (labeled A to G) and the approximate size of the sampling area (from Ball et al. 2015)

Fifteen foreoptics are mounted on three of the arms and one foreoptic is located at the nadir viewing position ($\theta_v = 0$) at the top of the structure. Each foreoptic was separated by 10° in viewing angle and approximately 30° in azimuth angle, the maximum viewing angle was 50° for the configuration used in this study. A maximum view angle of 50° was chosen as previous field measurements by Marks (2015) showed that viewing angles in excess of 60° could be affected by reflections from the goniometer's base ring.

The radius of the circular base of the structure was 2 m, as was the distance between each foreoptic and the goniometer's centre point on the target surface. The goniometer arms were designed so that they can be manually rotated on the circular base of the structure to capture reflected radiance over the full upward facing hemisphere. Three rotations of approximately 90° enabled the arms holding the foreoptics to sample reflected radiance through 360° of

azimuth at approximately 30° intervals. A photograph GRASS undergoing construction in the field is given in Figure 2.3.

Figure 2.3. Construction of the goniometer's frame at the field site

Each of the goniometer's foreoptics consists of an 8° (full angle) collimating lens coupled by optical fibre to a multiplexer that gives a single output to a dual-field-of-view Visible to ShortWave Infrared Spectroradiometer (V-SWIR). A Labview program controlled the operation of the multiplexer and the spectrometer, which allowed the system to step through the optical input for each of the 16 foreoptics individually. Once a measurement of radiances had been recorded for all foreoptics in the first quarter of a hemisphere, the arms were rotated by approximately 90° and the foreoptics were used to measure radiances reflected into the subsequent quarter of the hemisphere. The process was repeated until radiances were acquired across the entire upward facing hemisphere at the desired angular resolution. An integrating cosine irradiance collector was attached to the top of the goniometer's frame and coupled to V-SWIR via a second input for a near-simultaneous measurement of downwelling irradiance. The HCRF acquisition over a full hemisphere took around 60-minutes. A

photograph of the GRASS system during the field campaign is given in Figure 2.4.

Figure 2.4. The GonioRAdiometric Spectrometer System (GRASS) with 15-foreoptics mounted on 3-arms and one foreoptic positioned in the nadir view position. The spectrometer, multiplexer and laptop are situated in the sled (left) and the all-sky camera is mounted and leveled on a tripod (out of view) (from Ball et al. 2015)

2.4.2.3 V-SWIR spectrometer

The V-SWIR spectrometer consists of two spectrometers, an Ocean Optics USB 2000+ and a B&WTek sol 1.7, allowing for measurements over the wavelength range 400 nm to 1700 nm at 1 nm sampling interval. V-SWIR consists of a beam splitter to spilt the input light between the two spectrometers, and a motorized mirror, which acts as an optical switch between the two inputs, allowing reflected radiance and downwelling irradiance to be measured near simultaneously (separated by less than 2 seconds). The V-SWIR spectroradiometer was controlled by a Panasonic Toughbook laptop. Radiometric calibration of V-SWIR was carried out at NERC FSF prior to its use in the field using an integrating sphere source and a standard FEL lamp.

2.4.3 GRASS laboratory testing and repeatability

Prior to its use in the field, the GRASS system underwent laboratory testing to assess the instrument's mechanical optical stability and pointing accuracy.

2.4.3.1 Mechanical stability of optical system

The repeatability of the measurement setup upon rotating the goniometer's arms was tested in the laboratory at Royal Holloway University of London (RHUL). The 3-arms were rotated on the circular base through 8-rotations (each of approximately 90°), and radiances were recorded by the spectrometer for each foreoptic for each rotation while viewing an intensity stabilized integrating sphere source. The integrating sphere source consisted of a tungsten halogen lamp, with a regulated and stabilized power supply, coupled to a Spectralon integrating sphere. The integrating sphere exit port surround was designed so that each foreoptic located in the same position in the integrating sphere, ensuring that the distance between the exit port aperture and the collimating lens was the same for each replicate measurement. The exit port of the integrating sphere was designed to snuggly surround each foreoptic to avoid any extraneous light contributing to the measurement. The relative standard deviation of the radiances recorded by the spectrometer between 450 nm and 1600 nm for all foreoptics and respective fibres over 8-replicate measurements (excluding data from a single damaged fibre) was less than 5 % (1σ) and was typically 2 %. There was minimal wavelength dependence to the relative standard deviation in the replicate measurements, although wavelengths greater than 1650 nm had a relative increase in the standard deviation by up to a factor of 6, which was the result of poor signal to noise at the detection limit of the spectrometer. The relative standard deviation of the 8-replicate measurements is given in Figure 2.5 as function of wavelength.

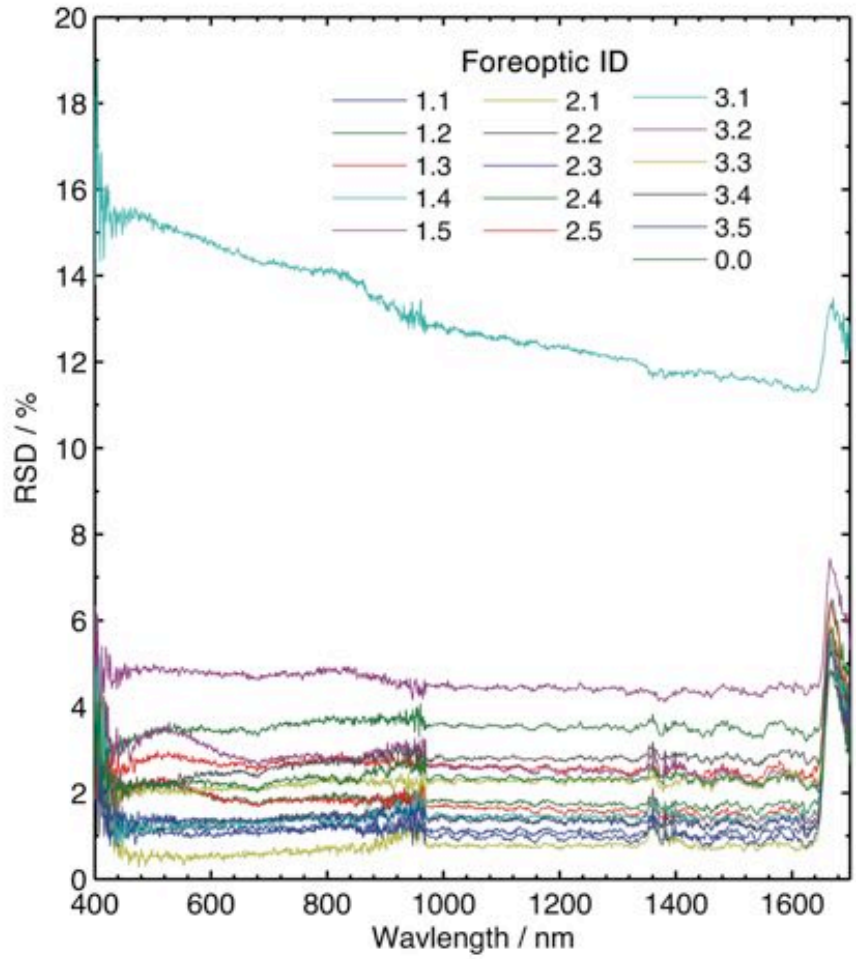

Figure 2.5. Relative standard deviation (RSD) of the replicate foreoptic measurements upon rotation of the goniometer's frame

Foreoptic 1.4 had the greatest variance, with a relative standard deviation of 11 %, which increased to a maximum of 18.9 % at 405 nm. The instability in the radiances recorded by the foreoptic 1.4 was the result of a damaged fibre, which was not used during field campaign. In order to test for damaged fibres during the field campaign, measurements of radiance were made for each foreoptic while viewing an intensity stabilised integrating sphere source at the end of each HCRF acquisition at each field site. The relative standard deviations for the radiances recorded by each foreoptic during the field campaign are presented in Figure 2.6, and were less than 30 % for all foreoptics, and were typically 15 %. Given that the transmission efficiencies were expected to change between sites owing to movement and reassembly of the structure, the results do not indicate

damage to any particular fibre. The variability in transmission efficiencies of the fibres at each site was accounted for by applying an intercalibration factor as described in Section 2.4.4.2.

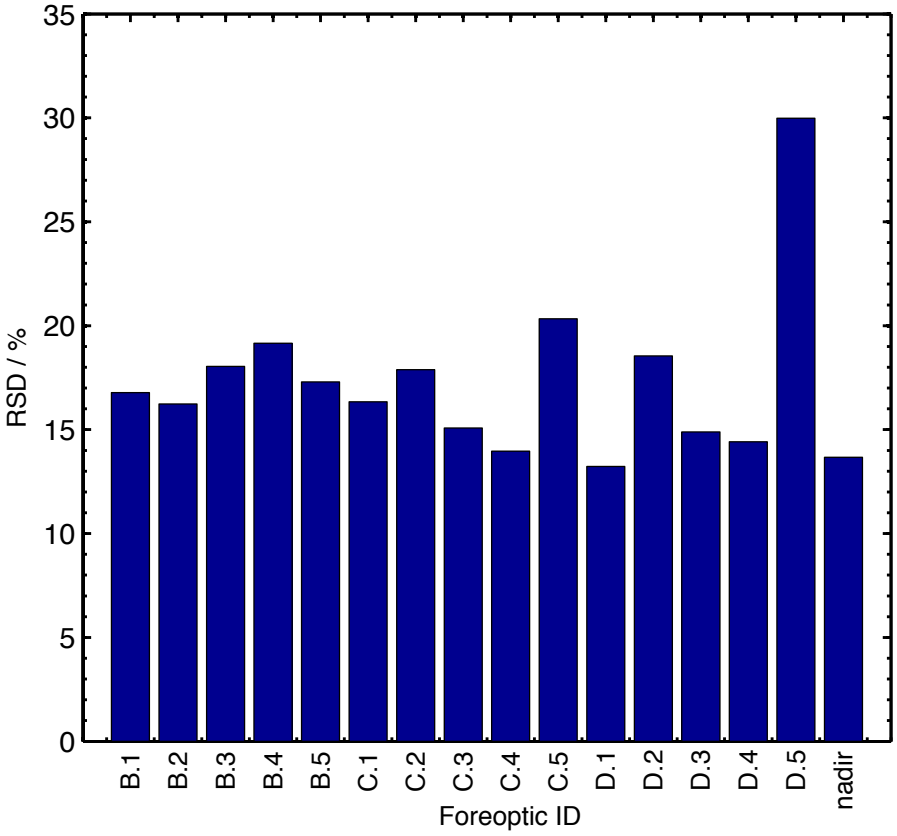

Figure 2.6. Relative standard deviation of foreoptics while viewing a stabilised integrating sphere source at each field site during the field campaign

2.4.3.2 Pointing accuracy and foreoptic footprint overlap

The footprint overlap was assessed by measuring the pointing accuracy of the goniometer in a dark laboratory at RHUL. The spectrometer and multiplexer were disconnected from the 6 foreoptics on the middle arm of the goniometer and a diode laser was shone back down each optical fibre and foreoptic to illuminate an area of white linoleum flooring that corresponds to the area of the foreoptic footprint or ground instantaneous field of view (GIFOV). The centre point of the footprint was recorded by tracing the major and minor axes of the illuminated area. The position of the footprint centre points were recorded for the

same viewing angles as used in the field study (0° to 50°), and for 4 different azimuth positions (0°, 90°, 180°, 270°), totaling 24 different viewing positions. The size and shape of the footprint was calculated with the knowledge of the foreoptics FOV (8° full angle), and the approximate distance to the goniometer's centre point (2 m). The footprints and centre points for the 24 view positions are plotted in Figure 2.7.

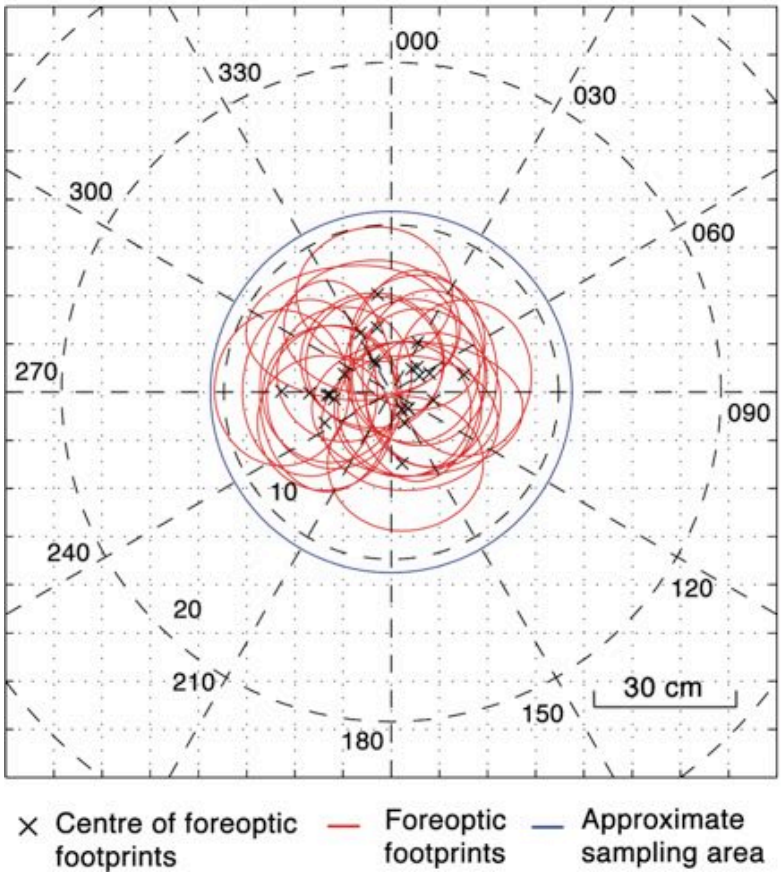

Figure 2.7. Overlap of foreoptic footprints at 6 different zenith positions ($\theta_r = 0° - 50°$) and at 4 different azimuth positions ($\phi_r = 0° - 270°$) (from Ball et al. 2015)

The maximum distance of the foreoptic footprint centre from the goniometer centre was found to be 20.49 cm; implying a pointing accuracy of roughly ± 20 cm, and an approximate sample area size of 0.4 m^2, which is not sampled fully or equally. At 50° viewing angle, the footprint had a major axis diameter of 47 cm, and at the nadir view position the footprint was circular and had a diameter of 28 cm. Given the relatively large footprint the pointing accuracy was

considered satisfactory for sites where the snow surface was homogeneous. The impact of the imperfect footprint overlap for sites that were considered heterogeneous, owing to the presence of roughness elements, is discussed in Section 2.4.5.2.

2.4.4 Field measurements

This section describes the HCRF measurements and the ancillary sky and snow measurements that were carried out at each of the field sites.

2.4.4.1 HCRF acquisition

The HCRF of the snow surface at each site was measured using the GRASS system. Reflected radiance was recorded for each quarter of the hemisphere by the V-SWIR spectrometer. The arms holding the sixteen foreoptics were manually rotated on the instruments base ring through each quarter of the hemisphere and the azimuthal position of the arms was recorded. A typical set-up showing the position of each of the foreoptics over the hemisphere is given in Figure 2.8. The large diameter of goniometer's base ring (4 m) compared to the diameter of the sampling area (0.8 m), combined with the ability to manually adjust the azimuthal positioning of the arms, allowed the goniometer's arms to be manually positioned so that there is was no shadowing of the sampling area during the HCRF acquisition. Consequently, the foreoptics do not always measure radiance at equal intervals in azimuth angle (as seen in Figure 2.8), and no measurement could be taken in the backward direction in the solar principal plane. The distance between the base of arms A and B in Figure 3 is 60°, or 1 m.

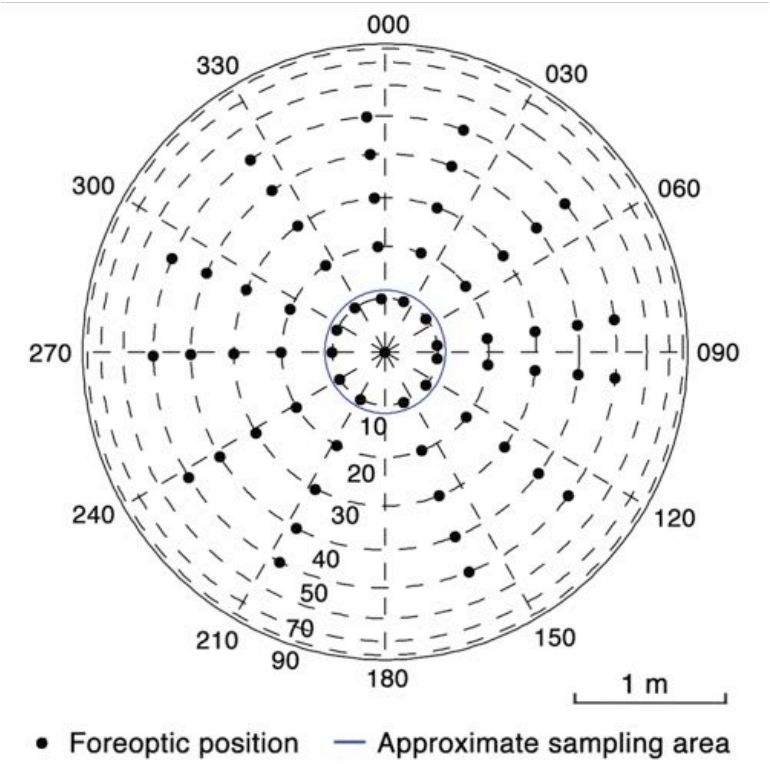

Figure 2.8. Typical sampling positions of the GRASS foreoptics and the approximate size of the sampled area. The sunlight intersects the plot at the 180° index (from Ball et al. 2015)

The radiance reflected by a calibrated Spectralon reference panel placed on the snow surface at the end of each HCRF acquisition was measured using V-SWIR and the foreoptic at the nadir viewing position. An integration time of 2-seconds was necessary to achieve the required signal-to-noise ratio for V-SWIR, resulting in a typical total measurement time of approxmately 60-minutes for a complete measurement of one target.

2.4.4.2 Foreoptic intercalibration

Foreoptics and fibres were intercalibrated at each field site at the end of each HCRF acquisition to account for their respective transmission efficiencies. Variability in radiances were recorded as a function of wavelength for each individual foreoptic while viewing a stabilized integrating sphere source described in Section 2.4.3.1. Intercalibration correction factors were calculated

by normalizing the radiance for each of the 15-foreoptics, to the radiance recorded by the foreoptic at the nadir viewing position as follows:

$$C_f(\lambda) = \frac{L_{IS,f=nadir}(\lambda)}{L_{IS,f}(\lambda)}, \qquad \text{Eq. 2.1}$$

where $C_f(\lambda)$ is the intercalibration correction factor for the foreoptic f, $L_{IS,f=nadir}(\lambda)$ is the radiance recorded by the spectrometer while viewing the intensity stabilized integrating sphere source with the nadir foreoptic. $L_{IS,f}(\lambda)$ is the radiance recorded by the spectrometer while viewing the stable integrating sphere source with the foreoptic f.

2.4.4.3 Spectralon reference panel

The HCRF is defined as the ratio of radiance reflected by the target surface into a particular direction to that reflected by a lossless Lambertian reflector under ambient illumination. A Spectralon panel viewed from nadir ($\theta_r = 0°$) and positioned on the snow surface at the end of the measurement sequence was used to approximate a lossless Lambertian reflector. The Spectralon panel was calibrated at the National Physical Laboratory (NPL), using the National Reference Reflectometer (NRR) (Williams, 1999; Chunnilall et al., 2003) for the solar and view geometries used in the field to account for the departure of our panel from a lossless Lambertain reflector (Sandmeier et al., 1998). The calibration yielded a reflectance correction factor β for the wavelength range 400 nm to 1000 nm, which is defined as the ratio of the radiance reflected by the Spectralon panel in a given direction θ, to that of a lossless Lambertian reflector identically irradiated (Williams, 1999):

$$\beta = \frac{R(2s/d)^2}{cos(\theta)}, \qquad \text{Eq. 2.2}$$

where R is the measured ratio of reflected power to incident power, s is the

distance between the sample surface and the detectors aperture and d is the diameter of the aperture. The reflectance correction factors β for the Spectralon panel as a function of incidence angle are given in Figure 2.9.

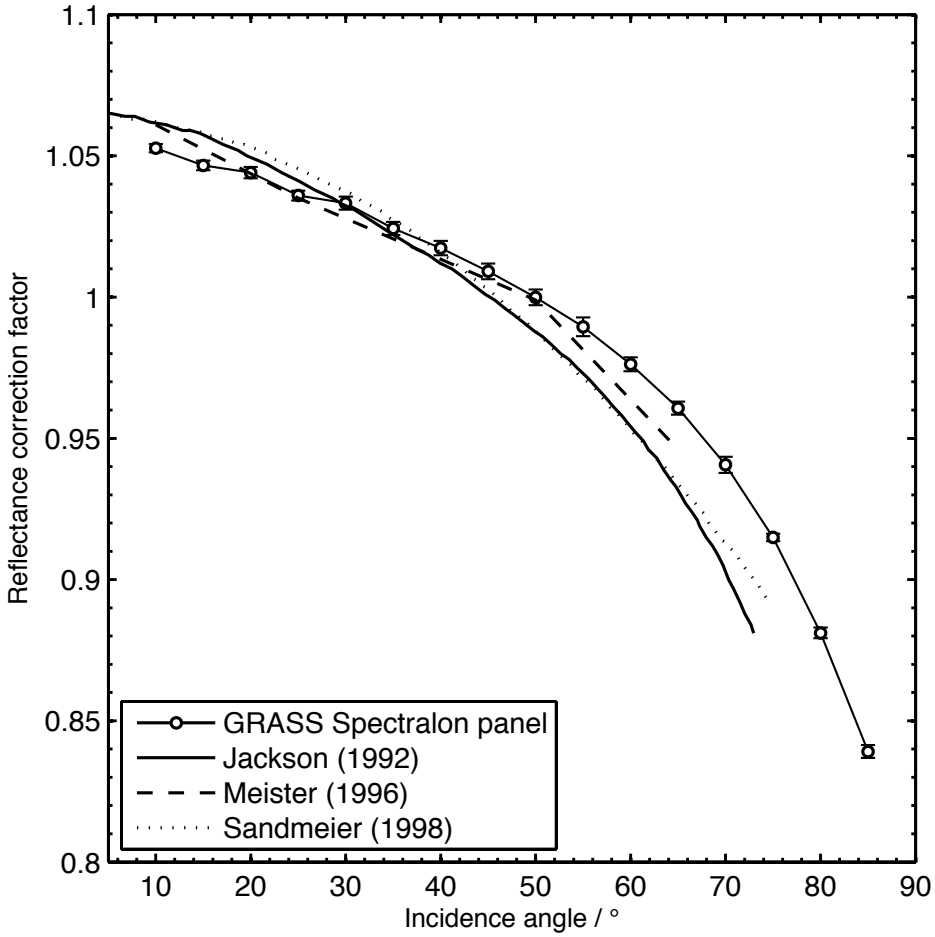

Figure 2.9. Reflectance correction factors for the Spectralon panel used with GRASS. Reflectance correction factors made by other researchers for different Spectralon panels are given for comparison. Uncertainty bars are given to 2 standard deviations

The reflectance correction factors as a function of wavelength for the Spectralon panel used with GRASS are given in Figure 2.10.

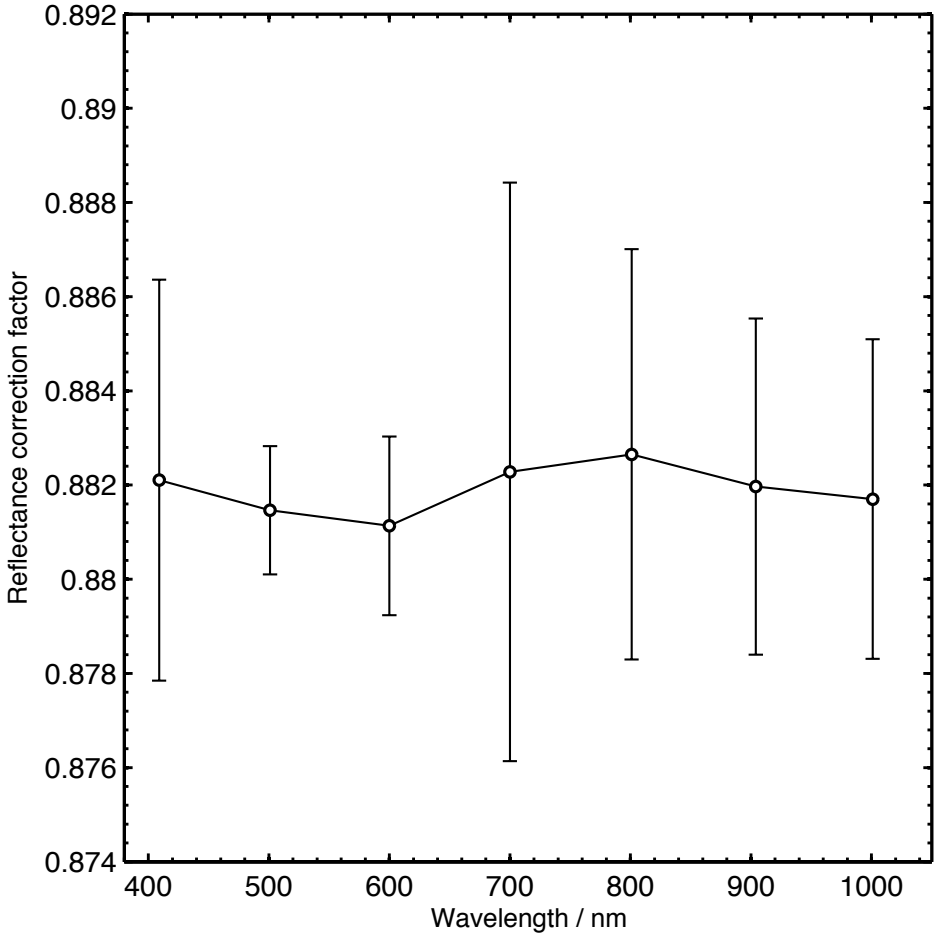

Figure 2.10. Reflectance correction factors as a function of wavelength for the Spectralon panel used with GRASS. Uncertainty bars are given to 2 standard deviations of the averaged measurements

The spectrally averaged value of β (0.88) was used, since the wavelength dependency over the range 400 nm to 1000 nm was found to be less than 0.5 %. Correction factors were assumed to be valid up to 1700 nm as the wavelength dependency of the hemispherical reflectance of Spectralon (the average of 7 panels), presented by Jackson et al. (1992), was less than 1 % over the wavelength range 1000 nm to 1700 nm.

The reflectance correction factor is measured with an incident beam angle of 0° zenith angle and a viewing angle of 80°. To obtain the approximate configuration used in the field the directions were exchanged by applying the

Helmholtz reciprocity principal (Clarke and Parry, 1985). The reflectance characteristics of the Spectralon panel were assumed to be rotationally symmetric to nadir (Sandmeier et al., 1998). Given that a Lambertian surface has a constant radiance independent of view angle, the radiance measured from nadir was applied to all other foreoptics when calculating the HCRF. The radiance reflected by the Spectralon panel was subject to correction by the intercalibration correction factor, $C_f(\lambda)$, derived in Section 2.4.4.2, when applied to each of the individual foreoptics. Temperature differences between ambient laboratory and field conditions were considered unlikely to significantly affect the reflectance of the Spectralon reference standard (Ball et al., 2013).

2.4.4.4 Calculating the HCRF

The HCRF is calculated here as follows:

$$HCRF(\theta_i,\phi_i,2\pi;\theta_r,\phi_r;\lambda) = \frac{L_r(\theta_i,\phi_i,2\pi;\theta_r,\phi_r;\lambda)}{L_{r,Spectralon}(\theta_i,\phi_i,2\pi;\lambda)} C_f(\lambda)\beta \quad \text{Eq. 2.3}$$

where $C_f(\lambda)$ is the foreoptic intercalibration correction factor defined in Section 2.4.4.2 and β is the reflectance correction factor for the Spectralon reference panel defined in Section 2.4.4.3. The measured HCRF function was then projected onto a 2-D grid and linearly interpolated using a Delaunay triangle-based method (de Berg et al., 2008).

The extent of anisotropy in the HCRF over all viewing angles can be described using the anisotropy index, ANIX, defined in Chapter 1 as the following:

$$ANIX(\lambda) = \frac{HCRF_{\max}(\lambda)}{HCRF_{\min}(\lambda)} \quad \text{Eq. 2.4}$$

2.4.4.5 Ancillary sky measurements

During the HCRF acquisition ancillary measurements were made in order to characterize the sky conditions. All-sky camera imagery was acquired at 1-minute intervals using a Nikon Coolpix E4500 digital camera and fish-eye lens. Broadband shortwave global and diffuse radiation (200 nm to 4000 nm) is measured at 1-minute intervals near to the field site at the AWIPEV research station using a Kipp & Zonen CMP22 pyranometer, as part of the Baseline Surface Radiation Network (BSRN). Measurements of aerosol optical thickness (AOT) were made at the field site using a handheld Microtops II sunphotometer (Morys et al., 2001) at approximately 15-minute intervals during each HCRF acquisition. The sunphotometer had five filters centered at 440 nm, 675 nm, 870 nm, 936 nm and 1020 nm with a full-width half-maxima of 10 nm and full field of view of 2.5°. The results of the sunphotometer measurements for each 6 sites are given in Table 2.1.

Site ID	Average aerosol optical thickness (%)				
	440 nm	675 nm	870 nm	936 nm	1020 nm
S1	0.16	0.11	0.08	0.08	0.09
S4	0.17	0.12	0.09	0.1	0.1
S2	0.1	0.08	0.05	0.06	0.06
S3	0.14	0.13	0.09	0.1	0.11
S6	0.11	0.08	0.05	0.06	0.07
S5	0.19	0.12	0.08	0.09	0.1

Table 2.1. Average aerosol optical thicknesses during the HCRF acquisitions

2.4.4.6 Analysis of snowpack

At each site snow pits were sampled at 5 cm depth intervals to obtain measurements of snow depth, temperature and grain size. The scale of the surface roughness at each site was estimated by measuring the height (the vertical distance between the trough and the peak) and the wavelength (the horizontal distance between two peaks) of the roughness elements. The

snowpack was heavily reworked and regular structures were difficult to identify, thus a range of heights and wavelengths were recorded. The ranges are presented in Table 2.2, and are typical over the sampling area and characteristic of the area surrounding the measurement. Grain size was recorded according to the international classification for seasonal snow on the ground (Fierz et al., 2009) using a hand lens and crystal card. Snowpack density was measured in the top 10 cm, other than at S3, where snow was sampled from the top 9 cm owing to thin snow cover. The snow samples were collected by pressing three 240 ml wide-mouth PTFE sample jars downwards into the top of the snow surface and measuring the mass of snow samples. A list of the HCRF acquisition sites and the snow pit data are presented in Table 2.2.

Site ID	Date of acquisition	Average solar zenith angle (°)	Grain size (mm)	Density (kg m-3)	Tempera-ture (°C)	Total snow depth (cm)	Roughness scale: height/ wavelength (cm)	Max concentration of black carbon (ng g-1)
S1	20/03/13	85	1	322 ± 13	-14.2	57	< 1 / < 1	299 ± 72
S2	21/03/13	84	0.5	308 ± 23	-4.9	26	1 to 2 / 5 to 20	130 ± 31
S3	24/03/13	80	1.5	316 ± 10	-4.6	9	1 to 6 / 5 to 30	102 ± 24
S4	20/03/13	81	1	324 ± 21	-11	41	< 1 / < 1	238 ± 57
S5	01/04/13	79	1.5	272 ± 46	-10.8	49	< 1 / < 1	92 ± 22
S6	25/03/13	81	1	303 ± 22	-4.2	14	< 1 / < 1	192 ± 46

Table 2.2. List of the HCRF acquisitions and snow pit data. Grain size and temperature has been averaged for the top 10 cm of the snowpack. The uncertainty in the density and maximum black carbon measurements is calculated as one standard deviation of the replicate measurements. Adapted from Ball et al. (2015)

Photographs of the snow surface at the time of the HCRF acquisition are given in Figure 2.11.

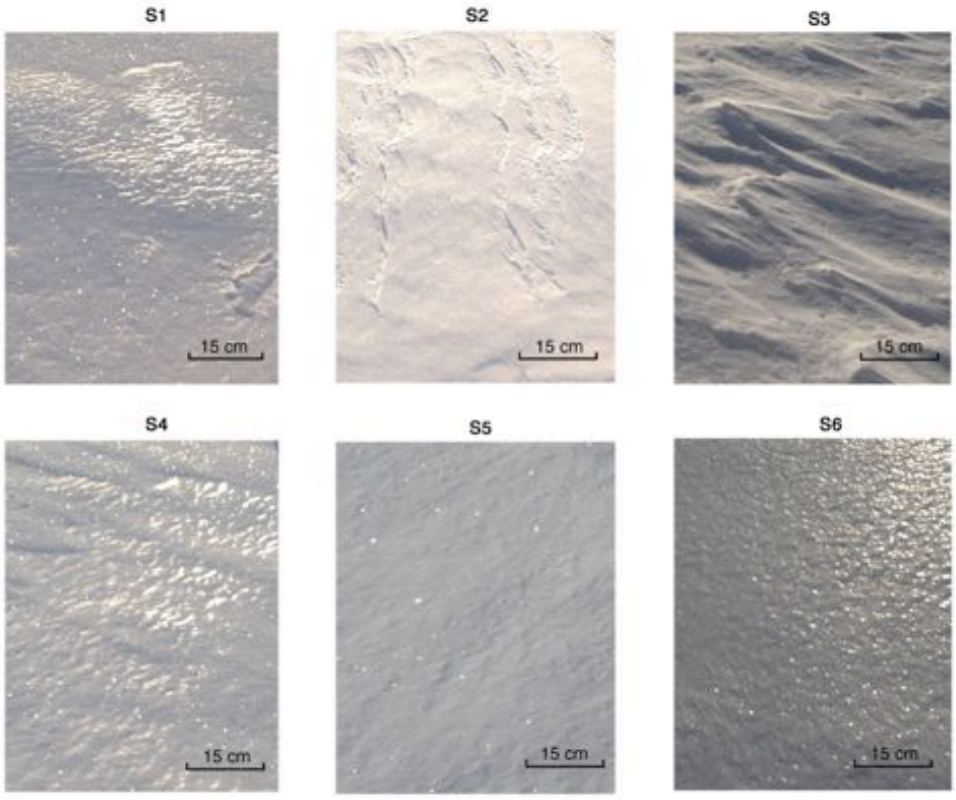

Figure 2.11. Photographs of the snow surface at each of the field sites

2.4.4.7 Light absorbing impurities

An upper limit on the mass ratio of black carbon in the top 10 cm of the snowpack was determined for each site by spectrophotometric analysis of filters following the methodology described in this section.

2.4.4.7.1 Collection of snow samples for filtration

Snow samples for measuring the maximum mass ratio of black carbon in snow were collected from each snow pit by pressing a 240 ml wide-mouth PTFE sample jar horizontally into the top 10 cm of the snowpack. The PTFE jars were filled and emptied 3 times before taking the sample that was used for filtration. The operator faced upwind while collecting samples and wore dust free disposable rubber over gloves.

2.4.4.7.2 Filtration

Snow samples were transported to the laboratory in Ny-Ålesund where 1500 ml of melted snow was filtered through a 0.4 μm Nucleopore membrane filter within a few hours of collecting each sample. Filtration of the meltwater was carried out according to the methodology described by Doherty et al. (2010). All apparatus was rinsed with distilled water prior to use and the filtration was performed inside an inflatable polyethylene glove bag to prevent contamination from airborne particles in the laboratory. The meltwater was passed through the filter using a hand-pump to create a partial vacuum and the filtered meltwater was discarded, the process of filtration typically took around 10 minutes for each 1500 ml sample of melted snow. The filter papers were sealed in airtight bags and wrapped in foil for transportation to the laboratory at RHUL where the spectrophotometric analysis was carried out. A photograph of the filtration apparatus and glove bag is given in Figure 2.12.

Figure 2.12. Photograph of filtration equipment in an inflatable polyethylene glove bag

2.4.4.7.3 Field reference filters

Prior to the field campaign in Svalbard a set of reference filters were loaded with different quantities of black carbon. A stock solution of 1600 ml of water and 400 ml of isopropanol was mixed with 1 g of commercially available Cabot (M120) black carbon, which was as close as possible match to the Monarch-71 soot used in the seminal study by Clarke and Noone (1985) (Reay, 2013). The stock solution was placed within an ultra-sonic bath for 1-hour to fully saturate the solution with black carbon particles. The stock solution was then filtered through 2 μm and a 0.8 μm Nucleopore membrane filters using the method outlined in Section 2.4.4.7.2. Filtering of the stock solution by the 2 μm and the 0.8 μm filters consecutively produced a particle size distribution that was representative of atmospheric black carbon (Clarke and Noone, 1985; Grenfell

et al., 2011). The concentration of black carbon in the filtered stock solution was obtained by evaporating 1500 ml of the filtered stock solution in three 500 ml beakers in an oven set at 80 °C over a period of several hours. The beakers were weighed before and after evaporation, ensuring that the beakers were at approximately the same temperature when weighed. The beakers were covered with and set on clean foil when not inside the oven to prevent contamination by airborne particles in the laboratory. The difference in the beaker weights after evaporation of 500 ml of stock solution was used to estimate the mass of black carbon in solution as follows:

$$S_{bc} = \frac{W_b - W_a}{V} \qquad \text{Eq. 2.5}$$

where S_{bc} is the concentration of black carbon in the filtered stock solution,

is the weight of the beaker prior to evaporation of the filtered stock solution,

is the weight of the beaker after evaporation of the filtered stock solution, and

is the volume of the filtered stock solution. The differences in the weights of the 3 beakers after evaporation of the filtered stock solution are given in Table 2.3.

Beaker ID	Wb - Wa (g)
A	0.014
B	0.010
C	0.006
Average	0.010
Standard deviation	0.004
Relative standard deviation	40%

Table 2.3. Differences in beakers weights after evaporating 500 ml of filtered stock solution

The average difference in weight was used from Table 2.3 and the concentration of black carbon in the filtered stock solution was calculated as $1.99 \pm 0.80 \times 10^{-5}$ g ml^{-1}. The filtered solution was progressively diluted with pure water to obtain a range of solutions with different mass ratios of black carbon. Each solution was filtered through a 0.4 μm Nucleopore membrane filter and the mass of black carbon retained on the filter was calculated as the product of the concentration of the filtered solution and the volume filtered. Visual inspection of the filtrate indicated that all black carbon was retained on the filter. The dilution factor for each solution of black carbon and the resulting mass of black carbon retained on the reference filter for each solution is given in Table 2.4.

Filter ID	Dilution factor	Concentration (g/ml)	Mass on filter (g)	Mass ratio (ng/g)	Uncertainty (± ng/g)
1_250/0	1	1.99×10^{-5}	2.48×10^{-3}	1656	662
2_125/2	2	9.93×10^{-6}	1.24×10^{-3}	828	331
3_125/3	3	6.62×10^{-6}	8.28×10^{-4}	552	221
4_125/4	4	4.97×10^{-6}	6.21×10^{-4}	414	166
5_125/6	6	3.31×10^{-6}	4.14×10^{-4}	276	110
6_125/8	8	2.48×10^{-6}	3.10×10^{-4}	207	83
7_125/12	12	1.66×10^{-6}	2.07×10^{-4}	138	55
8_125/16	16	1.24×10^{-6}	1.55×10^{-4}	103	41
9_125/24	24	8.28×10^{-7}	1.03×10^{-4}	69	28

Table 2.4. Field reference filters with black carbon loading after filtering 125 ml of black carbon solution. Mass ratios are calculated per 1500 g of snow. Uncertainties are calculated as one standard deviation of the averaged black carbon concentration of the filtered stock solution

The reference filters were used in the field to enable a visual estimate of maximum black carbon mass ratio in the snowpack. The filter paper was air-dried inside a petri dish in the laboratory upon filtering meltwater from the field sites. Once dry, the field filters were visually compared with the field reference filters to find the best match between the sets of filters, and an estimate for

maximum black carbon ratio for the snow at each site was made. The visual comparison was made with both sets of filters placed on a white diffusing background under ambient illumination conditions in the laboratory. Two different people made the visual comparison under the same lighting conditions. Photographs of the field reference filters are given in Figure 2.13, and the visual estimates of the black carbon mass ratios at each site are presented in Table 2.5.

Figure 2.13. Photograph of field reference filters used to estimate the maximum black carbon mass ratios in snow at the field sites

Site ID	Est. 1 (ng/g)	Est. 2 (ng/g)	Average (ng/g)
S1	200	100	150
S2	100	100	100
S3	100	100	100
S4	200	100	150
S5	200	400	300
S6	300	300	300

Table 2.5. Visual estimates of black carbon maximum mass ratios for field filters at sites S1 to S6. Visual estimates are rounded to the nearest 100 ng g^{-1}

The appearance of the filters can vary depending on the ambient lighting conditions, particularly under non-isotropic illumination (Grenfell et al., 2011) (see Figure 2.13). It was not possible to fully control lighting conditions in the field-based laboratory, and as a consequence visual estimates made relative to the set of field reference filters are uncertain. Additional uncertainties include personal biases and difficulties ignoring colour. The field filters were often a brownish colour owing to presence of dust or soil and the field reference filters were grey. Grenfell et al. (2011) estimated the uncertainty in the maximum black carbon mass ratio using the visual comparison technique as approximately a factor of 2.

2.4.4.7.4 Spectrophotometry

In order to obtain a quantitative estimate of the maximum black carbon mass ratios in the snowpack at the field sites an integrating sandwich spectrometer (ISSW) was used in the laboratory at Royal Holloway University of London, following the technique given by Grenfell *et al.* (2011). The technique was initially developed and tested by Clarke and Noone (1982), and involves the use of two highly scattering diffusers that surround the black carbon loaded filter producing an isotropic light field around the sample. Multiple scattering between the two diffusers results in attenuation of incident light that is primarily due to

absorption, with very little loss owing to scattering. The system consists of an intensity stabilized quartz-halogen lamp light source that transmits light into a Spectralon integrating sphere producing a diffuse radiation field at the output port of the sphere. At the exit port of the integrating sphere diffuse light is transmitted through the sample filter, which is sandwiched between two 20 mm sapphire windows. A highly reflective quartz fibre filter acts as a diffuser on the upper side of the sandwich. The radiation between the upper quartz fibre filter and the integrating sphere undergoes multiple reflections through the sample filter, enhancing the absorption signal (Grenfell et al., 2011). Radiation transmitted through the upper quartz diffuser is transmitted to an Ocean Optics USB 2000+ spectrometer and the spectrum is recorded on a Panasonic Toughbook laptop via a USB connection. The absorption by black carbon is calculated by comparing the attenuation of the black carbon loaded filters with that of a blank filter. A schematic of the ISSW is present in Figure 2.14.

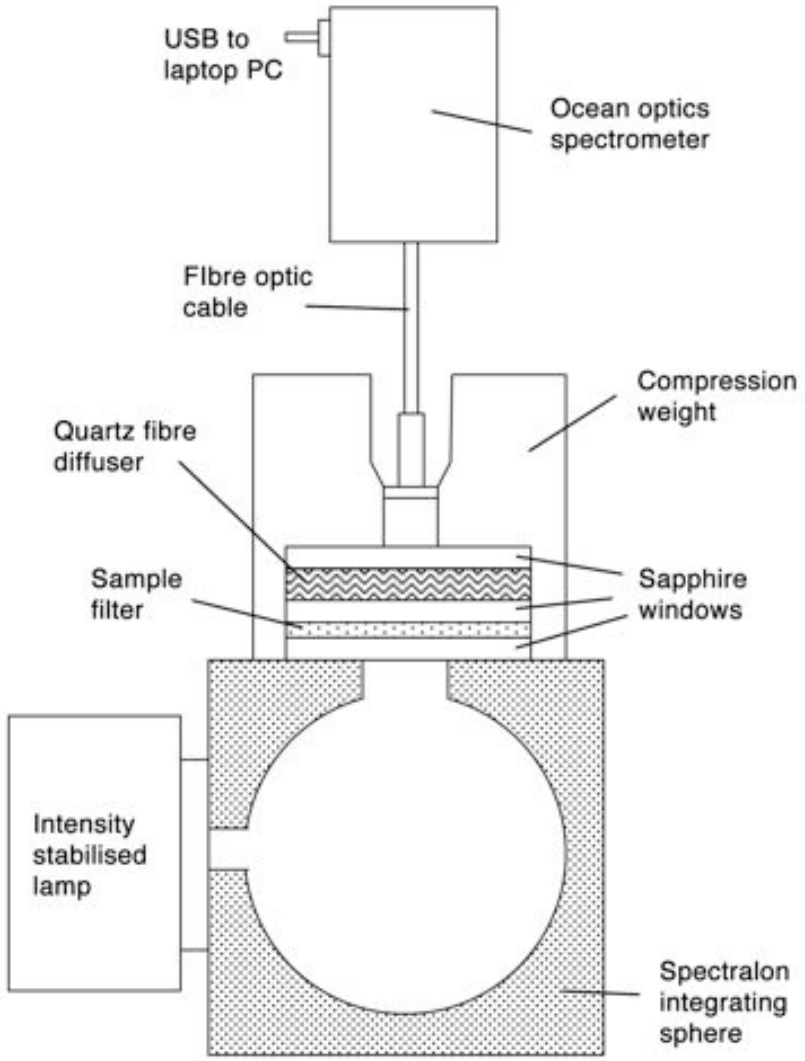

Figure 2.14. Schematic of the integrating sandwich spectrometer (ISSW) used to measure maximum mass ratios of black carbon in snow at the field sites

A photograph of the ISSW in the laboratory at Royal Holloway University of London is given in Figure 2.15.

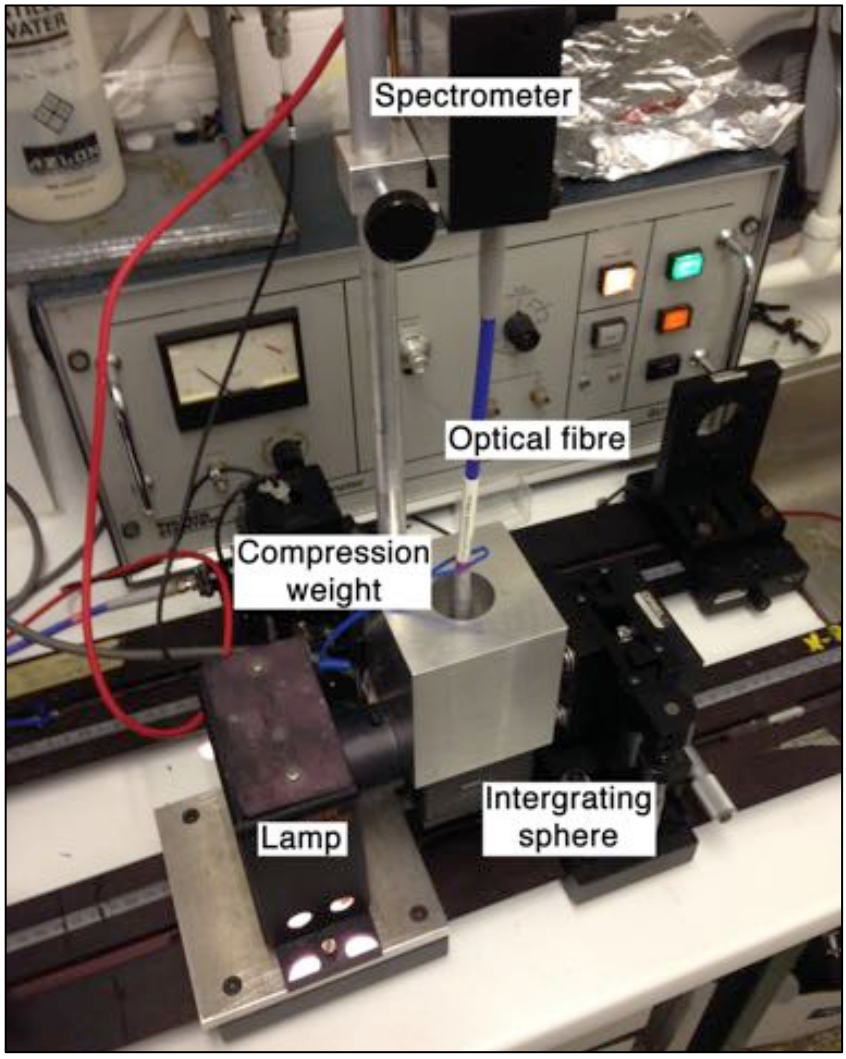

Figure 2.15. Photograph of the integrating sandwich spectrometer (ISSW) at Royal Holloway University of London

In order to derive the mass of black carbon from the attenuation of radiation by the filter a set of calibration filters were required (Grenfell et al., 2011). The calibration filters were loaded with known masses of black carbon following the technique described in Section 2.4.4.7.3 using commercially produced Cabot (M120) black carbon. The difference in the weights of the beakers after evaporation of the filtered stock solution for the calibration filters is given in Table 2.6. The mass ratio of black carbon in the filtered stock solution is the mass in solution divided by the volume evaporated (400 ml), and was 4.61 $x10^{-5}$

±1.12 x10^{-5} g ml^{-1} for the filtered stock solution for the black carbon calibration filters.

Beaker ID	Wb - Wa (g)
A	0.019
B	0.023
C	0.014
Average	0.018
Standard deviation	0.004
Relative standard deviation	24%

Table 2.6. Differences in beakers weights after evaporating 400 ml of filter stock solution

The stock solution was diluted by the dilution factors given in Table 2.7. The mass ratios were calculated for reference, on the basis that 1500 ml of meltwater had been filtered. The uncertainty in the mass ratio was calculated from one standard deviation of the mass of black carbon in the filtered stock solution.

Filter ID	Dilution factor	Concentration (g/ml)	Mass on filter (ng)	Filter loading ($\mu g/cm^2$)	Mass ratio (ng/g)	Uncertainty (± ng/g)
A_100/10	10	4.61 x10^{-6}	4.61 x10^{5}	36.7	307	74
B_100/20	20	2.30 x10^{-6}	2.30 x10^{5}	18.3	154	37
C_100/40	40	1.15 x10^{-6}	1.15 x10^{5}	9.2	77	18
D_100/80	80	5.76 x10^{-7}	5.76 x10^{4}	4.6	38	9
E_100/160	160	2.88 x10^{-7}	2.88 x10^{4}	2.3	19	5
F_100/320	320	1.44 x10^{-7}	1.44 x10^{4}	1.1	10	2
G_100/640	640	7.20 x10^{-8}	7.20 x10^{3}	0.6	5	1
H_100/1280	1280	3.60 x10-8	3.60 x10^{3}	0.3	2	1

Table 2.7. Calibration filters with black carbon loading after filtering 100 ml of black carbon solution. Mass ratios are calculated per 1500 g of snow. Uncertainties are calculated as one standard deviation of the averaged black carbon concentration of the filtered stock solution

Spectra were recorded for light transmitted by the ISSW for each calibration filter $I(\lambda)$ and for a blank filter $I_0(\lambda)$. The average of 3 spectra was taken, each with an integration time of 0.6 seconds. The filter paper was rotated by approximately 90° between each measurement and the sapphire windows were cleaned with methanol prior to placing the filter onto the sapphire window. The order of transmittance measurements for each calibration filter was semi-random. Dark measurements were taken by inserting a black screen between the lamp and the integrating sphere, and where subtracted from the measured spectrum during post processing. The light transmitted by the black carbon loaded filter was compared to the light transmitted by a blank filter, and the relative attenuation χ_λ is expressed as:

$$\chi_\lambda \equiv -ln\left(\frac{I(\lambda)}{I_0(\lambda)}\right) \qquad \text{Eq. 2.6}$$

where $I(\lambda)$ is the intensity measured by the spectrometer for the calibration filter and $I_0(\lambda)$ is the intensity measured by the spectrometer for the blank filter.

The measurement system required calibration filters with different black carbon loadings because the attenuation as a function of black carbon loading is not exponential (i.e. attenuation does not follow the Beer Lambert Law) (Grenfell et al., 2011). The calibration curve presented in Figure 2.17 and gives the relative attenuation as a function of black carbon loading on the filter papers at 675 nm, and is the average of two sets of measurements. The black carbon loading was calculated per unit of filtered area on the filters, which was approximately 13 cm^2. A third-order polynomial was fitted to the calibration curve in order to convert the relative attenuation to the maximum black carbon loading for the

field filters. The maximum black carbon loading was converted to the maximum mass ratio of black carbon in snow by applying the following relationship:

$$C_{max} = \frac{L\,A}{M} \qquad \text{Eq. 2.7}$$

where C_{max} is the maximum mass ratio of black carbon, L is the black carbon loading on the filter, A is the area on the filter and M is the mass of snow or meltwater filtered.

The relative attenuation as the function of wavelength for the 7 calibration filters is given in Figure 2.16.

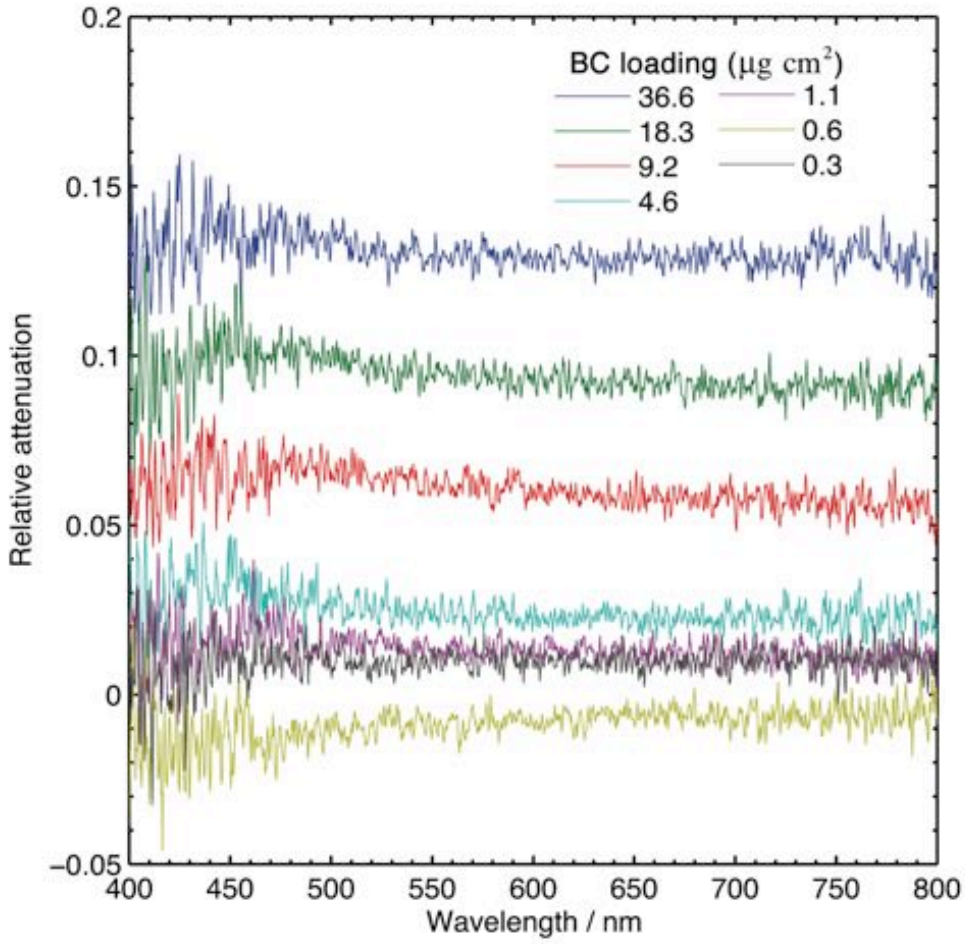

Figure 2.16. Relative attenuation as a function of wavelength for the 7 calibration filters with different loadings of black carbon. The black carbon loading on the filters is given in units of μg cm^{-2}

Given that black carbon absorbs light strongly across visible wavelengths there is effectively no wavelength dependence to the relative attenuation. The calibration curve for the integrating sandwich spectrometer is given in Figure 2.17.

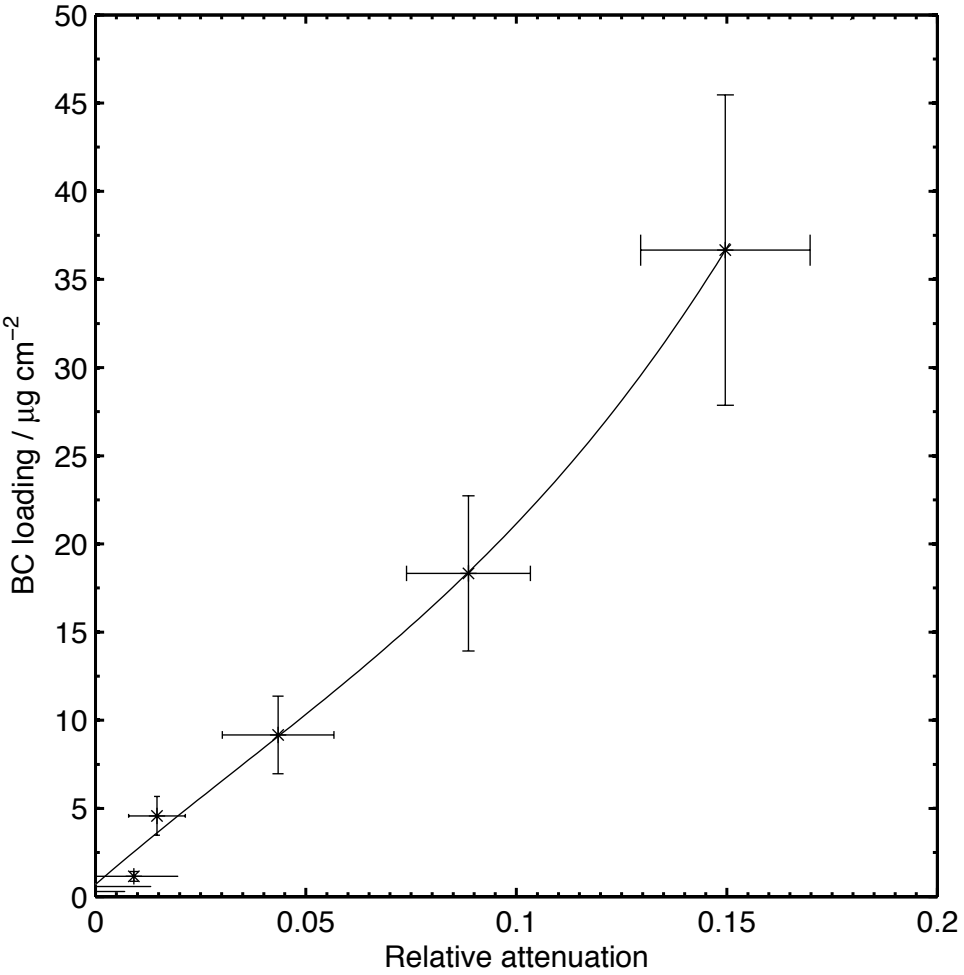

Figure 2.17. Calibration curve for the integrating sandwich spectrometer at a wavelength of 675 nm. The uncertainty bars are two standard deviations of the replicate measurements

Relative attenuation as a function of wavelength is presented for each site in Figure 2.18 to Figure 2.23. The black carbon loading on each field filter was calculated using the calibration curve given in Figure 2.17 and the relative attenuation averaged for the band 665 nm to 685 nm for each site. Uncertainty in the black carbon loadings was calculated as one standard deviation of the

replicate measurements of the black carbon concentration in the filtered stock solution.

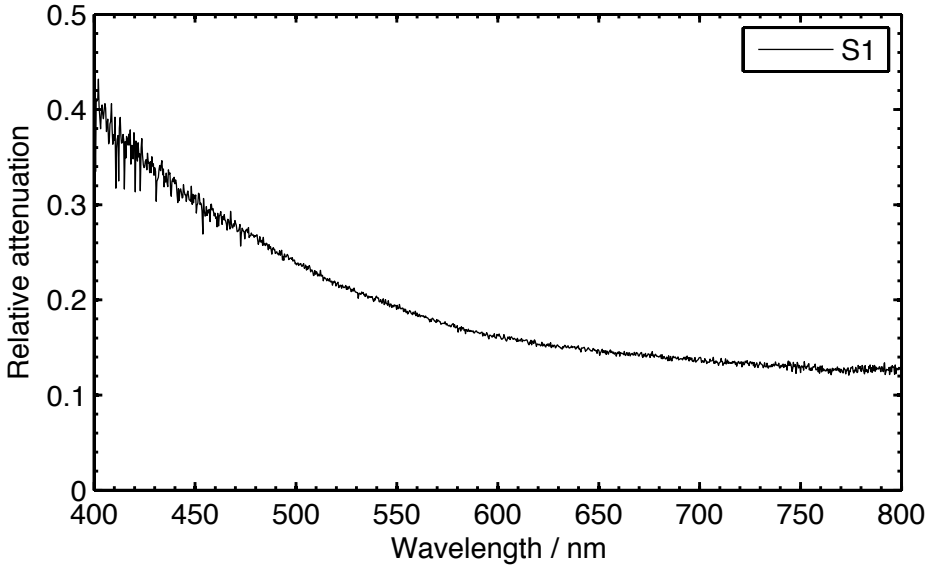

Figure 2.18. Relative attenuation with wavelength for the field filter at site S1

The maximum mass ratio of black carbon for S1 was 299 ± 72 ng g^{-1}, giving S1 the greatest maximum mass ratio of black carbon of the 6 sites studied. S1 is the closest site to the Ny-Alesund research base (approximately 127 m) and the level is much greater than typical black carbon mass ratios for Svalbard, which are in the range 11 ng g^{-1} to 22 ng g^{-1} (Forsström et al., 2013; Clarke and Noone, 1985; Doherty et al., 2010). There is a strong wavelength dependence to the attenuation of light for the S1 filter, with a greater than a factor of 2 decrease between 400 nm and 650 nm, which is the result of absorption by impurities other than black carbon. These impurities are likely to be a combination of soil, dust or HULIS (humic like substances). France et al. (2012) and Reay (2013) carried out measurements on Arctic snow and detected a similar spectral shape for absorption. France et al. (2012) found that the absorption cross section was explained by the presence of HULIS in the snow pack, which absorbs light more strongly at shorter wavelengths. In addition, Doherty et al. (2010) calculated that 20 % to 50 % of the light absorbing

impurities in Arctic snow was by non-black carbon constituents. As such, the measurements of maximum black carbon were made for the wavelength band centered at 675 nm, where absorption by HULIS is weaker. However, it should be noted that the measurements provide only the maximum mass ratio of black carbon in the snow pack, with unknown concentrations of other absorbers possibly contributing towards the measured attenuation.

The maximum mass ratio of black carbon for S2 was 130 ± 31 ng g^{-1}. The relative attenuation as a function of wavelength for the filter at S2 is given in Figure 2.19 and had wavelength dependence with a fractional decrease in relative attenuation of 65 % between 400 and 675 nm. S2 was approximately 161 m from the Ny-Ålesund research base.

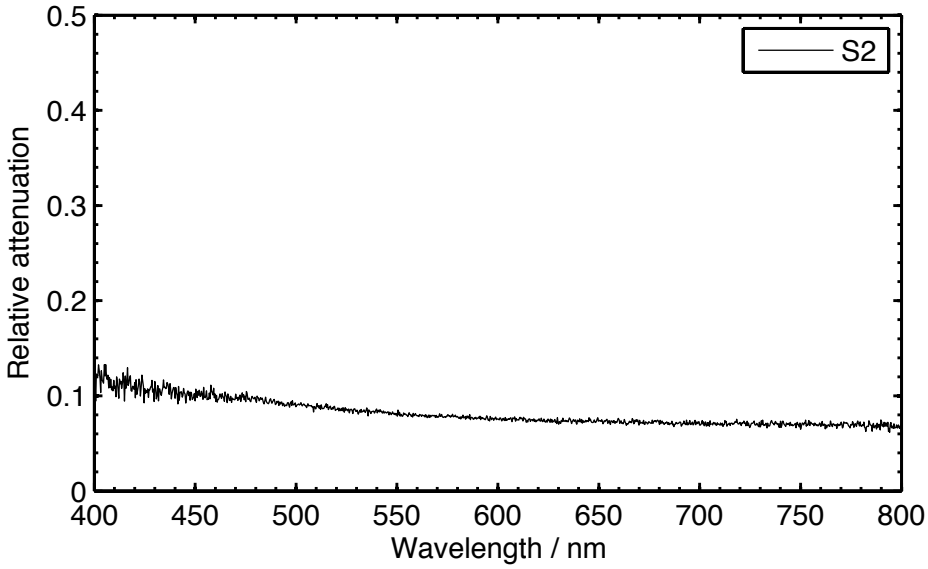

Figure 2.19. Relative attenuation with wavelength for the field filter at site S2

The maximum mass ratio of black carbon for S3 was 102 ± 24 ng g^{-1}. The relative attenuation as a function of wavelength for the filter at S3 is given in Figure 2.20 and had wavelength dependence with a fractional decrease in relative attenuation of 45 % between 400 nm and 675 nm. S3 was approximately 184 m from the Ny-Ålesund research base.

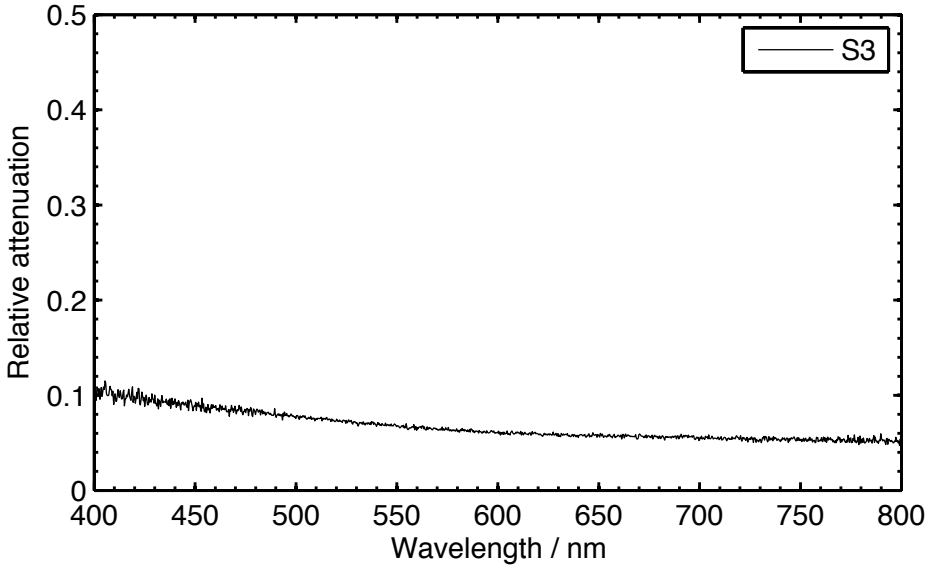

Figure 2.20. Relative attenuation with wavelength for the field filter at site S3

The maximum mass ratio of black carbon for S4 was 238 ± 57 ng g^{-1}. The relative attenuation as a function of wavelength for the filter at S4 is given in Figure 2.21 and had wavelength dependence with a fractional decrease in relative attenuation of 41 % between 400 nm and 675 nm. S4 was the second nearest field site to the Ny-Ålesund research base (approximately 138 m) and had the second greatest maximum mass ratio of black carbon.

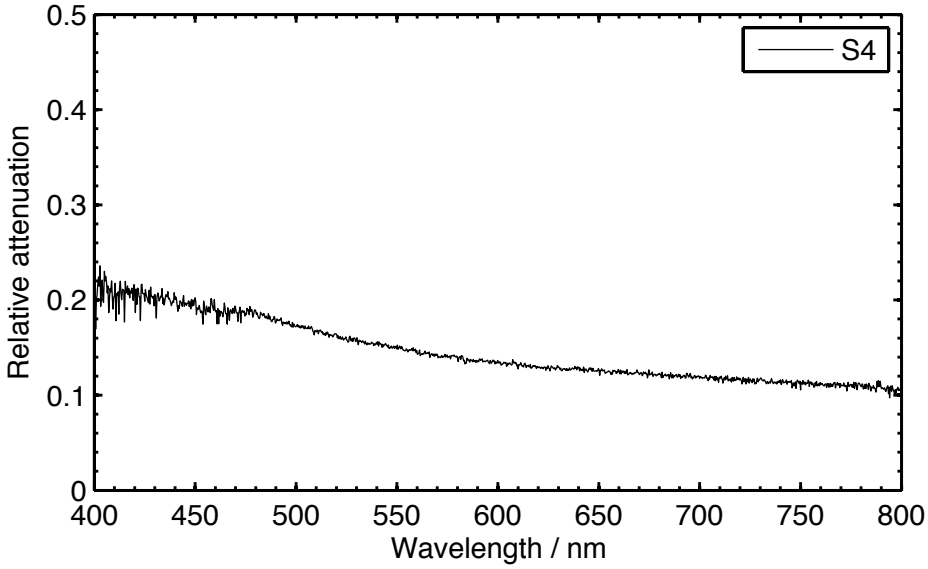

Figure 2.21. Relative attenuation with wavelength for the field filter at site S4

The maximum mass ratio of black carbon was lowest for S5, which had a maximum mass ratio of 92 ± 22 ng g^{-1}. The relative attenuation as a function of wavelength for the filter at S5 is given in Figure 2.22 and had wavelength dependence with a fractional decrease in relative attenuation of 37 % between 400 nm and 675 nm. S5 was approximately 3115 m from the Ny-Ålesund research base, and was the only field site from the second transect located to the northwest of the Ny-Ålesund.

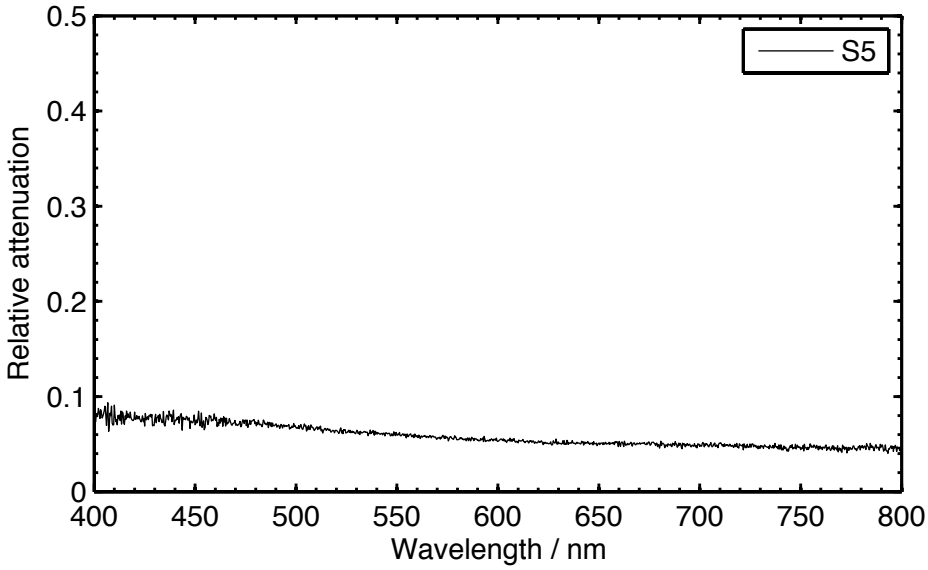

Figure 2.22. Relative attenuation with wavelength for the field filter at site S5

The maximum mass ratio of black carbon for S6 was 192 ± 46 ng g^{-1}. The relative attenuation as a function of wavelength for the filter at S6 is given in Figure 2.23 and had wavelength dependence with a fractional decrease in relative attenuation of 48 % between 400 nm and 675 nm. S6 was approximately 193 m from the Ny-Ålesund research base.

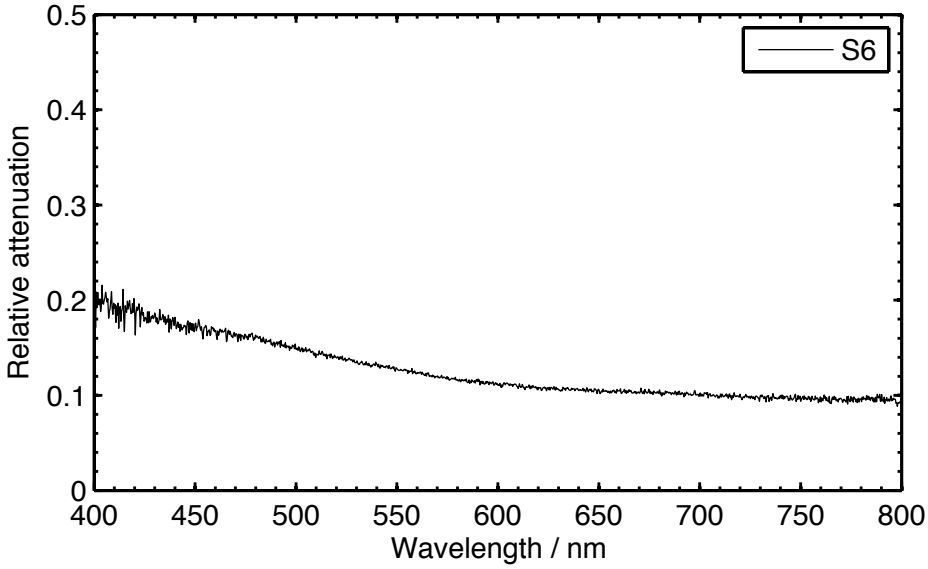

Figure 2.23. Relative attenuation with wavelength for the field filter at site S6

The upper limit on the concentration of black carbon in the snowpack at each site was found to be large when compared with typical values in Svalbard (Doherty et al., 2010; Forsström et al., 2013; Clarke and Noone, 1985), which is caused by the proximity of the field sites to the Ny-Ålesund research station and the use of diesel generators for power and snow machines. There was wavelength dependence to absorption by the snow at all sites, with fractional decreases in attenuation of typically 40 % between 400 nm and 675 nm, which was related to absorption by non-black carbon impurities. Generally, the measured maximum black carbon ratios decreased with distance from the Ny-Ålesund research base, having a weak negative correlation coefficient of -0.51 $(p = 0.3)$ for the 6 sites measured. S1, which was nearest to the research base, had a maximum mass ratio of 299 ± 72 ng g^{-1}, compared to a maximum mass ratio of 92 ± 22 ng g^{-1} at S5, which was the furthest site from the research station.

The estimates of maximum black carbon concentration in the snowpack made using the visual comparison method (described in Section 2.4.4.7.3) agreed to within a factor of 3 with the measurements made using the ISSW. Differences between the maximum black carbon concentration in the snowpack derived using each method was greatest for site S5, which was located furthest from the Ny-Ålesund research base. The differences were within a factor of 2 for S1, S2, S3, S4 and S6, which is inline with the uncertainty in the visual comparison technique estimated by Grenfell et al. (2011). The field filters had a brownish appearance owing to presence of dust or soil in the snowpack, which increased the uncertainty in our visual comparison estimates owing to difficulties ignoring colour when conducting the visual comparison of the field filters with the reference filters.

2.4.5 Data processing and reduction procedures

In total, 11 HCRF acquisitions were performed at 11 sites, but only 6 were retained for analysis. The data processing and reduction procedures are described in this section.

2.4.5.1 Diffuse and direct sky irradiance

Even under clear sky conditions the HCRF does not equal the BRDF of the surface due to the presence of diffuse irradiance (Lyapustin and Privette, 1999; Grenfell et al., 1994). The long atmospheric path length of light for large solar zenith angles results in increased scattering, especially in the Rayleigh scattering dominated wavelength region (400 nm to 800 nm), making it impossible to measure the HCRF at these angles without a high proportion of diffuse irradiance being present. In order to maximize the portion of direct irradiance a number of the acquisitions were omitted on inspection of the

downwelling direct irradiance, which was recorded simultaneously at the AWIPEV research station in Ny-Ålesund. In total, 11 HCRF acquisitions were obtained at sites along both transects, the downwelling broadband direct irradiance over the wavelength range 200 nm to 4000 nm recorded by the AWIPEV pyranometer during each acquisition is presented in Figure 2.24 to Figure 2.31.

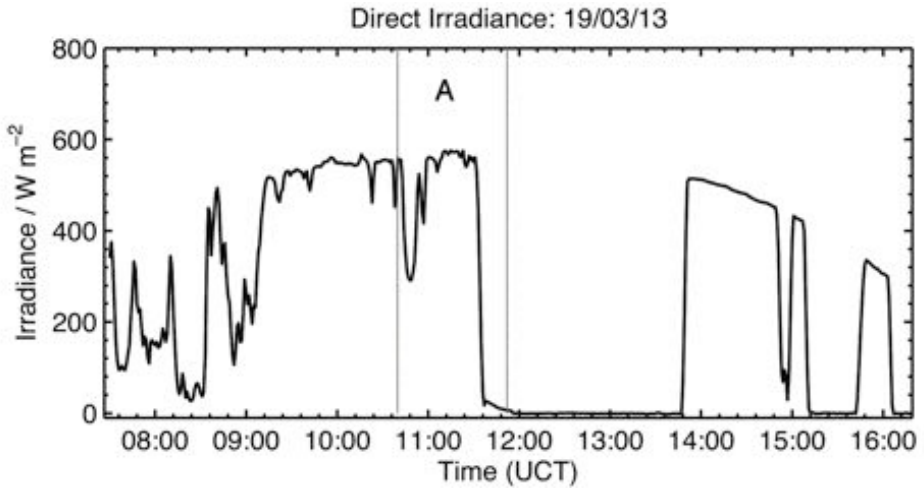

Figure 2.24. Downwelling direct irradiance recorded by the AWIPEV pyranometer on the 19th of March 2013. The vertical lines correspond with the HCRF acquisition start and end times for acquisition A

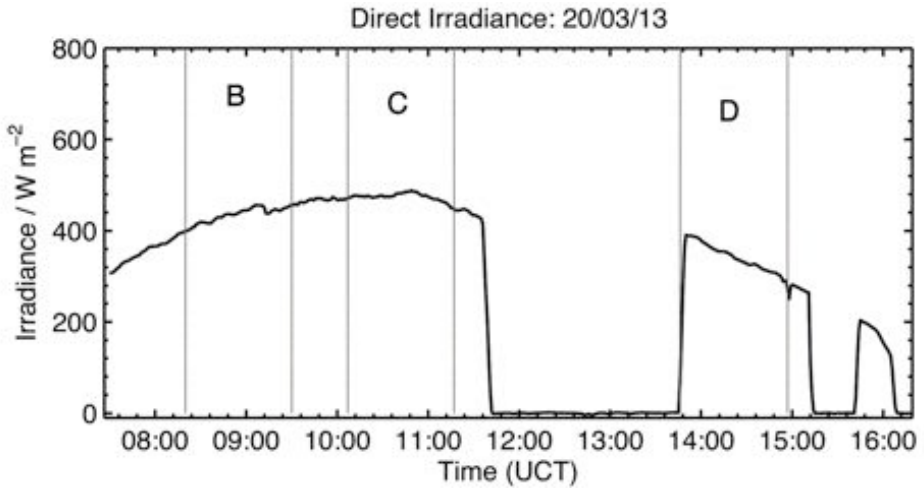

Figure 2.25. Downwelling direct irradiance recorded by the AWIPEV pyranometer on the 20th of March 2013. The vertical lines correspond with the HCRF acquisition start and end times for acquisitions B, C and D

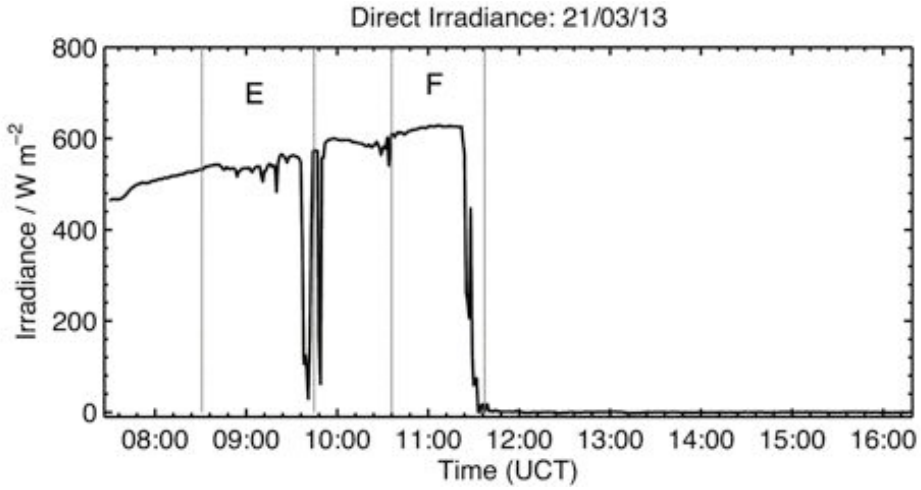

Figure 2.26. Downwelling direct irradiance recorded by the AWIPEV pyranometer on the 21th of March 2013. The vertical lines correspond with the HCRF acquisition start and end times for acquisitions E and F

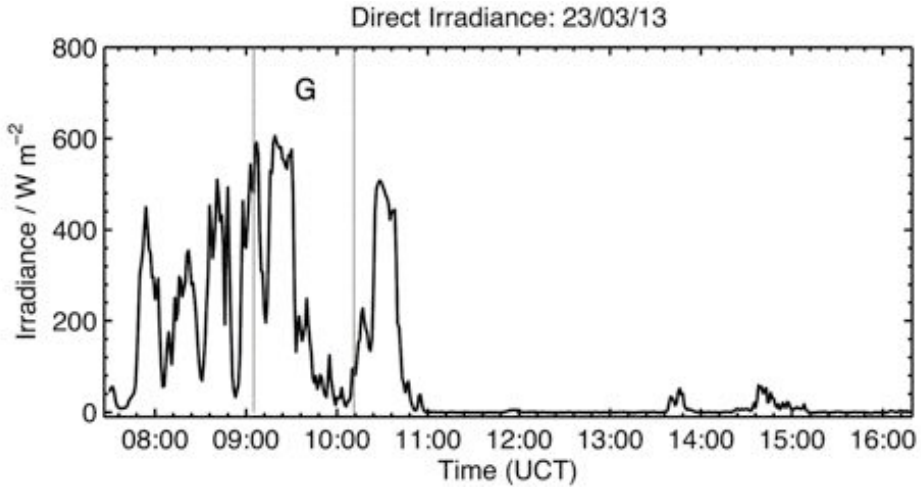

Figure 2.27. Downwelling direct irradiance recorded by the AWIPEV pyranometer on the 23rd of March 2013. The vertical lines correspond with the HCRF acquisition start and end times for acquisition G

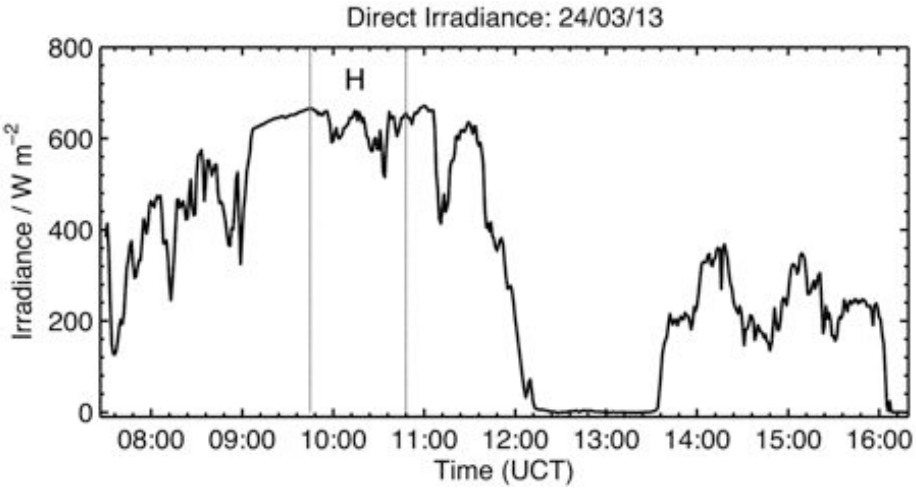

Figure 2.28. Downwelling direct irradiance recorded by the AWIPEV pyranometer on the 24th of March 2013. The vertical lines correspond with the HCRF acquisition start and end times for acquisition H

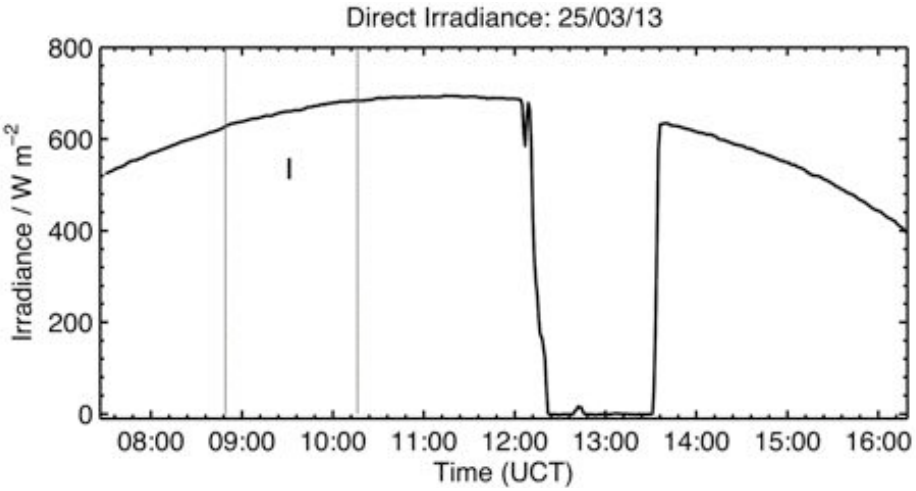

Figure 2.29. Downwelling direct irradiance recorded by the AWIPEV pyranometer on the 25th of March 2013. The vertical lines correspond with the HCRF acquisition start and end times for acquisition I

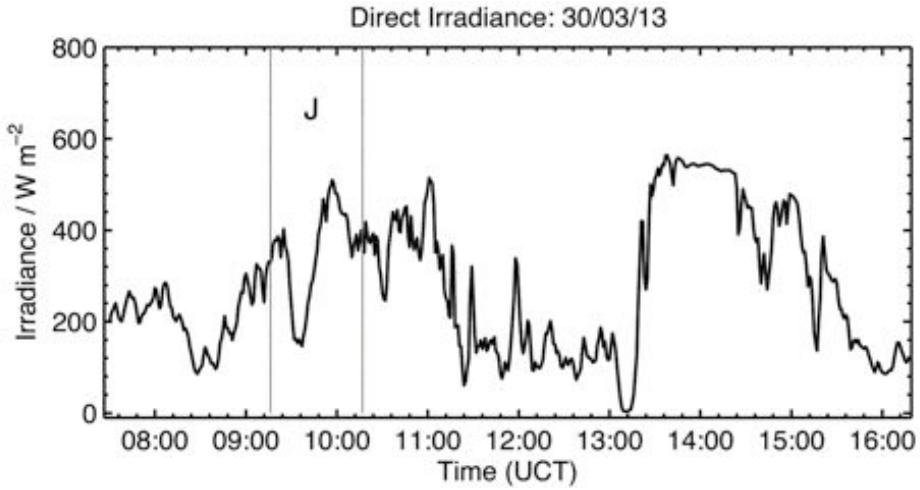

Figure 2.30. Downwelling direct irradiance recorded by the AWIPEV pyranometer on the 30th of March 2013. The vertical lines correspond with the HCRF acquisition start and end times for acquisition J

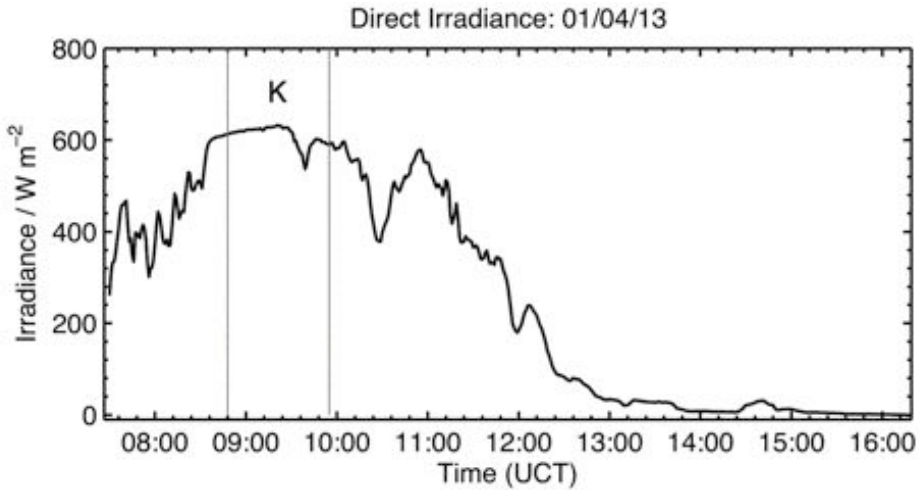

Figure 2.31. Downwelling direct irradiance recorded by the AWIPEV pyranometer on the 1st of March 2013. The vertical lines correspond with the HCRF acquisition start and end times for acquisition K

The HCRF acquisitions are labeled A to K in Figure 2.24 to Figure 2.31, the vertical bars in each figure give the start and end times for each acquisition. Acquisition A, D, F, G and J were omitted based on visual inspection owing to instability in the direct portion of irradiance. Acquisitions B, C, E, H, I and K were retained for analysis and are presented in this chapter. Sites S1, S2, S3, S4, S5 and S6 in Table 2.2 correspond with acquisitions B, E, H, C, K and I respectively. Sky conditions during each acquisition were also recorded using

Nikon Coolpix E4500 digital camera and fish-eye lens. On visual inspection of the imagery, only sites that showed clear sky conditions with no cumulus cloud and minimal visible cirrus cloud cover during the HCRF acquisition were retained for analysis. The ratio of broadband diffuse irradiance to global irradiance (200 nm to 3600 nm) was recorded by a Kipp & Zonen CMP22 pyranometer at AWIPEV research station and was on average less than 0.5 for the remaining sites (S1 to S6) during each the HCRF acquisition.

2.4.5.2 Spatial resolution and surface roughness

Surface roughness of the target surface is an important parameter in the measurement of HCRF (Warren et al., 1998; Leroux and Fily, 1998), to take a representative measurement typical surface roughness elements, such as sastrugi and ripples, needed to be sampled. To test whether the footprint size and the goniometer's pointing accuracy were sufficient to sample a representative number of roughness elements, the ratio of shaded to sunlit areas within a circular footprint of 0.28 m diameter (the size of the footprint used in the field measurements) was compared to the ratio of shaded to sunlit areas for a footprint with a 1 m diameter. The size and shape of the shadows were computed for a 1.5 m^2 grid according to the solar geometry and the height (sas_h) and wavelength (sas_λ) of the roughness elements observed at the sites S2 and S3, by taking the middle value for each range (for site S2 $sas_h = 1.5$ and $sas_\lambda = 12.5$, for site S3 $sas_h = 3.5$ $sas_\lambda = 17.5$). For simplicity, the roughness elements were assumed to be regularly spaced linear ridges with vertical walls, as in Leroux and Fily (1998). The ratio of shaded to sunlit areas for each footprint size was calculated and averaged for 100 different positions around the centre of the grid by varying the x and y coordinates of the footprint centre point

by up to ± 20 cm using a random number generator, in order to resemble the pointing accuracy of the goniometer. The distribution of shadows on the grid and position of the sensors footprint for 9 of the 100 simulations is given for the roughness element at S3 in Figure 2.32.

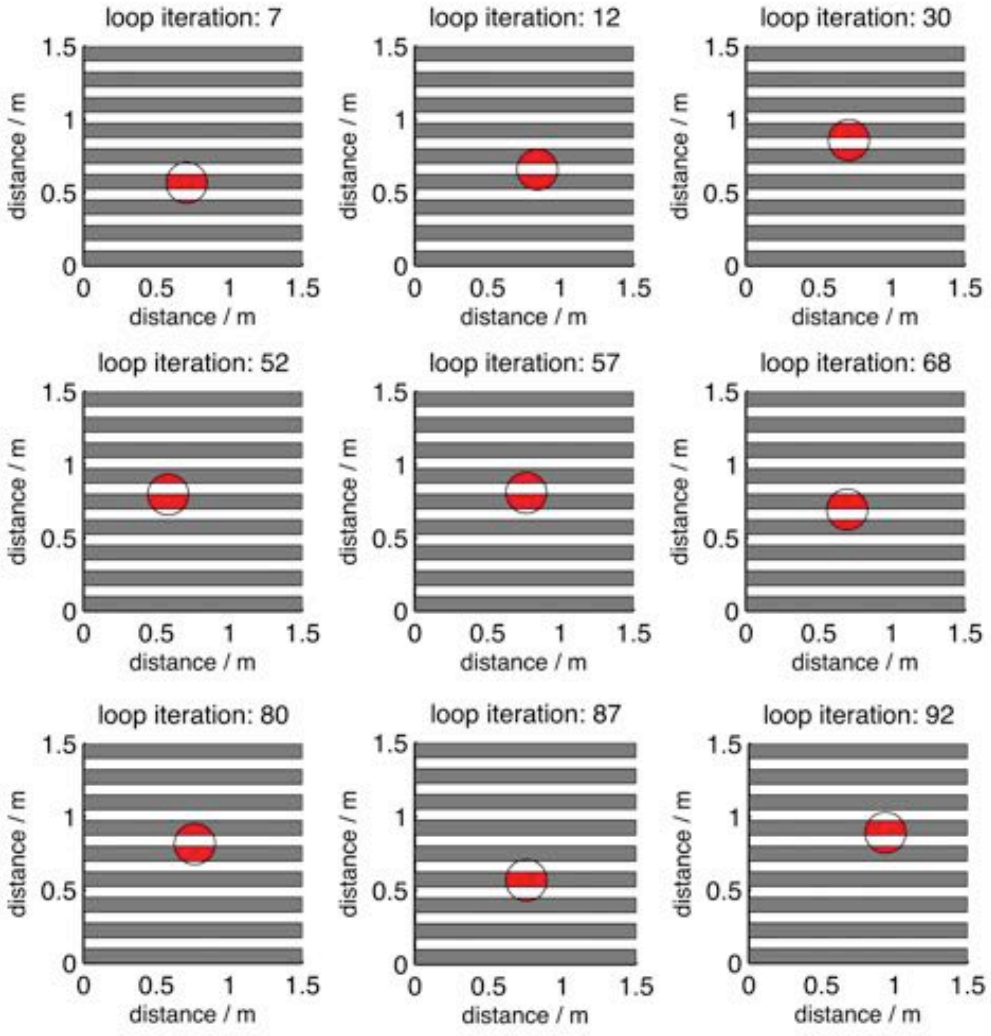

Figure 2.32. Simulated shadowed to sunlit areas at S3 for 9 of the 100 different foreoptic footprint positions with a footprint radius of 0.14 m

The relative difference between the averaged ratio of shaded to sunlit areas with a footprint diameter of 0.28 m, and a footprint diameter of 1 m was 18.5 % for S3. The relative standard deviation of the averaged ratio with a 0.28 m diameter footprint was 24.5 % for S3; indicating that a footprint size of 0.28 m in diameter was probably sufficient to obtain a representative sample of shaded to sunlit

area at S3, although errors in excess of 49 % (2 standard deviations from the mean) owing to positioning of the sensor footprint could not be eliminated. The ratio of shaded to sunlit areas for all 100 simulations are presented as a function of sensor footprint radius in Figure 2.33.

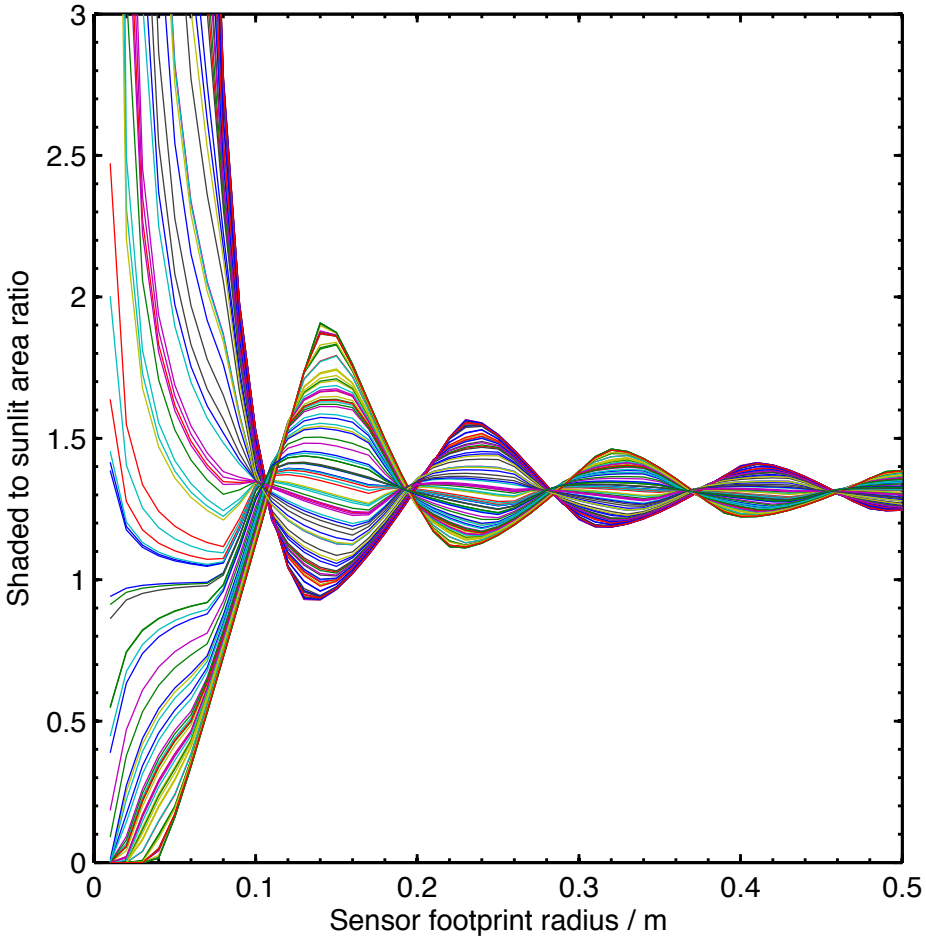

Figure 2.33. Ratio of shaded to sunlit areas within the sensor footprint as a function of sensor footprint radius for 100 different sensor positions at S3

Variance in the ratio of shaded to sunlit areas in Figure 2.33 generally decreases with the radius of the sensors footprint, but owing to the simplified geometry used in the model there a number of footprint radii which produce a smaller variance despite a smaller footprint radius. For example, for a footprint radii of 0.11 m, 0.2 m, 0.28 m, 0.37 m and 0.46 m, the shaded to sunlit area ratio is consistently around 1.3 for all simulations despite different footprint

locations. These footprint radii happen to be large enough to span across an equal integer number of shaded and sunlit strips, hence the ratio within the circular footprint becomes independent of position. The simulated distribution of shaded to sunlit areas for the S2 roughness elements are given in Figure 2.34.

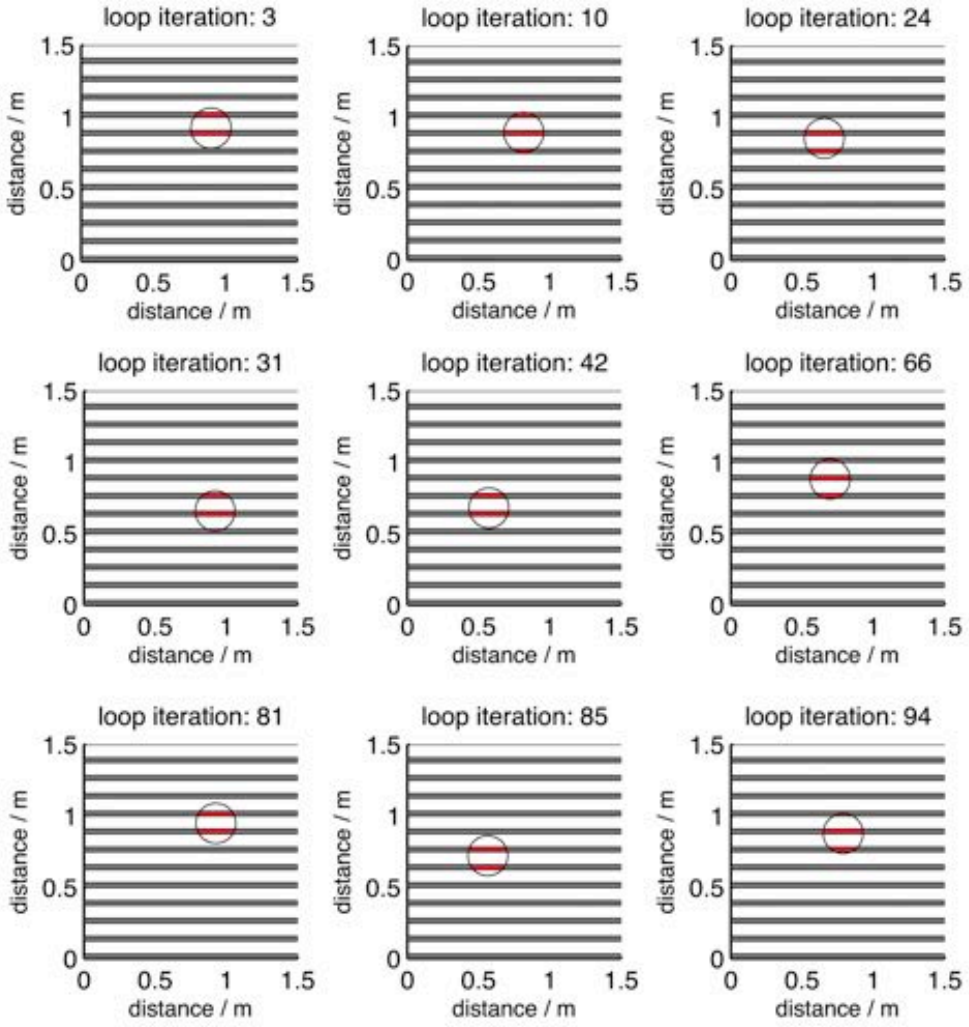

Figure 2.34. Simulated shadowed to sunlit areas at S2 for 9 of the 100 different foreoptic footprint positions with a footprint radius of 0.14 m

The relative difference between the averaged ratio of shaded to sunlit areas with a footprint diameter of 0.28 m, and a footprint diameter of 1 m was 2.3 % for S3. The relative standard deviation of the averaged ratio with a 0.28 m diameter footprint was 2.6 % for S3; indicating that a footprint size of 0.28 m in diameter was sufficient to obtain a representative sample of shaded to sunlit areas at S2.

The ratio of shaded to sunlit areas for all 100 simulations for the S2 roughness elements are presented as a function of sensor footprint radius in Figure 2.35.

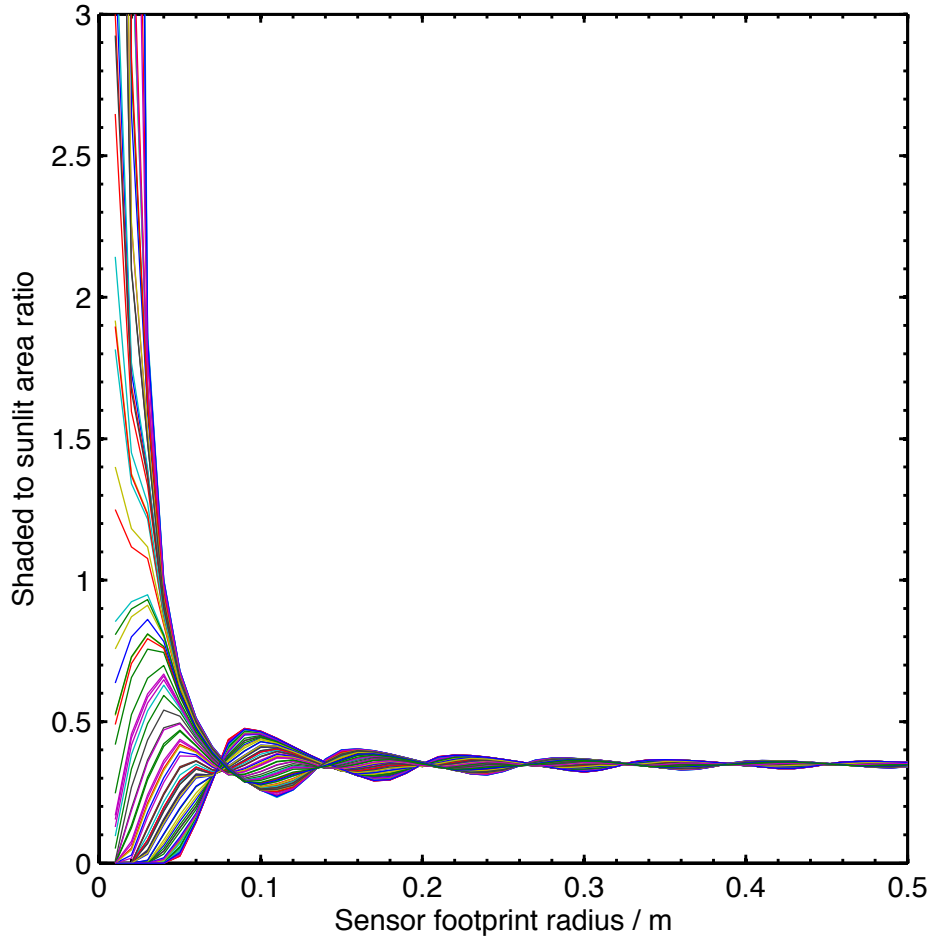

Figure 2.35. Ratio of shaded to sunlit areas within the sensor footprint as a function of sensor footprint radius for 100 different sensor positions at S2

The model grossly oversimplifies the geometry of the roughness elements and was intended to provide an approximation of the scale of the error introduced as a result of the footprint size relative to the size of the roughness elements. Given the irregular distribution and size of the roughness elements at S2 and S3 the possibility of any foreoptic capturing an unrepresentative sample that causes errors in excess of what is estimated above could not be eliminated without an improved characterization of the roughness elements geometry, and thus the sites were omitted from the final analysis, but are retained in the discussion section. The MATLAB code used to model the roughness elements and

generate Figure 2.32, Figure 2.33, Figure 2.34, and Figure 2.35 is given in Appendix 2.

2.4.5.3 Change in solar zenith and azimuth angles

The measurement time for a single HCRF acquisition was typically 60-minutes, which for the measurement location and time of year corresponds to a change of approximately 3° in solar zenith and approximately 16° in solar azimuth angle. To avoid geometric perturbations in the HCRF distribution due to changes in solar azimuth angle the actual solar azimuth angle was determined for each radiance measurement during the HCRF acquisition. The solar azimuthal offset since the start of the measurement sequence for each radiance measurement was calculated and a correction was then applied to the distribution in post processing. The correction is not valid for heterogeneous sites with roughness elements, as such, no correction for changes in solar azimuth were applied for S2 and S3. To account for the change in global irradiance during a measurement owing to the change in the solar zenith angle, a correction determined from the quotient of the radiance recorded by each foreoptic and the global irradiance recorded near-simultaneously (less than 2 seconds) by an integrating cosine irradiance collector positioned on top of the GRASS frame was applied.

2.5 Experiment results

The HCRF was acquired using GRASS at 11 sites during the field campaign. Five of the 11 sites were omitted due to the presence of cumulus or cirrus cloud, which was detected by instability in the ratio of direct to diffuse irradiance recorded at the AWIPEV research station during the acquisitions. Bivariate and contoured polar plots of the HCRF over the upward facing hemisphere for the

remaining sites, S1 to S6, are presented in the following sections. The polar plots are the HCRF projected onto a 2-D surface and linearly interpolated using a Delaunay triangle based method (de Berg et al., 2008); the distance from the center of the plots correspond with the viewing zenith angle, and rotation about the center of the plots corresponds to azimuth angle; the contour intervals are set to 0.1 and the color scale is consistent for all plots. The anisotropy in the HCRF for each site is quantified by the anisotropy index (ANIX), which was defined as the ratio of the maximum to the minimum HCRF values over the hemisphere. Data was omitted in the wavelength band 920 nm to 970 nm and beyond 1350 nm owing to poor signal to noise.

2.5.1 Site 1 (S1)

Polar plots of the HCRF are presented for S1 for the wavelengths 500 nm, 900 nm and 1300 nm in Figure 2.36 to Figure 2.38. The HCRF as a function of viewing angle in the solar principal plane is given in Figure 2.39, and the anisotropy index (ANIX) is given as a function of wavelength in Figure 2.40.

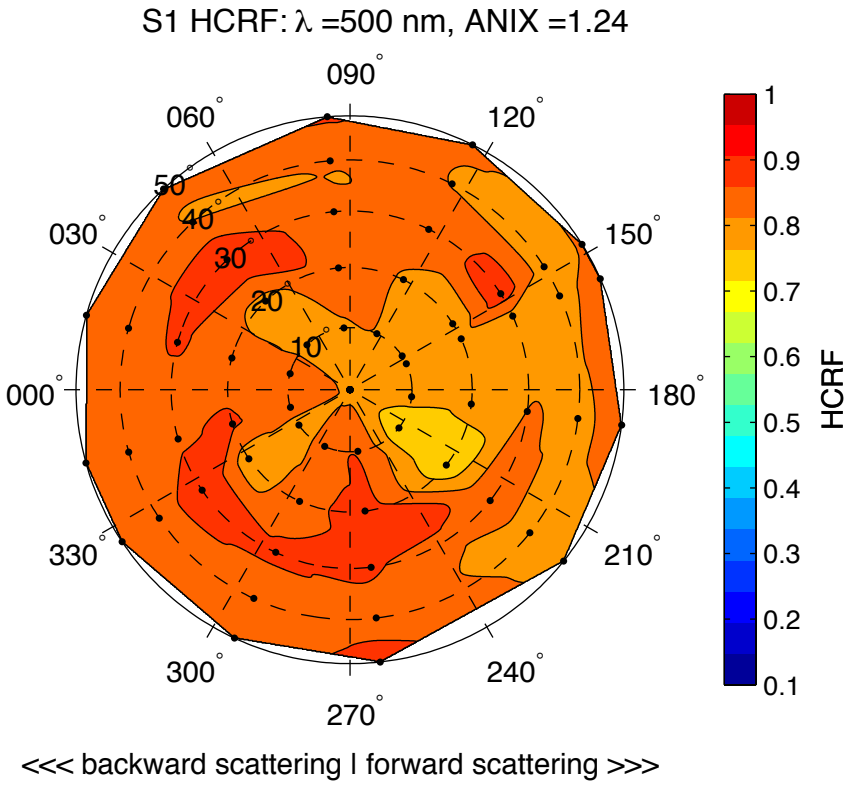

Figure 2.36. HCRF of snow at S1 for a wavelength of 500 nm

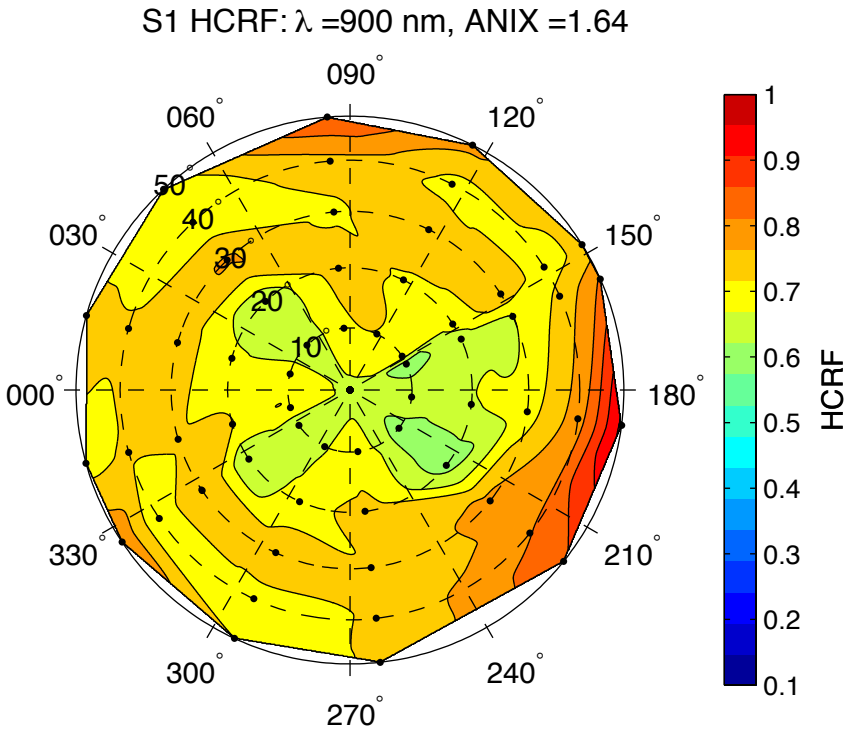

Figure 2.37. HCRF of snow at S1 for a wavelength of 900 nm

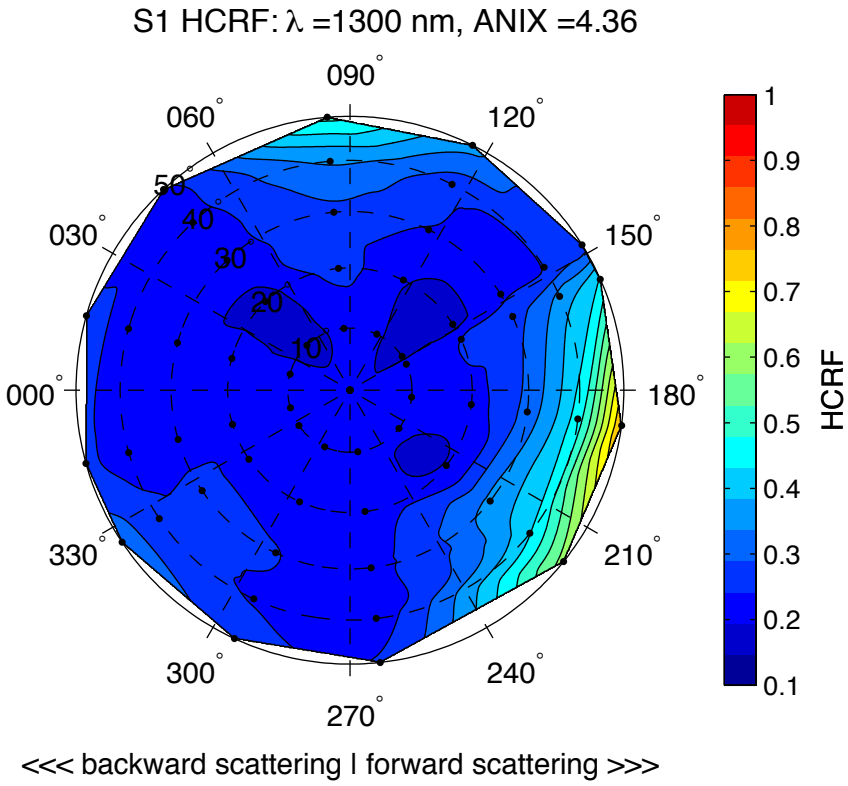

Figure 2.38. HCRF of snow at S1 for a wavelength of 1300 nm

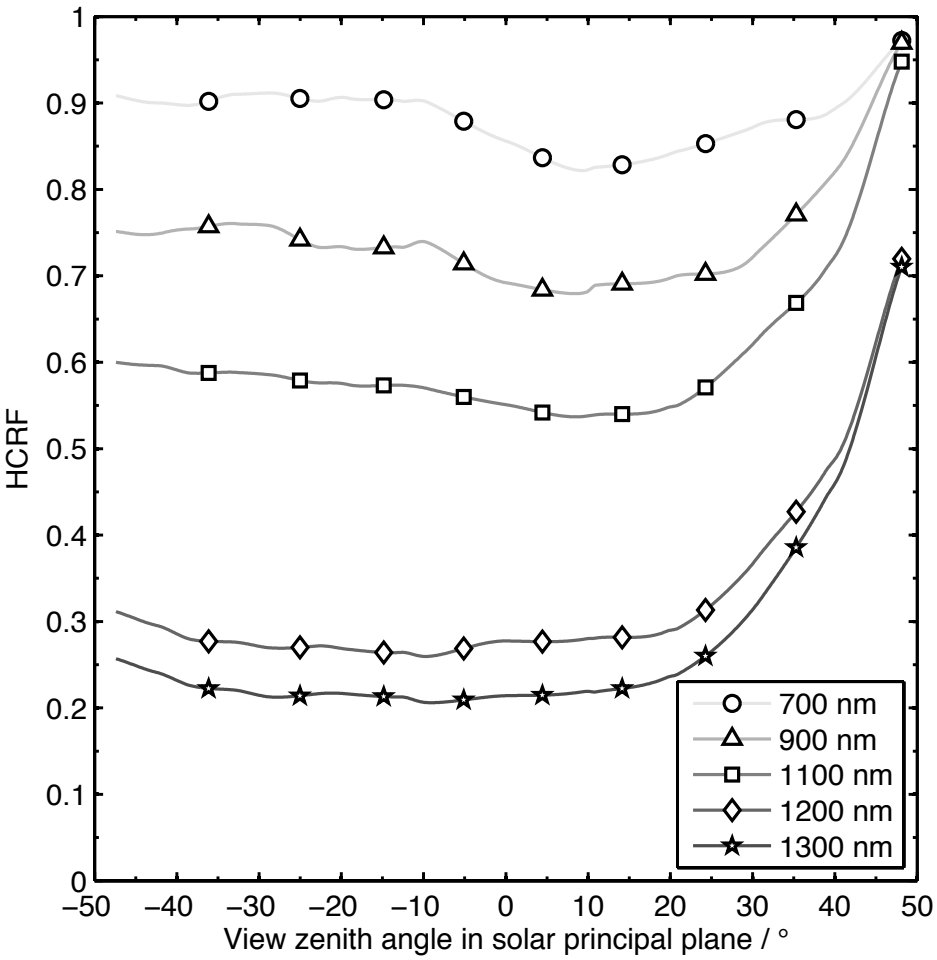

Figure 2.39. HCRF as a function of viewing angle in the solar principal plane at S1

The HCRF generally decreased with wavelength for all viewing angles to a minimum value of 0.1 at 1268 nm, although the rate of decrease with wavelength is smaller for viewing angles in the forward scattering peak. There was minimal angular dependence to the HCRF over the hemisphere for all wavelengths less than 800 nm, with ANIX values typically less than 1.3. However, the angular dependence to the HCRF strongly increased with wavelength. The anisotropy index (ANIX) increased from 1.2 at 400 nm to a maximum of 6.4 at 1270 nm. The increase in anisotropy was the result of smaller HCRF values for viewing angles outside of the forward peak. Despite the increase in anisotropy for wavelengths greater than 800 nm, minimal angular dependence to the HCRF persisted for viewing angles less than 20°,

and for viewing angles in the backward direction. The maximum HCRF value over the hemisphere for all wavelengths was 1.2 at 1127 nm.

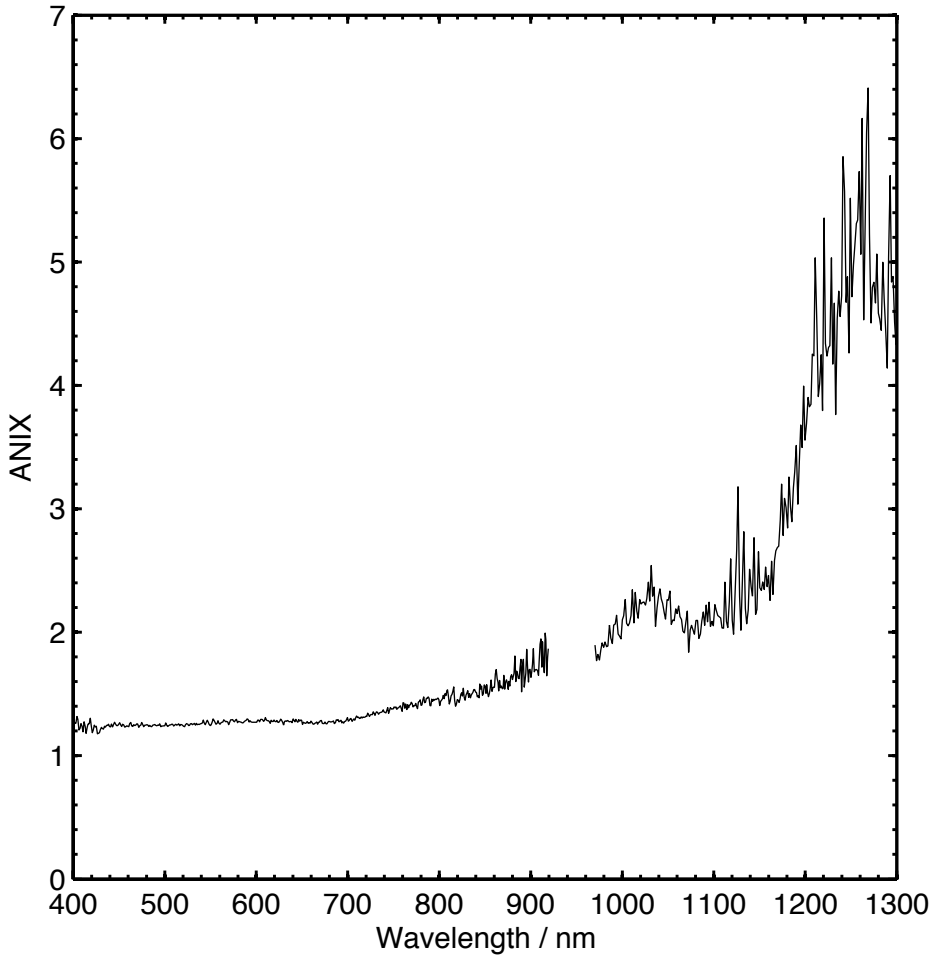

Figure 2.40. Anisotropy index (ANIX) as a function of wavelength at S1

2.5.2 Site 2 (S2)

Polar plots of the HCRF are presented for S2 for the wavelengths 500 nm, 900 nm and 1300 nm in Figure 2.41 to Figure 2.43. The HCRF as a function of viewing angle in the solar principal plane is given in Figure 2.44, and the anisotropy index is given as a function of wavelength in Figure 2.45. S2 had small surface roughness elements; a photograph of the roughness elements is given in Figure 2.15, and estimates of the scale of the roughness elements are given in Table 2.2.

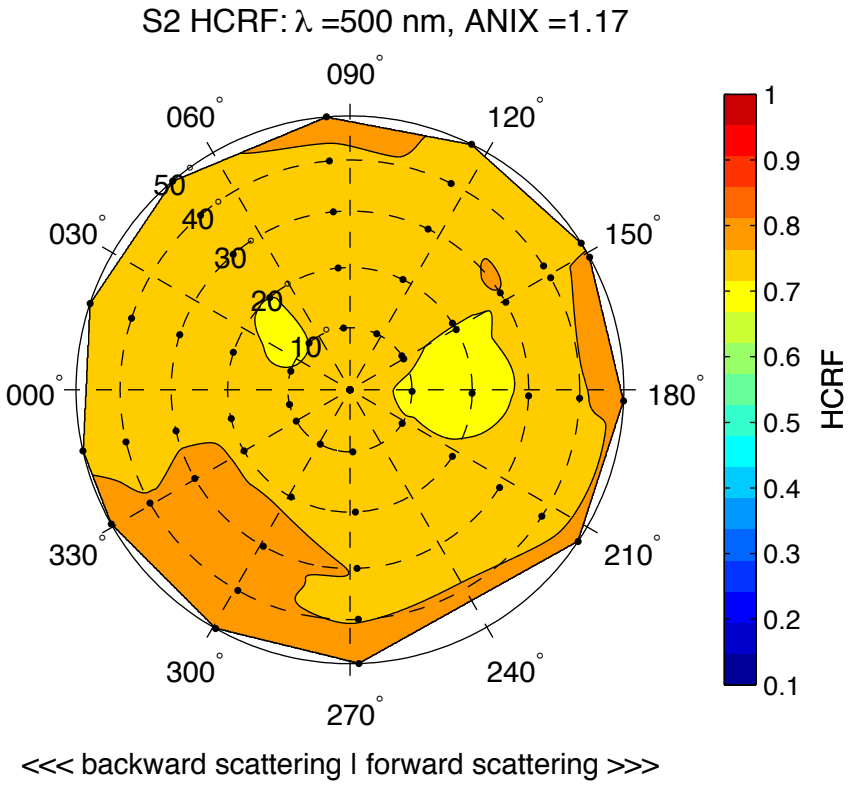

Figure 2.41. HCRF of snow at S2 for a wavelength of 500 nm

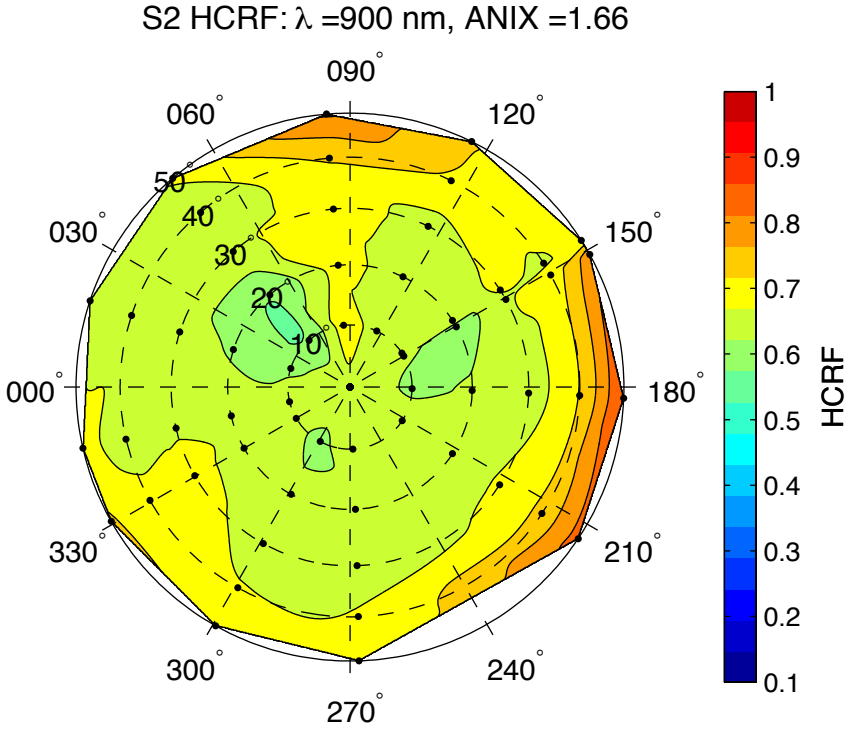

Figure 2.42. HCRF of snow at S2 for a wavelength of 900 nm

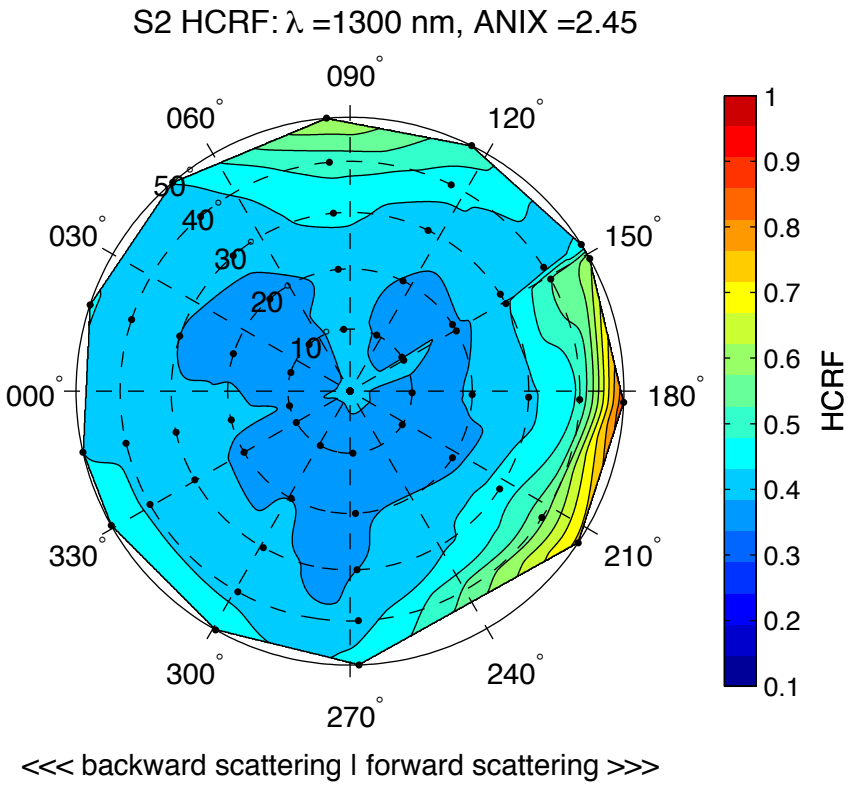

Figure 2.43. HCRF of snow at S2 for a wavelength of 1300 nm

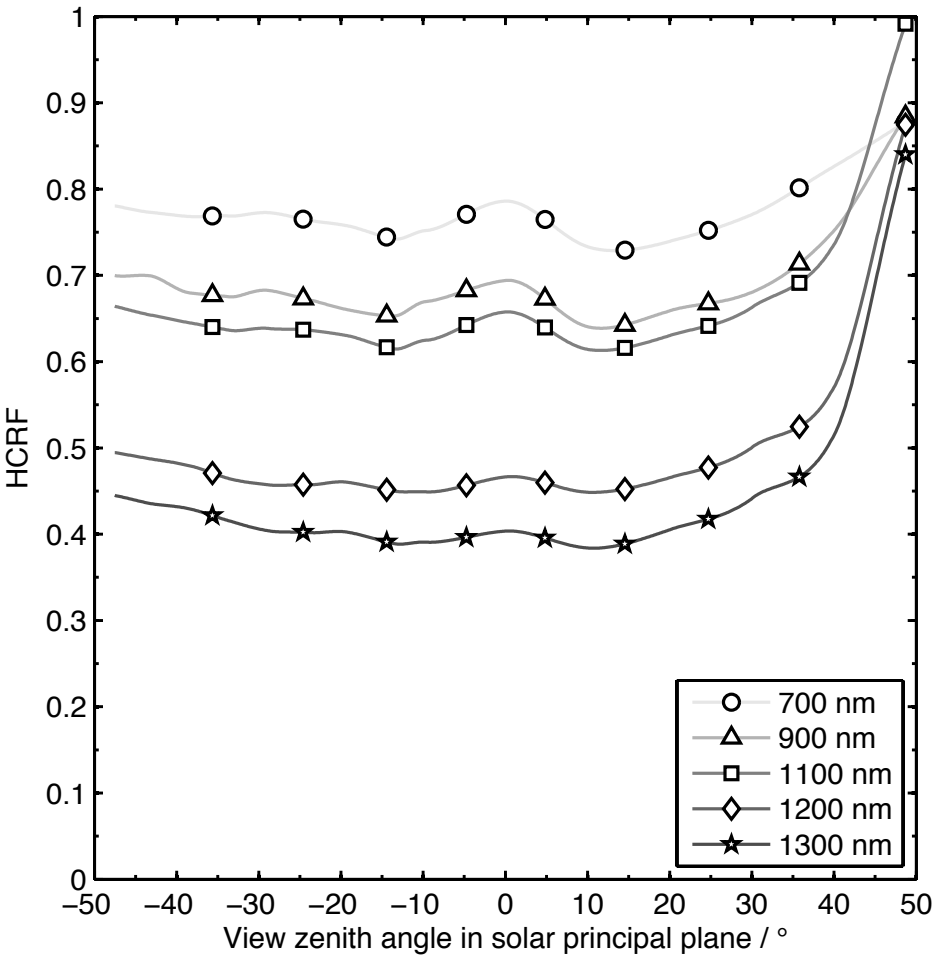

Figure 2.44. HCRF as a function of viewing angle in the solar principal plane at S2

S2 had a weak angular dependence to the HCRF for wavelengths less than 800 nm, with typical ANIX values of around 1.2. As was observed for S1, there was strong wavelength dependence to the HCRF values at S2, with the HCRF for viewing angles outside of the forward peak generally decreasing with wavelength at a faster rate than for viewing angles inside the forward scattering peak. The anisotropy index (ANIX) at S2 increased with wavelength to a maximum of 2.9 at 1272 nm. The forward scattering peak became evident in the HCRF distribution for wavelengths greater than 800 nm, and increased in strength to a maximum value of 1.1 at 1120 nm. While the strength of the forward peak increased with wavelength, the HCRF for all other viewing angles generally decreased with wavelength. Despite a decrease in the maximum

HCRF value over the hemisphere beyond 1120 nm, the anisotropy in the distribution continued to increase with wavelength, and peaked around 1270 nm. The minimum HCRF over the hemisphere at S2 was 0.3 at 1269 nm, which was 0.2 greater than the minimum at S1. S2 had a thinner snow cover than at S1, and had small-scale roughness elements.

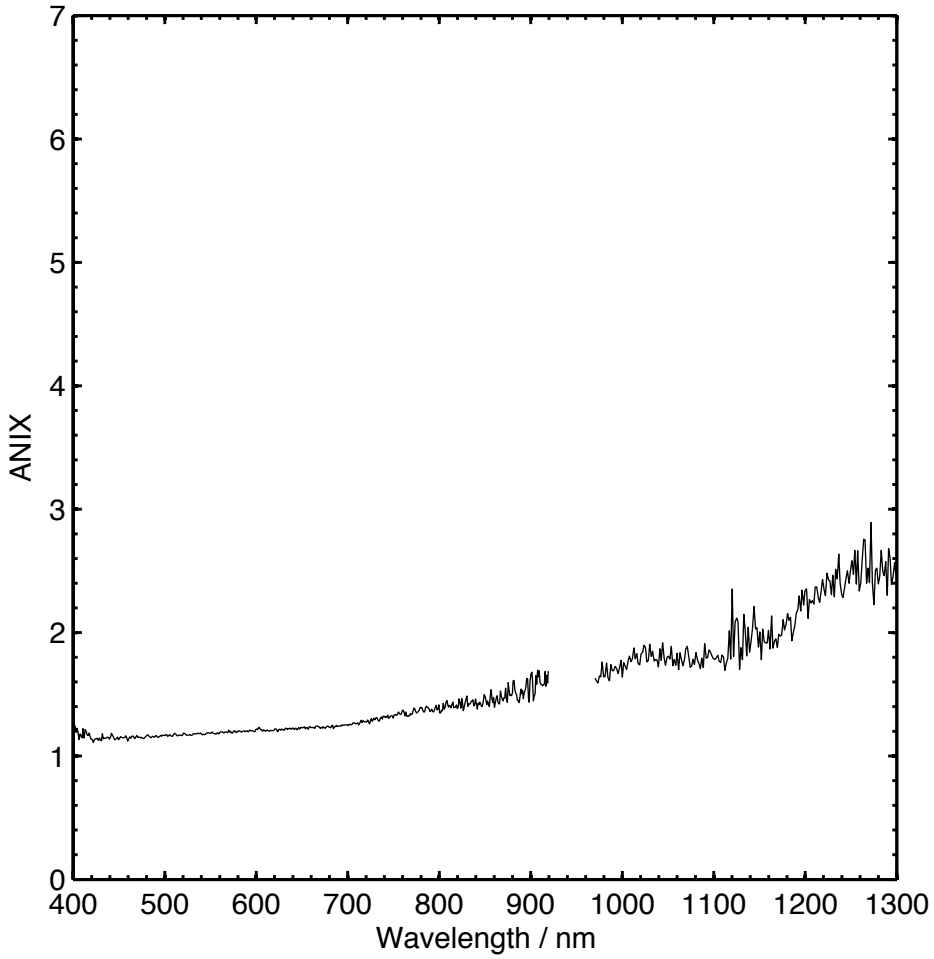

Figure 2.45. Anisotropy index (ANIX) as a function of wavelength at S2

2.5.3 Site 3 (S3)

Polar plots of the HCRF are presented for S3 for the wavelengths 500 nm, 900 nm and 1300 nm in Figure 2.46 to Figure 2.48. The HCRF as a function of viewing angle in the solar principal plane is given in Figure 2.49, and the anisotropy index is given as a function of wavelength in Figure 2.50. S3 had the largest surface roughness elements, a photograph of the roughness elements is

given in Figure 2.15, and estimates of the scale of the roughness elements are given in Table 2.2.

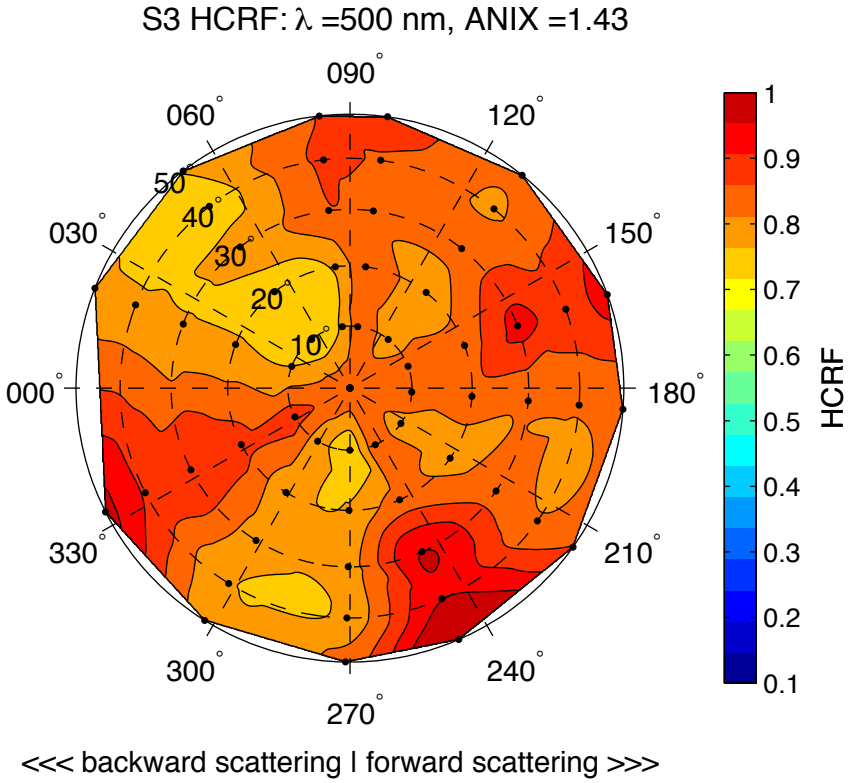

Figure 2.46. HCRF of snow at S3 for a wavelength of 500 nm

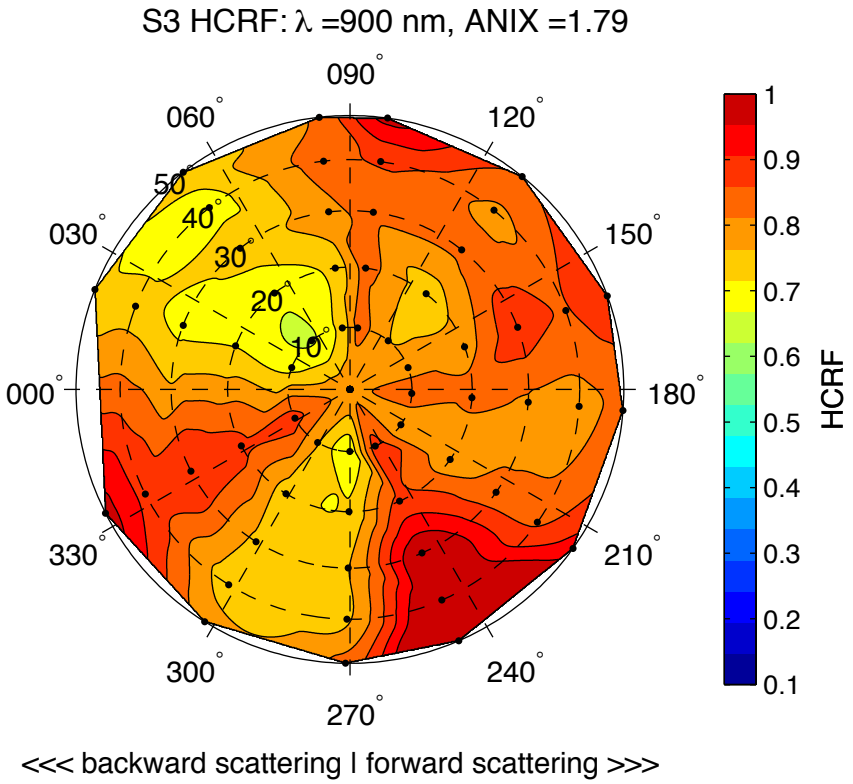

Figure 2.47. HCRF of snow at S3 for a wavelength of 900 nm

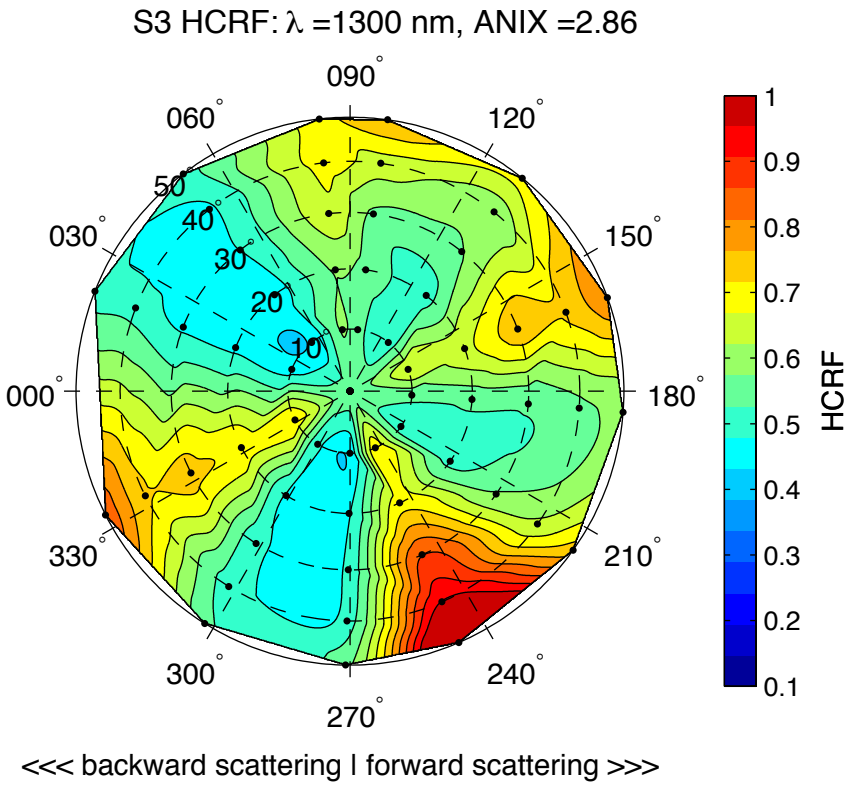

Figure 2.48. HCRF of snow at S3 for a wavelength of 1300 nm

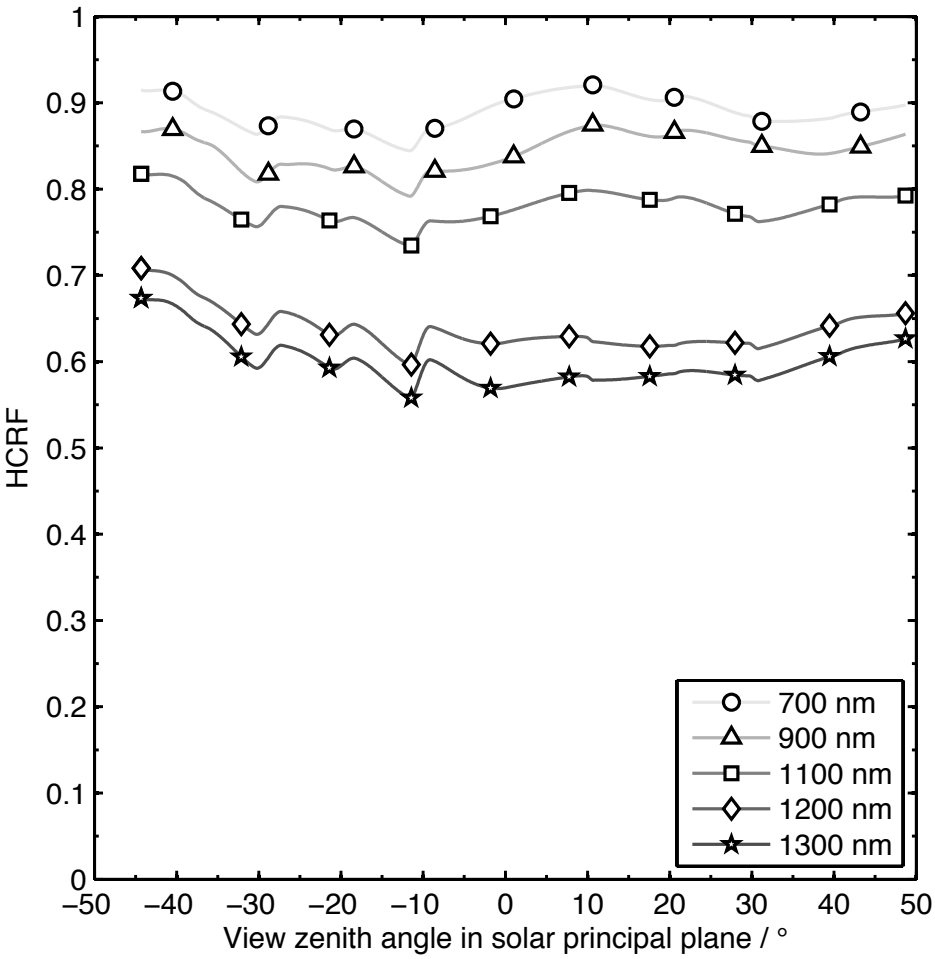

Figure 2.49. HCRF as a function of viewing angle in the solar principal plane at S3

There was no evidence of a forward scattering peak within ± 30° azimuth angle of the 180° degree index over the full wavelength range at S3. There was minimal angular dependence to the HCRF in the solar principal plane, but considerable angular dependence to the HCRF outside of the solar principal plane, with the ANIX value increasing with wavelength to a maximum of 2.8 at 1264 nm. Given that the anisotropy was observed outside of the principal plane, the reflected distribution was highly asymmetric, with differences of up to 28 % of the mean HCRF value on either side of the principal plane. Similarly to S1 and S2, the HCRF generally decreased with wavelength and the anisotropy generally increased with wavelength. Despite having a much thinner snowpack than the other sites the HCRF values at S3 were generally greater, with a

minimum HCRF value over the hemisphere for all wavelengths of 0.4 at 1273 nm. The maximum HCRF value over the hemisphere for all wavelengths was 1.4 at 1154 nm.

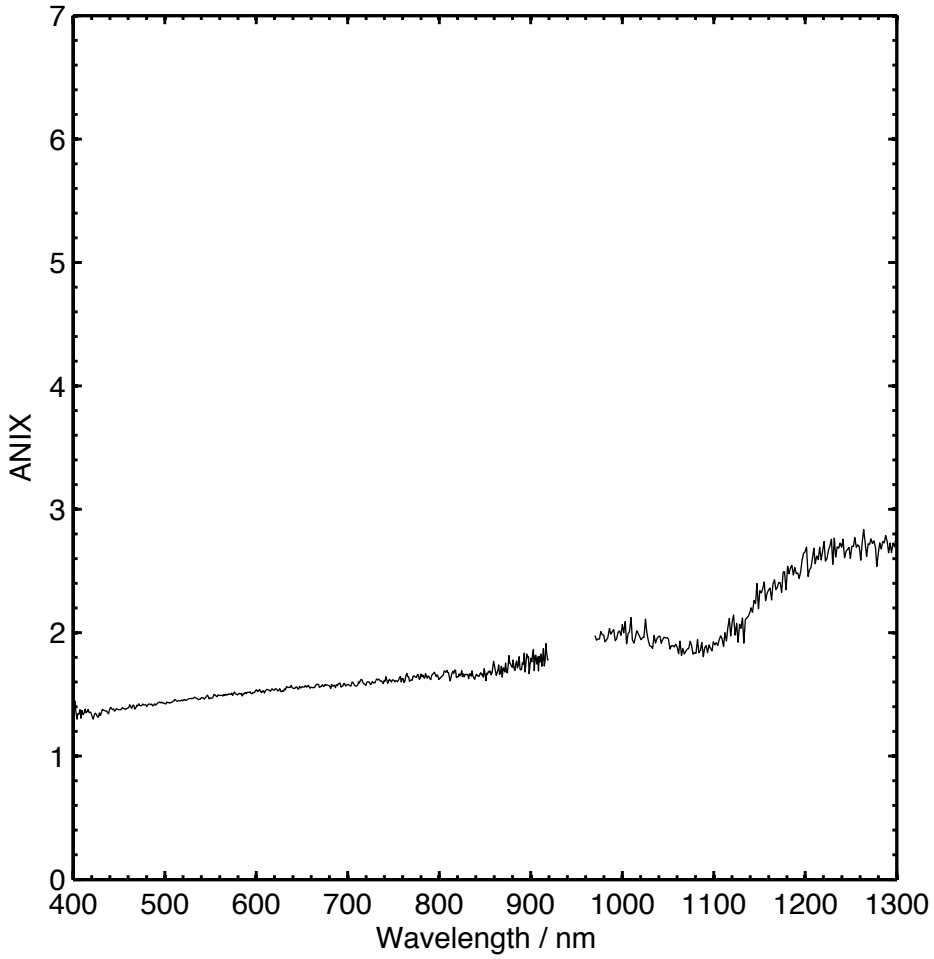

Figure 2.50. Anisotropy index (ANIX) as a function of wavelength at S3

2.5.4 Site 4 (S4)

Polar plots of the HCRF are presented for S4 for the wavelengths 500 nm, 900 nm and 1300 nm in Figure 2.51 to Figure 2.53. The HCRF as a function of viewing angle in the solar principal plane is given in Figure 2.39, and the anisotropy index is given as a function of wavelength in Figure 2.40.

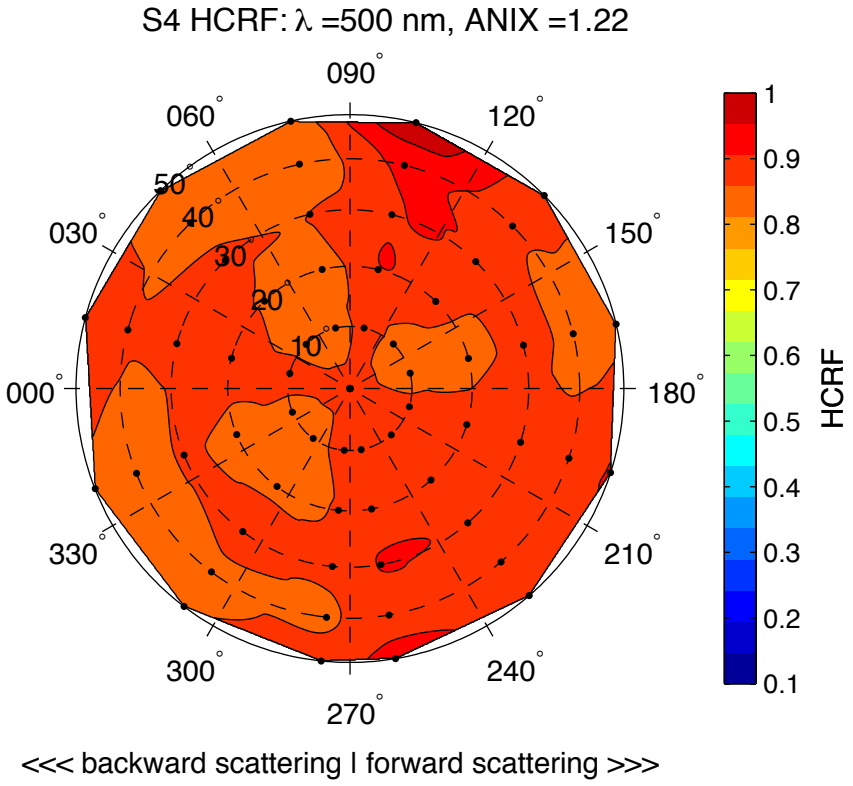

Figure 2.51. HCRF of snow at S4 for a wavelength of 500 nm

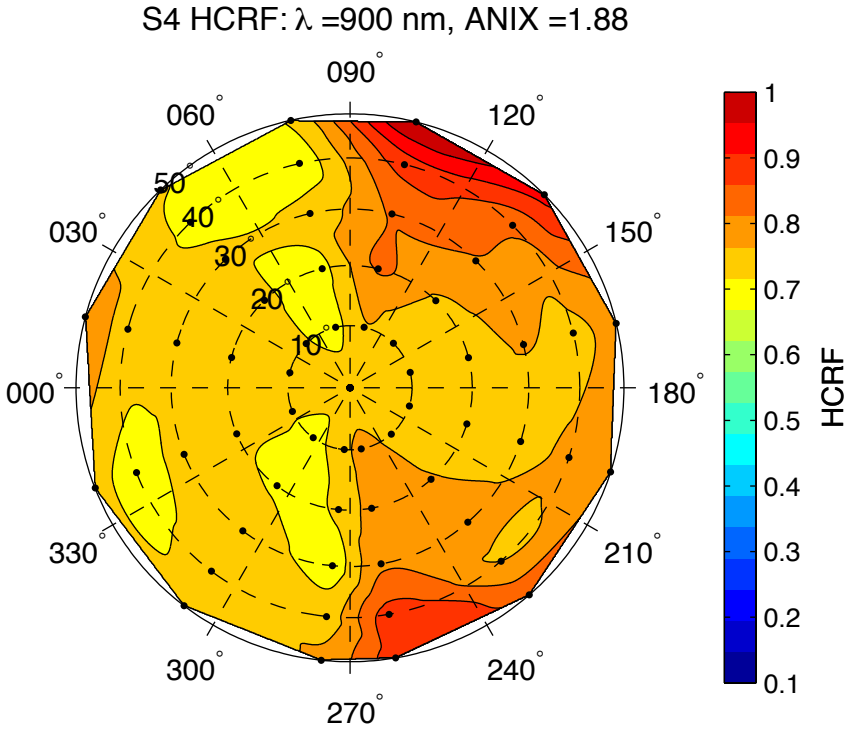

Figure 2.52. HCRF of snow at S4 for a wavelength of 900 nm

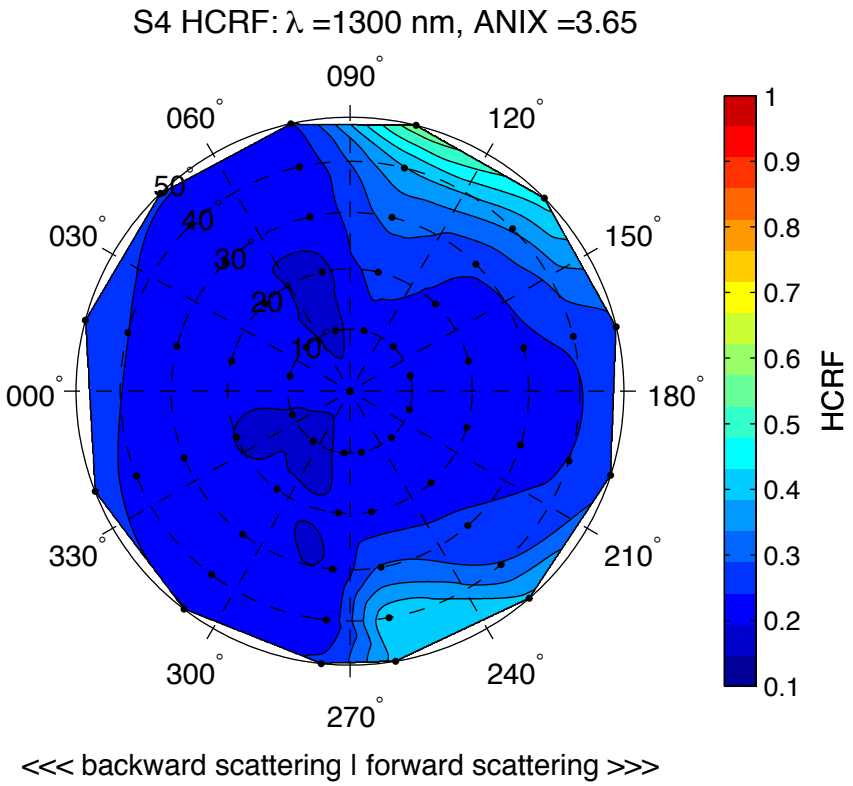

Figure 2.53. HCRF of snow at S4 for a wavelength of 1300 nm

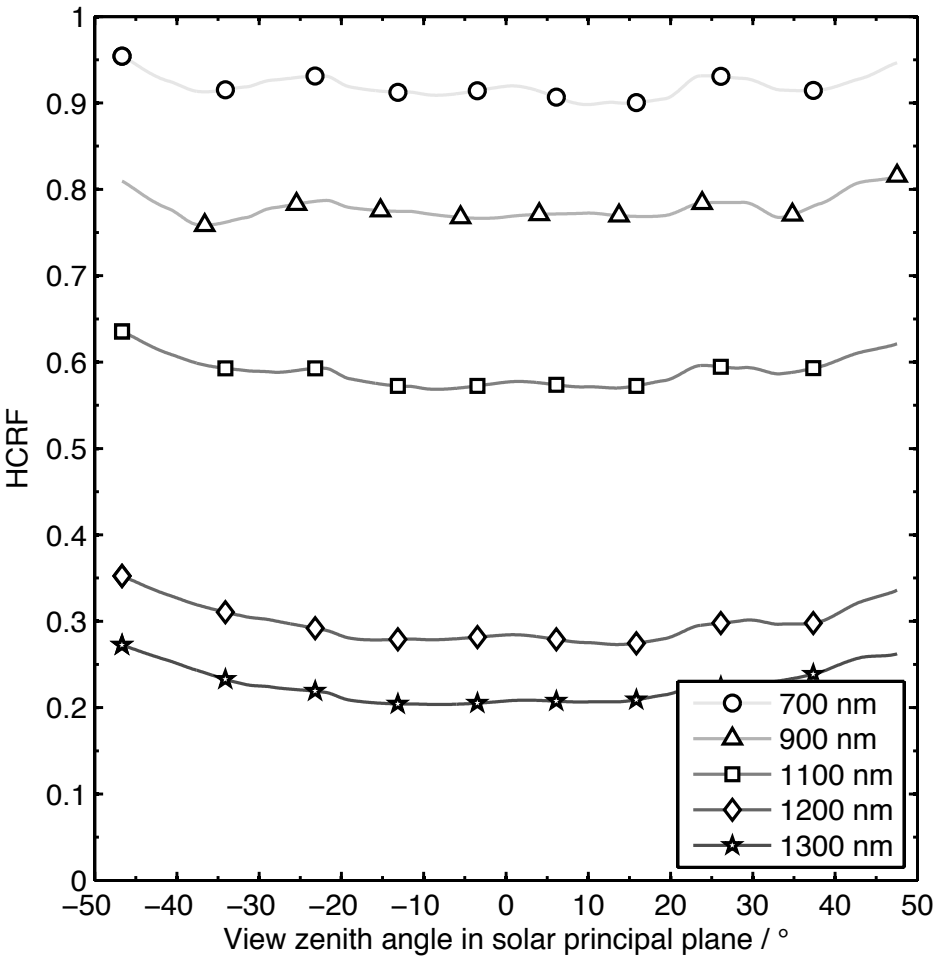

Figure 2.54. HCRF as a function of viewing angle in the solar principal plane at S4

There was no evidence of a forward scattering peak in the solar principal plane for S4, despite no roughness elements being present. The forward peak appears to be offset from the specular direction of 180° and is present at the 120° and 240° azimuthal indices. Similarly to S1, S2, and S3, the HCRF distribution showed strong wavelength dependence, with an increase in the ANIX value with wavelength to a maximum of 5.3 at 1264 nm. The maximum HCRF value over the hemisphere was 1.2 at 917 nm, and the minimum was 0.1 at 1264 nm. HCRF generally decreased with wavelength, and the anisotropy index (ANIX) generally increased with wavelength, with a peak around 1260 nm. Similarly to S1 and S2, there was minimal angular dependence to the HCRF for all wavelengths less than 800 nm, with ANIX values typically less than 1.4.

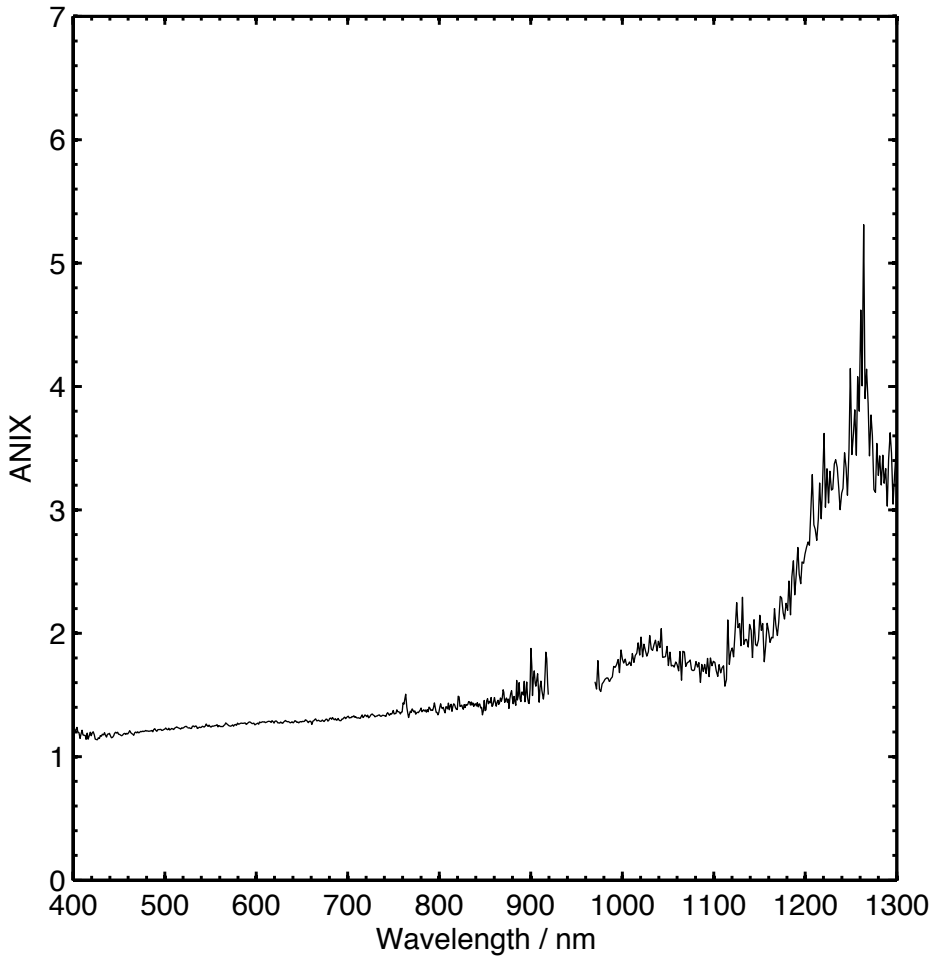

Figure 2.55. Anisotropy index (ANIX) as a function of wavelength at S4

2.5.5 Site 5 (S5)

Polar plots of the HCRF are presented for S5 for the wavelengths 500 nm, 900 nm and 1300 nm in Figure 2.56 to Figure 2.58. The HCRF as a function of viewing angle in the solar principal plane is given in Figure 2.59, and the anisotropy index is given as a function of wavelength in Figure 2.60.

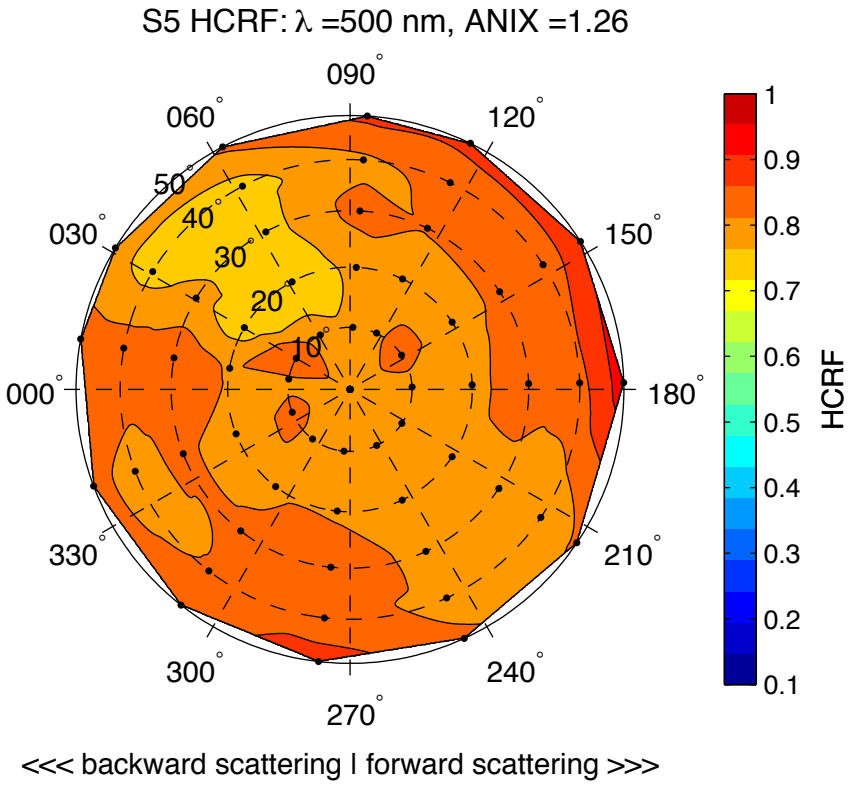

Figure 2.56. HCRF of snow at S5 for a wavelength of 500 nm

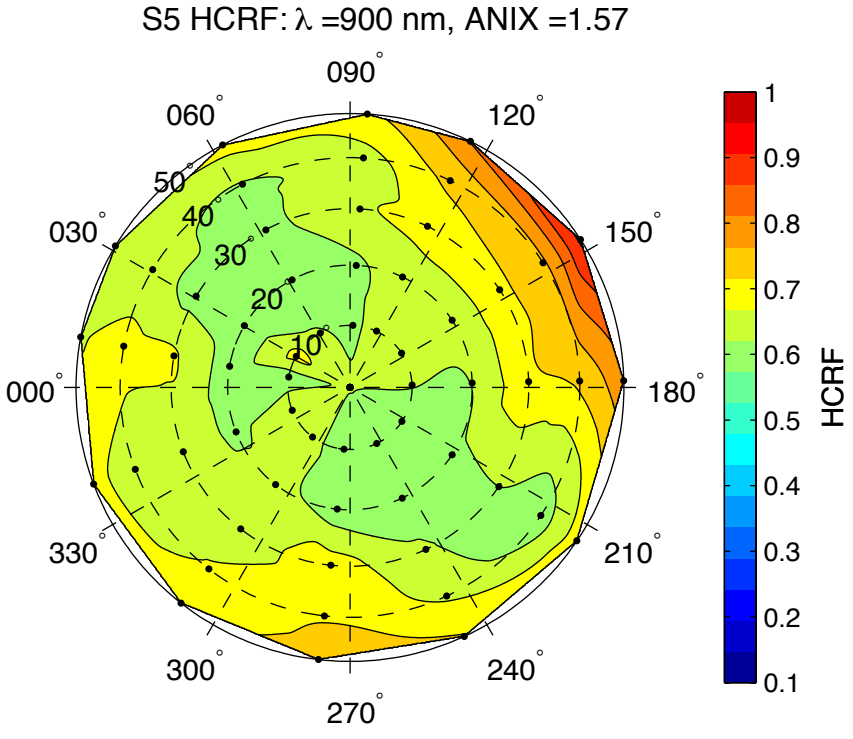

Figure 2.57. HCRF of snow at S5 for a wavelength of 900 nm

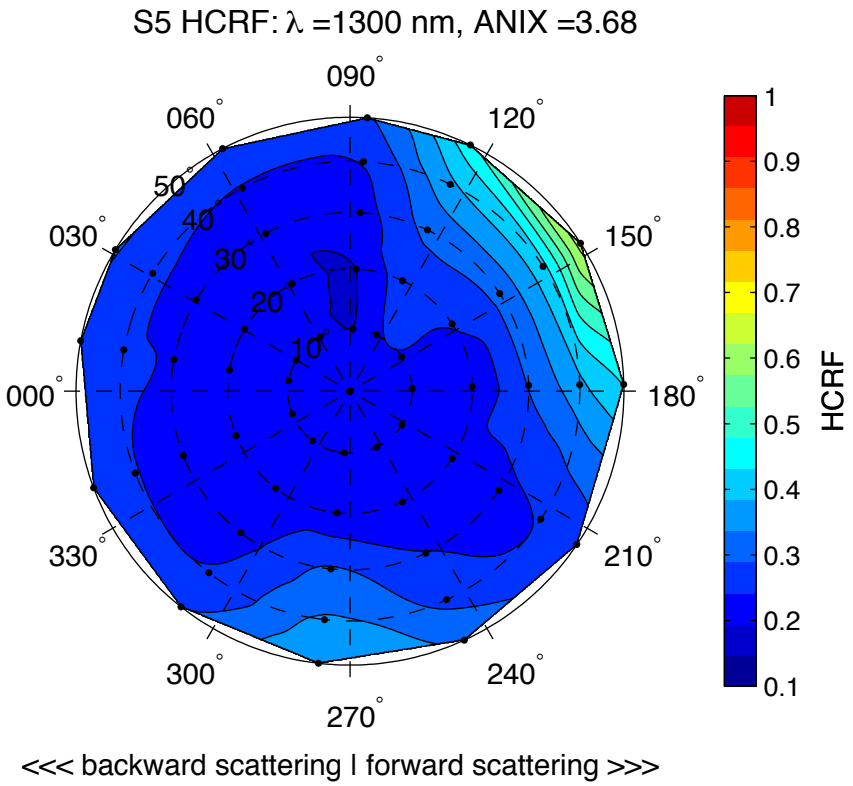

Figure 2.58. HCRF of snow at S5 for a wavelength of 1300 nm

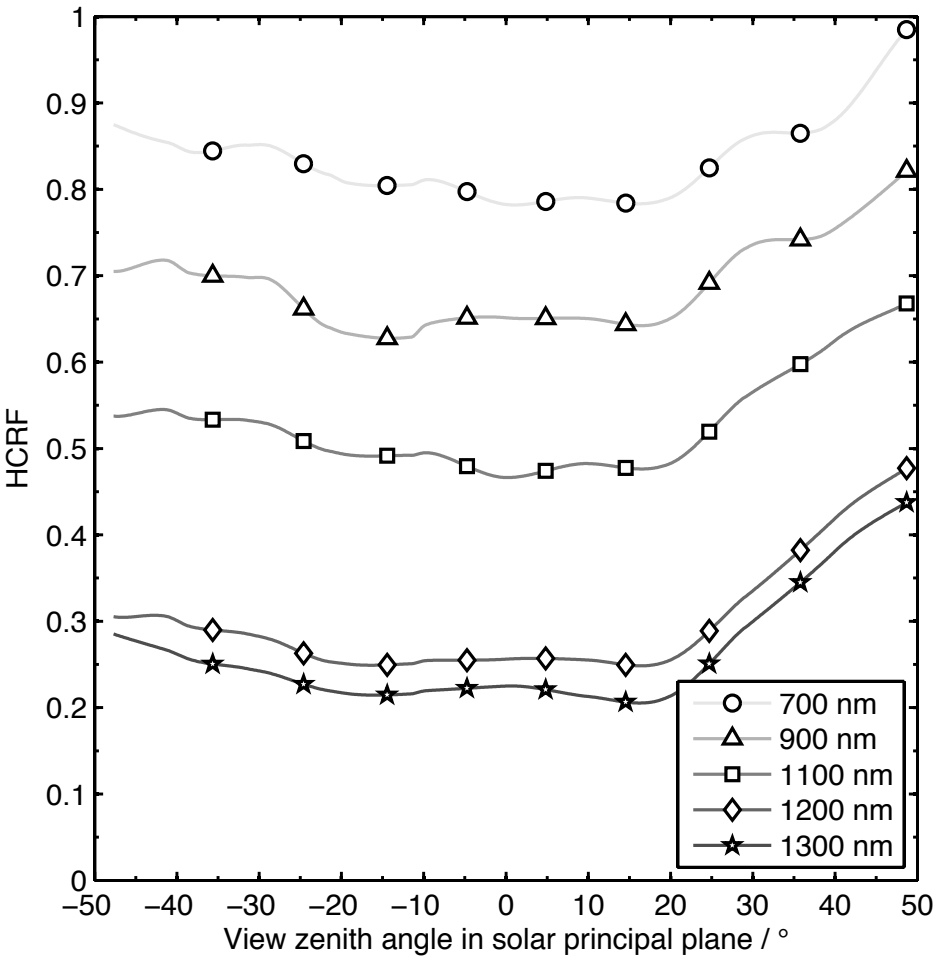

Figure 2.59. HCRF as a function of viewing angle in the solar principal plane at S5

The HCRF over the hemisphere at S5 has a forward scattering peak that was strongest at the 150° azimuthal index, and the anisotropy to the HCRF distribution was strongly wavelength dependent. S5 had the deepest snowpack and its maximum HCRF value of 1.6 had a wavelength of 400 nm, compared to 917 nm for S4 (which had the second deepest snowpack), 1154 nm for S3, 1120 nm for S2, and 1127 nm for S1. The angular dependence to the HCRF was minimal for wavelengths below 700 nm, with ANIX values typically around 1.3. The ANIX value generally increased with wavelength to a maximum value of 5 at 1267 nm. The ANIX values as a function of wavelength indicates that the strength of the peak – relative to viewing angles outside of the peak – was

strongly wavelength dependent. The minimum HCRF value over the hemisphere for the full wavelength range was 0.11 at 1267 nm.

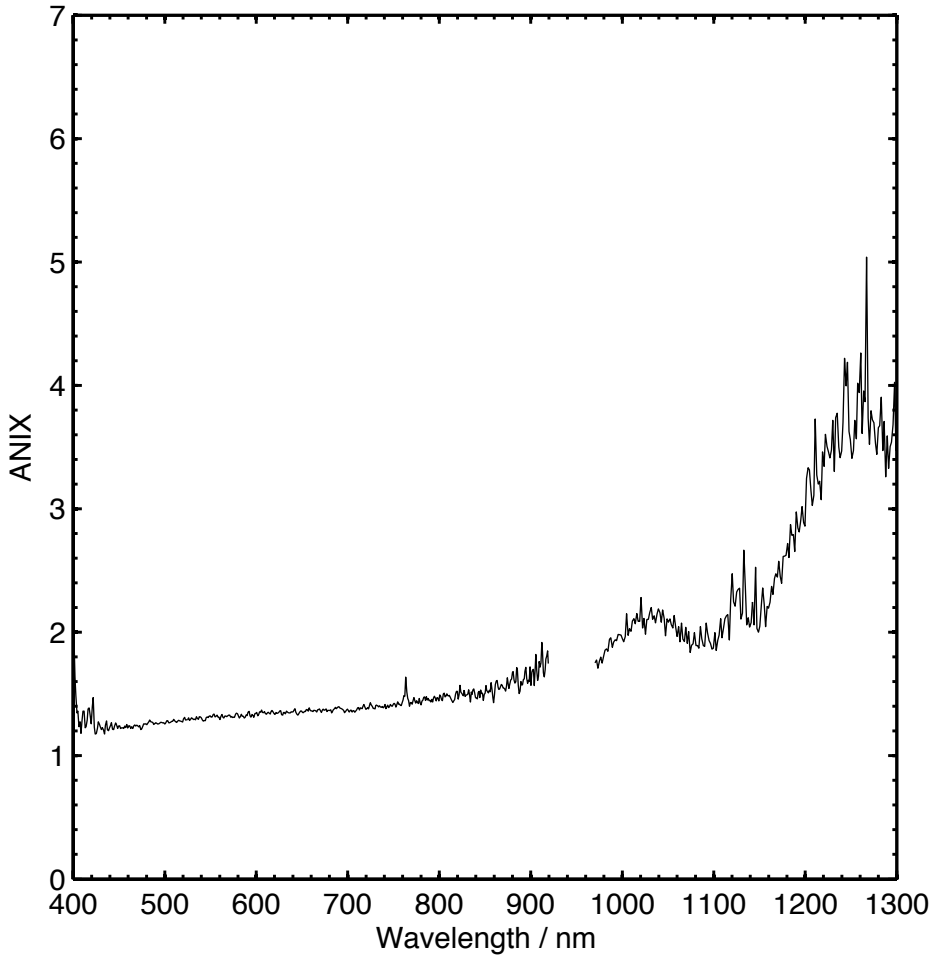

Figure 2.60. Anisotropy index (ANIX) as a function of wavelength at S5

2.5.6 Site 6 (S6)

Polar plots of the HCRF are presented for S6 for the wavelengths 500 nm, 900 nm and 1300 nm in Figure 2.61 to Figure 2.63. The HCRF as a function of viewing angle in the solar principal plane is given in Figure 2.64, and the anisotropy index is given as a function of wavelength in Figure 2.65.

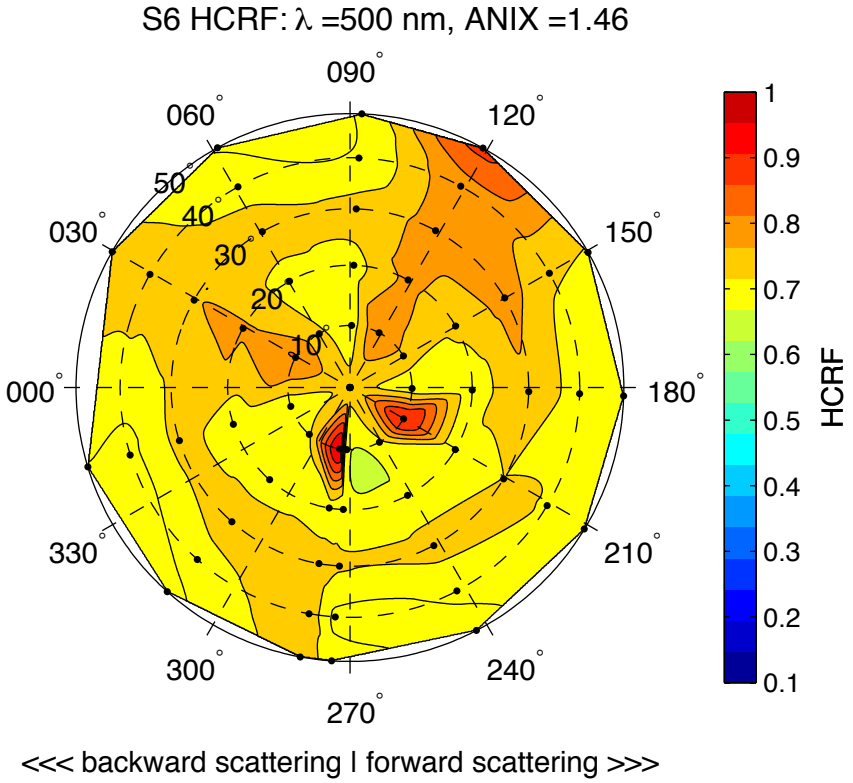

Figure 2.61. HCRF of snow at S6 for a wavelength of 500 nm

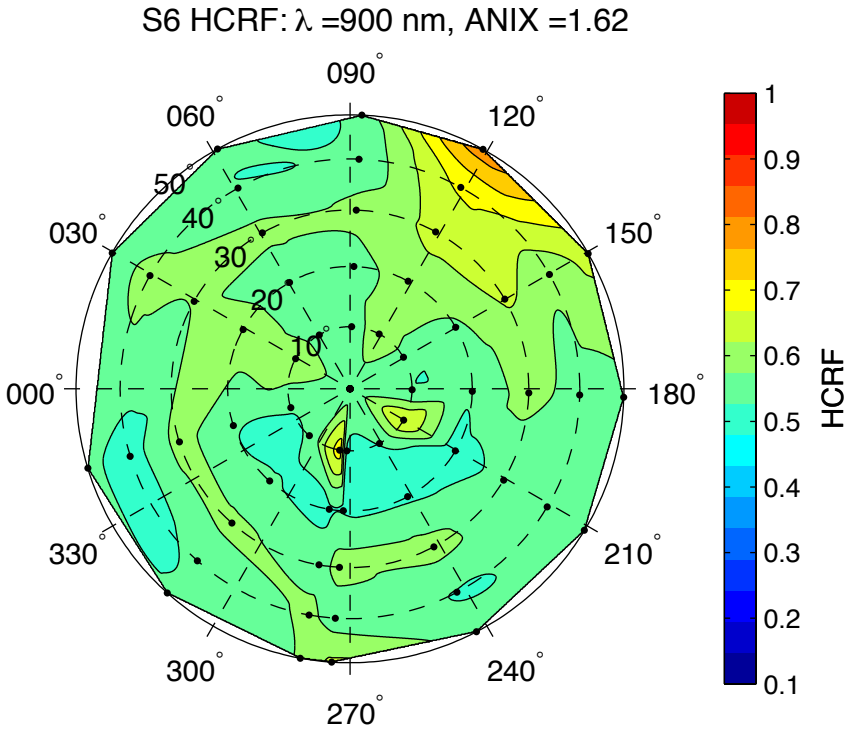

Figure 2.62. HCRF of snow at S6 for a wavelength of 900 nm

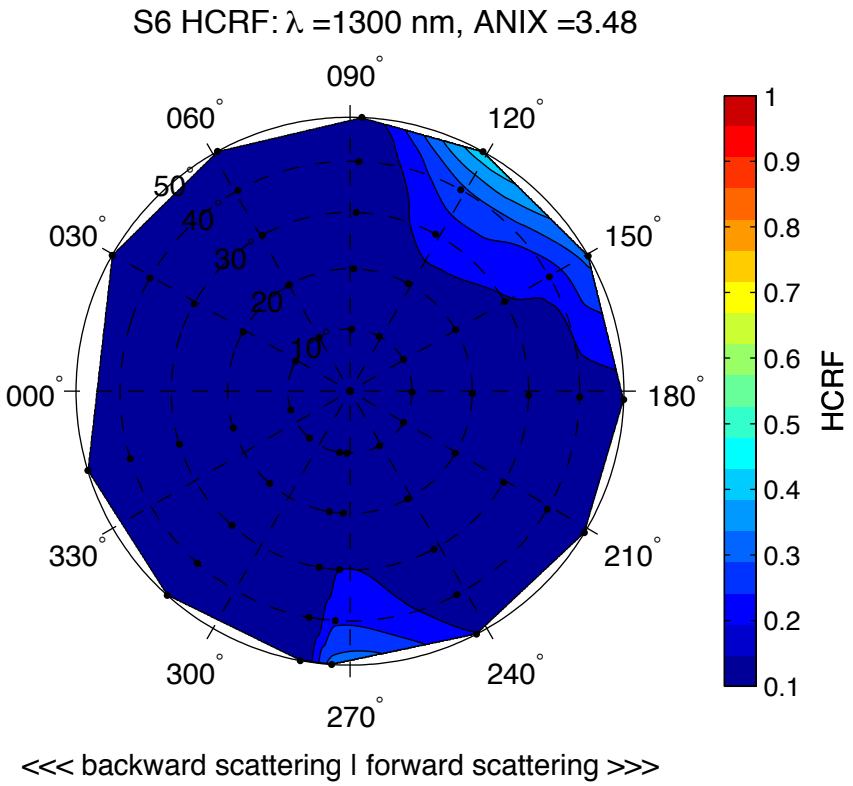

Figure 2.63. HCRF of snow at S6 for a wavelength of 1300 nm

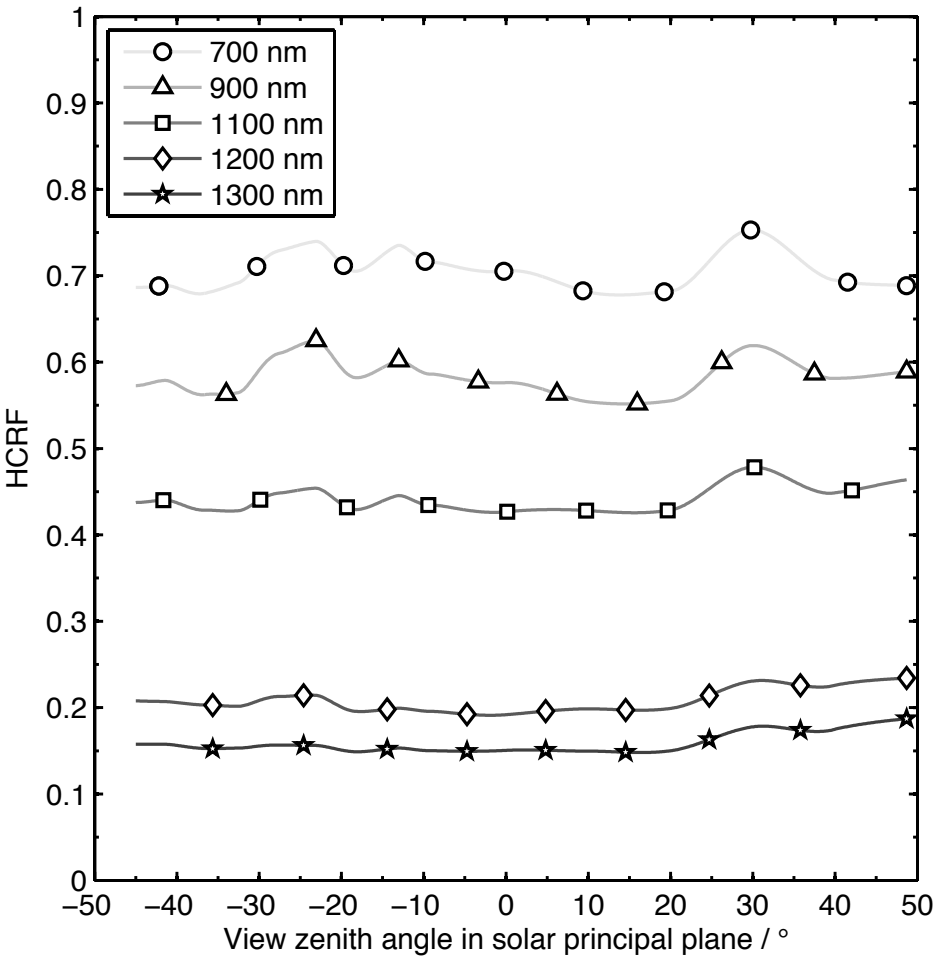

Figure 2.64. HCRF as a function of viewing angle in the solar principal plane at S6

Similarly to S4, S6 shows no forward scattering peak in the solar principal plane, despite having no roughness elements. However, there was a forward peak in the reflected distribution at the 120° azimuthal index, which has a maximum HCRF value of 1.2 at 400 nm. The greatest HCRF value for all viewing angles and wavelengths was 1.2 at 400 nm despite a snowpack thickness of only 14 cm, although lake ice was observed underneath the snowpack at S6. HCRF generally decreased with wavelength and the anisotropy increased with wavelength, with a maximum ANIX value of 4.5 at 1264 nm. The wavelength for the peak in anisotropy at S6 was similar to S5, S4, S3, S2 and S1, which all have a peak in anisotropy in the 1264 nm to 1272 nm wavelength range. The wavelength range for the peak anisotropy generally corresponds with the

wavelength range in which the minimum HCRF values over the hemisphere are found. There was a general decrease in reflectance with wavelength for S6 – as was observed for all other sites – with a minimum HCRF value was 0.1 at 1264 nm at S6.

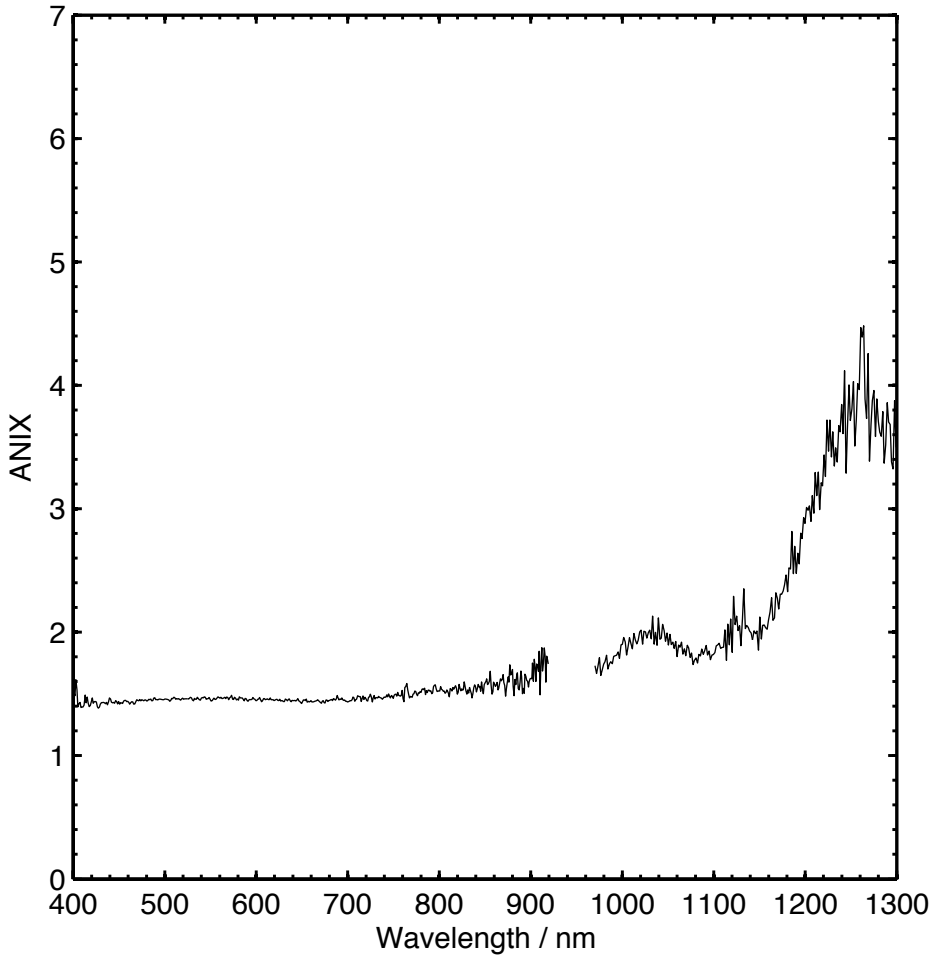

Figure 2.65. Anisotropy index (ANIX) as a function of wavelength at S6

2.5.7 Averaged HCRF

For sites which had a snow depth greater than 40 cm and the snow surface was smooth (S1, S4, S5) the HCRF was averaged and is presented in the form of polar plots for wavelengths 500 nm, 900 nm and 1300 nm in Figure 2.66 to Figure 2.68. The averaged HCRF as a function of viewing zenith angle in the solar principal plane is given in Figure 2.69. The averaged HCRF is presented as a function of wavelengths for viewing angles in the forward directions is given

in Figure 2.70. The averaged HCRF in Figure 2.70 is compared to measurements made by Painter and Dozier (2004) (dashed lines), who used a similar methodology to measure HCRF of snow near the Mammoth Lakes, California, for solar zenith angles 47° to 51°.

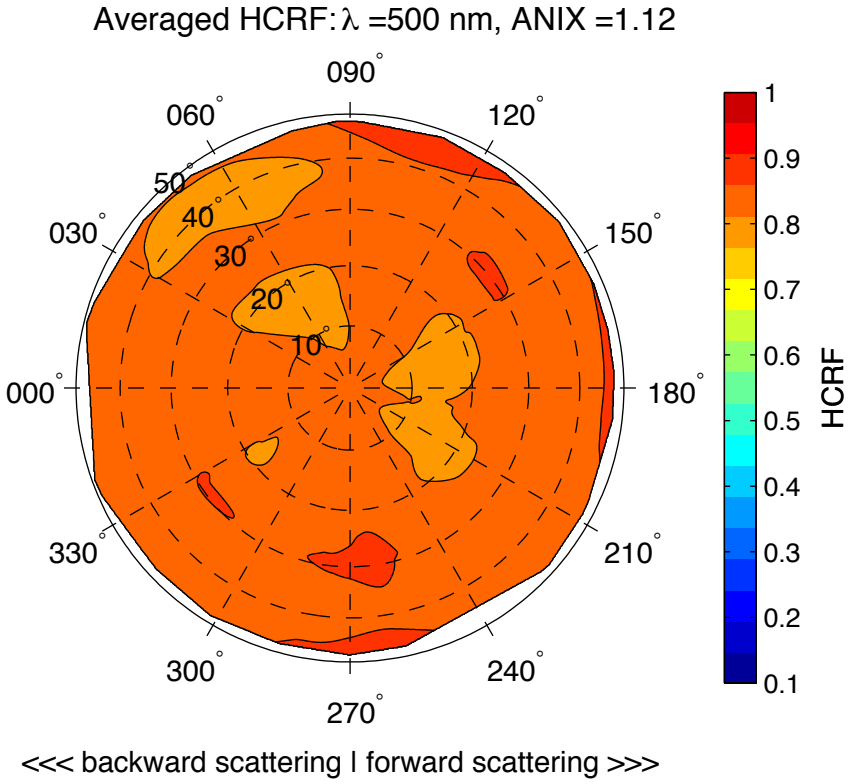

Figure 2.66. Average HCRF of S1, S4 and S5 for a wavelength of 500 nm

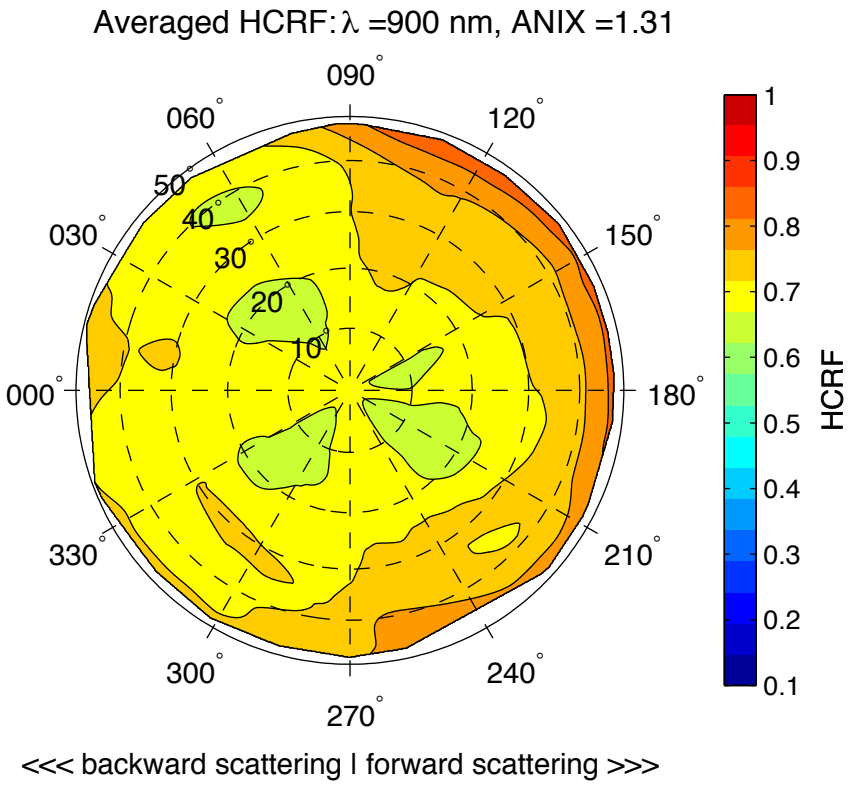

Figure 2.67. Average HCRF of S1, S4 and S5 for a wavelength of 900 nm

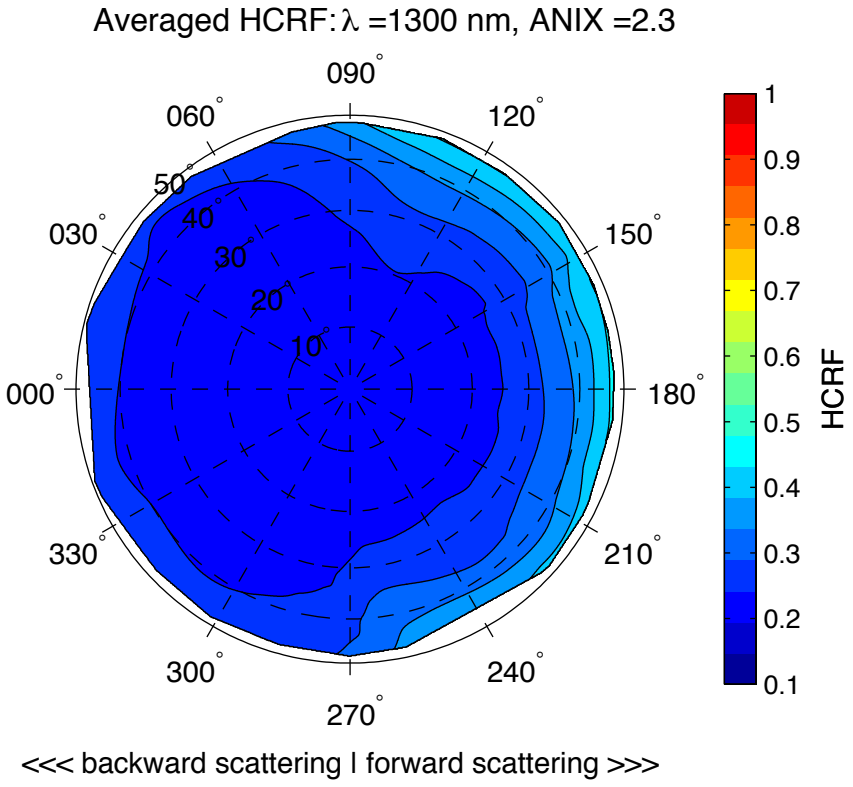

Figure 2.68. Average HCRF of S1, S4 and S5 for a wavelength of 1300 nm

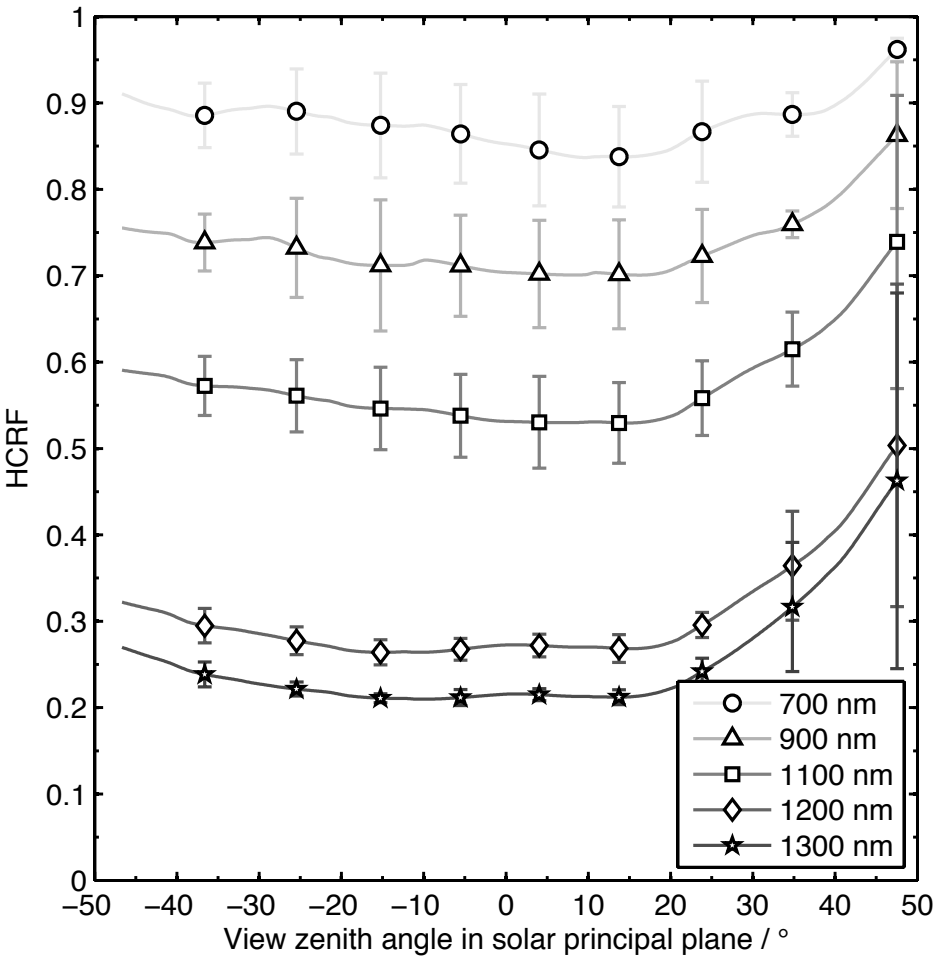

Figure 2.69. Averaged HCRF as a function of viewing angle in the solar principal plane. Uncertainty bars are one standard deviation of the averaged measurements.

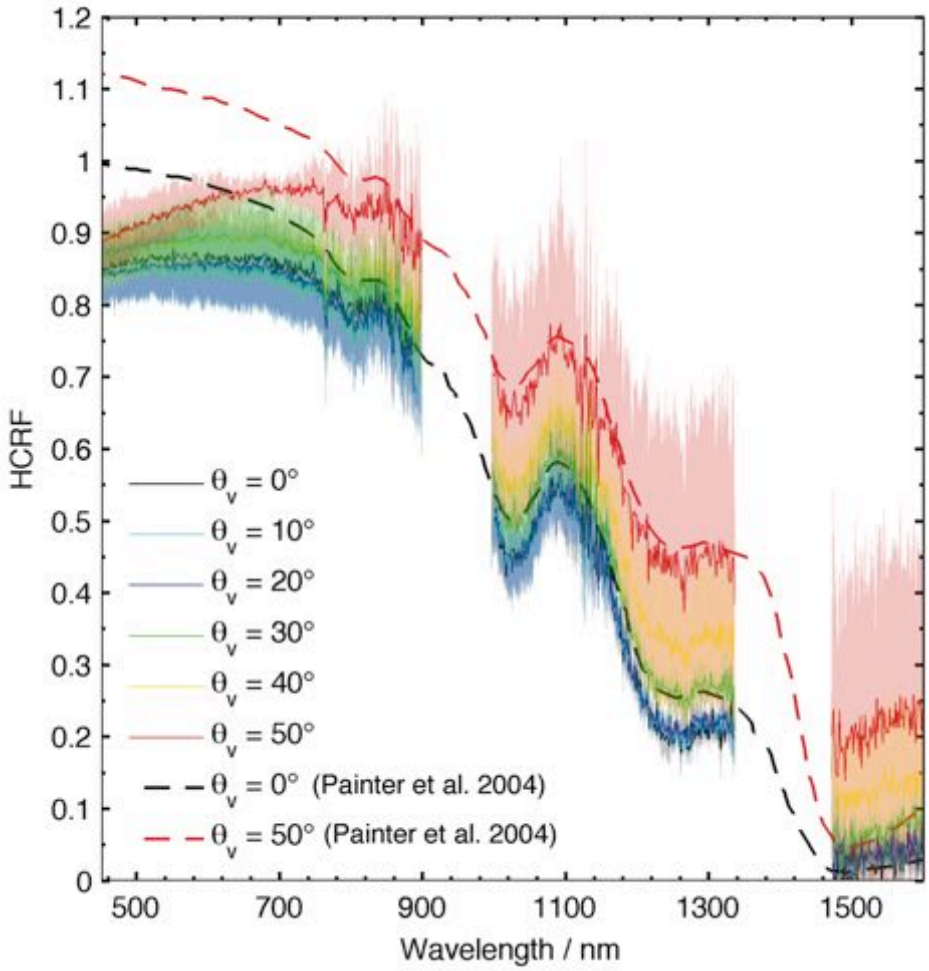

Figure 2.70. Averaged HCRF as a function of wavelength for different viewing angles in the solar principal plane in the forward direction. Two regions of low signal to noise at 1400 nm and at 900 nm have been removed. The solid line is the averaged HCRF measurement and the solid pale color represents one standard deviation from the mean, the dashed lines are the HCRF of snow in California recorded by Painter and Dozier (2004) with a solar zenith angle of 47°.

The relative standard deviation in the HCRF for the averaged sites (S1, S4, S5) was less than 10 % for viewing angles outside of the forward scattering peak, implying good agreement in the measurements at sites where the snowpack was thick and the snow surface was smooth. Although there was considerably more variation for viewing angles in the forward scattering peak, with a maximum relative standard deviation of 54 % at 1300 nm. The standard deviation of the averaged sites in solar principal plane was 0.17 at 1300 nm for a view angle of 45° compared to 0.01 at 1300nm at the nadir viewing angle

Anisotropy in the solar principal plane for the averaged sites was minimal for wavelengths shorter than 700 nm, but strongly increased with wavelength. For example, at 1300 nm, the HCRF increased from 0.22 ± 0.01 at the nadir view position, to 0.42 ± 0.17 at 45° in the forward direction in the solar principal plane, whereas at 700 nm there was no detectable increase in the HCRF over the same viewing angle range. Anisotropy for the averaged sites increased with wavelength, from a minimum of 1.1 at 400 nm to a maximum of 2.4 at 1260 nm. The HCRF spectra for different view angles in the solar principal plane is given in Figure 2.70 and is compared with measurements made by Painter and Dozier (2004) (Painter, 2004) (dashed lines). For the wavelength range 800 nm to 1300 nm the spectra agree well with Painter and Dozier's measurements, but were up to 0.24 lower for wavelengths less than 800 nm for the same viewing angles.

2.6 Discussion

The discussion section is spilt into separate sections discussing the HCRF for the individual sites, the averaged HCRF, and the averaged HCRF compared to measurements by Painter and Dozier (2004).

2.6.1 Individual sites

There was considerable variability between sites in the HCRF over the hemisphere. The differences are in part due to variability in the snow surface roughness elements, snow depth, grain size, concentration of light absorbing impurities, and the reflectivity of the underlying surface; all of which are known to affect the HCRF of snow (Peltoniemi et al., 2005; Painter, 2004; Bourgeois et al., 2006). There were, however, some key similarities between the sites: (1) HCRF generally decreased with wavelength to a minimum around 1260 nm to

1270 nm (2) anisotropy generally increased with wavelength to a maximum around 1260 nm to 1270 nm. HCRF values for sites that had a smooth snow surface and a thicker snowpack agreed more closely, with an average relative standard deviation of 14 % over the hemisphere for S1, S4 and S5.

S3, which had the largest roughness elements, was most strongly asymmetric with respect to the solar principal plane, with differences of up to 28 % of the mean HCRF value, and had no clearly defined forward scattering peak, implying that the roughness elements at S3 reduced scattering in the forward direction. Both sites that exhibited surface elements (S3 and S2) showed increased HCRF values at larger wavelengths, despite a thinner snowpack compared to the averaged sites. For example, the average HCRF value for all viewing angles at S3 was 0.6 at a wavelength of 1300 nm, compared to 0.3 at 1300 nm for averaged sites (S1, S4 and S5). S2, which exhibits some small-scale roughness elements, showed an increase in the average HCRF of all viewing angles of 0.2 at 1300 nm compared to the average of S1, S4 and S5. There are two explanations for the increase in HCRF in the infrared region of the spectrum at S2 and S3, either a difference in grain size in the surface layer, or a change in the effective solar zenith angle as a result of the surface roughness elements (Wiscombe and Warren, 1980). The data available does not indicate what is the dominant cause for the observed effect at sites S2 and S3, because grain size was not recorded in the surface layer, and because of possible errors introduced as a result of the limited footprint size and imperfect overlap as discussed in Section 2.4.5.2. However, the roughness elements observed at S2 and S3 highlight the potential influence of surface roughness on the HCRF, and the importance of sampling surface roughness in order to obtain a representative HCRF, especially at large solar zenith angles.

2.6.2 Averaged sites

The HCRF for the averaged sites had improved symmetry over the solar principal plane. The averaging process reduced errors caused by localized undulations of the snowpack and the imperfect footprint overlap discussed in Section 2.4.5.2. The angular effects on the HCRF are strongest in the forward scattering direction for the averaged sites, and have considerably less influence for viewing angles less than 30°, particularly the in backward viewing direction. For example, for viewing angles less than 30° in the backward direction, the anisotropy index (ANIX) is 1.3 at 1300 nm and 1.1 at 1100 nm, for viewing angles less than 15° over the wavelength range 400 nm to 1300 nm the ANIX is less than 1.1. The increase in anisotropy in the HCRF with wavelength for snow has been observed in previous studies for different solar zenith angles (e.g. Painter, 2004; Bourgeois et al., 2006; Hudson et al., 2006), and is the consequence of increasing absorption of radiation with wavelength, which results in a shorter penetration depth into the snowpack and reduced scattering (Warren, 1982). Greater anisotropy in the HCRF with wavelength is also influenced by the smaller proportion of incident diffuse irradiance at longer wavelengths, caused by a reduction in Rayleigh scattering (Lyapustin and Privette, 1999; Grenfell et al., 1994).

2.6.3 Comparison with other snow HCRF measurements

For wavelengths greater than 800 nm, the averaged HCRF measurements agree well with Painter and Dozier's (2004) measurements of snow HCRF, but were up to 0.24 lower for wavelengths less than 800 nm. The smaller HCRF values measured in Ny-Alesund for wavelengths in the visible band is the result of absorption by impurities in the snowpack, given that the maximum mass ratio of black carbon was found to be large at our sites when compared with typical

values in Svalbard. The large maximum mass ratio of black carbon in snow is the result of the proximity of the field sites to the Ny-Ålesund research base, and has been reported in other studies at the same location (e.g. France et al., 2011). Black carbon has the effect of reducing the reflectance for visible wavelengths, but not in the near infrared (Warren, 2013), and explains the flattened spectra for the visible range compared to the measurements by Painter and Dozier (2004). The difference between the HCRF value at nadir and at 50° viewing angle becomes smaller as the wavelength decreases from 700 nm to 500 nm, whereas the difference between Painter and Dozier's measurements (the dashed lines in Figure 2.70) remains constant over this range. The decrease in HCRF with wavelength is related to non-black carbon impurities in the snowpack, such as humic material, which is known to absorb light more strongly at shorter wavelengths (France et al., 2012). The HCRF at 50° viewing angle for wavelengths greater than 1480 nm was much larger than that recorded by Painter and Dozier (2004), which is explained by the larger solar zenith angle and the shorter radiation penetration depths at longer wavelengths, as under larger solar zenith angles there is an increased probability that a photon will exit the snowpack before it is absorbed.

2.6.4 Implications for current state-of-the-art

Accurate surface albedo measurements of the Arctic from space are needed to measure changes in the radiation budget of the Arctic and improve forecasts made by global climate models (Fox et al., 2011; Pistone, 2014). The MODIS BRDF/albedo algorithm is used to derive surface albedo (Strahler et al., 1999) and has recently been validated over the Greenland ice sheet with an RMSE of 3.3 % for the shortwave product, using only high-quality retrievals (Wright, 2014). BRDF/albedo retrieval algorithms are known to become increasingly

unreliable under large solar zenith angles (Stroeve et al., 2005; Schaaf et al., 2002), which are common to the Arctic region, especially in the spring when negative radiative forcing in the Arctic is strongest (Flanner et al., 2011). In addition, at large solar zenith angles the effects of snow surface roughness on the HCRF are greatest (Warren et al. 1998), and snow HCRF is most anisotropic (Dumont et al., 2010; Bourgeois et al, 2006; Hudson et al. 2006). Despite this, very few field measurements are available for snow at large solar zenith angles which can be used to assist in the development and validation of BRDF models for snow, ultimately improving satellite sensor retrievals at large solar zenith angles.

The systematic sampling of snow surfaces at the field sites in Svalbard in this study demonstrate the variability of the snow surfaces roughness for windblown Arctic snow, and the impact of snow surface roughness on the HCRF at large solar zenith angles. Snow surface roughness decreased the strength of the forward scattering peak and caused the HCRF to become highly asymmetric over the solar principal plane. In order to improve the accuracy of satellite derived measurements of albedo for observations acquired at large solar zenith angles, the effects of surface roughness should be fully considered in the BRDF model. Not including snow surface roughness in the BRDF model has previously been shown to result in order of magnitude errors in the retrieval of snow grain size (Kuchiki et al., 2011). In addition, the study highlights the importance of considering the sensor footprint size relative to the size of the surface roughness elements. There was considerable uncertainty in the field measurements at sites with heterogeneous surfaces, owing to the limited size of the footprint area, and the imperfect footprint overlap for different viewing angles.

2.7 Conclusion

The HCRF of Arctic snow was measured at large solar zenith angles (79° to 85°) for six sites near to the international research base in Ny-Ålesund, Svalbard in Spring 2013. The measurements were made over the viewing angles 0° to 50°, and azimuth angles 0° to 360° using the goniometric system GRASS. The HCRF measurements agreed well between sites where the snow surface was smooth and snow depth was greater than 40 cm, with a relative standard deviation of less than 10 % for backward and near nadir viewing angles. The averaged HCRF showed good symmetry with respect to the solar principal plane, and exhibited a forward scattering peak that was strongly wavelength dependent, with a greater than a factor of 2 increase in the anisotropy index over the wavelength range 400 nm to 1300 nm. The angular effects on the HCRF had minimal influence for viewing angles less than 15° in the backward viewing direction for the averaged sites, with an anisotropy index of less than 1.1 over the wavelength range 400 nm to 1300. The averaged sites agreed well with another study of snow HCRF at a different location for infrared wavelengths, but showed differences of up to 0.24 in the HCRF for the visible wavelength range, owing to light absorbing impurities in the snowpack. The mass ratio of black carbon in the top 10 cm of snow was measured at each site and was found to be in the range 90 ng g^{-1} to 299 ng g^{-1}, which was large compared to background levels for Svalbard, and was the result of the proximity of the field sites to the Ny-Alesund research base. The site with the largest roughness elements showed no forward peak and the strongest asymmetry over the solar principal plane, with differences in the mean HCRF value of up to 28 %. An improved pointing accuracy and a larger footprint area is required to reduce sampling errors related to the heterogeneous surface and to provide a

full explanation for the observed effect of macroscale surface roughness. In addition, an improved characterization of grain size in the upper surface layer is required to rule out potential effects of snow grain size in the infrared region of the spectrum. The measurements show the potential influence of snow surface roughness on the HCRF at large solar zenith angles, and highlight the importance of sampling multiple surface types to obtain measurements of HCRF that are representative at the larger spatial scale.

2.8 References

Ball, C.P., Levick, A.P., Woolliams, E.R., Green, P.D., Dury, M.R., Winkler, R., Deadman, A.J., Fox, N.P., and King, M.D., 2013, Effect of polytetrafluoroethylene (PTFE) phase transition at 19°C on the use of Spectralon as a reference standard for reflectance: Applied Optics, v. 52, p. 4806–4812.

Ball, C.P., Marks, A., Green, P.D., MacArthur, A., Maturilli, M., Fox, N.P., King, M.D. Hemispherical-Directional Reflectance (HDRF) of windblown snow-covered Arctic tundra at large solar zenith angles. IEEE Transactions on Geoscience and Remote Sensing, in press.

Bourgeois, C.S., Calanca, P., and Ohmura, A., 2006, A field study of the hemispherical directional reflectance factor and spectral albedo of dry snow: Journal of Geophysical Research, v. 111, p. D20108.

Chunnilall, C.J., Deadman, A.J., Crane, L., and Usadi, E., 2003, NPL scales for radiance factor and total diffuse reflectance: Metrologia, v. 40, p. S192–S195.

Clarke, A.D., and Noone, K.J., 1985, Soot in the Arctic snowpack: a cause for perturbations in radiative transfer: Atmospheric Environment, v. 19, p. 2045–2053.

Clarke, F.J.J., and Parry, D.J., 1985, Helmholtz Reciprocity: its validity and application to reflectometry: Lighting Research and Technology, v. 17, p. 1–11.

de Berg, M., Cheong, O., Kreveld, M., and Overmars, M., 2008, Computational Geometry: Algorithms & Applications: Springer-Verlag.

Doherty, S.J., Warren, S.G., Grenfell, T.C., Clarke, A.D., and Brandt, R.E., 2010, Light-absorbing impurities in Arctic snow: Atmospheric Chemistry and Physics, v. 10, p. 11647–11680.

Fierz, C., Armstrong, R.L., Durand, Y., Etchevers, P., Greene, E., McClung, D.M., Nishimura, K., Satyawali, P.K., Sokratov, S.A., 2009, The International classification for seasonal snow on the ground; Technical documents in Hydrology, UNESCO, v. 83 p. 1–90.

Flanner, M.G., Shell, K.M., Barlage, M., Perovich, D.K., and Tschudi, M.A., 2011, Radiative forcing and albedo feedback from the Northern Hemisphere cryosphere between 1979 and 2008: Nature Geoscience, v. 4, p. 151–155.

Forsström, S., Isaksson, E., Skeie, R.B., Ström, J., Pedersen, C.A., Hudson, S.R., Berntsen, T.K., Lihavainen, H., Godtliebsen, F., and Gerland, S., 2013, Elemental carbon measurements in European Arctic snow packs: Journal of Geophysical Research: Atmospheres, v. 118, p. 1–14.

Fox, N., Kaiser-Weiss, A., Schmutz, W., Thome, K., Young, D., Wielicki, B., Winkler, R., and Woolliams, E., 2011, Accurate radiometry from space: an essential tool for climate studies: Philosophical Transactions of the Royal

Society A: Mathematical, Physical and Engineering Sciences, v. 369, p. 4028–4063.

France, J.L., King, M.D., Lee-Taylor, J., Beine, H.J., Ianniello, A., Domine, F., and MacArthur, A., 2011, Calculations of in-snow NO 2and OH radical photochemical production and photolysis rates: A field and radiative-transfer study of the optical properties of Arctic (Ny-Ålesund, Svalbard) snow: Journal of Geophysical Research, v. 116, p. F04013.

France, J.L., reay, H.J., King, M.D., Voisin, D., Jacobi, H.W., Domine, F., Beine, H., Anastasio, C., MacArthur, A., and Lee-Taylor, J., 2012, Hydroxyl radical and NO xproduction rates, black carbon concentrations and light-absorbing impurities in snow from field measurements of light penetration and nadir reflectivity of onshore and offshore coastal Alaskan snow: Journal of Geophysical Research, v. 117, p. D00R12.

Grenfell, T.C., Doherty, S.J., Clarke, A.D., and Warren, S.G., 2011, Light absorption from particulate impurities in snow and ice determined by spectrophotometric analysis of filters: Applied Optics, v. 50, p. 2037–2048.

Grenfell, T.C., Light, B., and Sturm, M., 2002, Spatial distribution and radiative effects of soot in the snow and sea ice during the SHEBA experiment: Journal of Geophysical Research, v. 107.

Grenfell, T.C., Warren, S.G., and Mullen, P.C., 1994, Reflection of solar radiation by the Antarctic snow surface at ultraviolet, visible, and near-infrared wavelengths: Journal of Geophysical Research, v. 99, p. 18669.

Hakala, T., Riihela, A., Lahtinen, P., and Peltoniemi, J.I., 2014, Hemispherical-directional reflectance factor measurements of snow on the Greenland Ice Sheet during the Radiation, Snow Characteristics and Albedo at Summit (RASCALS) campaign: Journal of Quantitative Spectroscopy and Radiative Transfer, v. 146, p. 280–289.

Hall, D.K., Foster, J.L., and Chang, A.T.C., 1992, Reflectance of snow measured in situ and from space in sub-Arctic areas in Canada and Alaska: IEEE Transactions on Geoscience and Remote Sensing, v. 30, p. 634–637.

Hansen, J., and Nazarenko, L., 2004, Soot climate forcing via snow and ice albedos: Proceedings of the National Academy of Sciences, v. 101, p. 423–428.

Hudson, S.R., Warren, S.G., Brandt, R.E., Grenfell, T.C., and Six, D., 2006, Spectral bidirectional reflectance of Antarctic snow: Measurements and parameterization: Journal of Geophysical Research, v. 111.

Jackson, R.D., Clarke, T.R., and Susan Moran, M., 1992, Bidirectional Calibration Results for 11 Spectralon and 16 BaSO4 Reference Reflectance Panels: Remote Sensing of Environment, v. 40, p. 231–239.

Jin, Z., and Simpson, J., 2001, Anisotropic reflectance of snow observed from space over the Arctic and its effect on solar energy balance: Remote Sensing of Environment, v. 75, p. 63–75.

Kuchiki, K., Aoki, T., Niwano, M., Motoyoshi, H., and Iwabuchi, H., 2011, Effect of sastrugi on snow bidirectional reflectance and its application to MODIS data: Journal of Geophysical Research, v. 116, p. D18110.

Kuhn, M., 1985, Bidirectional reflectance of polar and alpine snow surfaces: Annals Glaciology, v. 6, p. 164–167.

Leroux, C., and Fily, M., 1998, Modeling the effect of sastrugi on snow reflectance: Journal of Geophysical Research, v. 103, p. 25779–25788.

Liu, J., Schaaf, C., Strahler, A., Jiao, Z., Shuai, Y., Zhang, Q., Roman, M., Augustine, J.A., and Dutton, E.G., 2009, Validation of Moderate Resolution Imaging Spectroradiometer (MODIS) albedo retrieval algorithm: Dependence of albedo on solar zenith angle: Journal of Geophysical Research, v. 114, p. D01106.

Lyapustin, A.I., and Privette, J.L., 1999, A new method of retrieving surface bidirectional reflectance from ground measurements: Atmospheric sensitivity study: Journal of Geophysical Research, v. 104, p. 6257–6268.

Marks, A., Fragiacomo, C., MacArthur, A., Zibordi, G., Fox, N., and King, M.D., 2015, Characterisation of the HDRF (as a proxy for BRDF) of snow surfaces at Dome C, Antarctica, for the inter-calibration and inter-comparison of satellite optical data: Remote Sensing of Environment, v. 158, p. 407–416.

Marks, A.A, 2014. Sea ice response to anthrapogenic pollution: an experiment and modeling study: PhD thesis, Royal Holloway University of London.

Miesch, C., Briottet, X., and Kerr, Y., 2002, Bidirectional reflectance of a rough anisotropic surface: International Journal of Remote Sensing, v. 23, p. 3107–3114.

Milton, E.J., Schaepman, M.E., Anderson, K., Kneubühler, M., and Fox, N., 2009, Progress in field spectroscopy: Remote Sensing of Environment, v. 113, p. S92–S109.

Morys, M., Mims, F.M., III, Hagerup, S., Anderson, S.E., Baker, A., Kia, J., and Walkup, T., 2001, Design, calibration, and performance of MICROTOPS II handheld ozone monitor and Sun photometer: Journal of Geophysical Research, v. 106, p. 14573–14582.

Nicodemus, F.E., Richmond, J.C., Hsia, J.J., Ginsberg, I.W., and Limperis, T., 1977, Geometrical considerations and nomenclature for reflectance: United States National Bureau of Standards.

Painter, T.H., 2004, Measurements of the hemispherical-directional reflectance of snow at fine spectral and angular resolution: Journal of Geophysical Research, v. 109, p. D18115.

Painter, T.H., Rittger, K., McKenzie, C., Slaughter, P., Davis, R.E., and Dozier, J., 2009, Retrieval of subpixel snow covered area, grain size, and albedo from MODIS: Remote Sensing of Environment, v. 113, p. 868–879.

Pegrum, H., Fox, N., Chapman, M., and Milton, E., 2006, Design and testing a

new instrument to measure the angular reflectance of terrestrial surfaces, IEEE Geoscience and Remote Sensing Symposium, 2006. p. 1119–1122.

Pegrum-Browning, H., Fox, N., and Milton, E., 2008, The NPL Gonio RAdiometric Spectrometer System (GRASS): Proceedings of the Remote Sensing and Photogrammetry Society Conference 2008.

Peltoniemi, J.I., Kaasalainen, S., Naranen, J., Matikainen, L., and Piironen, J., 2005, Measurement of directional and spectral signatures of light reflectance by snow: Geoscience and Remote Sensing, IEEE Transactions on, v. 43, p. 2294–2304.

Pistone, K., Eisenman I., Ramanathan V., 2014. Observational determination of albedo decrease caused by vanishing Arctic sea ice: Proceedings of the National Academy of Sciences, no. 9, p. 3322-3326.

Qu, X., and Hall, A., 2005, Surface contribution to planetary albedo variability in cryosphere regions: Journal of Climate, v. 18, p. 5239–5252.

Reay, H.J., 2013, Optical properties of snow and sea-ice a field and modelling study: PhD Thesis, Royal Holloway University of London, p. 1–427.

Sandmeier, S., Müller, C., Hosgood, B., and Andreoli, G., 1998, Sensitivity analysis and quality assessment of laboratory BRDF data: Remote Sensing of Environment, v. 64, p. 176–191.

Schaaf, C.B., Gao, F., Strahler, A.H., Lucht, W., Li, X., Tsang, T., Strugnell, N.C., Zhang, X., Jin, Y., Muller, J.P., Lewis, P., Barnsley, M., Hobson, P., Disney, M., et al., 2002, First operational BRDF, albedo nadir reflectance products from MODIS: Remote Sensing of Environment, v. 83, p. 135–148.

Schaepman-Strub, G., Schaepman, M.E., Painter, T.H., Dangel, S., and Martonchik, J.V., 2006, Reflectance quantities in optical remote sensing—definitions and case studies: Remote Sensing of Environment, v. 103, p. 27–42.

Strahler, A.H., and Muller, J., 1999, MODIS BRDF/albedo product: Algorithm theoretical basis document version 5.0: MODIS BRDF, p. 1–53.

Stroeve, J., Box, J.E., Gao, F., Liang, S., Nolin, A., and Schaaf, C., 2005, Accuracy assessment of the MODIS 16-day albedo product for snow: Comparisons with Greenland in situ measurements: Remote Sensing of Environment, v. 94, p. 46–60.

Warren, S.G., 2013, Can black carbon in snow be detected by remote sensing?: Journal of Geophysical Research: Atmospheres, v. 118, p. 779–786.

Warren, S.G., 1982, Optical properties of snow: Reviews of Geophysics, v. 20, p. 67–89.

Warren, S.G., Brandt, R.E., and Hinton, P., 1998, Effect of surface roughness on bidirectional reflectance of Antarctic snow: Journal of geophysical research, v. 103, p. 25.

Williams, D.C., 1999, Establishment of absolute diffuse reflectance scales using the NPL Reference Reflectometer: Analytica Chimica Acta, v. 380, p. 165–172.

Wiscombe, W.J., and Warren, S.G., 1980, A Model for the Spectral Albedo of Snow. I: Pure Snow: Journal of the Atmospheric Sciences, v. 37, p. 2712–2733.

Wright, P., Bergin, M., Dibb, J., Lefer, B., Domine, F. Carman, T., Carmagnola, C., Dumont, M., Courville, Z., Schaaf, C., Wang, Z., 2014, Comparing MODIS daily snow albedo to spectral albedo field measurements in central Greenland: Remote Sensing of Environment, v. 140, p. 118-129.

Chapter 3

Bidirectional reflectance of laboratory-generated sea ice

3.1 Abstract

Knowledge of the spectrally resolved bidirectional reflectance of sea ice is required in order to derive the albedo of sea ice from satellite sensor measurements of radiance. Radiative-transfer models, such as PlanarRad, can be used to convert measured radiance in a particular direction to albedo, but the accuracy of the derived albedo depends on the accuracy of the radiative-transfer model itself. The study presented here characterizes the bidirectional reflectance, or the biconical reflectance factor (CCRF), of laboratory-generated sea ice over the wavelength range 400 nm to 740 nm, for viewing zenith angles 0° to 60° at 15° intervals, and for viewing azimuth angles 0° to 360° at 30° intervals. Two acquisitions of the CCRF of laboratory-generated sea ice were carried out for ice with different thicknesses: M1, which had a thickness of 23 cm and M2, which had a thickness of 28 cm. The CCRF of the laboratory

generated sea ice had a strong forward scattering peak, which was greatest in the specular direction of 60° viewing zenith angle, and increased up to a maximum reflectance factor of 1.63 at 510 nm. The reflectance factors over the hemisphere had an anisotropy that was strongly wavelength dependent, with a maximum anisotropy index (ANIX) of 4.9 at 730 nm. The reflectance factors were relatively constant for viewing angles in the backward direction and for viewing angles less than 15° in the forward direction over the wavelength range 400 nm to 740 nm. The relative change in reflectance owing to a 5 cm increase in sea ice thickness was around 4 % for wavelengths between 450 nm and 690 nm, but the reflectance decreased by up to 3.2 % for wavelengths greater than 690 nm, owing to increased absorption of light at longer wavelengths. The wavelength dependence of the reflectance of sea ice was dominated by the absorption coefficient of sea ice, but the reflectance at the lower boundary (the bottom of the sea ice tank) was shown to influence the reflectance at the surface. The measured CCRF for the M1 and M2 measurements were compared with the results from the radiative-transfer model, PlanarRad. The radiative-transfer model was able to reproduce the general shape and the wavelength dependence of the bidirectional reflectance over the hemisphere, with differences in the reflectance factors between the modeled and measured results of typically less than 0.05, and with a coefficient of variation of the root-mean-square deviation (RMSE) of less than 9 % over all wavelengths, for both the M1 and M2 CCRF acquisitions. The surface roughness elements were not fully characterized during individual M1 and M2 CCRF acquisitions, and as a result the surface roughness parameters in the model was adjusted within a realistic range to obtain a fit between the measured and modeled reflectance factors. All other model input parameters apart from the ice thickness and the sea ice absorption coefficient were held constant for both CCRF acquisitions. A

HULIS absorber had to be added to the modeled bidirectional reflectance for the M2 acquisition, in order to obtain a fit within the measured uncertainty for wavelengths below 490 nm, owing to the growth of algae in the batch of seawater used for the M2 CCRF acquisition.

3.2 Aims of the study

The aim of this study was to characterize the bidirectional reflectance of laboratory-generated sea ice; in order to test the agreement between the laboratory-measured bidirectional reflectance and the bidirectional reflectance calculated using the radiative-transfer model, PlanarRad. Demonstrating that PlanarRad can reproduce laboratory sea ice bidirectional reflectance will enable the model to be used in a predictive capacity. The study aims to: (1) grow sea ice in the laboratory that is representative of first year Arctic sea ice; (2) design and construct a goniometer and spectrometer system and conduct measurements of radiance reflected from the sea ice for multiple viewing angles; and (3) obtain physical properties of the sea ice including ice thickness, temperature with depth, and surface roughness, in order to model the observed bidirectional reflectance. The overarching aim of this study was to compare the laboratory results to those calculated using the radiative-transfer model.

3.3 Introduction

Arctic sea ice cover extends seasonally up to 15 million km^2 (Rees, 2006), which is approximately 4 % of the sea surface area globally, although there is considerable inter-annual variability (Walsh and Chapman, 2001). The interaction of solar radiation with sea ice is important in studies of the Earth's energy budget, as sea ice, and especially snow-covered sea ice, is strongly reflective of incident shortwave solar radiation (Grenfell et al., 1994; Perovich,

1996; Wiscombe and Warren, 1980). Flanner et al. (2011) estimated the mean annual radiative forcing of Arctic sea ice on the Earth's energy budget at the top of the atmosphere as -1.2 W m^{-2}, which is about 40 % of the total mean annual cryospheric radiative forcing (Flanner et al., 2007).

In winter, prior to the melt season, Arctic sea ice is usually covered by a few tens of centimeters of snow (Weeks, 2010), and its albedo is primarily a function of the optical properties of the snow (Perovich, 2002). However, the underlying sea ice strongly influences the albedo of Arctic sea ice during the summer melt season (Perovich, 1999) and during the autumn freeze-up, before snow accumulates on the ice (Perovich and Polashenski, 2012). In addition, despite accounting for a relatively small percentage of ice cover, thin, bare ice transmits large amounts of energy to the ocean (Maykut, 1978). With the lengthening of the summer melt season (Markus et al., 2009), and the increasing proportion of first-year sea ice in the Arctic (Maslanik et al., 2011; Comiso, 2012), the reflectance of bare sea ice is becoming an increasingly important term in energy budget calculations of the Arctic upper ocean. In addition, despite the presence of snow cover in winter, the albedo of snow-covered sea ice is influenced by the underlying ice at ultraviolet and visible wavelengths, owing to the deep penetration of light through the snowpack (Marks and King, 2013; Warren, 2013).

Sea ice is a translucent medium, and on the microscopic scale it exhibits a complex internal structure of air bubbles, brine channels and precipitated salts in a matrix of frozen water (Perovich, 2003). The interface between air and ice is not usually an idealized planar boundary, but rather an irregular surface, caused by the formation of ice clumps or frost flowers of varying scales (Perovich and

Richter Menge, 1994; Martin et al., 1995). As a result, the angular distribution of radiation reflected by sea ice is neither purely specular nor diffuse, but rather a combination of specular and Lambertian-like features, the extent to which is dependent on the physical and optical properties of the ice. The empirical characterization of the angular distribution of light reflected from sea ice is critical for: (a) the interpretation of satellite sensor radiances that are measured at discrete angles over a limited number of spectral bands (Lindsay and Rothrock, 1994; Zhonghai Jin and Simpson, 2000); and (b) as a boundary condition in Arctic upper ocean and atmospheric radiative-transfer models.

The quantity that describes the angular distribution of reflected radiation as a function of incidence and viewing angle is the Bidirectional Reflectance Distribution Function (BRDF) (Nicodemus et al., 1977). The BRDF is a ratio of infinitesimal quantities but it can be approximated closely by field measurements of the Hemispherical Conical Reflectance Factor (HCRF), or laboratory measurements of the biconical (Conical-Conical) Reflectance Factor (CCRF) (Schaepman-Strub et al., 2006). There has been considerable effort to characterize the bidirectional reflectance distribution function (BRDF) of snow in the field (Kuhn, 1985; Hall et al., 1992; Aoki and Aoki, 2000; Li and Zhou, 2004; Painter, 2004; Peltoniemi et al., 2005; Hudson et al., 2006) and in the laboratory (Dumont et al., 2010), but very few studies have attempted to characterize the BRDF of sea ice (Perovich, 1994; Schlosser, 1988; Arnold et al., 2002), particularly at high spectral resolution for a full range of viewing and illumination angles.

In this study, a methodology was developed to characterize the BRDF of first year sea ice generated in the laboratory. Sea ice was generated in a 2000L tank

and stored in a cold room at a temperature of –15 °C. Artificial seawater (Tropic Marine) was heated from below and cooled from above in order to simulate ocean conditions. Measurements of the CCRF of sea ice were taken for a wavelength range of 400 nm to 740 nm, for viewing angles 0° to 60° at 15° intervals, and azimuth angles 0° to 360° at 30° intervals. A specially designed goniometer – the Sea Ice Laboratory Goniometer (SILG) – was used to undertake the multi-angular measurements of radiance for two different ice thicknesses. The laboratory measurements were compared with the BRDF calculated using the plane-parallel radiative-transfer model, PlanarRad (Hedley, 2008), using input parameters derived from the physical properties of the sea ice where possible.

3.4 Methodology

The methodology is divided in 3 main sections describing: (1) the generation of laboratory sea ice using the Royal Holloway Sea Ice Simulator; (2) a description of the sea ice laboratory goniometer and the artificial illumination source; and (3) sensitivity testing of the plane-parallel radiative-transfer model PlanarRad.

3.4.1 Sea ice simulator

Measurements of CCRF were made on sea ice generated using the sea ice simulator at Royal Holloway University of London. Professor Martin King originally developed the sea ice simulator at Royal Holloway. It was Marks (2014) that assisted in the development of a prototype simulator, and the design and construction of a second-generation tank, which she used to investigate the effect of black carbon on albedo and light penetration in sea ice. An overview of the design and the relevant details of the simulator are provided in this section,

a detailed description of the design and initial testing of the prototype apparatus is given by Marks (2014).

3.4.1.1 Cold store

A Daikin cold store shown in Figure 3.1 was used to simulate polar temperatures. The container had stainless steel walls, aluminum flooring and ceiling. The internal dimensions are 12.0 m in length, 2.6 m in height and 2.3 m in width. Air temperature inside the container can be regulated to –25 °C through a vapor compression cycle. Refrigerant fluid evaporates while circulated in coils at the rear wall of the container, resulting in cooling of the air inside the container. The vapor is then compressed and condensed outside of the unit, causing the release of latent heat from the system. A pressure release valve then lowers the boiling point of the refrigerant fluid causing it to evaporate as it circulates back through the evaporating coils inside the container.

Figure 3.1. Daiken cold store used to simulate polar temperatures

A fan that blows cold air along ridges at the base of the container circulates the air inside. The temperature of the return air is monitored and a processor activates the compressor once the temperature drops 1 °C below the setpoint. The refrigeration system results in a small degree of instability in the air temperature inside the container near to the ice tank, as shown in Figure 3.2.

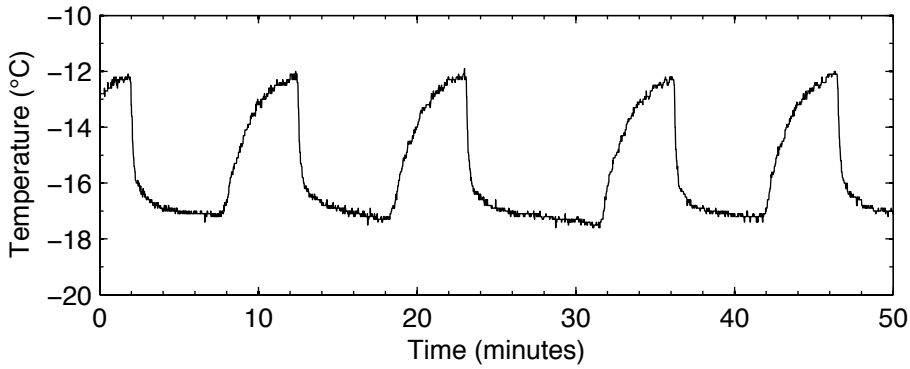

Figure 3.2. Air temperature measured inside the cold store near to the sea ice tank. The average temperature over the 50 minute period was –15.5 °C

The average temperature in Figure 3.2 was –15.5°C, the maximum temperature was –11.9 °C, and the minimum was –17.6 °C, implying an instability in the air temperature near to ice tank of approximately ± 3 °C, which wasn't considered sufficient to disrupt ice growth. Owing to the presence of heat produced by components in the container an average air temperature of ~ –15 °C at the ice tank was obtained with a setpoint on the containers computer of –18 °C.

3.4.1.2 Sea ice tank

Sea ice was grown in a polyethylene cylindrical tank, which was 1.3 m tall and had a diameter of 1.4 m. A cylindrical design was chosen to avoid stress concentration on the tank walls, and reduce the risk of rupturing the tank during ice growth. The tank was held within a custom-made 'Unistrut' frame, which provided additional structural support and held in place multiple layers of neoprene and expanded foam insulation. The sea ice tank and objects within the tank were chosen to be plastic to avoid corrosion and were white or translucent in order to give a diffuse reflection at the boundaries of the tank.

In order to simulate realistic ocean conditions the simulated seawater inside the tank needed to be heated from below and cooled from above (Weeks, 2010). To

achieve these conditions and prevent water freezing at the base of the tank, the temperature of the seawater at the bottom of the tank was regulated at around –1 °C using a chiller/heater unit and a closed loop network of pipes (Figure 3.3 photo [a]). A NESLAB Merlin M150 chiller unit was used to pump a 50:50 mix of glycol and water through the closed loop system, the chiller unit is shown in Figure 3.3 in the bottom right of photo [c].

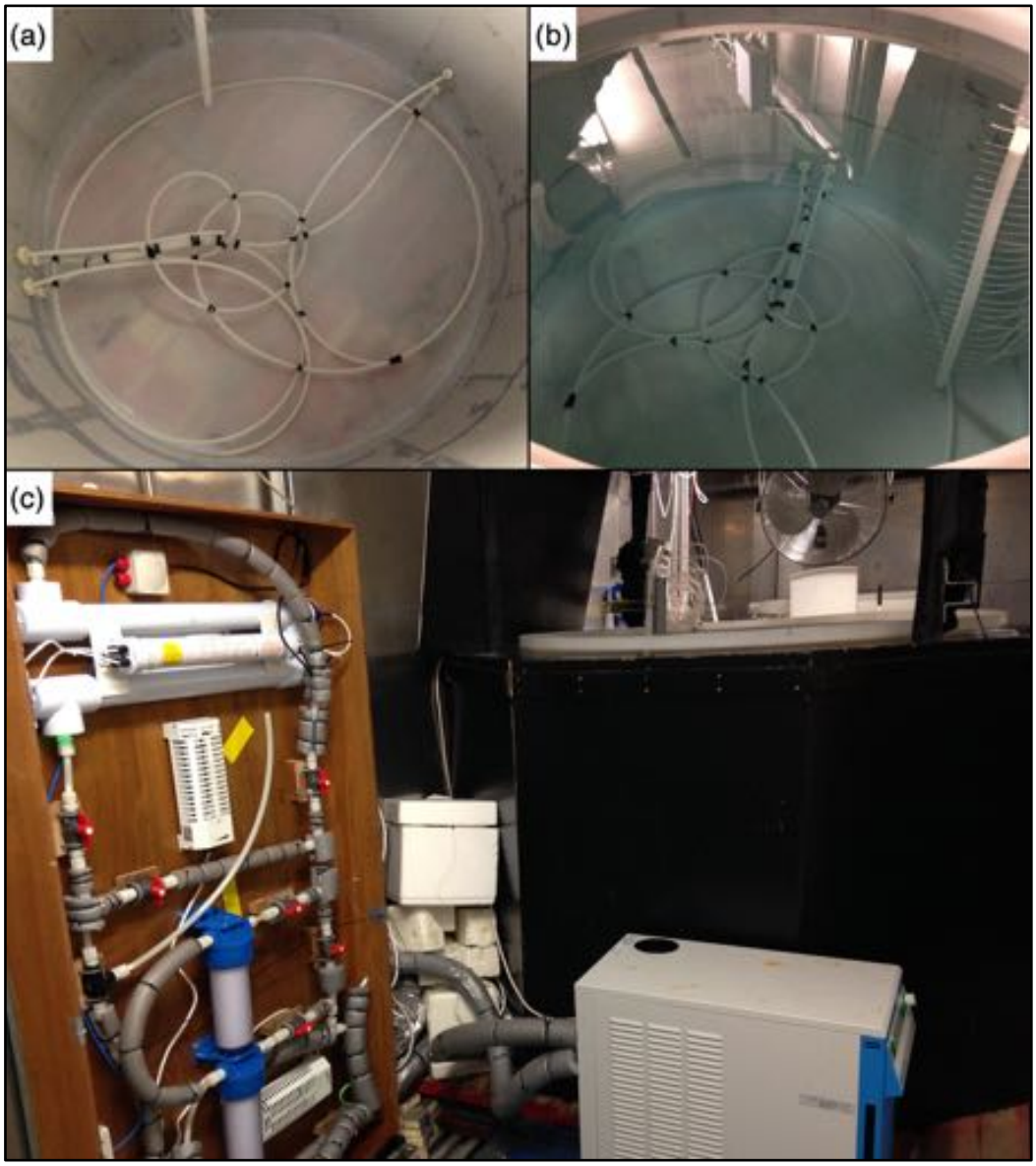

Figure 3.3. Sea ice simulator and the components used to circulate and filter the seawater. External enclosure is in the left of photo [c] and the chiller unit is in the bottom right of photo [c]

In addition, the sides and bottom edges of the tank were well insulated. The innermost layer of insulation was a 1 cm thick layer of black neoprene, which was held flush against the outside of the tank. Followed by a 10 cm air gap, followed by a 5 cm layer of polystyrene insulation, which was held flush against an outer shell of plywood. Gaps between the plywood boards were filled with silicon sealant to reduce airflow through the layers of insulation. The tank was positioned on top of wooden pallets filled with foam insulation to raise the tank well above the aluminum floor of the container. The neoprene layer, polystyrene insulation and plywood shell surrounding the ice tank are presented in Figure 3.4.

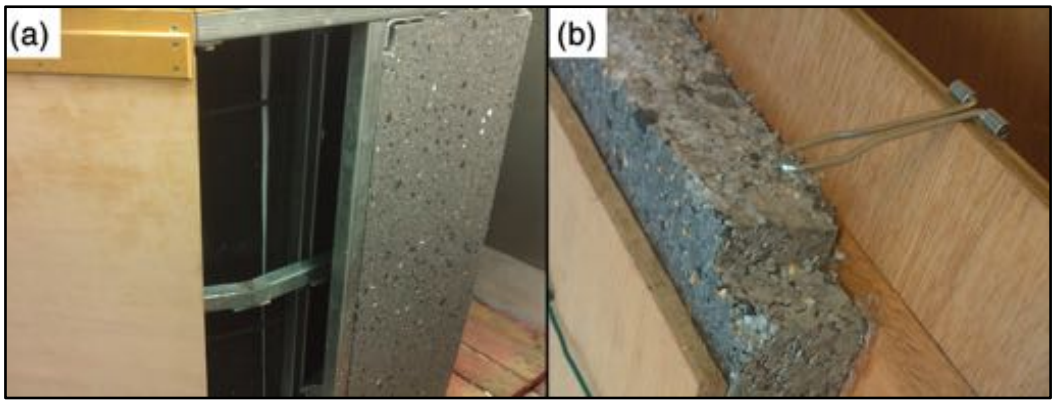

Figure 3.4. Insulation surrounding the ice tank. Neoprene inner layer (center of photo [a]), polystyrene insulation (right of photo [a]; and middle of photo [b]); and plywood shell (left of photo [a]; and right of photo [b])

The seawater in the ice tank was continuously circulated through a network of pipes housed within a separate external enclosure (left of photo [c] in Figure 3.3) to prevent the temperature stratification of the seawater. An Iwaki MD-40RZ magnetic drive pump was used to circulate seawater from the tank around the enclosure at a flow rate of ~ 10 L min^{-1}. In addition, the enclosure housed a 10 μm particulate filter, a 5 μm particulate filter and a UV sterilizer that was used to removed contaminants and limit algae growth in the seawater solution. Taps in the enclosure could be turned on or off in order to direct seawater through the

filtration equipment. During the CCRF measurements seawater was not directed via the filters, but was directed back to the tank from the pump in the external enclosure. The enclosure was insulated with an outer layer of expanded foam ('Celotex') as shown in photo [c] in Figure 3.5. Air temperature inside the enclosure was kept above zero using two thermostatically controlled 200W 'frost' heaters. The individual transfer pipes were insulated with foam and the temperature of the seawater in the transfer pipes was kept above freezing temperature using heat trace cable as shown in photo [d] in Figure 3.5.

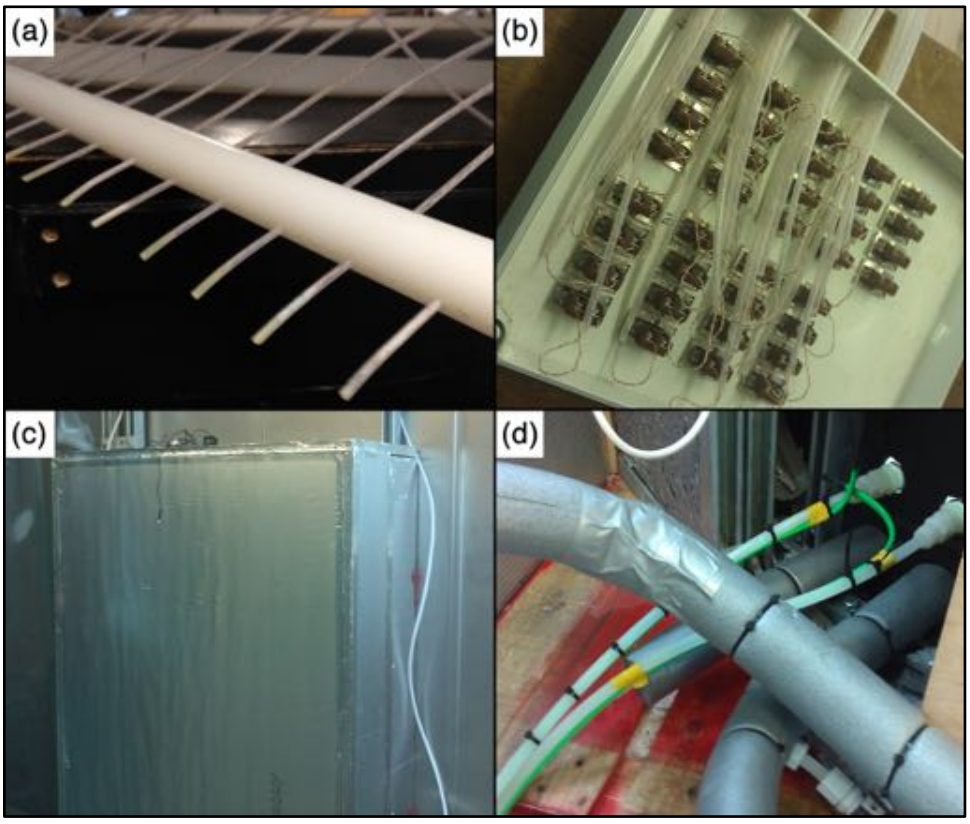

Figure 3.5. Thermocouples attached to nylon rod [a] and connected to a thermocouple switch box [b]. External enclosure insulated in 'Celotex' [c] and transfer pipes with heat trace cables insulated in foam [d]

To monitor the temperature profile in the ice tank 30 type T thermocouples were held at regularly spaced depth intervals of 4 cm along a 1.5 m long nylon rod shown in photo [a] in Figure 3.5. The bottom thermocouple was 12.5 cm from the base of the tank and is shown in situ in photo [b] in Figure 3.3 on the right

side of the photograph. Each thermocouple was wired to a thermocouple switch box (photo [b] in Figure 3.5). The thermocouple switch box was connected to a 4-channel thermocouple datalogger and a laptop PC, which were stored in an insulated box. The laptop PC was connected via a remote desktop connection to a computer outside of the cold store so that readings could be taken without removing the datalogger from the temperature controlled box, ensuring that the cold junction remained in its recommended operating temperature range above 0 °C. Temperature profiles of the sea ice were measured by manually connecting a single channel from the thermocouple datalogger to each socket on the switch box with a thermocouple transfer cable. A reading from the datalogger at each depth was recorded using a PC outside the cold store via a remote desktop connection.

3.4.1.3 Cleaning the sea ice tank

Prior to generating the sea ice, the tank and the circulatory system were cleaned with 4 L of domestic thin bleach that was free from fragrance and detergent, and which was diluted with 50 L of tap water. The solution was flushed through the system with fresh tap water over a 4-hour time period. The tank was emptied and rinsed 5 times by filling the tank with 30 L of fresh tap water and draining the tank completely. A lid was fitted over the tank when the simulator was not in use to prevent contamination by airborne particles. Domestic thin bleach (NaClO) was chosen as the disinfectant as it is decays to water, sodium and chloride ions, so any residue that remained after rinsing did not affect sea ice growth.

3.4.1.4 Ocean water

Ocean water was simulated by mixing the medical grade synthetic sea salt 'Tropic Marine' with tapwater. It was not possible to use distilled water owing to the quantity of seawater required. Atkinson and Bingman (1997) analyzed 35 chemical parameters in a solution of 'Tropic Marine' sea salt and found major cations and anions of the solution to be within 10 % of that for seawater. Marks (2014) showed that there was a negligible difference in the salinity of solutions made with pure water, or with tap water. In addition, Tropic Marine contains no nitrates or phosphates, which may otherwise encourage growth of algae in the seawater solution. Approximately 68 kg of 'Tropic Marine' sea salt was required to produce a solution with salinity representative of Arctic ocean salinity, which has an average salinity of around 31 to 32 practical salinity units (PSU) (Boyer et al., 2013). The synthetic sea salt was added to approximately 2000 L of tap water and was stirred until dissolved. The resulting salinity was measured using a Fisher Scientific seawater refractometer as 31 PSU.

3.4.1.5 Estimating ice thickness

Temperature-depth profiles of the ice tank were taken during sea ice growth. Ice thickness was estimated by plotting the temperature profile and finding the depth at which the sea ice transitioned to seawater. The transition point was characterized by a straightening of the temperature curve with depth as illustrated in Figure 3.6. The ice thickness derived from the temperature measurements agreed well with ice thickness measurements made by drilling through the ice.

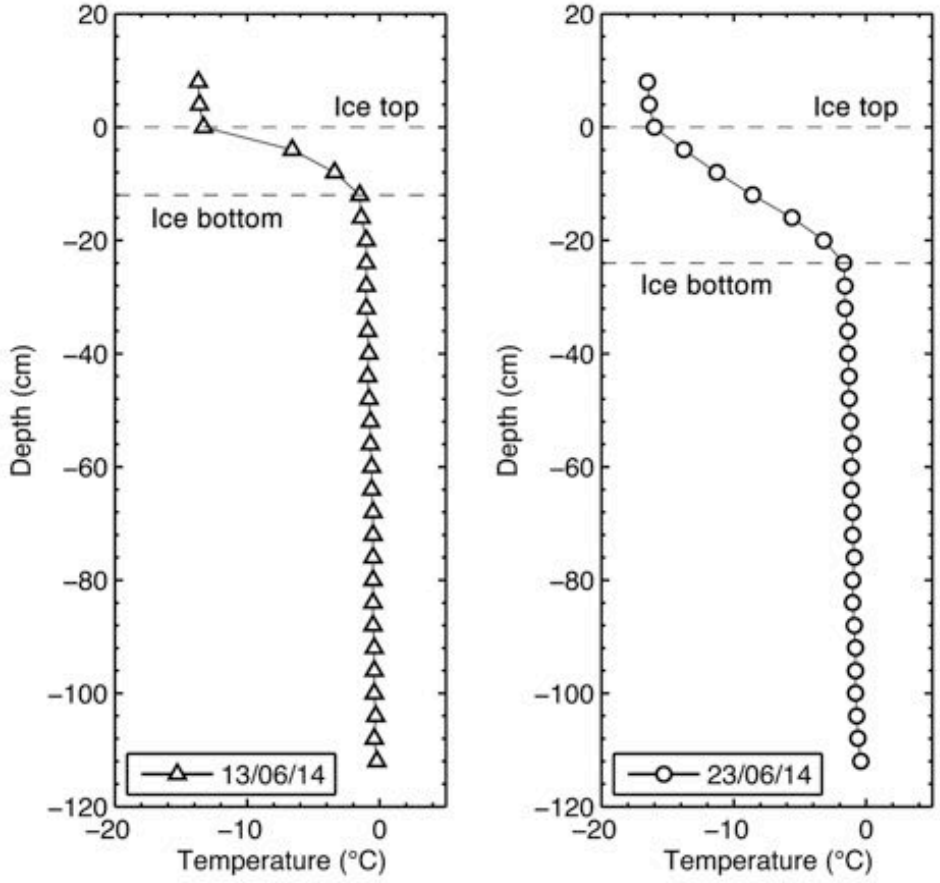

Figure 3.6. Temperature profiles of laboratory generated sea ice with different thicknesses

The uncertainty in the ice thickness measurements was ± 4 cm because of the spacing of the thermocouples along the thermocouple rod was 4 cm.

3.4.1.6 Sea ice surface roughness

During sea ice growth, brine rejection and the clumping of ice crystals caused small-scale (up to ~ 4 mm peak to peak height) roughness elements to develop on the surface of the ice, as shown in Figure 3.7.

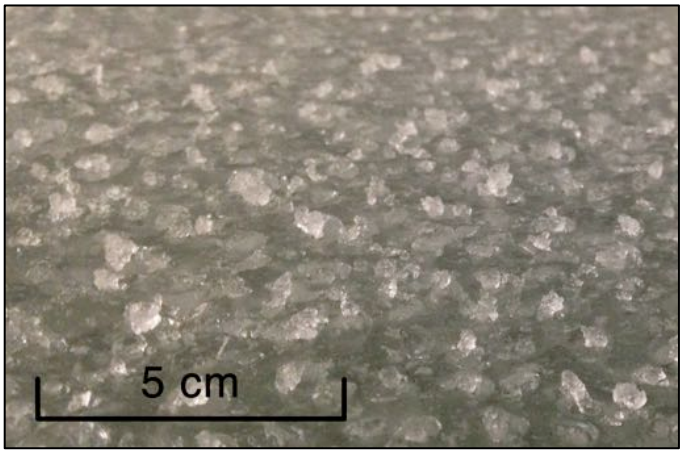

Figure 3.7 Surface roughness elements caused by brine rejection and clumping of ice crystals on the sea ice surface

The development of ice protrusions on first year sea ice has been observed in previous studies and they are thought to serve as nucleation sites for the development of frost flowers (Perovich and Richter Menge, 1994; Martin et al., 1995). To represent the surface roughness elements in the BRDF radiative transfer model, a Monte Carlo ray-tracing method was applied following an approach given by Mobley (1994), which is introduced in Section 3.4.4.1.2.

3.4.2 Sea ice laboratory goniometer

The Sea Ice Laboratory Goniometer (SILG) was specifically designed to measure the CCRF of laboratory sea ice generated with the Royal Holloway sea ice simulator. Goniometers are instruments that measure angles, many such instruments have been designed to characterize the BRDF in the field (Schopfer et al., 2008; Painter et al., 2003; Bourgeois et al., 2006b; Pegrum et al., 2006) and in the laboratory (Dangel et al., 2003; Brissaud et al., 2004). This section provides details of the SILG goniometer used for the CCRF experiments presented in this study.

3.4.2.1 Goniometer specifications

The diameter of the goniometer's base ring was 77 cm, which was the largest possible size that allowed for full movement of the goniometer arm when positioned on the ice surface. The base ring was constructed from steel and had 8 PTFE feet with adjustable extension of up to 3 cm allowing leveling of the goniometer on an uneven ice surface. A small carriage was designed to carry the aluminium arm of the goniometer full circumference around the base ring, allowing the carriage to be manually positioned at any azimuth angle relative to the target surface in the centre of the base ring. Wheels connected to the base of the carriage operated a set of gears that measured the azimuthal position of the carriage by distance travelled around the base ring, and digital readout was given. The arm of the goniometer was made from two straight sections of aluminium fixed at right angles and supported by an aluminium brace as shown in Figure 3.8. The vertical section of the arm was fixed to a cylinder, which was attached to the underside of the carriage. The cylinder was held within a mechanism that allowed the cylinder and aluminium arm to pivot through ± 80° in the plane perpendicular to the target surface. The pivot mechanism included a clamp that is operated manually and enables the arm to be fixed at a chosen zenith angle. An electronic tilt sensor was fixed to the to the top of the vertical arm which gave a digital readout of the current zenith angle to ± 0.1°. The horizontal section of the goniometer's arm extended to the centre point of the goniometer's base ring where a mounting bracket for the foreoptic and laser pointer was located. The foreoptic was positioned exactly over the centre of the goniometer's base ring to ensure adequate pointing accuracy. Distance between foreoptic and sea ice surface was measured as 48 cm prior to the CCRF

experiments. The goniometer was covered in matt black neoprene skin where possible to reduce the effects of stray reflectance.

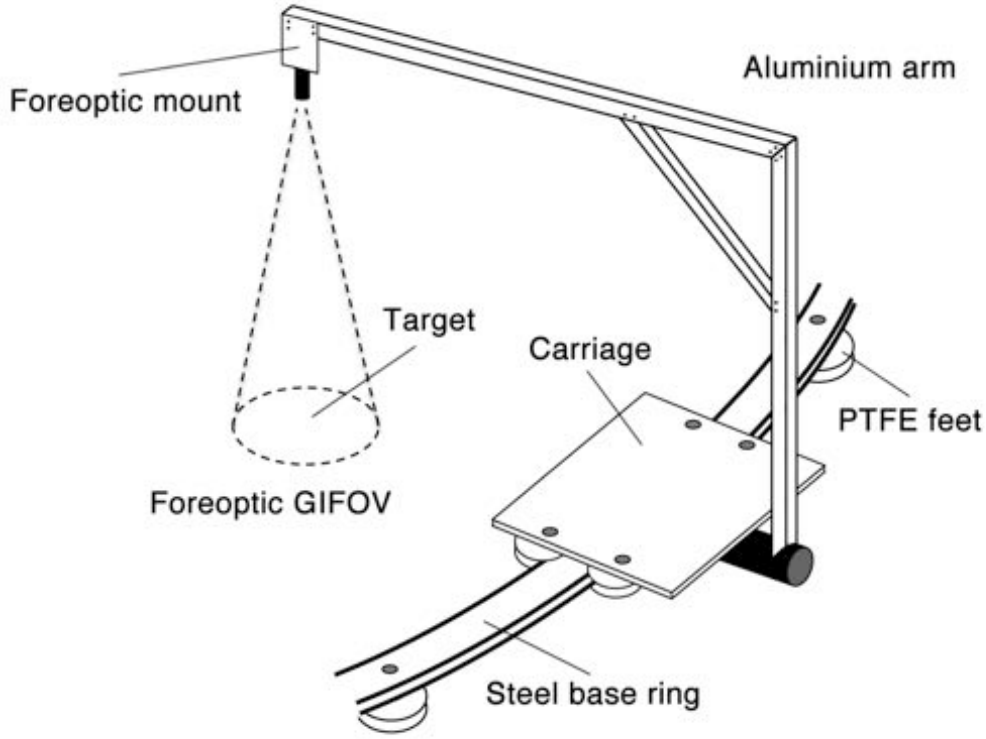

Figure 3.8. Schematic of the sea ice laboratory goniometer (SILG) used to obtain CCRF measurements. The carriage can be rotated to obtain any viewing azimuth angle in the horizontal plane, while the aluminum arm can be rotated to obtain zenith angles 0° to ± 80°. The arm is held in position by a clamp mechanism on the carriage (not shown)

A straight arm design was chosen primarily for easier construction and lower cost, but a straight arm design also offers the following advantages over an arc shaped design: (1) shadowing effects are reduced when taking measurements in the backward direction in the solar principal plane; and (2) the straight arms provide a rigid frame making it easier to obtain a better pointing accuracy.

3.4.2.2 Spectrometer

The foreoptic mounted on the goniometer's arm was connected to an UV-VIS Ocean Optics USB2000+ spectrometer via fibre optic cable. The spectrometer had a 2048-element CCD-array detector, with a spectral resolution of 0.34 nm

(full width at half maximum), and a spectral range of 180 nm to 880 nm. A wavelength calibration was performed for the spectrometer using a mercury-argon 'Pen-Ray' lamp. A correction for dark current was made by subtracting the average signal between 200 nm to 250 nm from the total signal at each wavelength interval for each measurement. There was no light in the laboratory in the wavelength range 200 nm to 250 nm. The spectrometer was mounted on the arm of the goniometer during the CCRF acquisition and connected to a Panasonic Toughbook laptop via a USB connection. A photograph of the goniometer on the sea ice is given in Figure 3.9.

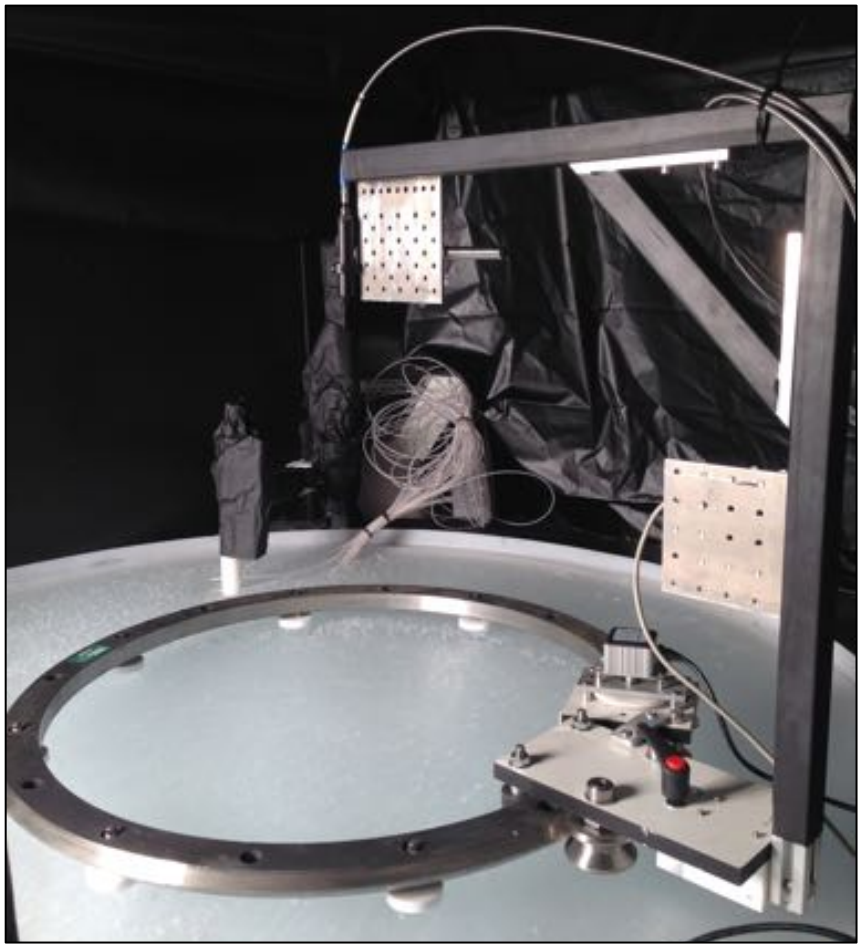

Figure 3.9. Photograph of the sea ice laboratory goniometer (SILG) used to measure the CCRF of simulated sea ice

3.4.2.3 Sensor ground field of view and pointing accuracy

To ensure that the foreoptic pointed directly towards the centre of the base ring a laser pointer was temporarily inserted into the foreoptic mount. With the goniometer's arm at the nadir viewing position the laser pointer illuminated a spot near to the centre of the base ring as shown in Figure 3.10. The illuminated spot was traced on a white piece of paper while the carriage was rotated through 360° of azimuth. The procedure was repeated and the mount was translated until the illuminated spot moved within a circle of less than 2 cm diameter. Thus the goniometer had a pointing accuracy at the nadir viewing position of approximately ± 2 cm.

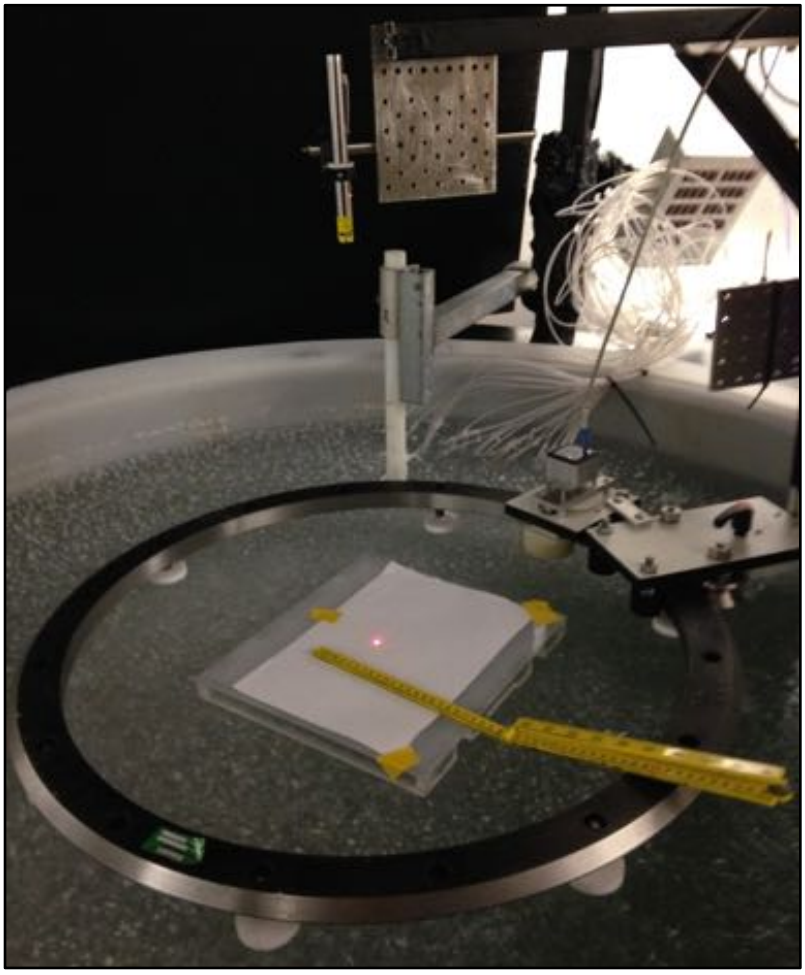

Figure 3.10. The foreoptic mount was aligned to the centre of the base ring of the goniometer by replacing foreotpic with a laser pointer

The goniometer's foreoptic had a full angle Field Of View (FOV) of 8°, which corresponded to a footprint diameter at nadir of approximately 7 cm. For zenith angles greater than 0° the shape of footprint was not circular, but was quasi-elliptical. As the foreoptic was rotated through the zenith arc the shape of the footprint becomes more elongated. The footprint area, or Ground Instantaneous Field Of View (GIFOV), can with calculated with knowledge of the sensors FOV and the distance from the sensor to the surface. The GIFOVs for zenith angles 0° to 75° were calculated for an FOV of 8° and a distance between the sensor and the surface of 48 cm, the footprints and associated areas are presented in Figure 3.11.

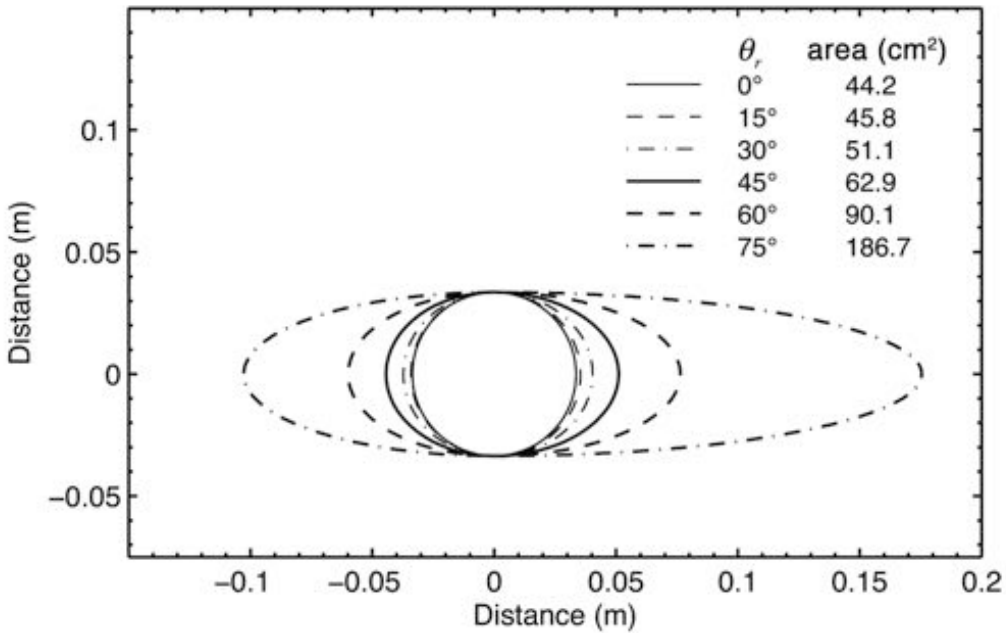

Figure 3.11. Foreoptic GIFOV with viewing zenith angle

The pivot point of the goniometer was approximately 3 cm from the ice surface during the CCRF measurements. As a consequence, the pointing accuracy of the goniometer decreased by up to 11 cm for viewing zenith angles at 75°. The offset in the x-coordinate in the GIFOV was calculated as a function of viewing zenith angle as follows:

$$|x_1 - x_2| = \beta \tan(\theta_r) \quad \text{Eq. 3.1}$$

where $|x_1 - x_2|$ is the offset in the x coordinate, θ_r is the viewing zenith angle, and β is the of the distance between the pivot and the ice surface.

Owing to the imperfect footprint overlap, a circle centred on the goniometer's centre point with a diameter of 62 cm characterized the maximum area sampled. All measurements taken with a viewing angle less than, or equal to 60°, were within a circular area with a diameter of 30 cm. The poor pointing accuracy at large viewing angles was considered acceptable because: (1) the footprint area remained within the goniometer base ring for all viewing angles; (2) the sea ice was considered homogenous over the area sampled; and (3) a correction was applied to account for heterogeneity in the intensity of the lamp footprint over the sampling area, as described in Section 3.4.2.8. The assumption of homogeneity over the sensors footprint was considered valid given the size of the footprint area relative to the size of the sea ice roughness elements, brine inclusions and air bubbles.

3.4.2.4 Spectralon reference panel

A Spectralon panel, which approximates a lossless Lambertian reflector (Sandmeier et al., 1998), was used as a reference standard for reflectance during the CCRF measurements. For each measurement of radiance reflected by sea ice, a measurement of radiance reflected into the nadir viewing direction by the Spectralon panel was taken quasi-simultaneously (less than 60 seconds) under identical illumination conditions. The panel was mounted on a Perspex stand that had 3 adjustable feet in order to avoid disturbing the ice surface while taking a reference measurement. To correct for the inherent non-lossless and

non-Lambertian properties of the reference panel, a calibration was performed at the National Physical Laboratory (NPL) using the technique described in Chapter 2 Section 3.4.3. The calibration yielded a series of reflectance correction factors R_{cf} for incidence angles 0° to 80° over a wavelength range of 409 nm to 1001 nm. The correction factors are presented as a function of incidence angle at 600 nm in Figure 3.12.

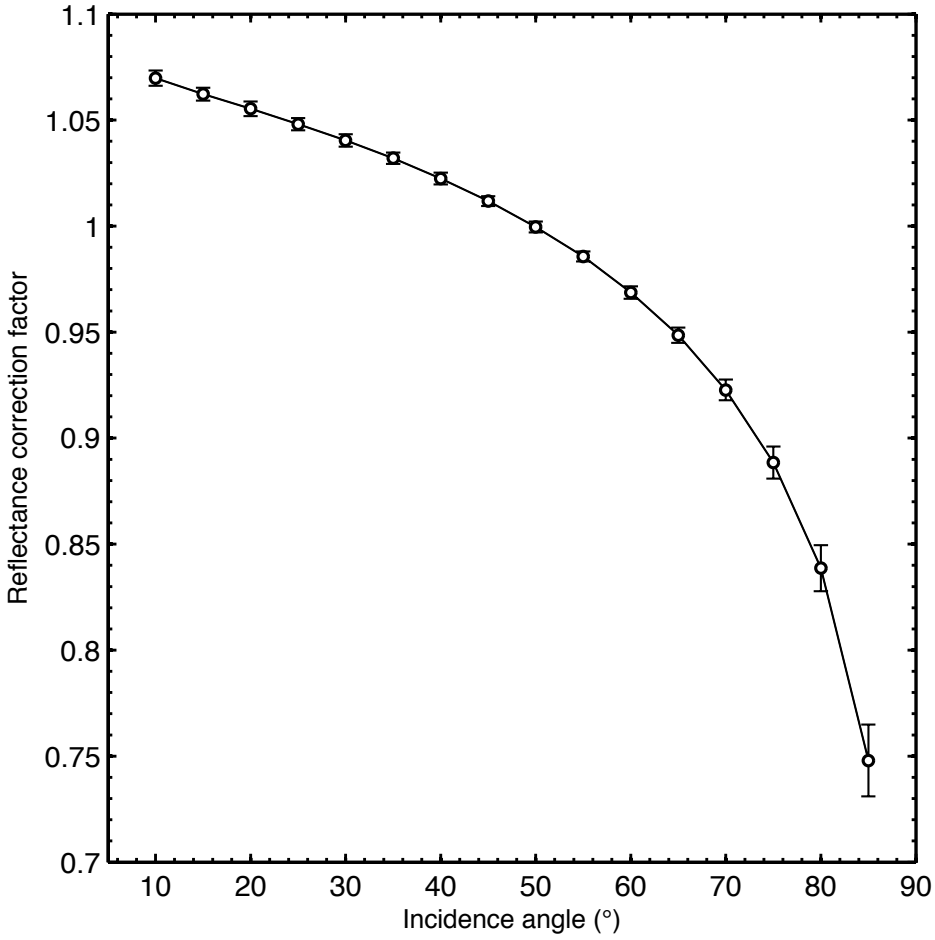

Figure 3.12. Reflectance correction factors at 600 nm as a function of incidence angle for the Spectralon reference standard

CCRF measurements where performed under an illumination incidence angle of 60°, which corresponds with a reflectance correction factor of 0.969 ±

0.003. Reflectance correction factors are given as a function of wavelength for an incident angle of 60° in Figure 3.13.

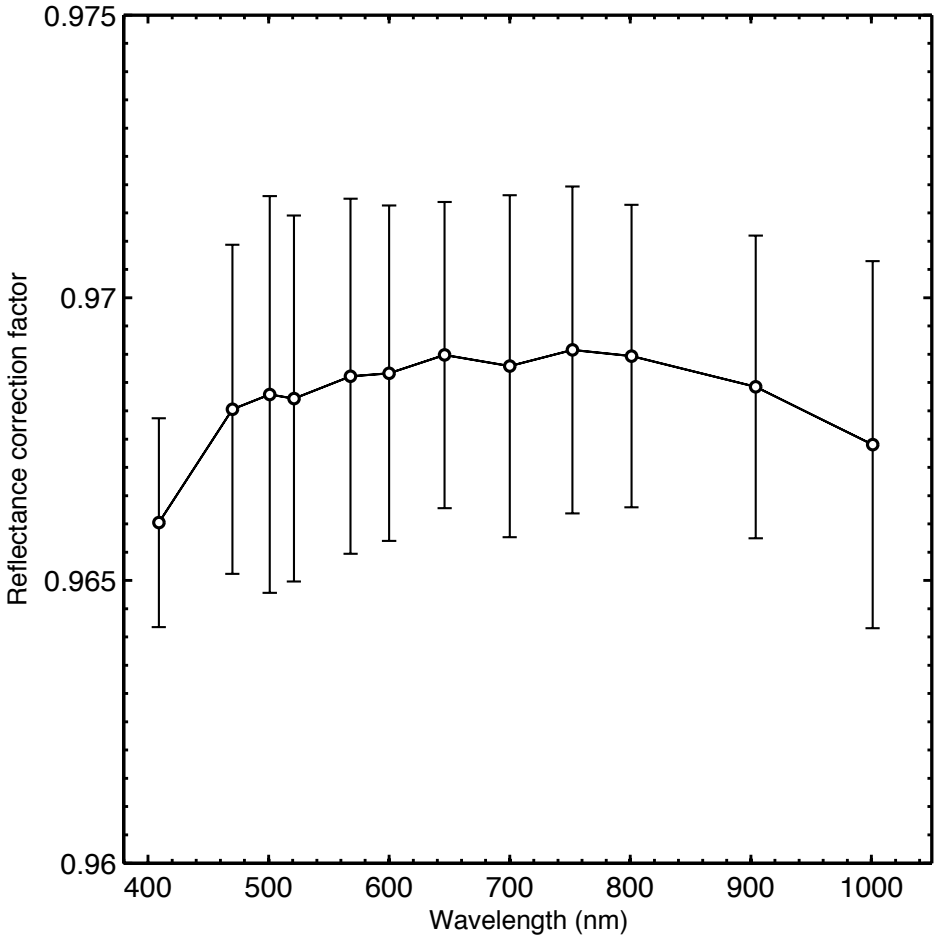

Figure 3.13. Reflectance correction factors as a function of wavelength for an incidence angle of 60° for the Spectralon reference standard

There was no wavelength dependence detectable above the level of uncertainty for the Spectralon reflectance correction factors. As such, a broadband correction factor of 0.97 was applied to all measurements.

3.4.2.5 Light source

Accurate characterization of the BRDF requires a light source that is well collimated and subtends a small solid angle (as viewed from the target surface) (Schaepman-Strub et al., 2006). In addition, irradiance from the light source

should be homogenous over the target surface sampled (Dangel et al., 2003; Sandmeier et al., 1998). These conditions are rarely fully satisfied for laboratory experiments without collimating mirrors or lenses (Sandmeier and Strahler, 2000), especially for experiments that require large amounts of optical power over a large area. A large illuminated area was required because the absorption coefficient of sea ice is weak, and multiple scattering causes incident light to travel a relatively long distance in the medium before it is absorbed, meaning that light incident from outside the foreoptic footprint may contribute to the reflected flux inside the foreoptic footprint. In order to achieve a relatively homogenous irradiance over a large sampling area an array of six 500W tungsten halogen lamps were used at the expense of confining the irradiance to a narrow beam. The lamps were mounted on a reinforced plywood board in 3 banks of 3 covering an area of 55.5 cm x 46.5 cm. To achieve an incidence angle of 60° the lamp mounting board was tilted 30° from the normal to sampling area surface, which results in an incidence angle of 60° as is illustrated in Figure 3.14.

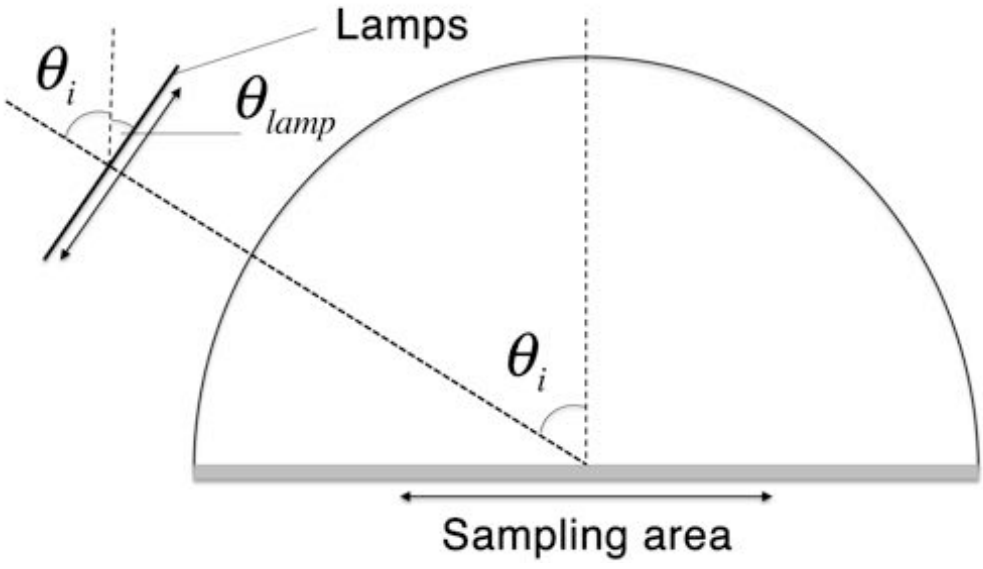

Figure 3.14. The angle of tilt of the lamp mounting board θ_{lamp} was used to calculate the incidence angle at the centre of the sampling area. The incidence angle is given by $\theta_i = 90 - \theta_{lamp}$

Once the mounting board was set to the correct amount of tilt the centre point of the lamp array was aligned with the centre point of the sampling area using a laser pointer attached to base the lamp mounting board. The height of the lamp array was adjusted until the illuminated spot matched the correct position on the ice surface, taking into account the offset of the laser pointer mounting position from the centre point on the lamp array. Once the lamps were set up with the correct incidence angle the distance between the lamp array centre point and the sampling area centre point was measured as 140 cm. A photograph of the laser pointer attached to the base of the lamp mounting board is shown in Figure 3.15.

Figure 3.15. Laser pointer attached to the base of the lamp mounting board

3.4.2.6 Light collimator

In order to improve the collimation of incident light a set of baffles were designed to reduce the divergence of the incident beam. A sheet of aluminium

honeycomb mesh was held within an aluminium frame 71 cm wide and 61 cm tall. The holes within the honeycomb structure had a diameter of 0.64 cm and the thickness of the mesh was 2 cm. In total, two sheets of aluminium mesh were constructed and a mounting bracket was fitted to the front of the lamp array. The mounting bracket was large enough for both aluminum sheets to be used simultaneously. In order to estimate the effectiveness of the baffles the beam divergence θ_{div} was approximated using the relationship given in Figure 3.16 and Eq. 3.2.

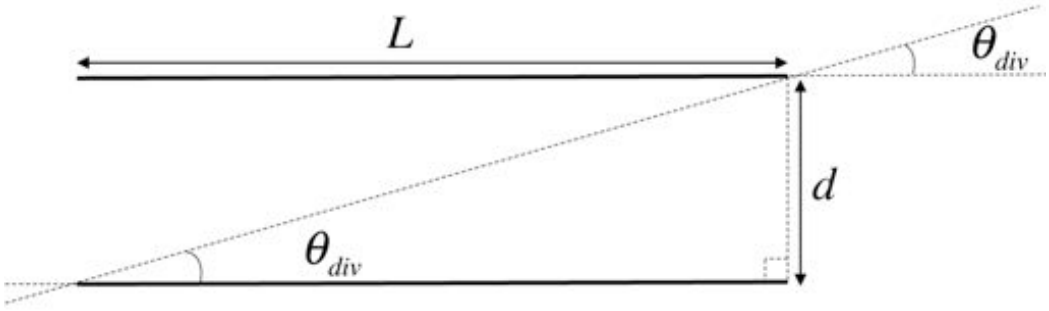

Figure 3.16. Method used to calculate divergence of light exiting the beam collimator

The beam divergence is given by:

$$\theta_{div} = \tan^{-1}(d / L) \qquad \text{Eq. 3.2}$$

where θ_{div} is the beam divergence exiting the collimator, d is the maximum diameter of the collimators holes and L is the length of the holes. The beam divergence for a mesh with a hole diameter of 0.64 cm and a thickness of 2 cm was 17.7°. A photograph of the aluminium mesh is given in Figure 3.17.

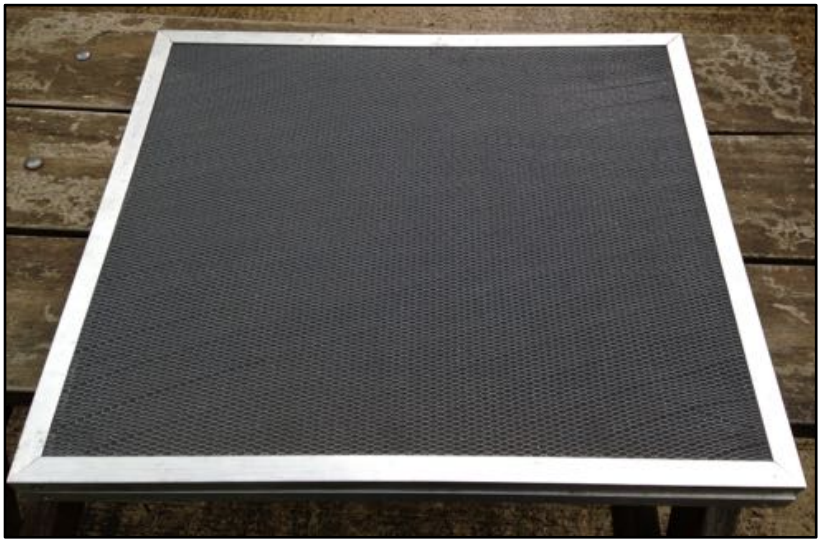

Figure 3.17. Baffle made of aluminium mesh in a honeycomb structure

A decrease in the divergence of the beam was evident when projecting a cross section of the beam onto a black wooden board. Photographs of the projected cross section are given in Figure 3.18.

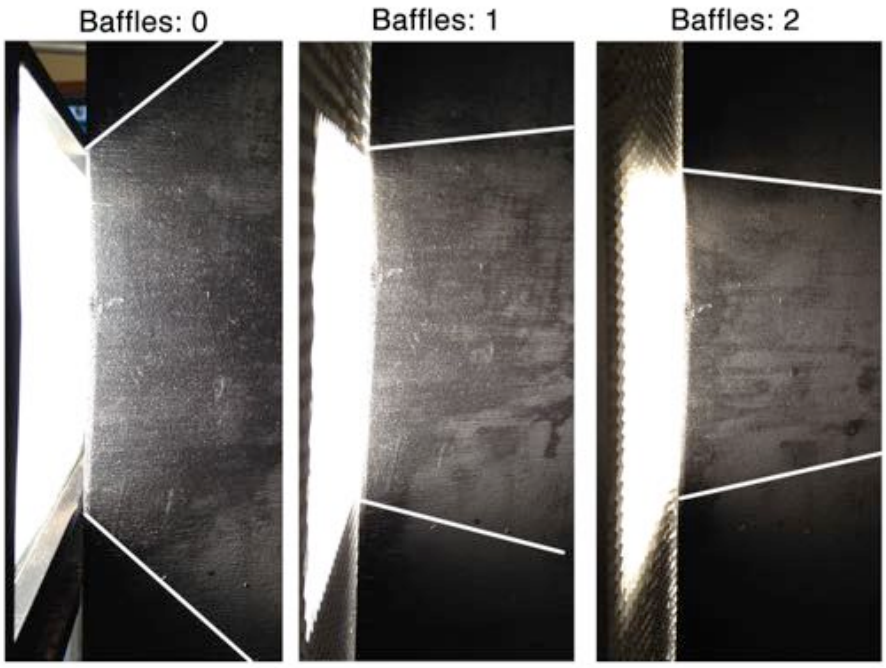

Figure 3.18. Projection of the beam cross-section with no baffles fitted (left), one baffle fitted (middle) and two baffles fitted (right). The beam cross sections have been highlighted with white bars

3.4.2.7 Characterization of the lamp footprint

Sampling different areas of the target surface is unavoidable when conducting CCRF measurements for reasons explained in Section 3.4.2.3. Given that the sampling area is not sampled equally or fully by the foreoptic for different angular configurations, irradiance over the sampling area needs to be characterized and a correction should be applied given a heterogeneous illumination footprint (Sandmeier et al., 1998). To characterize the lamp footprint the intensity of light reflected from a Spectralon panel was measured over a gridded area within the lamp footprint. The gridded area was 40 cm by 40 cm and the sampling points where positioned at 10 cm intervals in the x and y directions. A schematic of the sampling points on the grid is given in Figure 3.19.

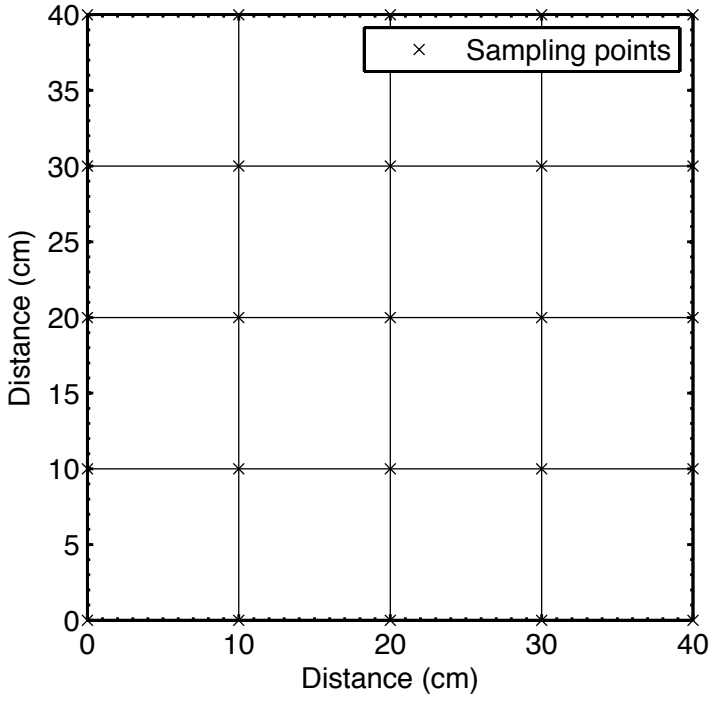

Figure 3.19. Schematic of the sampling grid used to characterize the footprint of the lamp array

The gridded area in Figure 3.19 was drawn onto a 2m by 2m plywood board and the board was leveled on a bench. The lamp array was set up following the

procedure given in Section 3.4.2.5 in order to obtain an incident angle of 60° in the centre of the grid. The arm of the goniometer was used to point the 8° FOV foreoptic (full angle) at sampling points on the grid. A Spectralon reference panel was used as the target surface and its centre was aligned to each sampling point during the measurement. The goniometer's arm was leveled manually so that the foreoptic viewed the centre of the Spectralon panel from nadir. During each measurement the foreoptic had a footprint diameter of approximately 7 cm on the surface of the Spectralon panel. The intensity of the radiation reflected by the Spectralon panel was recorded using an Ocean Optics USB2000+ spectrometer for each sampling point on the grid. The stability of the output from the lamp array was monitored simultaneously by recording the intensity of radiation reflected from another Spectralon panel positioned in the lamp footprint, and viewed by a fibre optic cable coupled to a PTFE diffuser and a second Ocean Optics USB2000+ spectrometer. The experiment was conducted outside in an open space during the night, to reduce the effect of the diffuse light and light reflected off the laboratory walls. The experiment was repeated with no baffles, one baffle, and two baffles, in order to assess the effect of the baffles on the footprint of the lamp array. A photograph of the experiment set up is given in Figure 3.20.

Figure 3.20. Experiment to characterize the footprint of the lamp array

In order to assess the reproducibility of the results, the process of characterizing the lamp array for the 3 different baffle configurations was repeated 3-times, each on a different day and for the same sampling grid. The intensities measured were averaged and normalized to average intensity recorded at the centre of the grid. Contour plots of the averaged normalized intensities and the standard deviation (1σ) of the 3 replicate measurements for each baffle configuration were produced from the respective matrices. Contour plots for each baffle configurations are given in Figure 3.21 to Figure 3.26 for a wavelength of 600 nm.

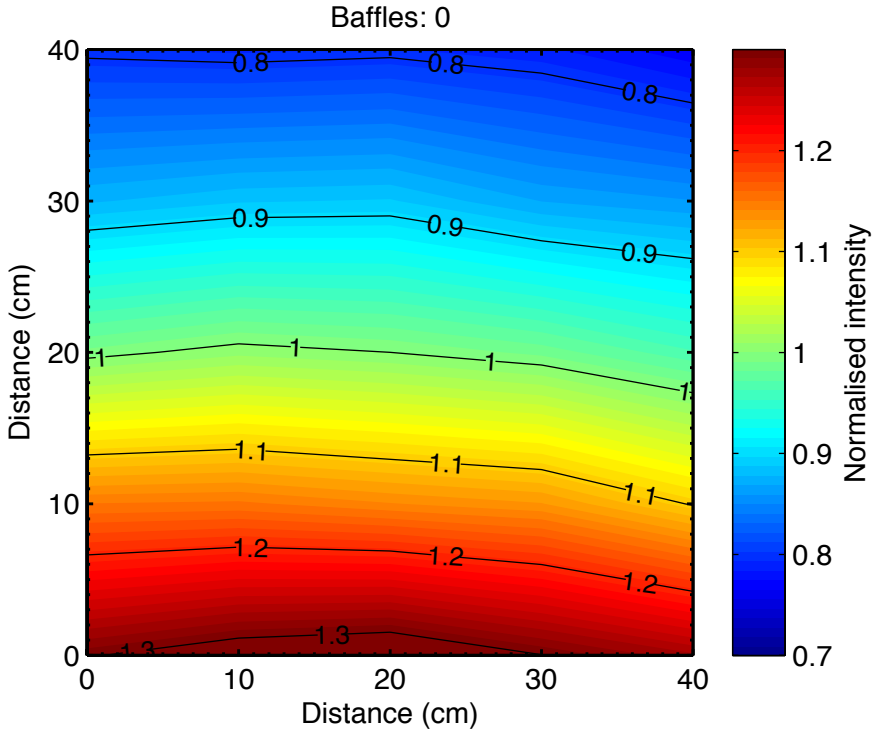

Figure 3.21. Lamp array intensity distribution with zero baffles. Intensity is normalized to the intensity measured at the centre of the grid

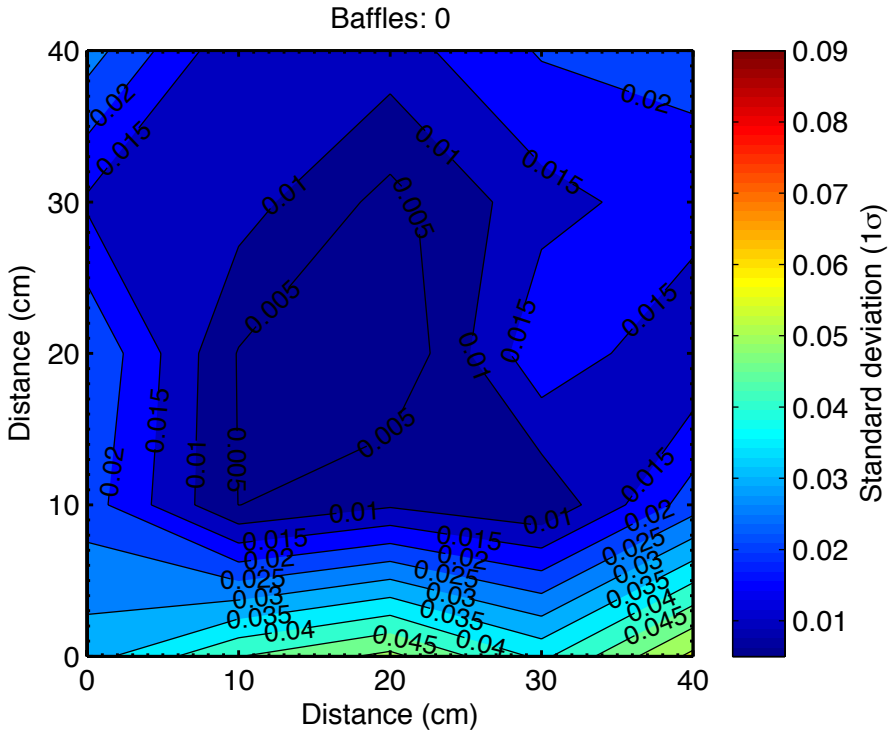

Figure 3.22. Filled contour plot of the standard deviation (1σ) of the 3 replicate measurements with zero baffles

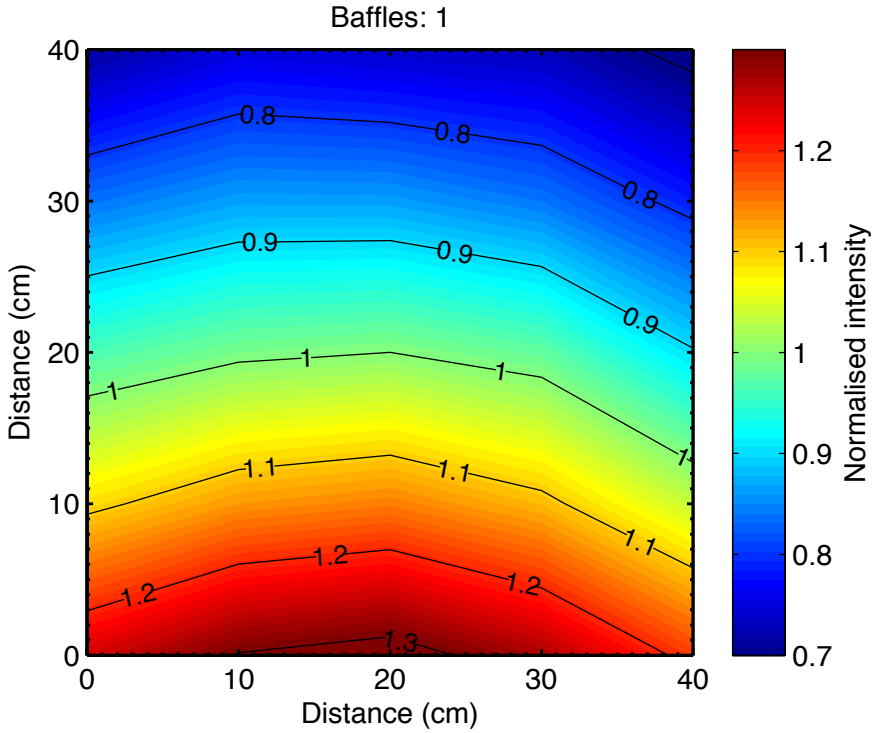

Figure 3.23. Lamp array intensity distribution with one baffle. Intensity is normalized to the intensity measured at the centre of the grid

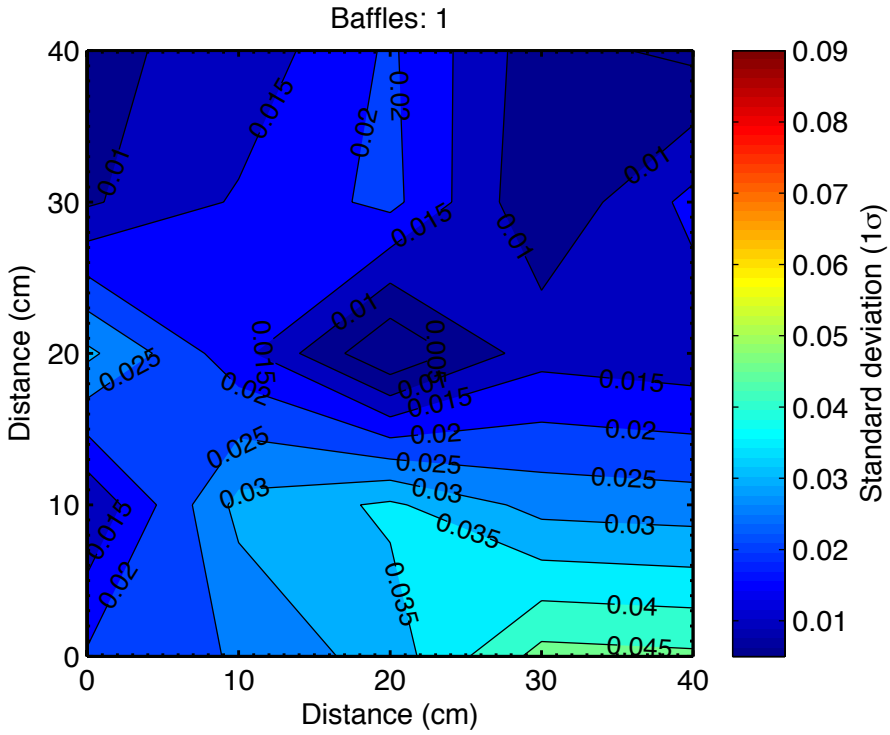

Figure 3.24. Filled contour plot of the standard deviation (1σ) of the 3 replicate measurements with one baffle

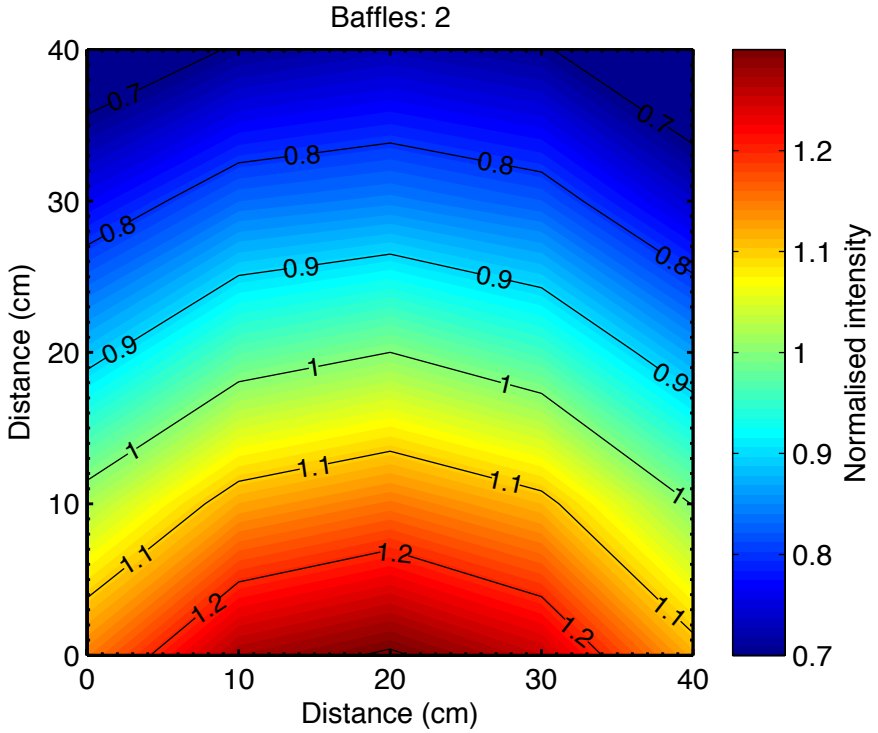

Figure 3.25. Lamp array intensity distribution with two baffles. Intensity is normalized to the intensity measured at the centre of the grid

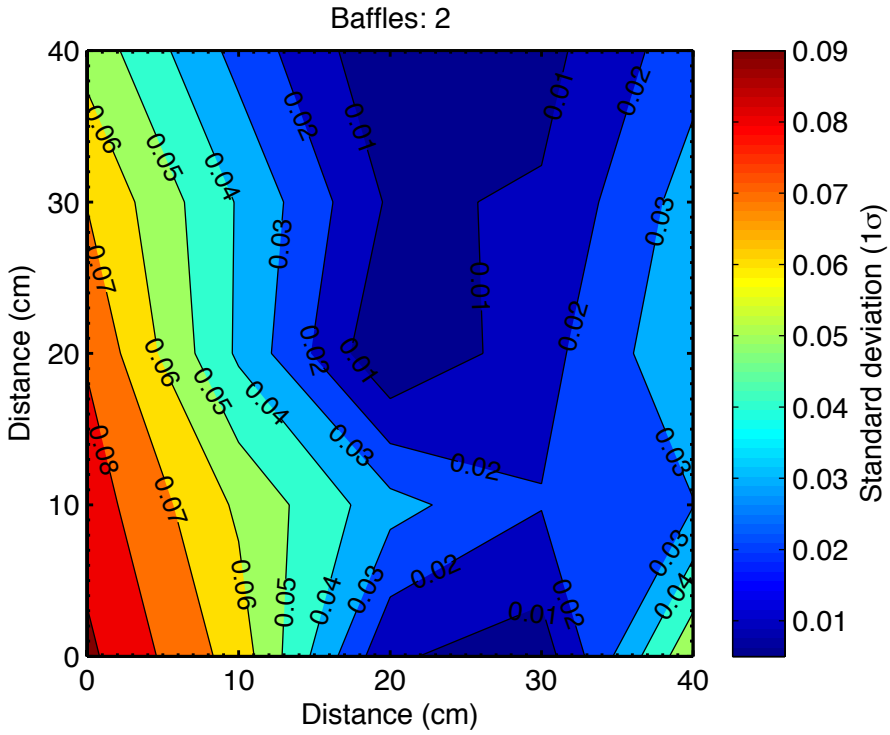

Figure 3.26. Filled contour plot of the standard deviation (1σ) of the 3 replicate measurements with two baffles

The monitored intensity of the lamp footprint during one series of measurements is presented in Figure 3.27.

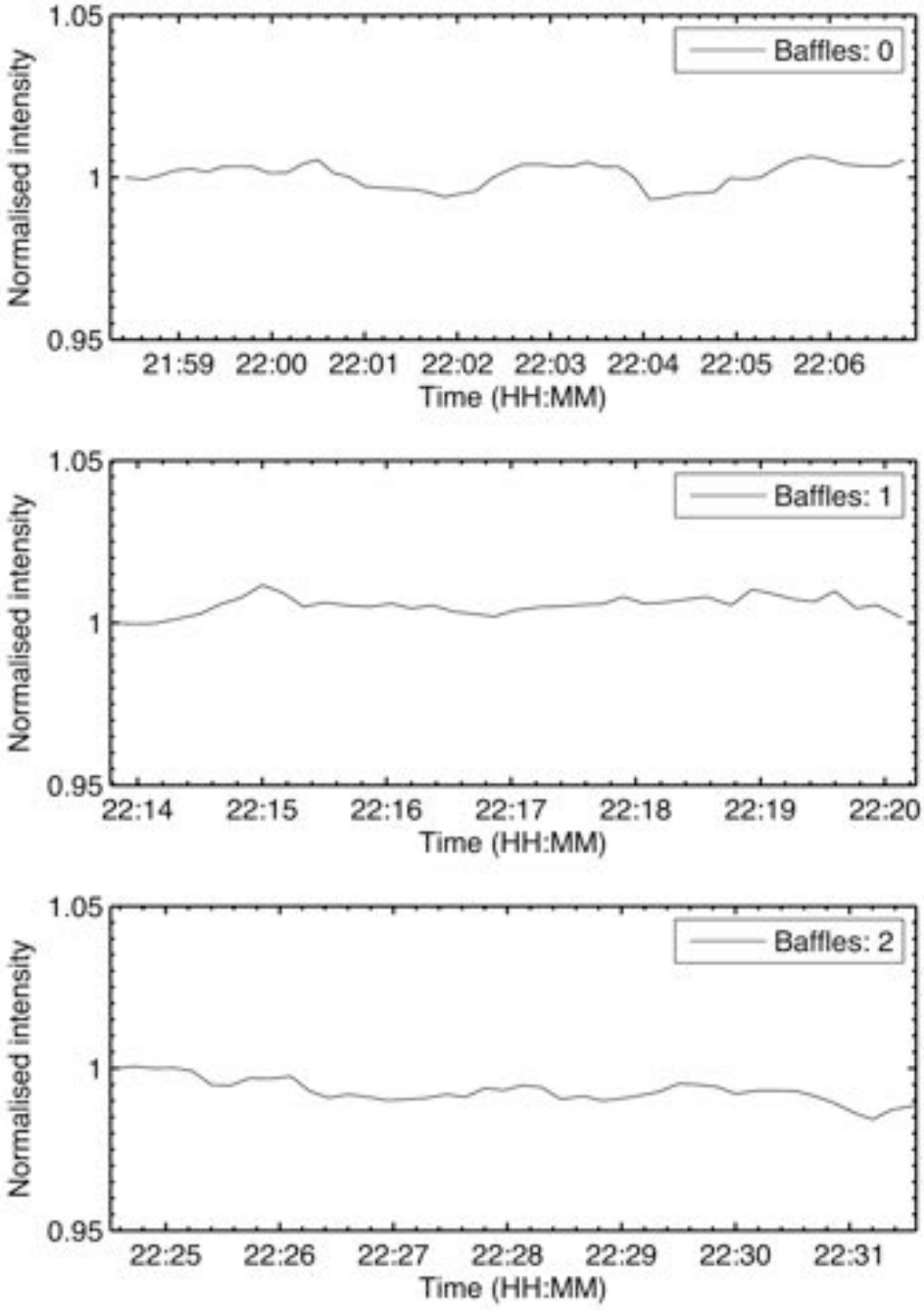

Figure 3.27. Lamp stability recorded using a separate spectrometer and Spectralon panel. Results are normalized to the intensity at the start of each experiment

The mean normalized intensity across the grid was 0.019 from unity for zero baffles and was 0.020 from unity with one baffle, but was 0.040 from unity with two baffles. Indicating that footprint uniformity was marginally more homogenous

when zero baffles were used. Using one baffle produced a much more homogenous footprint compared to using two baffles. The decrease in the uniformity of the lamp footprint when using baffles was probably the result of decreased incident light intensity and a narrowing of the incident beam. Given a narrower beam of reduced intensity the intensity of the footprint is likely to drop off faster for a given distance from the centre of the footprint compared to the configuration with no baffles, which gives a more even intensity over a larger area. In addition, the contoured plots of the standard deviation of the averaged measurement indicate that the set up with zero baffles is more easily reproduced. The average standard deviation within the gridded area was 0.02 with zero baffles, 0.02 for one baffle, and 0.04 for two baffles. The standard deviation of the points in the middle of the grid (i.e. $10 \leq x \leq 30$, $10 \leq y \leq 30$) was on average 0.008 for zero baffles, 0.0187 for one baffle and 0.0251 for two baffles. Indicating that the footprint is more reproducible in the area central to the footprint when zero baffles were used. Improved reproducibility of the footprint with zero baffles may be related to the alignment of the baffles during the set up of the lamp array, as the baffles were not in exactly the same position for each measurement. For the reasons examined above, zero baffles were used for the CCRF measurements reported in this study and a correction was made for non-uniformity of the lamp footprint, as described in Section 3.4.2.8.

3.4.2.8 Correction for non-uniformity of lamp footprint

The area of the foreoptic footprint for each viewing zenith angle (i.e. the foreoptic GIFOV) during the CCRF measurements was determined as described in Section 3.4.2.3. The calculations were performed with a FOV of 8° and the distance from the foreoptic to the ice surface of 48 cm. In order to account for the 3 cm difference in the height of the pivot point of the goniometer arm relative

to the height of the ice surface, the position of the GIFOV for each viewing zenith angle was adjusted by calculating an offset using equation Eq. 3.1. The raised position of pivot point resulted in an offset in the GIFOV of up to 11 cm for viewing zenith angles of 75°. GIFOVs were then calculated for all viewing azimuth angles by rotating the GIFOV for each viewing zenith angle about the z axis at $\pi/6$ intervals (30°). The following transformation was applied to calculate the coordinates of the rotated GIFOV:

$$x' = \cos(\alpha)x + \sin(\alpha)y \qquad \text{Eq. 3.3}$$

$$y' = -\sin(\alpha)x + \cos(\alpha)y \qquad \text{Eq. 3.4}$$

where x' and y' are the transformed coordinates and α is the angle of rotation about the z axis. Intensity distribution corrections factors were calculated for each GIFOV by linearly interpolating the lamp intensity distribution over a 400 by 400 pixel grid and overlaying the GIFOV for each viewing angle, as shown in Figure 3.28. At 75° viewing zenith angle the GIFOV was found to extend outside of the sampling grid for the lamp intensity footprint, and thus could not be included in the correction.

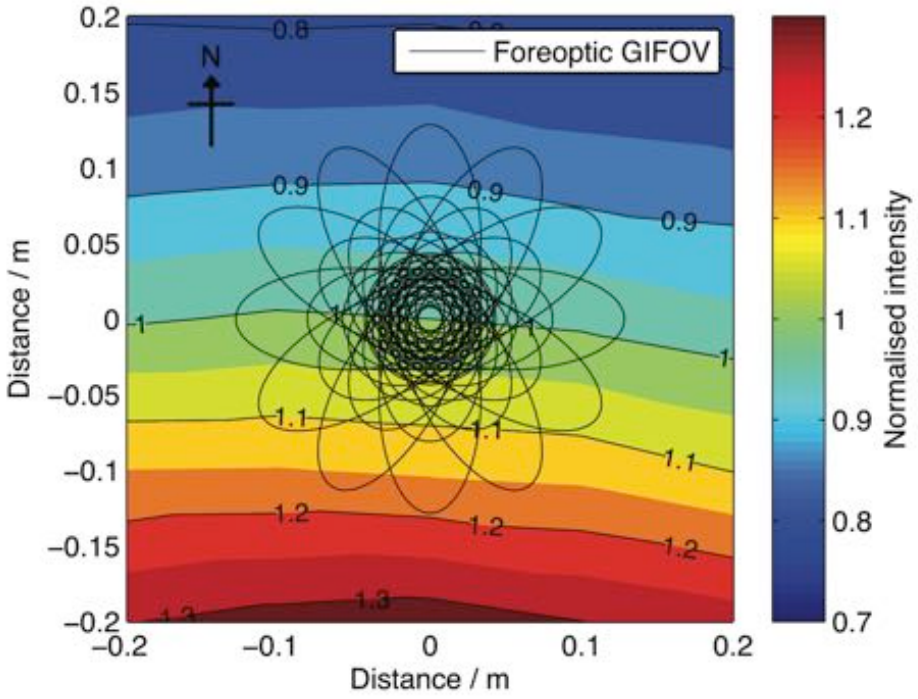

Figure 3.28. Ground instantaneous field of view (GIFOV) for each viewing angle overlying the intensity distribution of the lamp footprint. Axes give the distance form the centre of the lamp footprint, which corresponds with the centre of the goniometer's base ring. Viewing zenith angles of 75° are not plotted as these extend outside of the sampling grid for the lamp intensity footprint

An algorithm was developed to sum the intensities of all the pixels within each GIFOV; the intensity correction factors $I_{cf}(\theta_r;\phi_r)$ were calculated as follows:

$$I_{cf}(\theta_r;\phi_r) = \frac{\sum I_{\theta_r=0}}{\sum I(\theta_r;\phi_r)} \qquad \text{Eq. 3.5}$$

where $I_{\theta_r=0}$ is the normalized intensity for each pixel within the GIFOV at a zenith view angle of 0°. $I(\theta_r;\phi_r)$ is the normalized intensity for each pixel within the GIFOV at a viewing zenith angle θ_r and viewing azimuth angle ϕ_r. Intensity correction factors as a function of rotation about the z axis for a wavelength of 600 nm are plotted in Figure 3.29.

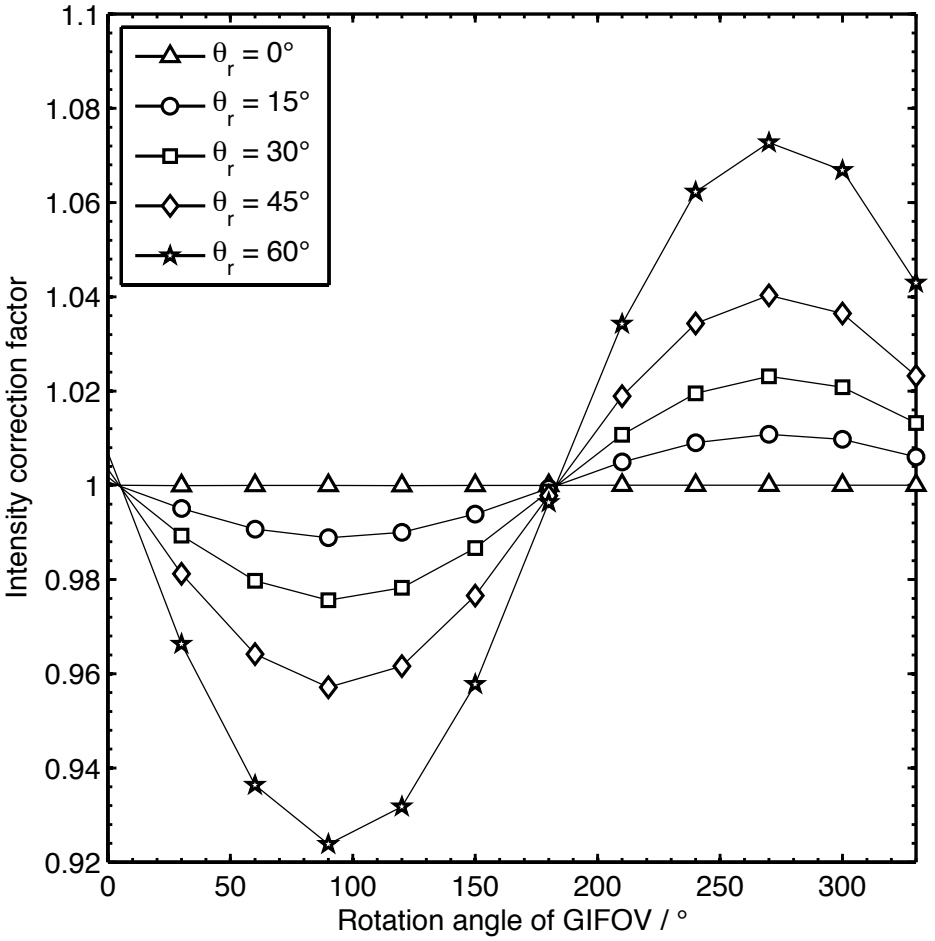

Figure 3.29. Intensity distribution correction factors with viewing angle. A rotation angle of 0° corresponds to a foreoptic viewing position from the easterly direction in Figure 3.28. A rotation angle of 90° corresponds with a foreoptic viewing position from the northerly direction in Figure 3.28.

The maximum correction factor was 1.07 at a viewing zenith angle of 60° and for a rotation of 90° in azimuth, which corresponds to the GIFOV that extends furthest in the southerly direction in Figure 3.28. The minimum correction factor was 0.92 at the viewing zenith angle of 60° and for a rotation of 270° in azimuth, which corresponds to the GIFOV that extends furthest in the northerly direction in Figure 3.28. The shape of the function observed in in Figure 3.29 is expected given the pattern of banded intensity observed in the lamp footprint. The wavelength dependence to the intensity correction factors was typically less than 2 %, so the correction factors calculated at 600 nm were applied to all

wavelengths. Correction factors were applied to the CCRF measurements at all wavelengths by multiplying the intensity recorded at each viewing angle by the respective correction factor.

3.4.2.9 Variation in source incidence angle

Owing to the relatively short distance between the lamps and the target surface each point on the target surface was illuminated from a slightly different direction. Variation in incident angle was assessed by calculating the maximum and minimum incidence angles from the centre point of the lamp array. The angles of interest are shown schematically in Figure 3.30.

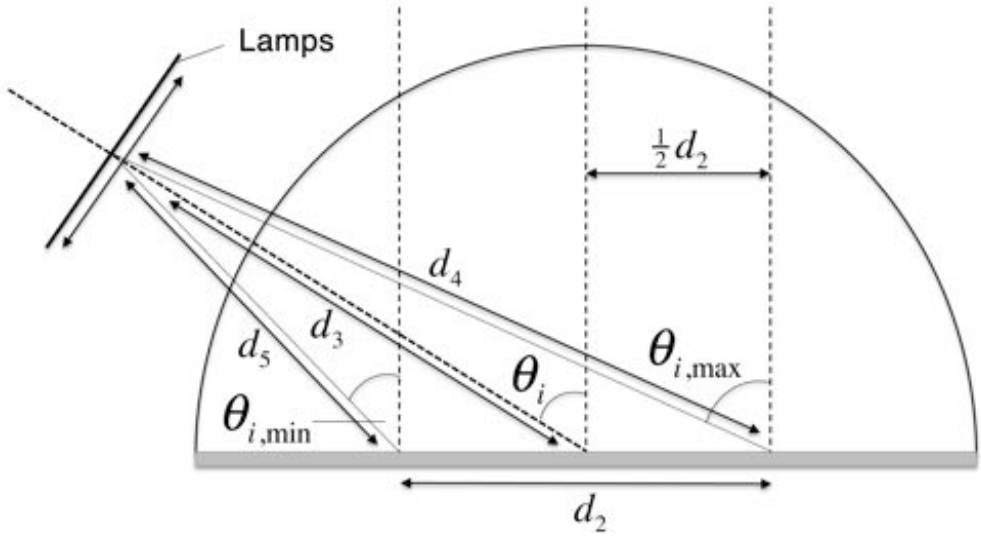

Figure 3.30. Change in incidence angle within the sampling area

The maximum sampling area d_2 was circular and had a maximum diameter of 44 cm as calculated in Section 3.4.2.3. Using the Law of Cosines lengths d_4 and d_5 can be calculated:

$$d_4 = \sqrt{{d_3}^2 + \left(\tfrac{1}{2}d_2\right)^2 - 2d_3 d_2 \cos\left(\tfrac{1}{2}\pi + \theta_i\right)} \qquad \text{Eq. 3.6}$$

$$d_5 = \sqrt{\left(\tfrac{1}{2}d_2\right)^2 + {d_3}^2 - d_2 d_3 \cos\left(\tfrac{1}{2}\pi + \theta_i\right)} \qquad \text{Eq. 3.7}$$

The minimum distance to a target point in the sampling area d_2 was 138 cm and the maximum distance d_4 was 159 cm. The minimum and maximum incident angles within d_2 were calculated as 59° and 64° respectively given the following relationships given using the Law of Sines:

$$\frac{d_4}{\sin(\theta_i + \frac{1}{2}\pi)} = \frac{d_3}{\sin(\frac{1}{2}\pi - \theta_{i\max})} \quad \text{Eq. 3.8}$$

$$\frac{d_5}{\sin(\frac{1}{2}\pi - \theta_i)} = \frac{d_3}{\sin(\frac{1}{2}\pi + \theta_{i\min})} \quad \text{Eq. 3.9}$$

So the nominal illumination angle of 60° varied between 55° and 64° owing to size of the lamp array.

3.4.2.10 Lamp array solid angle

The sampling area receives incoming light through a solid angle that is proportional to the size of the lamp array and distance from the point on the target surface, as illustrated by Figure 3.31.

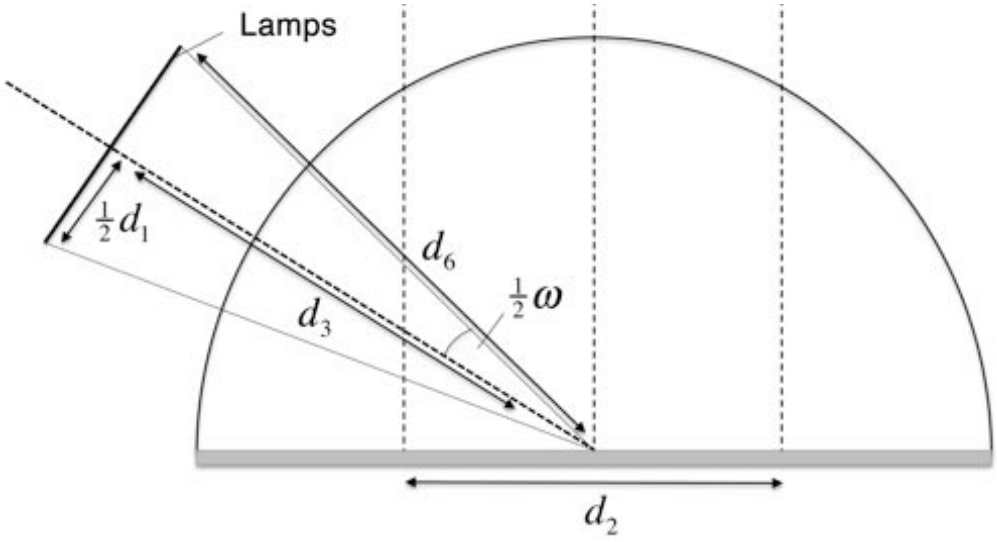

Figure 3.31. Cone angle of the light source as viewed from the centre of the sampling area

The half angle of the light cone $\frac{1}{2}\omega$ was calculated at the centre of the sampling area as 9.7°, and is given by:

$$\tfrac{1}{2}\omega = \sin^{-1}\left(\frac{\tfrac{1}{2}d_1}{d_6}\right) \qquad \text{Eq. 3.10}$$

3.4.2.11 Diffuse irradiance

Blackout curtains were fitted to a canopy above the sea ice tank and were draped along the sides of the canopy to reduce reflections from the walls of the container. During the CCRF acquisition the experiment operators were positioned behind a blackout curtain in order to reduce the effect of diffuse irradiance.

3.4.3 CCRF acquisitions

In total, two CCRF acquisitions were carried out. A single acquisition involved the measurement of the CCRF at 15° intervals in viewing zenith angle for 30° intervals in viewing azimuth angle. The first acquisition, M1, was carried out on the 7th of February 2014, for which the ice thickness was estimated using temperature profile data as 22 cm thick. Prior to the second acquisition on the 17th of February 2014, 75 L of seawater that was previously removed from the original solution was added on top of the existing sea ice, thus increasing the thickness of the ice to approximately 27 cm for the second acquisition. The seawater removed from the original solution was stored in 15 L containers in a dark and cold room prior to adding it to the lower layer of sea ice used for the M1 acquisition. The upper layer of seawater was left to freeze over a period of 24 hours prior to carrying out the M2 acquisition. Given that the height of the sea ice relative to the base of the tank increased upon adding the second layer, the lamps had to be realigned as described in 3.4.2.5.

3.4.3.1 Calculating the CCRF

The CCRF was calculated as follows:

$$CCRF(\theta_i,\phi_i;\theta_r,\phi_r;\lambda) = \frac{L_r(\theta_i,\phi_i;\theta_r,\phi_r;\lambda)}{L_{r,Spectralon}(\theta_i,\phi_i;\lambda)} I_{cf}(\theta_r,\phi_r) R_{cf} \quad \text{Eq. 3.11}$$

where $L_r(\theta_i,\phi_i;\theta_r,\phi_r;\lambda)$ is the radiance reflected by the sea ice surface, $L_{r,Spectralon}(\theta_i,\phi_i;\lambda)$ is the radiance reflected by the Spectralon reference panel, $I_{cf}(\theta_r,\phi_r)$ is the intensity correction factor defined in Section 3.4.2.8, and R_{cf} is the reflectance correction factor for the Spectralon panel defined in Section 3.4.2.4. The measured CCRF function was projected onto a 2D grid and is presented as a linear interpolation of the angles sampled using a Delaunay triangle-based method (de Berg et al., 2008).

3.4.4 PlanarRad radiative transfer model

PlanarRad is a program designed to model radiative-transfer in a homogenous, absorbing and scattering media (Hedley, 2008). PlanarRad uses the invariant imbedded method to solve the radiative-transfer equation (Mobley, 1989), which involves the directional discretization of the reflected radiance distribution into a grid of quadrilaterial regions, or 'quads' on the surface of the unit sphere. The quadrilaterial regions are separated by 15° in azimuth and 10° in zenith angle, and the model calculates the averaged reflected radiance for each quad as described in Section 1.10.3.1.

Realistic inherent optical properties (IOPs) for laboratory-generated sea ice were used as inputs into the PlanarRad model in order to simulate the reflected radiance distribution in terms of the quad-averaged BRDF. The quad-averaged BRDF was converted to the bidirectional reflectance factor (BRF) by multiplying

the BRDF by π (Schaepman-Strub et al., 2006), enabling a comparison between the model output and the laboratory-measured quantity (CCRF). An overview of the radiative-transfer model PlanarRad is given in Chapter 1, in Section 1.10.4. Results from a detailed sensitivity study of the PlanarRad radiative-transfer model are presented in this section.

3.4.4.1 Model input parameters

The model input variables were determined from physical measurements of the laboratory-generated sea ice where possible. The middle value from a range of realistic values cited from the literature was used for input variables that could not be determined by measurements. A list of the model input parameters, their sources, and their associated ranges are given in Table 3.1.

Input parameters	Default value*	Variable source	Variable range	Range justification
Band centres	410 nm to 730 nm at 20 nm intervals	n/a	none	n/a
Band widths	20 nm	n/a	none	n/a
Incident zenith angle	60°	Measured in this study	59° to 64°	Variation in incident angle over the sampling area (Section 4.3.2.9)
Incident azimuth angle	0°	Measured in this study	none	n/a
Refractive index of pure ice matrix	1.311	Measured by Warren and Brandt (2008)	1.307 to 1.315	± 1 standard deviation of the wavelength averaged value
Refractive index of air	1	n/a	none	n/a
Surface roughness parameter	0.11	Measured in this study	0.05 to 0.17	± 1 standard deviation of the averaged value
Absorption coefficient	Given in Figure 34	Measured by Warren and Brandt (2008) for pure ice; and Smith and Baker (1981) for brine	Calculated for brine volume fractions of 0.02, 0.06 and 0.4	Range of realistic brine volume fractions for sea ice given by Perovich (1996)
Scattering coefficient	210 m-1	Calculated by Mobley (1998)	175 m-1 to 250 m-1 (Mobley, 1998)	Range of realistic values for first year Arctic sea ice given by Mobley (1998)
Asymmetry parameter	0.93	Calculated by Mobley (1998)	0.86 to 0.99 (Mobley, 1998)	Range of values for first year Arctic sea ice given by Mobley (1998). Used to calculate HG phase function.
Ice thickness	M1 = 22, M2 = 32	Measured in this study	± 4 cm	Maximum uncertainty in ice thickness measurements
Lower boundary albedo	Given in Figure 35	Measured by Marks (2014)	± 10 %	Estimated uncertainty in measurements by Marks (2014)

* Input variables that are wavelength dependent are presented graphically in separate figures

Table 3.1. List of PlanarRad input parameters. Default values are the best estimate of a measured variable, or the middle value over a realistic range obtained from the literature

3.4.4.1.1 Incidence angle

Experiments were performed with a source incident angle of 60° from the surface normal. The incidence angle was measured from the centre of the lamp array to the centre of the sampling area as described in Section 3.4.2.5.

3.4.4.1.2 Surface roughness parameter

The surface roughness parameter (hsd) is the standard deviation of the vertex heights of a cosine wave fitted to the measured amplitude and wavelength of the sea ice roughness elements. In order to characterize the slope statistics of the sea ice surface the amplitude and wavelength of the roughness elements were measured along a 15 cm transect in a photograph of the sea ice surface given in Figure 3.32, the PTFE disc was used a reference for scale.

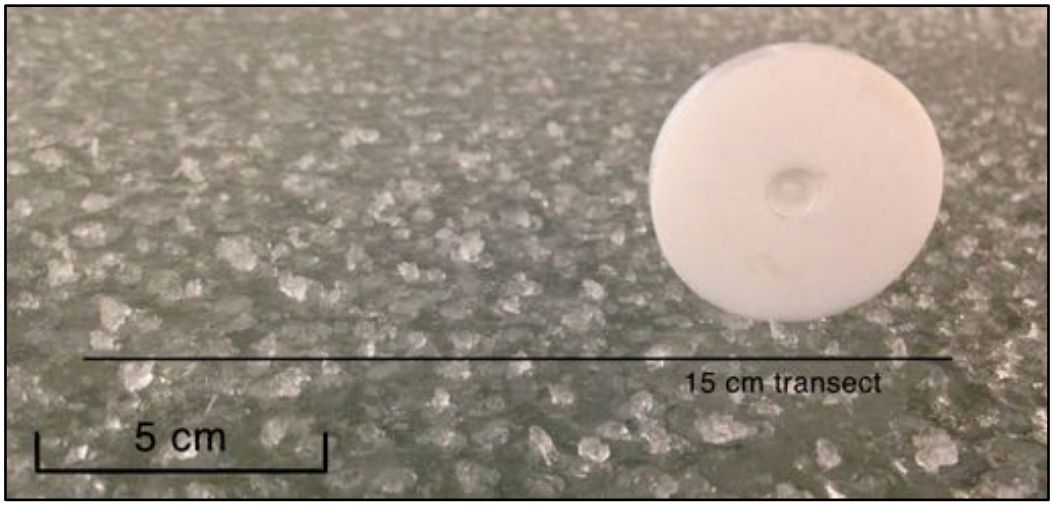

Figure 3.32. Photograph of sea ice surface elements and the position of the 15 cm transect used to determine the slope statistics

In total, 8 surface roughness elements were identified along the transect and the average ratio of amplitude to wavelength for each roughness element was 0.16 ± 0.08. The amplitude and wavelength of the individual roughness elements are given in Table 3.2.

Peak-to-peak height (mm)	Amplitude (mm)	Wavelength (mm)	Ratio
2.4	1.2	18.1	0.07
3.3	1.6	6.6	0.25
3.3	1.6	5.1	0.32
2.8	1.4	9.7	0.14
2.5	1.3	6.9	0.18
2.1	1.1	7.3	0.15
2.7	1.3	19.5	0.07
1.35	0.7	7.4	0.09
		Average:	0.16
		Standard deviation:	0.08

Table 3.2 Slope statistics measured for sea ice surface roughness elements

In order to calculate the surface roughness parameter for input into PlanarRad, 100 vertices were plotted along a cosine wave at equal intervals; the cosine wave had a ratio of amplitude to wavelength of 0.16 ± 0.08. The standard deviation of the amplitude of the vertices was calculated as 0.11 ± 0.06 mm. The uncertainty in the surface roughness parameter was propagated from the uncertainty of 0.08 in the measured ratio, by re-plotting the vertices along a cosine wave with a ratio of amplitude to wavelength of 0.08 and 0.24, and recalculating the standard deviation of the amplitude of the vertices.

3.4.4.1.3 Surface roughness model

The surface roughness model constructs an ensemble of 2000 simulated surfaces, each consisting of sloping congruent isosceles triangular facets known as triads. Surface realizations are constructed from the slope statistics obtained for the real surface roughness elements (i.e. the standard deviation of the amplitude of the vertices), as described in Section 3.4.4.1.2. Thus the model is able to reproduce the real surface to the extent that the slope statistics of the

simulated surface are identical to the slope statistics of the real surface (Mobley, 1994). An accurate statistical description of transmission and reflection across the interface was obtained by simulating the interaction of a single ray with thousands of different surface realizations and calculating the average reflected or transmitted power. The slopes of the triads in the model were determined from the height of 3 vertices, the height of each vertex was determined using a random number generator and a normal probability density function with a standard deviation of 0.11 and a mean of 0 cm. Three examples of the simulated surface realization are given in Figure 3.33, and a histogram of the vertex elevations for each surface is given in Figure 3.34.

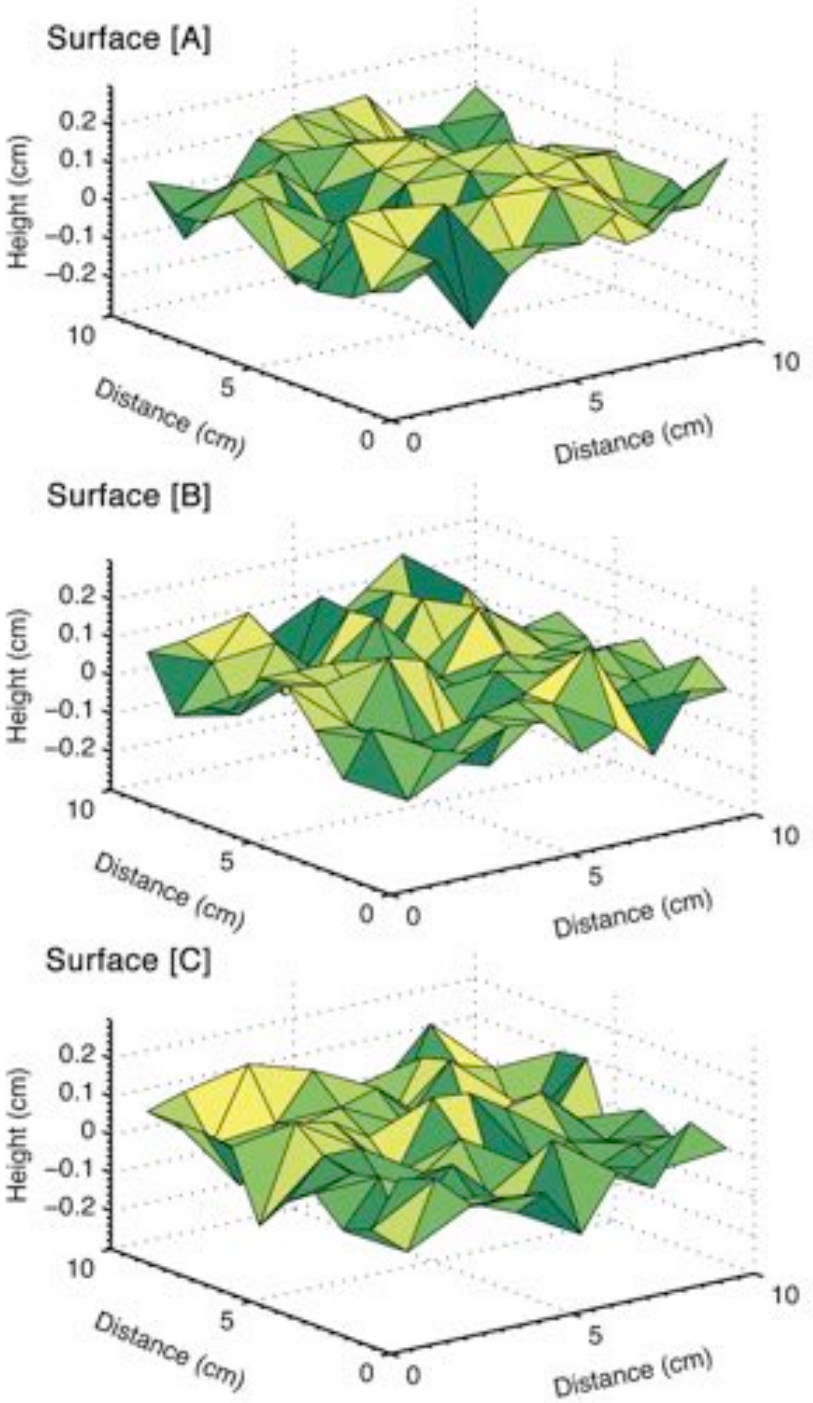

Figure 3.33. Three example constructs of a surface realization, each generated from 162 congruent isosceles triangles, or 'triads'. Each of the 3 surface realizations has identical slope statistics

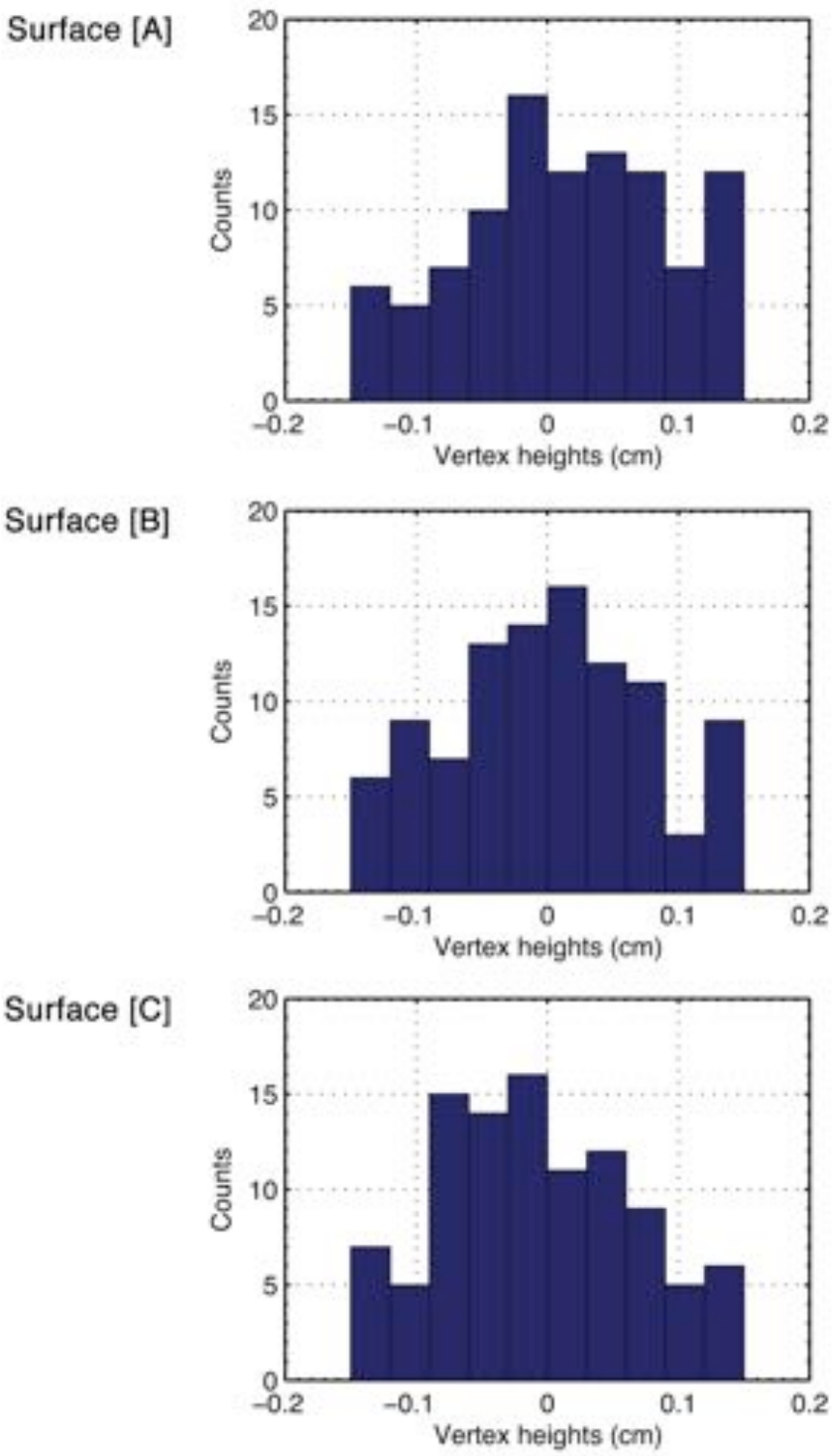

Figure 3.34. Histograms of vertex heights plotted in Figure 3.33

3.4.4.1.4 Surface roughness and ray tracing

In order to calculate the reflectance and transmittance for each surface realization a simulated parent ray is incident at a point on the interface. The incident parent ray produces two daughter rays: a refracted ray and a reflected

ray. The path of all daughter rays across the domain of each surface realization is calculated while tracking the rays associated power. With knowledge of the orientation of the triad and incidence angle θ_i the angle of reflection or refraction can be calculated. Given that the surface of the triad is smooth relative to the wavelength of light, the angle of reflection equals the angle of incidence, and lies in the same plane, but on the opposite side to θ_i. The angle of refraction of the incident ray can be calculated using Snell's law:

$$\frac{\sin(\theta_t)}{n_1} = \frac{\sin(\theta_i)}{n_2} \qquad \text{Eq. 3.12}$$

where n_1 and n_2 are the real indices of refraction of the first and second medium respectively, θ_t is the angle of the transmitted ray and θ_i is the angle of the incident ray. The incident parent ray has incident power $\Phi_i = 1$. As the ray interacts with the surface some of the power is transferred to the reflected ray and some is transferred to the transmitted ray. To determine the fraction of the reflected power, Fresnel's formula was applied:

$$r(\theta_i) = \frac{1}{2}\left(\left[\frac{\sin(\theta_i - \theta_t)}{\sin(\theta_i + \theta_t)}\right]^2 + \left[\frac{\tan(\theta_i - \theta_t)}{\sin(\theta_i + \theta_t)}\right]^2\right) \qquad \text{Eq. 3.13}$$

where $r(\theta_i)$ is the Fresnel reflectance factor. The reflected power is obtained simply by multiplying the Fresnel reflectance factor by the incident power Φ_i. Given the conversation of energy, the transmitted power is then $\Phi_t = \Phi_i - \Phi_r$.

Refracted daughter rays occasionally interact with the interface from below, emerging from a denser medium into a less dense medium. Under these circumstances the critical angle θ' defines the threshold for total internal reflection of a ray within the denser medium:

$$\theta' = \sin^{-1}(1/n_2) \approx 48° \quad \text{Eq. 3.14}$$

where n_2 is the real index of refraction for ice, which has minimal wavelength dependence and was averaged over the wavelength range 400 nm to 740 nm. Ray paths were calculated until each daughter ray emerged from the domain either above the interface (contributing to reflection), or below the interface (contributing to transmission). The power of each emerging ray was added to an accumulating sum for reflectance and transmittance functions. For a sufficiently large number of simulations using different surface realizations, the ratio of reflected to incident power will approach a limit, the limit is the desired reflectance (Mobley, 1994). The process of ray tracing is repeated for 2000 surface realizations with the same angle of incidence for the parent ray. The average reflectance and transmittance was calculated to give an acceptably accurate estimate of reflectance and transmittance over the surface.

3.4.4.1.5 Absorption coefficient

An absorption coefficient for sea ice was calculated by applying Eq. 1.44 from Chapter 1. The volume fraction of brine was estimated from measurements of temperature and salinity obtained by coring of sea ice generated using the Royal Holloway sea ice simulator by Marks (2014). Measurements were obtained for sea ice generated using the same methodology as in this study, and thus the brine volume fraction measured by Marks (2014) is considered representative of brine volume fraction for the sea ice generated in this study. The study by Marks (2014) reports a brine volume fraction that is a function of depth. Given the sea ice was modeled as a homogenous layer with depth independent IOPs, the brine volume fraction was averaged and yielded a value of 6 %, which was used in Eq. 1.44 to calculate the absorption coefficient for

sea ice. The spectral absorption coefficients over a realistic range of brine volume fractions from 0.02 to 0.4 (Perovich, 1996) were calculated and are given in Figure 3.35.

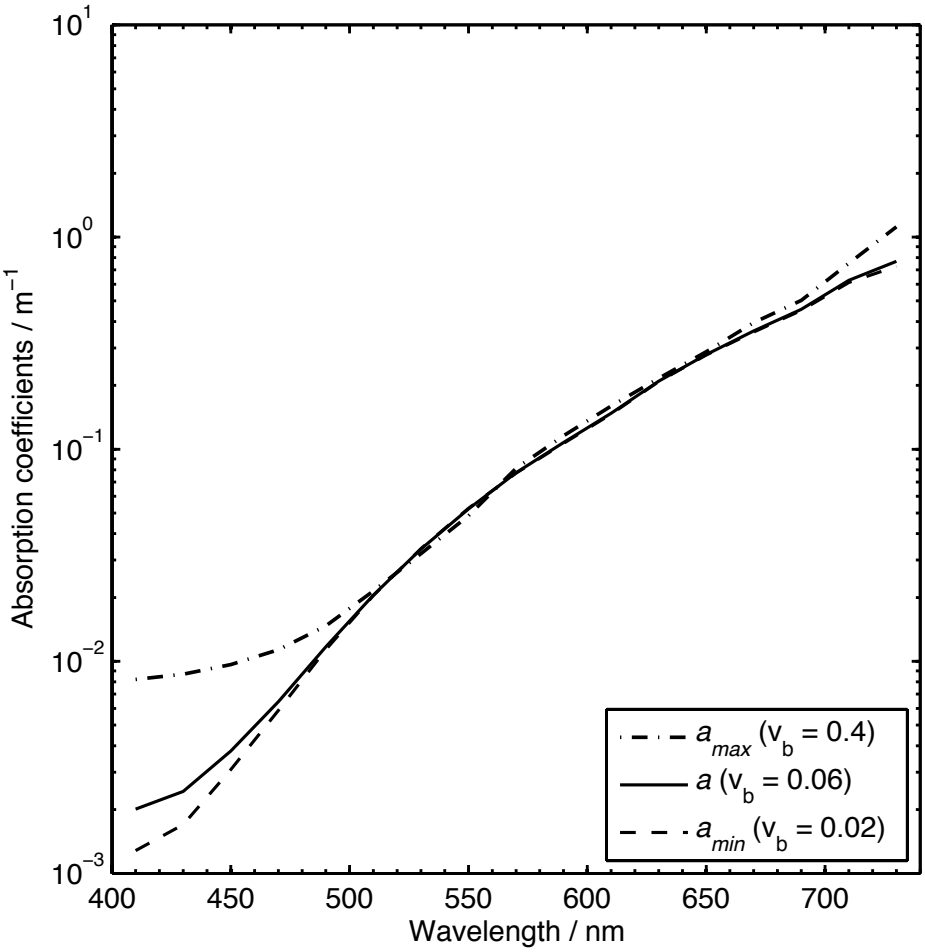

Figure 3.35. Absorption coefficients for laboratory-generated sea ice with brine volume fractions ranging from 0.02 to 0.4

3.4.4.1.6 Refractive index

The real index of refraction of the ice matrix was 1.311 ± 0.004. The value was determined by averaging the refractive index of pure ice over the wavelength range 400 nm to 740 nm using data from Warren and Brandt (2008). The refractive index outside the medium had a value equal to that of air, which is unity. The refractive index of brine was not considered in the model because (a) the brine content was small (6 %) and (b) absorption coefficients for brine and ice were very similar, as shown in Figure 3.35.

3.4.4.1.7 Phase function and scattering coefficients

The phase function and scattering coefficients for Arctic first year sea ice were estimated by Mobley (1998) with Mie calculations for sea ice with a similar brine volume fraction (5.5%). The calculations were performed using the indices of refraction for ice and brine, and particle size distributions for sea ice inclusions over a range of realistic conditions. The study by Mobley (1998) reported scattering coefficients ranging between 175 m^{-1} and 250 m^{-1} and asymmetry parameters ranging between 0.86 (for air bubbles) and 0.99 (for brine inclusions) (Mobley et al., 1998), which is consistent with estimates from previous studies (Perovich, 2003). It was not possible to determine the scattering coefficient and phase function empirically, so the middle value in each range given by Mobley (1998) was used as the default input variable in this study.

3.4.4.1.8 Lower boundary reflectance

The nadir reflectance of base of the tank (i.e. the lower boundary in the modeling study) was measured by Marks (2014) when the tank contained seawater and no sea ice. The nadir reflectance of the lower boundary measured by Marks (2014) is presented as a function of wavelength in Figure 3.36. The directional reflectance at the base of the polyethylene tank was assumed to be Lambertian and thus the measured nadir reflectance is numerically equal to the bihemispherical reflectance.

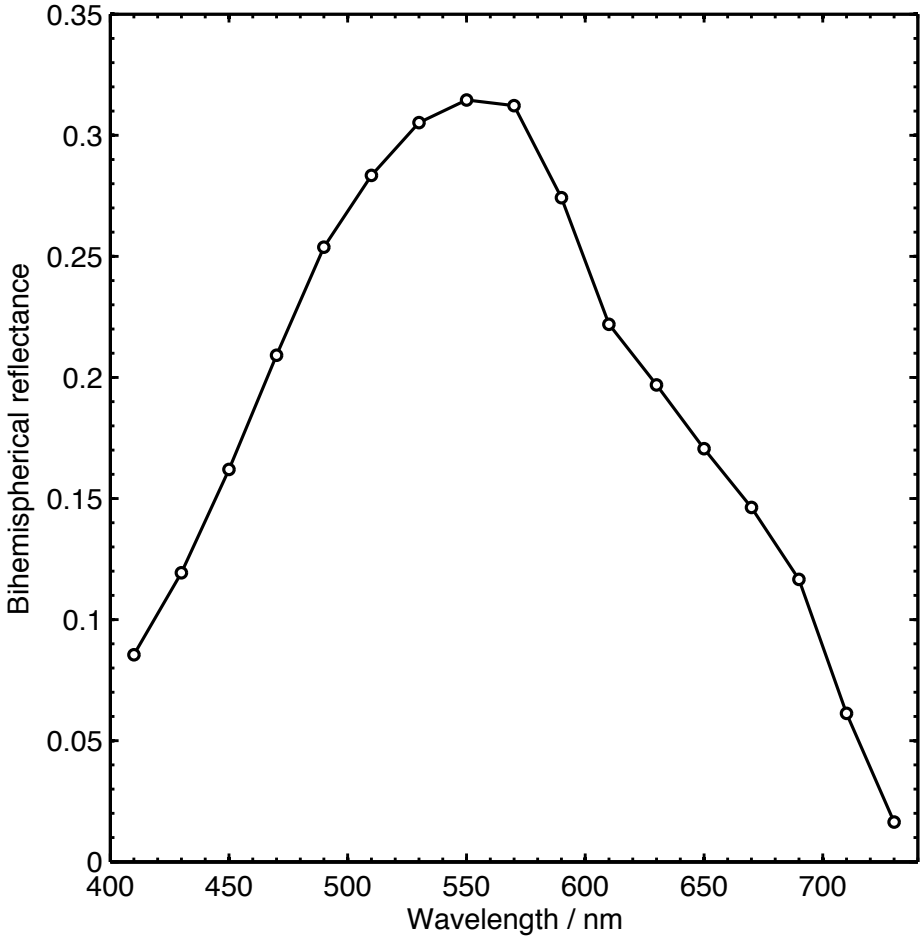

Figure 3.36. Reflectance of the lower boundary. Data from Marks (2014)

3.4.4.1.9 Ice thickness

Ice thickness was estimated from the temperature profile of the laboratory generated sea ice using the method described in Section 3.4.1.5. The ice thickness for the measurement M1 (22 cm ± 4 cm) was used as the input value during the model sensitivity study. The thickness of ice during the M1 measurement was used in the sensitivity study because it was the thinnest ice layer generated, and because the boundary conditions are expected to have a greater influence given a thinner layer of sea ice in the model.

3.4.4.2 Model sensitivity study

A sensitivity study was performed over the range of values presented in Table 3.1 by calculating the distribution of reflected radiance (quad-averaged BRF) while varying each parameter independently between its minimum and maximum value. The study was carried out in order to: (a) develop a better understanding of the relationships between input and output variables in the model; (b) identify sensitive parameters given a set of fixed boundary conditions; and (c) test the robustness of the results given uncertainty in the model inputs.

3.4.4.2.1 Lower boundary reflectance

The quad-averaged BRF was calculated using PlanarRad for a lower boundary with a bihemispherical reflectance (BHR) given in Figure 3.36 ± 10 %. All other input variables were held constant at the respective default values given in Table 3.1. Bivariate plots of the BRF in solar principal plane, the BRF at the nadir-viewing angle as a function of wavelength, and the anisotropy index (ANIX) as a function of wavelength are given in Figure 3.37, Figure 3.38 and Figure 3.39.

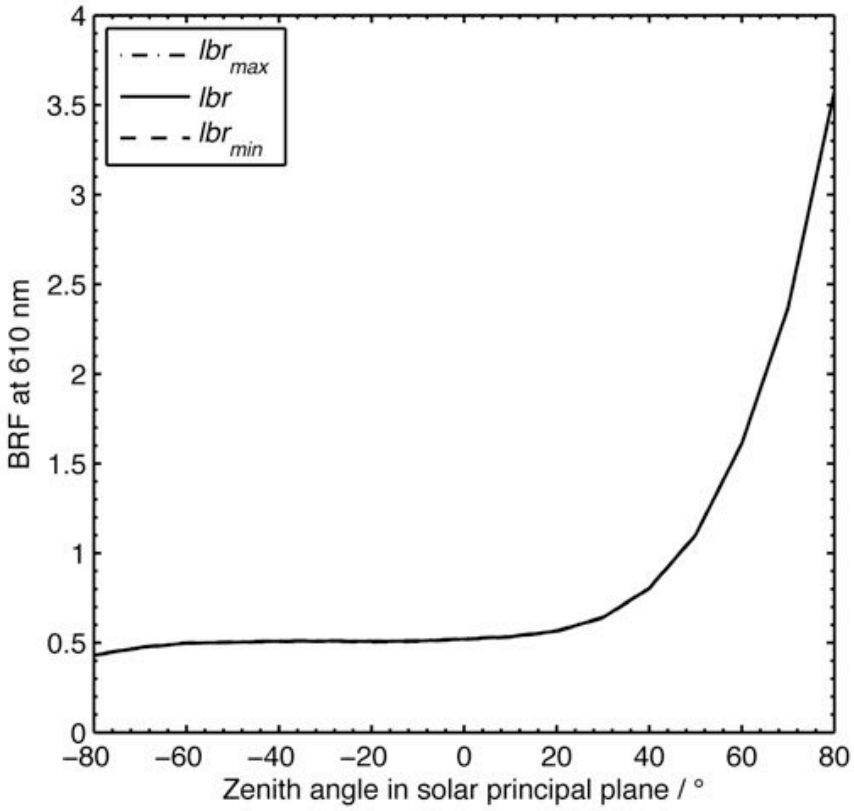

Figure 3.37. BRF in the solar principal plane at 610 nm for the lower boundary reflectance (lbr) given in Figure 3.36 ± 10 %

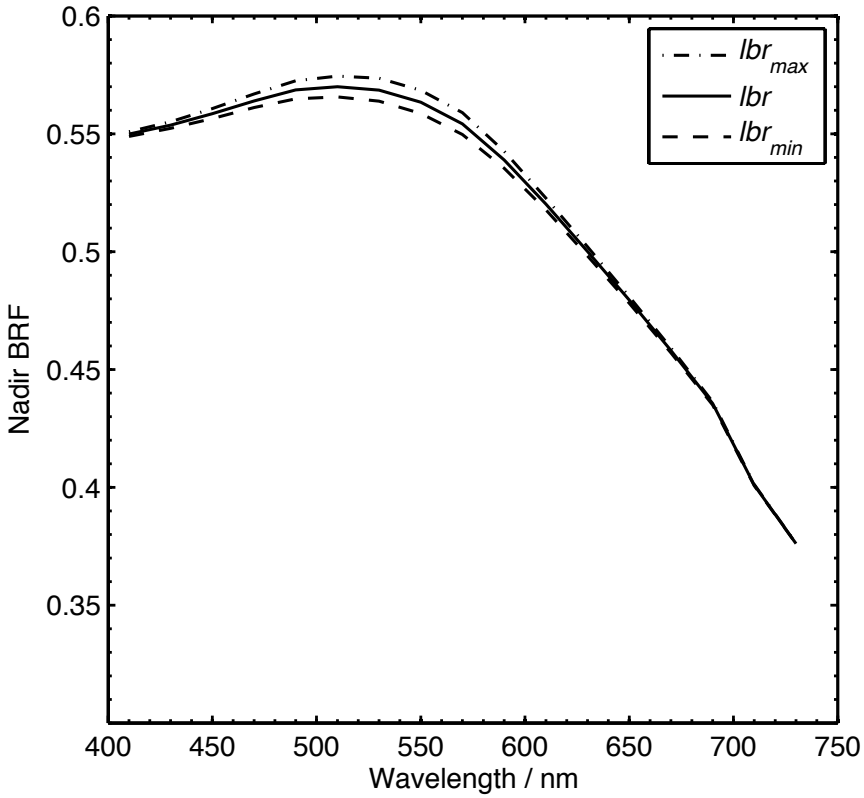

Figure 3.38. Nadir BRF as a function for wavelength for the lower boundary reflectance (lbr) given in Figure 3.36 ± 10 %

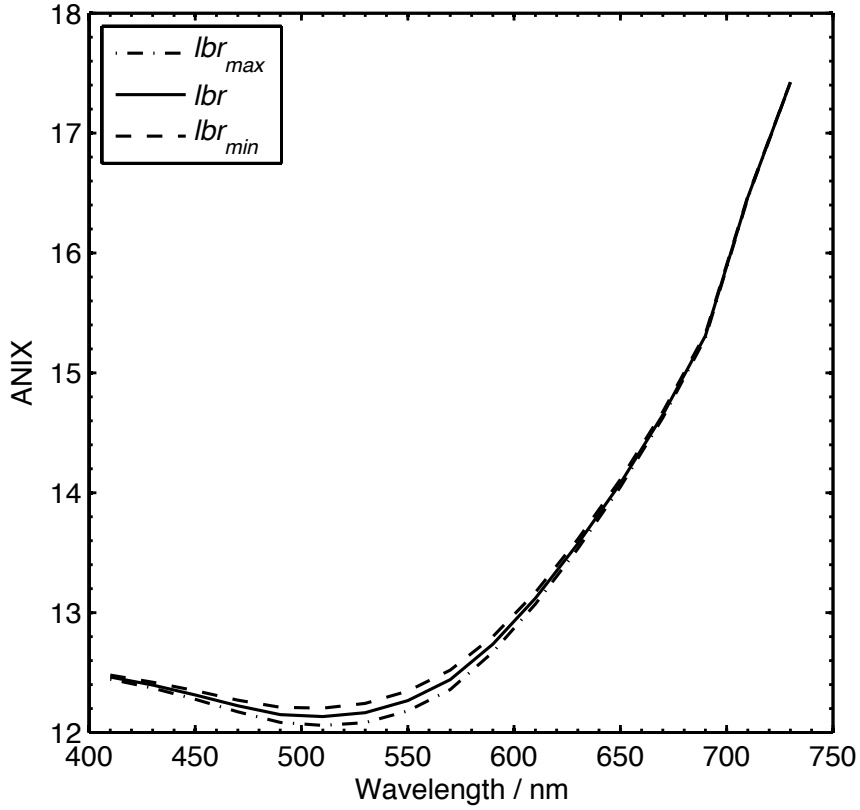

Figure 3.39. Anisotropy index (ANIX) as a function of wavelength for the lower boundary reflectance (lbr) given in Figure 3.36 ± 10 %

Increasing the bihemispherical reflectance (BHR) of the lower boundary by 10 % resulted in an increase of less than 0.5 % in the BRF for all viewing angles in the solar principal plane at 610 nm, and the maximum increase in the BRF was outside of the forward scattering peak. A near equivalent decrease (within 0.3 %) in the BRF in the solar principal plane at 610 nm was observed when the lower boundary BHR was reduced by 10 %. Changing the BHR had the greatest impact on the BRF at 550 nm, where a 10 % increase resulted in a 0.9 % increase in the BRF for the nadir viewing position. Indicating that the influence of the BHR correlated well with the peak in the reflectivity of the BHR at 550 nm, given in Figure 3.36. The BRF appears less sensitive to the BHR at longer wavelengths, for example, an increase of 10 % in the BHR resulted in a change of 0.02 % in the BRF at 730 nm, which is an order of magnitude smaller than the change in the BRF at 410 nm (0.2 %), given the same increase in reflectivity of

the lower boundary. The wavelength dependence is the combined effect of the absorption coefficient (which varies strongly with wavelength) and the spectral reflectance of the lower boundary. The ANIX value (which quantifies the anisotropy in the BRF over the hemisphere) decreased by less than 1 % over all wavelengths for a 10 % increase in the BHR, which is explained by the increase in the BRF outside of the forward peak.

3.4.4.2.2 Ice thickness

The quad-averaged BRF was calculated for an ice thickness of 18 cm, 22 cm and 26 cm, while holding all other input variables at their respective default values. Bivariate plots of the BRF in the solar principal plane, the BRF at the nadir-viewing angle, and the anisotropy index (ANIX) as a function of wavelength are given in Figure 3.40, Figure 3.41 and Figure 3.42.

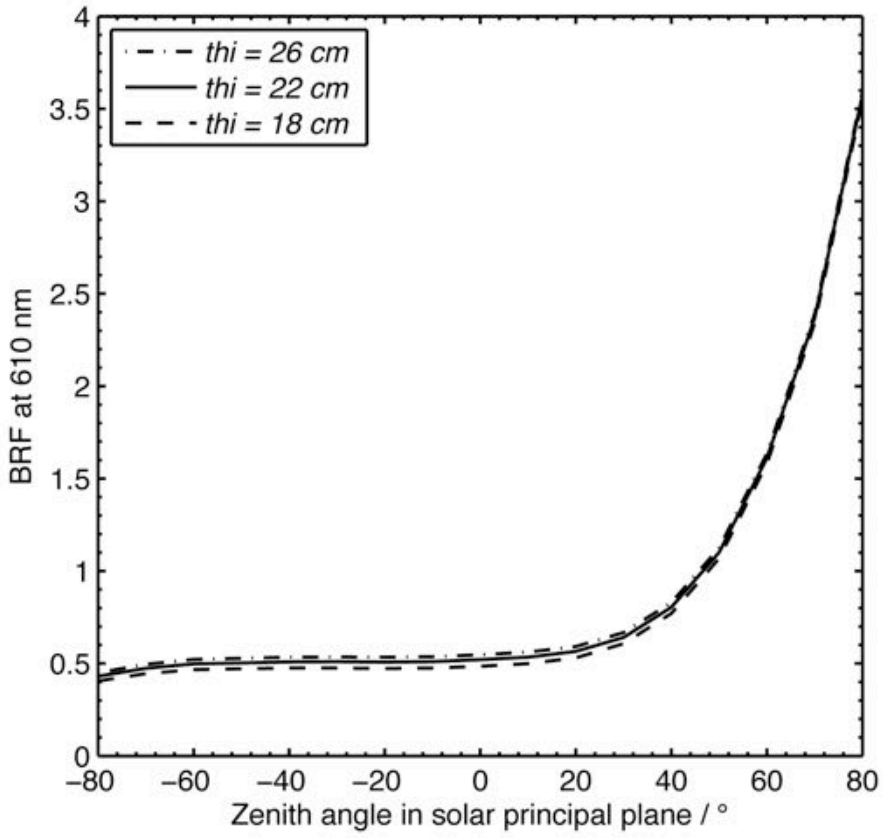

Figure 3.40. BRF in the solar principal plane at 610 nm for an ice thickness (thi) of 26 cm, 22 cm and 18 cm

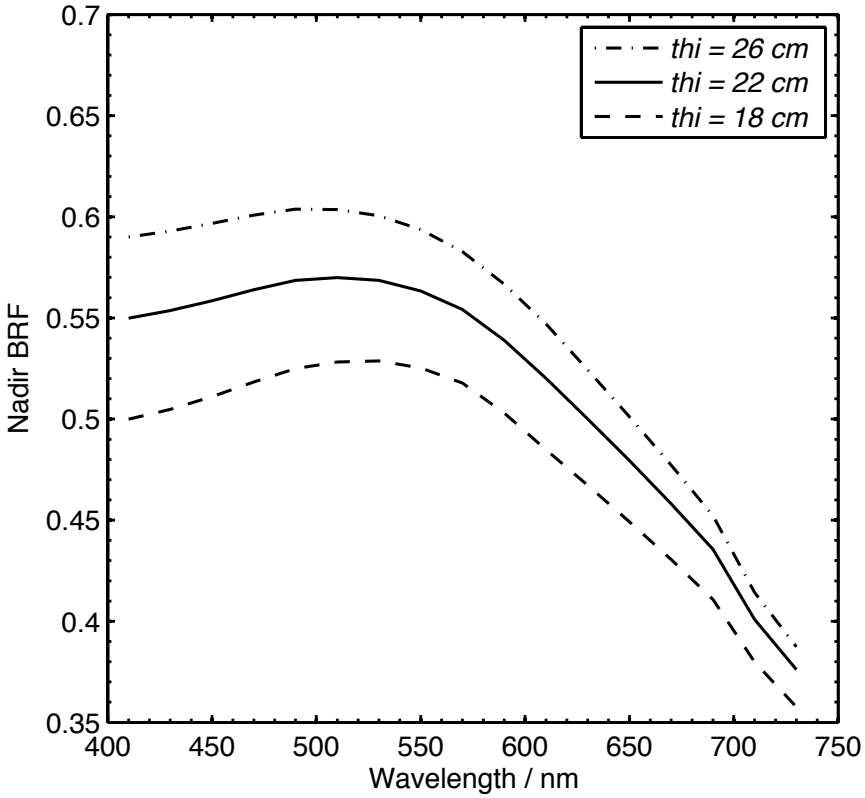

Figure 3.41. Nadir BRF as a function for wavelength for an ice thickness (thi) of 26 cm, 22 cm and 18 cm

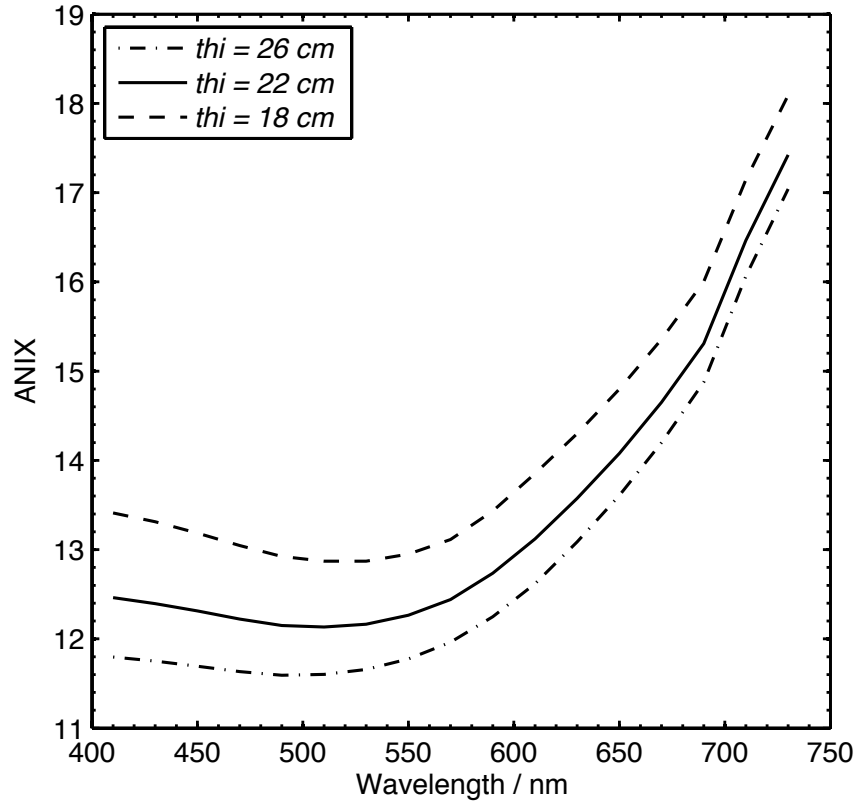

Figure 3.42. Anisotropy index (ANIX) as a function of wavelength for an ice thickness (thi) of 26 cm, 22 cm and 18 cm

Increasing the thickness of the sea ice by 4 cm resulted in an increase of up to 5.2 % in the BRF in the solar principal plane, with the greatest increase for viewing angles outside of the forward scattering peak. Decreasing the thickness of the sea ice by 4 cm resulted in a decrease of up to 6.9 % in the BRF in the solar principal plane, with the largest decrease outside of the forward scattering peak. Increasing the thickness of the sea ice by 4 cm resulted in an increase in the BRF that was greatest at shorter wavelengths. For example, the increase in the BRF with a 4 cm increase in thickness is 7.3 % at 410 nm for the nadir-viewing angle, compared to an increase of 3.0 % at 730 nm. The wavelength dependence is the combined result of the increased scattering and reduced influence of the lower boundary reflectivity on the BRF with increasing ice thickness. Flattening of the BRF function over the hemisphere with increasing thickness and its wavelength dependence is evident in the spectral ANIX values, which decreased by 5 % at 410 nm compared to 2 % at 730 nm, given a 4 cm increase in thickness. The BRF is less anisotropic with thicker ice as the average number of scattering events a photon undergoes increases, which in turn generates a more diffuse reflection. The response to changes in thickness depends on the original thickness, and is likely to be amplified for thinner ice.

3.4.4.2.3 Absorption coefficient

The quad-averaged BRF was calculated using PlanarRad for the spectral absorption coefficients given in Figure 3.35 for brine volume fractions of $v_b = 0.02$, $v_b = 0.06$ and $v_b = 0.4$. All other input variables were held constant at the respective default values given in Table 3.1. Bivariate plots of the BRF in the solar principal plane, the BRF as a function of wavelength at the nadir-viewing angle, and the anisotropy index (ANIX) as a function of wavelength, are given in Figure 3.45, Figure 3.44 and Figure 3.43.

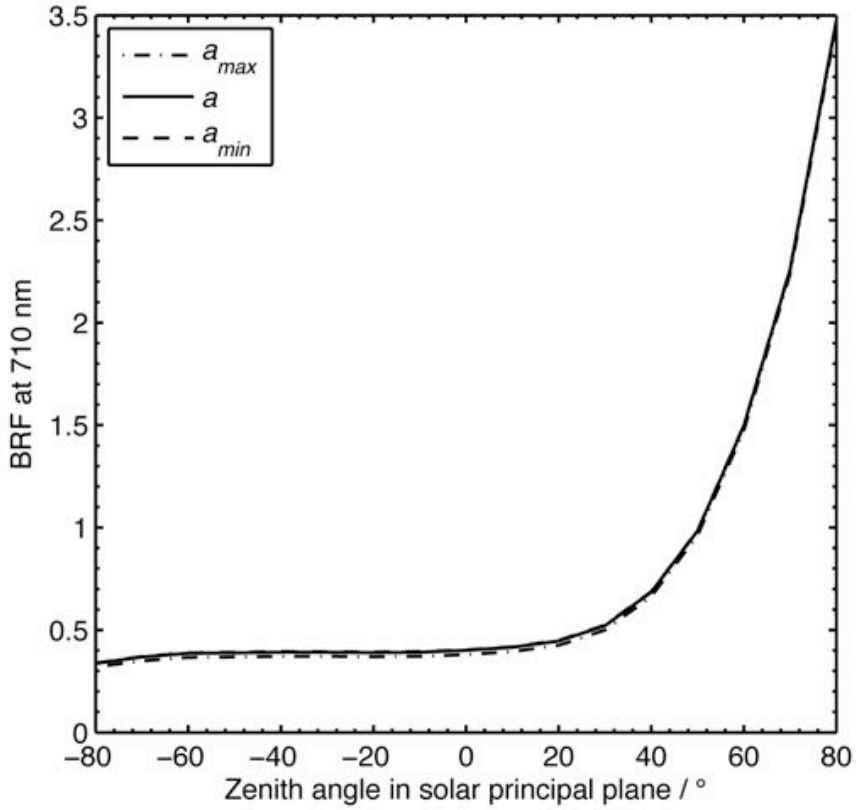

Figure 3.43. BRF in the solar principal plane at 710 nm for 3 different spectral absorption coefficients given in Figure 3.35

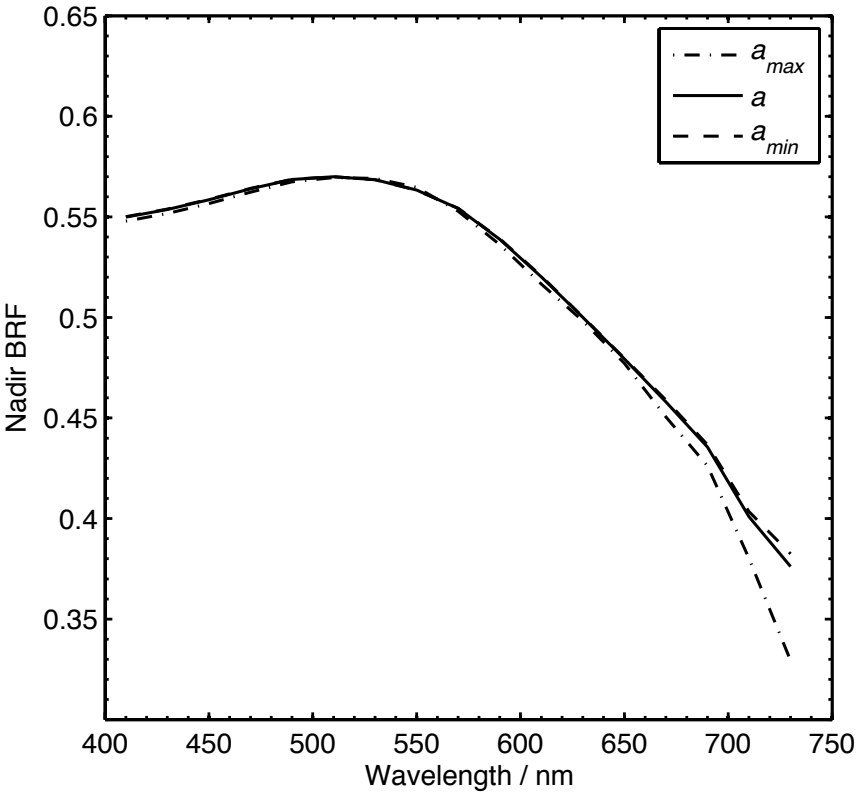

Figure 3.44. Nadir BRF as a function for wavelength for 3 different spectral absorption coefficients given in Figure 3.35

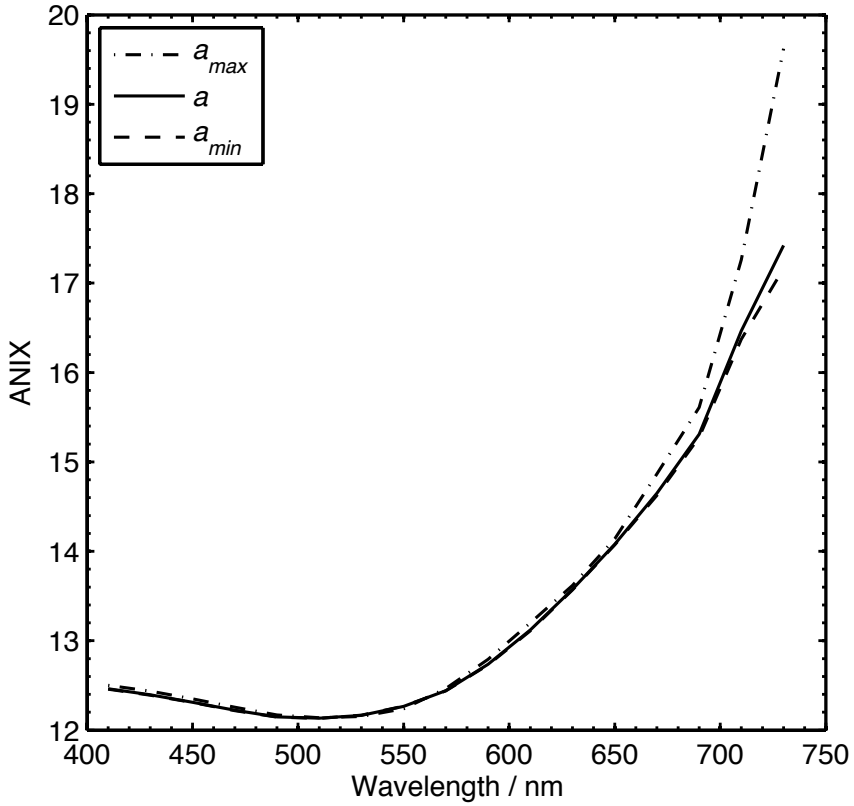

Figure 3.45. Anisotropy index (ANIX) as a function of wavelength for 3 different spectral absorption coefficients given in Figure 3.35

Given the similar spectral shape of absorption coefficients for brine and for pure ice (Chapter 1, Figure 13) there are only minor differences in the spectral shape of the absorption coefficients for sea ice with greatly different brine volume fractions (Figure 3.35). Increasing the volume of brine resulted in increased absorption below 500 nm and above 700 nm. Increasing the absorption coefficients over a realistic range of brine volume fractions resulted in a decrease in the BRF that was very small (less than 1 %), for wavelengths less than 650 nm, but decreased the BRF at nadir by up to 12.4 % at 730 nm. The BRF was less sensitive to an increase in the absorption coefficient at shorter wavelengths because of penetration of light through the entire slab of sea ice at shorter wavelengths. Resulting in a BRF that is more strongly influenced by the reflectivity of the lower boundary, rather than the absorption coefficient of sea ice. At longer wavelengths absorption by the sea ice is up to 3 orders of

magnitude stronger, and thus penetration depths are much shorter, and the BRF is more sensitive to changes in the absorption coefficients of the sea ice relative to the reflectivity of the lower boundary. Increased absorption at longer wavelengths owing to a larger brine volume fraction resulted in an increase in the anisotropy index (ANIX) of up to 12.6 % at 730 nm.

3.4.4.2.4 Scattering coefficient

The quad-averaged BRF was calculated using PlanarRad for the scattering coefficients 175 m^{-1}, 210 m^{-1} and 250 m^{-1} All other input variables were held constant at the respective default values given in Table 3.1. Bivariate plots of the BRF in the solar principal plane, the BRF as a function of wavelength at the nadir-viewing angle, and the anisotropy index (ANIX) as a function of wavelength are given in Figure 3.46, Figure 3.47 and Figure 3.48.

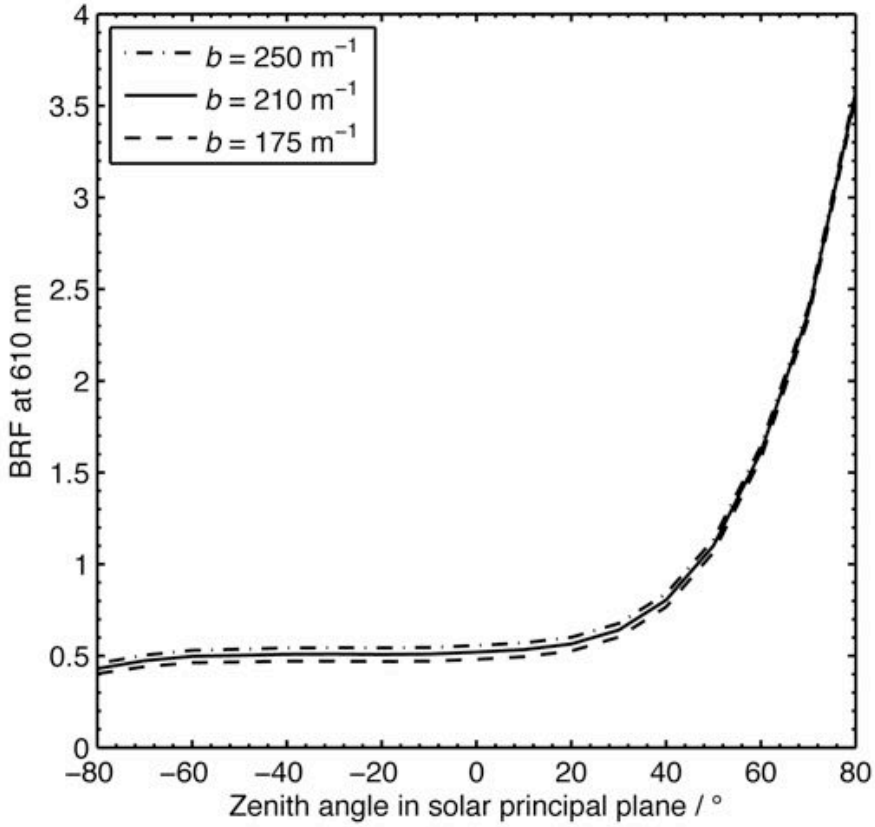

Figure 3.46. BRF in the solar principal plane at 610 nm for 3 different scattering coefficients of 175 m^{-1}, 210 m^{-1} and 250 m^{-1}

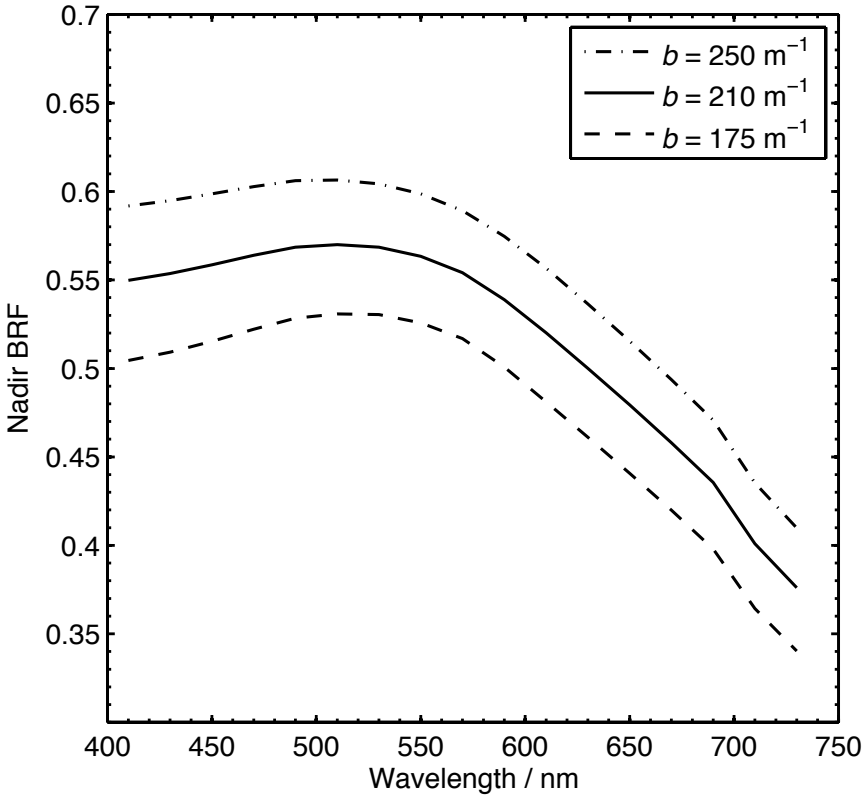

Figure 3.47. Nadir BRF as a function for wavelength for 3 different scattering coefficients of 175 m^{-1}, 210 m^{-1} and 250 m^{-1}

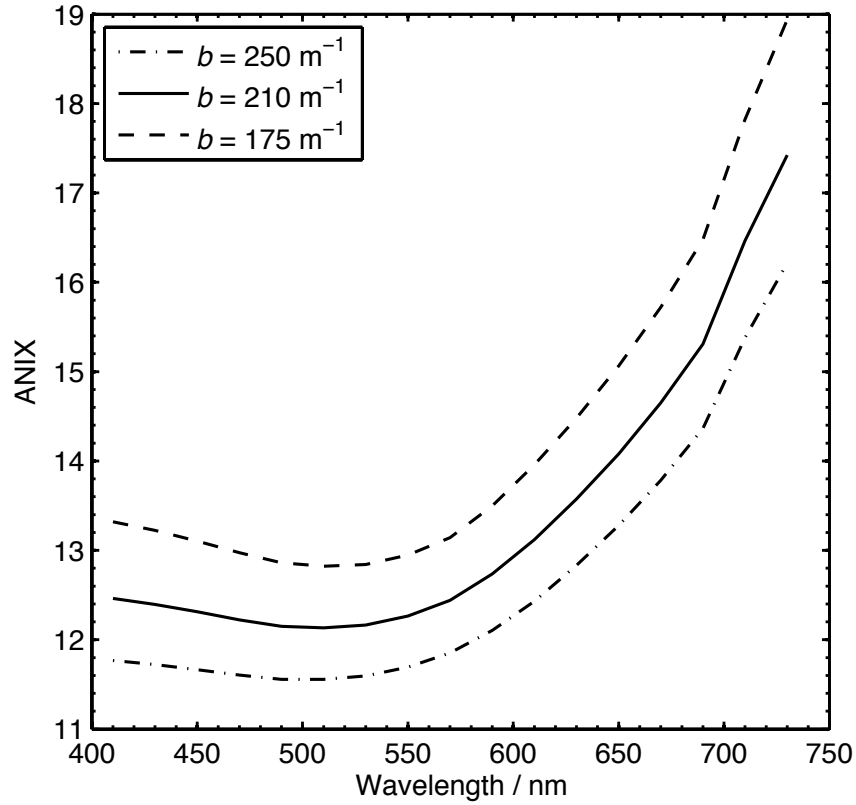

Figure 3.48. Anisotropy index (ANIX) as a function of wavelength for 3 different scattering coefficients of 175 m^{-1}, 210 m^{-1} and 250 m^{-1}

An increase in the scattering coefficient of 40 m^{-1} resulted in an increase in the BRF in the solar principal plane of up to 7 %, with the greatest increase outside of the forward scattering peak. A decrease in the scattering coefficient of 40 m^{-1} resulted in a decrease in the BRF in the solar principal plane of up to 8 %, with the greatest decrease outside of the forward scattering peak. As a result, the anisotropy index (ANIX) decreased by up to 7 % for an increase in the scattering coefficient, and increased by up to 9 % for a decrease of 40 m^{-1} in the scattering coefficient. Indicating that the anisotropy in the BRF over the hemisphere is inversely proportional to the scattering coefficient, which makes intuitive sense, because a larger scattering coefficient increases the average number of scattering events in the medium, which in turn produces a more diffuse reflection.

There was a small (less than 3 %) wavelength dependence to the change in the nadir BRF owing to increased scattering. For example, the BRF at the nadir-viewing angle increased by 7.6 % at 410 nm, compared to an increase of 9.0 % at 730 nm. A similar, but smaller (less than 1.5 %) wavelength dependence was observed for a decrease in scattering of the same amount. Given a uniformly increased scattering coefficient across all wavelengths, slightly more (2 %) light was reflected from the medium at larger wavelengths. The wavelength dependence is probably associated with stronger attenuation of the light by the lower boundary for shorter wavelengths. Light is attenuated more strongly by the lower boundary at shorter wavelengths because absorption is weaker and more light penetrates through the entire slab of sea ice, as a result, a uniform increase in scattering with wavelength had slightly less impact at shorter wavelengths.

3.4.4.2.5 Phase function

The quad-averaged BRF was calculated for 3 different values of the asymmetry parameter $g = 0.86$, $g = 0.93$ and $g = 0.99$. The asymmetry parameter was used to generate Henyey-Greenstein scattering phase functions, which were used to calculate the quad-averaged BRF using PlanarRad. All other input variables were held constant at the respective default values given in Table 3.1. Bivariate plots of the BRF in the solar principal plane, the BRF as a function of wavelength at the nadir-viewing angle, and the anisotropy index (ANIX) as a function of wavelength are given in Figure 3.49, Figure 3.50 and Figure 3.51.

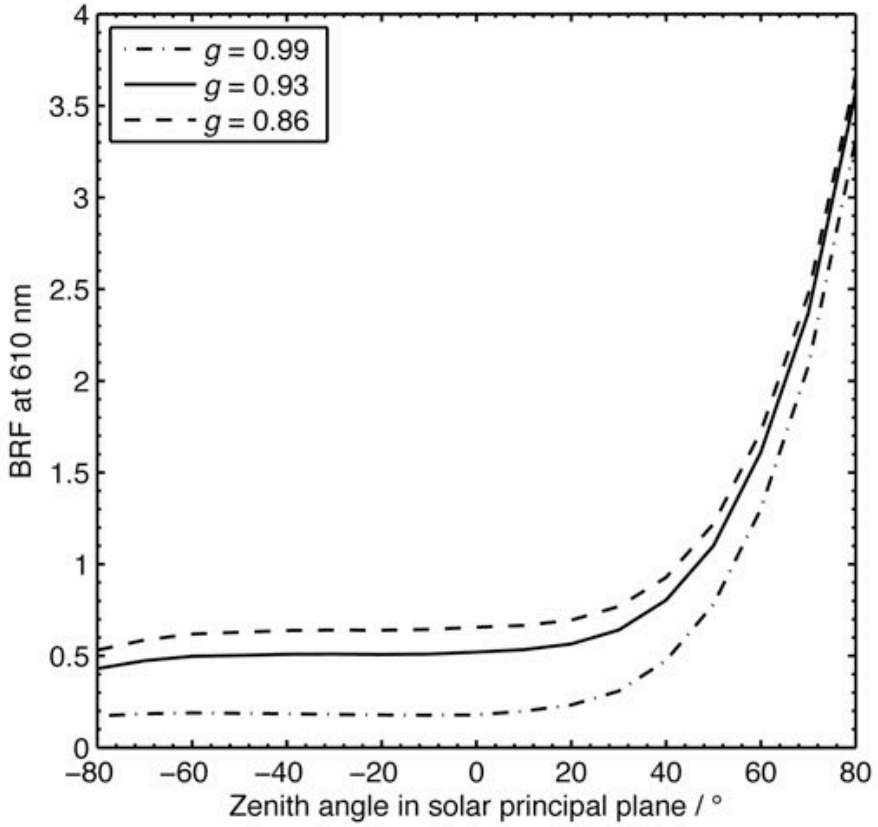

Figure 3.49. BRF in the solar principal plane at 610 nm for 3 different values of the asymmetry parameter *g* = 0.86, *g* = 0.93 and *g* = 0.99

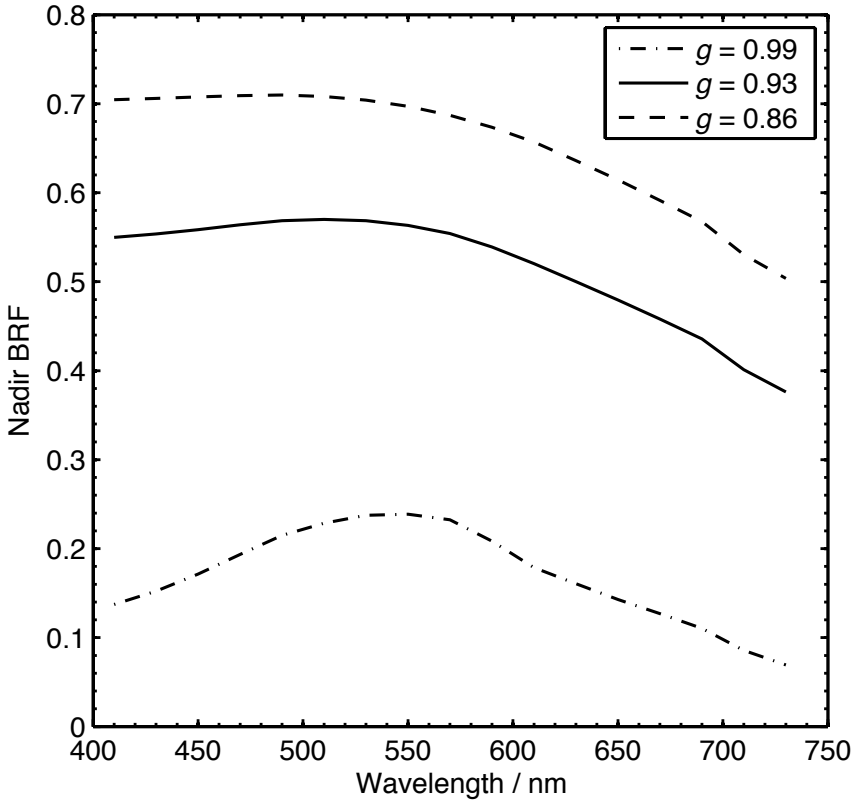

Figure 3.50. Nadir BRF as a function for wavelength for 3 different values of the asymmetry parameter $g = 0.86$, $g = 0.93$ and $g = 0.99$

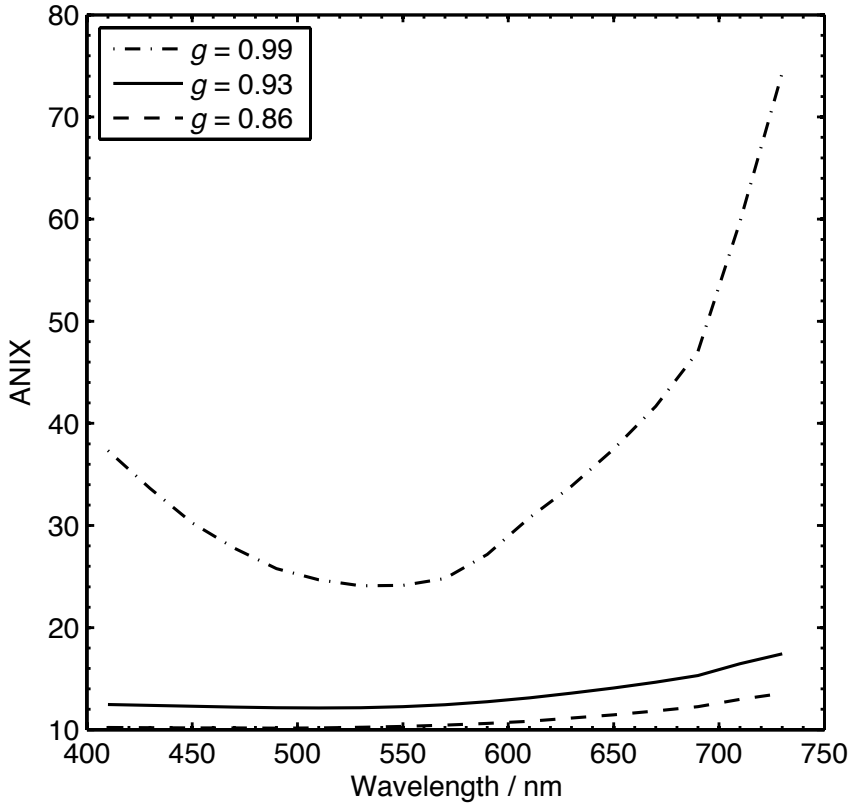

Figure 3.51. Anisotropy index (ANIX) as a function of wavelength for 3 different values of the asymmetry parameter g = 0.86, g = 0.93 and g = 0.99

An increase in the asymmetry parameter (g) of 0.06 resulted in a decrease in BRF in the solar principal plane of up to 65.9 % at 610 nm, with the greatest decrease outside of the forward scattering peak. The decrease in the BRF for viewing angles greater than 60° in the solar principal plane was less than 20 %. An equivalent decrease in g resulted in an increase of up to 26.3 % in the BRF in the solar principal plane at 610 nm, with the greatest increase outside of the forward scattering peak. An increase in g resulted in a BRF that was more strongly wavelength dependent. With the BRF decreasing less for wavelengths near to 550 nm (57.6 %), compared to a decrease in the BRF of 81.5 % at 730 nm, and a decrease of 75.0 % at 410 nm. The decrease in the BRF was smallest for the wavelength 550 nm, which corresponds with the wavelength for which the lower boundary reflectivity was greatest. Influence of the lower

boundary on the spectral BRF was less when g was decreased, with the BRF at nadir showing an increase of 23.7 % at 550 nm, compared to an increase of 34 % at 730 nm.

Both the BRF as a function of wavelength and as a function over the hemisphere appear to be strongly sensitive to the phase function. Increasing the g parameter strongly increased the anisotropy of the BRF function over the hemisphere. With the greatest increase in the ANIX value of 326.6 % at 730 nm, 199.6 % at 410 nm and a minimum increase of 96.8 % at 550 nm. The minimum increase in anisotropy corresponds with the wavelength for which the reflectivity of the lower boundary is strongest. Indicating that increased reflectivity of the lower boundary has a diffusing effect on the reflected radiance distribution, and has stronger influence when a more strongly forward scattering phase function is used in the calculations. Such a large increase in anisotropy given a stronger forward scattering phase function makes intuitive sense because photons will typically be required to undergo more scattering events before it is scattered out of the forward trajectory, producing a less diffuse reflection overall. In addition, owing to the greater tendency for a photon to be scattered into the forward direction given a increased value of g, more photons will on average penetrate deeper into the medium and will reach the lower boundary, and thus the spectral reflectivity of the lower boundary will have more influence on the BRF, as is evident by the shape of the bottom curve in Figure 3.50.

3.4.4.2.6 Surface roughness

The quad-averaged BRF was calculated for 3 different values of the surface roughness parameter (*hsd)*. The surface roughness parameter was defined as the standard deviation of the vertex heights of a cosine wave fitted to the

measured amplitude and wavelength of roughness elements, as described in Section 3.4.1.6. The range of *hsd* values used in the sensitivity analysis were calculated from the measured ratio of amplitude to wavelength of $0.16 \pm 1\sigma$, which correspond to a peak-to-peak amplitude for the roughness elements of 1.4 mm, 3.2 mm and 4.8 mm. The standard deviation of vertex heights in the 3 cosine waves used were: $hsd = 0.05$ mm, $hsd = 0.11$ mm and $hsd = 0.17$ mm. All other input variables were held constant at the respective default values given in Table 3.1. Bivariate plots of the BRF in the solar principal plane, the BRF as a function of wavelength at the nadir-viewing angle, and the anisotropy index (ANIX) as a function of wavelength are given in Figure 3.52, Figure 3.53 and Figure 3.54.

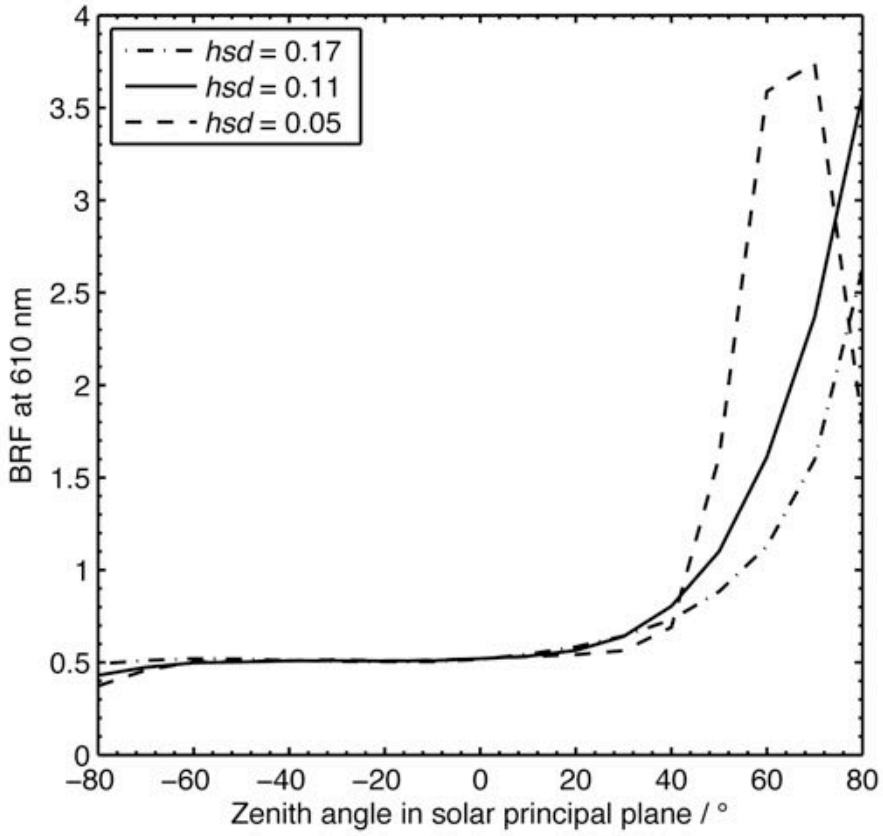

Figure 3.52. BRF in the solar principal plane at 610 nm for 3 different values of the surface roughness parameter (*hsd*) of 0.05 mm, 0.11 mm, 0.17 mm

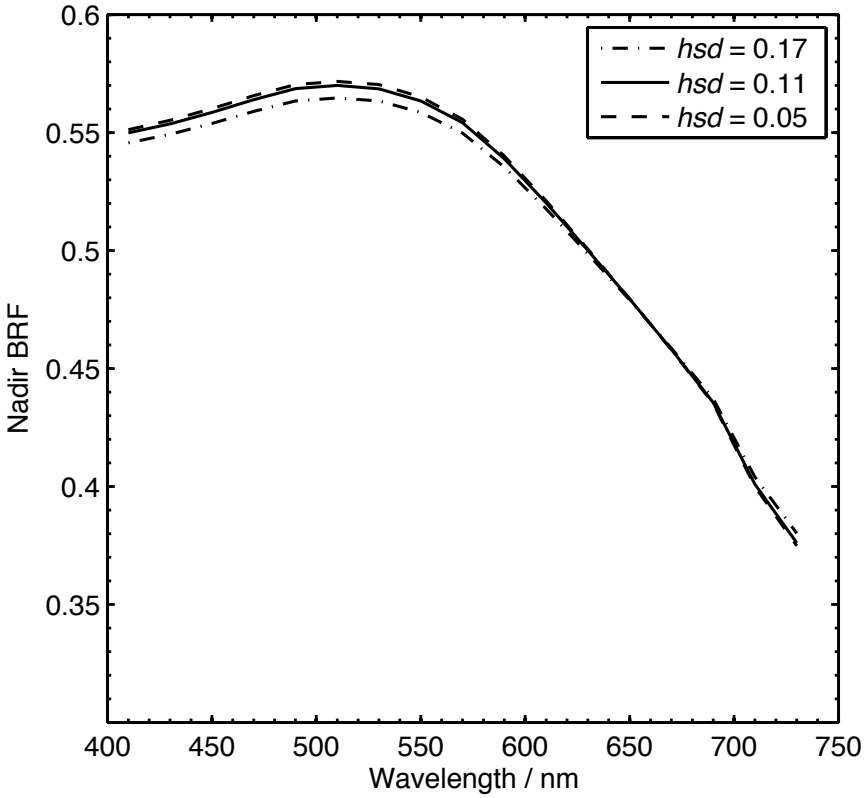

Figure 3.53. Nadir BRF as a function for wavelength for 3 different values of the surface roughness parameter (*hsd*) of 0.05 mm, 0.11 mm, 0.17 mm

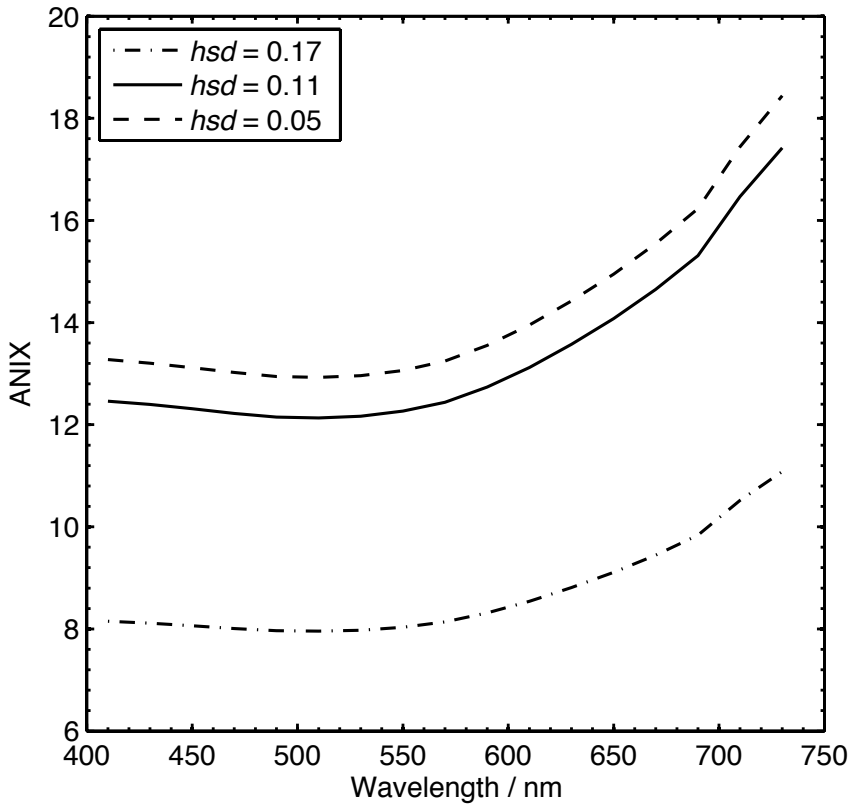

Figure 3.54. Anisotropy index (ANIX) as a function of wavelength for 3 different values of the surface roughness parameter (*hsd*) of 0.05 mm, 0.11 mm, 0.17 mm

Increasing the average height of the surface roughness elements (analogous to the hsd) results in a decrease in the BRF in the forward scattering direction in the solar principal plane of up to 32.6 % at 70° zenith angle at 610 nm, and an increase in the BRF in the backward direction of up to 14.2 % at 80° zenith angle, with a small change (less than 5 %) for viewing zenith angles within 30° of nadir. Decreasing the average height of the surface roughness elements moves the position of the forward scattering peak closer to the angle of specular reflection (60°) and decreases the BRF in the backward direction by up to 13.5 % at 80°. An increase or decrease in the hsd value had a very small (less than 1 %) impact on the nadir BRF for all wavelengths. An increase in the hsd strongly decreased the ANIX value by up to 36.4 % at 730 nm, and showed a small wavelength dependence of less than 2 %, with a decrease in the ANIX value of 34.6 % at 410 nm for the same increase in the hsd. Decreasing the hsd resulted in an increase in the ANIX value of around 6 %, which was effectively constant with wavelength. The observed decrease in the ANIX values with increasing surface roughness was the result of a broadening and flattening of the forward scattering peak. Which occurs because of an increasingly large number of photons that are not reflected directly into the specular direction, but rather are scattered into a wider range of angles owing to the uneven surface. The broadening and flattening of forward scattering peak is evident when the BRF is plotted as a function over the hemisphere in the form of a polar plot given in Figure 3.55 (for an hsd of 0.05 mm) and in Figure 3.56 (for an hsd of 0.17 mm).

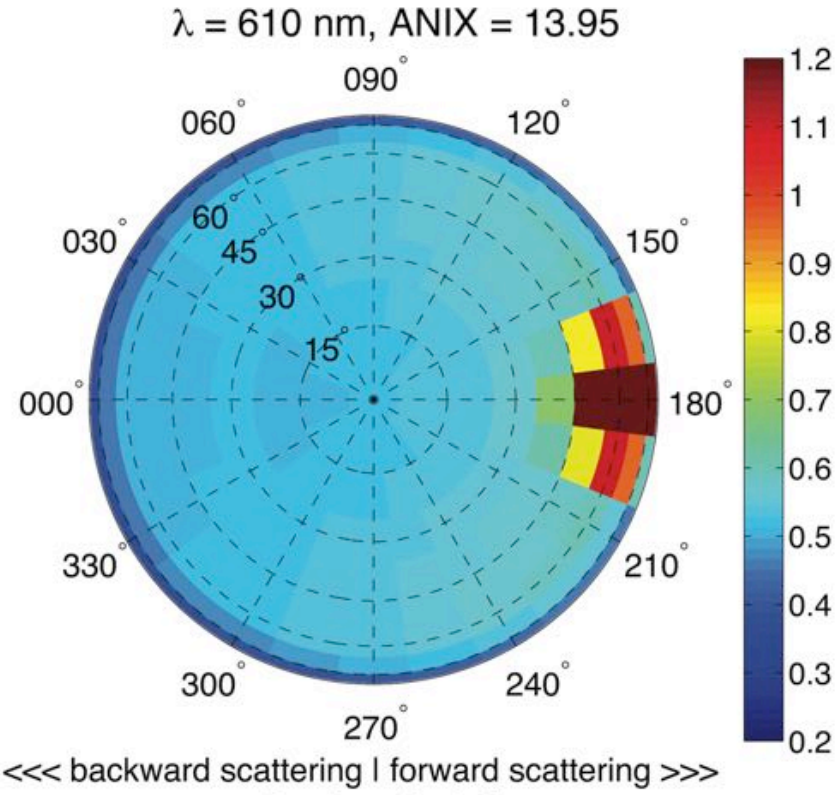

Figure 3.55. BRF at 610 nm with an *hsd* of 0.05 mm

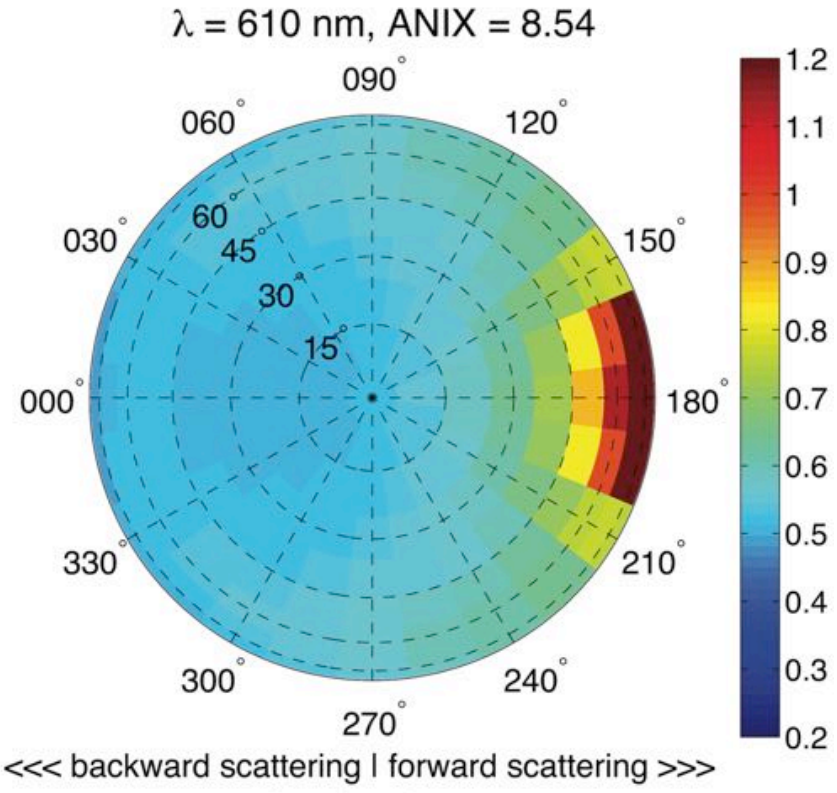

Figure 3.56. BRF at 610 nm with an *hsd* of 0.17 mm

The MATLAB code for processing and plotting the output from the PlanarRad radiative-transfer model 'report.txt' file is given in Appendix 3.

3.4.4.2.7 Sensitivity study summary

Given the default input variables and the associated ranges listed in Table 3.1, the anisotropy in the BRF over the hemisphere (quantified by the ANIX) is most sensitive to changes in the scattering phase function asymmetry parameter, which increases the ANIX by up to 326.6 % at 730 nm. The relative strength of forward scattering determines the likelihood of a photon penetrating deeper into the sea ice, and for a larger asymmetry parameter, increases the probability that the sea ice or the lower boundary absorbs the photon, which reduces the proportion of diffuse reflectance at the surface, increasing the ANIX value. The shape of BRF function over the hemisphere is also sensitive to the surface roughness parameter (*hsd*), particularly for large viewing zenith angles. For example, a decrease in the *hsd* of 0.06 mm resulted in a decrease of 50.1 % in the BRF at 80° in the forward scattering direction in the solar principal plane. The *hsd* appears to strongly influence the position, shape and size of the forward scattering peak, whereas the scattering phase function appears to primarily influence the shape of the BRF function over the hemisphere by changing the proportion of diffusely reflected light. A reduction in the asymmetry parameter of the scattering phase function primarily reduces the ANIX values by increasing the BRF for viewing angles outside of the forward peak, rather than by decreasing the BRF within the forward peak. In general, the BRF at viewing angles outside of the forward scattering peak are more sensitive to changes in the sea ice IOPs than the BRF in the forward peak itself, which makes sense given that a large proportion of photons scattered in the specular direction do not enter the medium, but are reflected at the interface. The *hsd* is therefore the

only parameter that significantly affects the magnitude and shape of the forward peak without strongly affecting the magnitude of the BRF for viewing angles near to nadir. Other parameters such as the ice thickness, scattering coefficients, and absorption coefficients generally vary the ANIX value by less than 10 %.

BRF at the nadir viewing position was most sensitive to the scattering phase function asymmetry parameter for all wavelengths, which decreased the BRF at the nadir viewing position by up to 81.5 % at 730 nm. Varying the ice thickness, scattering coefficients and absorption coefficients changed the BRF at nadir by less than 15 % for all wavelengths, while the varying the lower boundary reflectance resulted in a change to the nadir BRF of less than 1 % over all wavelengths. The wavelength dependence to the BRF appears to be strongly affected by an increase in the scattering phase function asymmetry parameter, owing to increased penetration depth at shorter wavelengths, which causes the reflectance of the lower boundary to impact more strongly on the spectral BRF. Varying the absorption coefficient changed the nadir BRF by up to 12.4 % at 730 nm, but changed the nadir BRF less than 1 % for wavelengths less than 650 nm.

3.5 Experiment results

The sea ice CCRF is presented for the two laboratory CCRF acquisitions: M1 and M2, which were conducted on the 7th and 17th of February 2014 respectively. M1 was performed with a sea ice thickness of 22 cm, and M2 was performed using the same batch of laboratory-generated sea ice, but with an increased thickness of 27 cm. Both acquisitions were performed under the same illumination conditions with an incident angle of 60°.

The input parameters for the ice thickness and surface roughness used in the modeling study were based on physical measurements of laboratory-generated sea ice. Ranges of realistic values for the scattering coefficient, phase function, extinction coefficient, absorption coefficient and refractive index were obtained from the literature and are given in Table 3.1. The middle value from each range was used as the input into the model. In order to the fit the model to the observed CCRF the scattering coefficient was adjusted over the range of realistic values. A scattering coefficient of 190 m^{-1} was found to provide the best fit between the observed CRCF for the M1 acquisition and the PlanarRad model simulation. To improve the fit of the model at viewing angles around the forward scattering peak the surface roughness parameter was adjusted within ±1 standard deviation of the measured surface roughness scale for laboratory-generated sea ice. The thickness of the sea ice in the model was increased by 5 cm to account for the thicker laboratory-generated sea ice used for the M2 acquisition. Identical values for the input parameters were used to model the M2 acquisition, excluding the surface roughness parameter and the ice thickness, which were varied as described above.

An accurate characterization of the surface roughness scale was not obtained for the M1 or M2 acquisitions so the surface roughness parameter was adjusted within a range of realistic values to improve the fit between the measured and the modeled data for the M1 and the M2 acquisitions. The range of realistic values for the surface roughness parameter was acquired by measuring the wavelength and amplitude of roughness elements of laboratory-generated sea ice as described in Section 3.4.4.1.2. The roughness elements that were measured were generated for a different batch of laboratory sea ice, but the sea

ice was grown using the same methodology and the roughness elements were considered characteristic of the roughness elements in the M1 and M2 acquisitions.

A summary of the input parameters used to model the M1 and M2 acquisitions are given in Table 3.3.

Input parameters	Value for M1	Value for M2
Incident zenith	60°	60°
Incident azimuth	0°	0°
Refractive index of pure ice matrix	1.31	1.31
Refractive index of air	1	1
Surface roughness parameter	0.16	0.11
Absorption coefficient	Given in Figure 3.35	Given in Figure 3.35
Scattering coefficient	190 m^{-1}	190 m^{-1}
Phase function	0.93	0.93
Ice thickness	22 cm	27 cm
Lower boundary albedo	Given in Figure 3.36	Given in Figure 3.36

Table 3.3. List of PlanarRad input parameters used to model the M1 and M2 CCRF acquisitions

The following sections present the measured CCRF and modeled quad-averaged BRF for all viewing angles over the upward facing hemisphere in the form of polar plots for the M1 and M2 acquisitions. As explained in Chapter 1, the BRF is not a measurable quantity and thus measured reflectance factors are reported as CCRF. However, the CCRF provides a close approximation of the BRF, and is numerically equivalent to the BRF assuming the BRDF is isotropic over the solid angle subtended by the detector (Bourgeois et al., 2006a). In

order to further improve the comparability between the measured and modeled quantities the CCRF was converted to the quad-averaged CCRF. Quad-averaged CCRF was calculated by linearly interpolating the CCRF over the hemisphere using a Delaunay triangle-based method (de Berg et al., 2008), and by taking the average value within each quad. Throughout this section the more general term 'reflectance factor' is used to refer to either the BRF or CCRF measurements. The polar plots are a 2-D projection of each quad in the upward facing hemisphere, the colour of each quad corresponds to the average value of the CCRF or BRF in that quad. The polar plots have a maximum viewing angle of 60° central to each quad, which was limited by the maximum viewing angle of the laboratory goniometer. The difference between the quad-average BRF and CCRF was calculated and plotted in the form of a polar plots for the M1 and M2 acquisitions. The root mean square error (RMSE) is the average of the differences in the quad-averaged reflectance factors and was calculated as follows:

$$RMSE = \sqrt{\frac{\sum_{i=0}^{n} (BRF - CCRF)^2}{n}} \qquad \text{Eq. 3.15}$$

where n is the number of quads.

The coefficient of variation of the RMSE $CV(RMSE)$ was calculated by normalizing the RMSE to the mean BRF:

$$CV(RMSE) = \frac{RMSE}{\overline{R}} \qquad \text{Eq. 3.16}$$

where $\overline{R}$ is the mean BRF value over the hemisphere.

The CV(RMSE) is plotted in the following sections as a function of wavelength in the form of a bivariate plots. The BRF and CCRF in the solar principal plane, and as a function of wavelength, are given in the form of bivariate plots for the

M1 and M2 acquisitions. The ANIX value describes the extent of the anisotropy in the reflectance factors over the hemisphere, and is defined as the ratio of the maximum reflectance factor to the minimum reflectance factor over the hemisphere. The ANIX values for the M1 and M2 acquisition are given as a function of wavelength in the form of bivariate plots in the following sections. The BRF and CCRF presented in this section are band-averaged quantities; each of the bands have a width of 20 nm, and are centered at wavelengths of 410 nm, 510 nm, 610 nm and 710 nm.

3.5.1 M1 acquisition

The M1 CCRF acquisition was carried out with a sea ice thickness of 22 cm. Modeled and measured reflectance factors for the M1 acquisition are presented in this section.

3.5.1.1 M1: CCRF and BRF over the hemisphere

Quad-averaged measured and modeled reflectance factors for the M1 acquisition for wavelength bands 410 nm, 510 nm, 610 nm and 710 nm are given in Figure 3.57 to Figure 3.68. The absolute difference in the quad-averaged modeled and measured values are given in Figure 3.59, Figure 3.62, Figure 3.65, and Figure 3.68 for the wavelengths bands 410 nm, 510 nm, 610 nm and 710 nm.

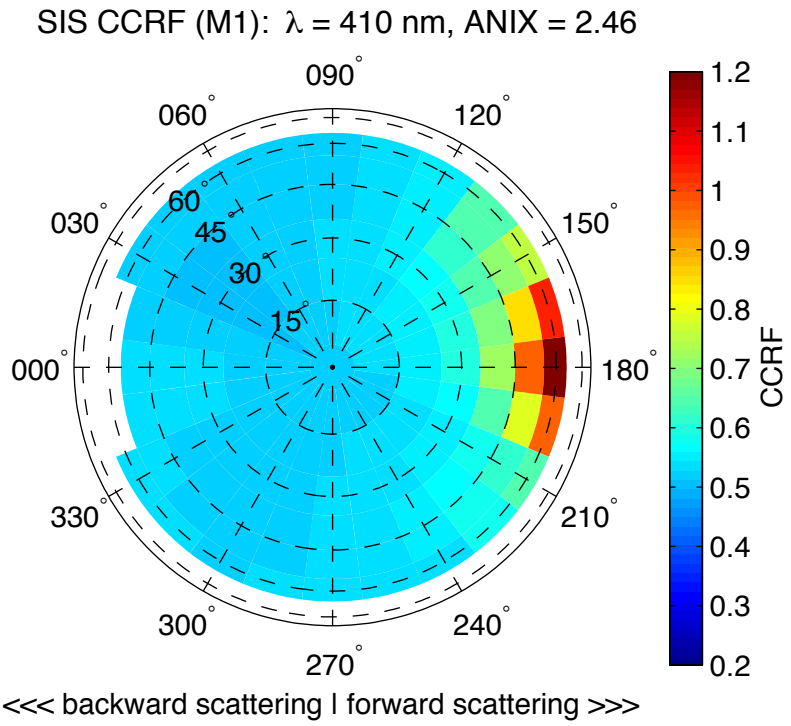

Figure 3.57. Quad-averaged CCRF measurements (M1) of laboratory generated sea ice with 22 cm thickness at 410 nm

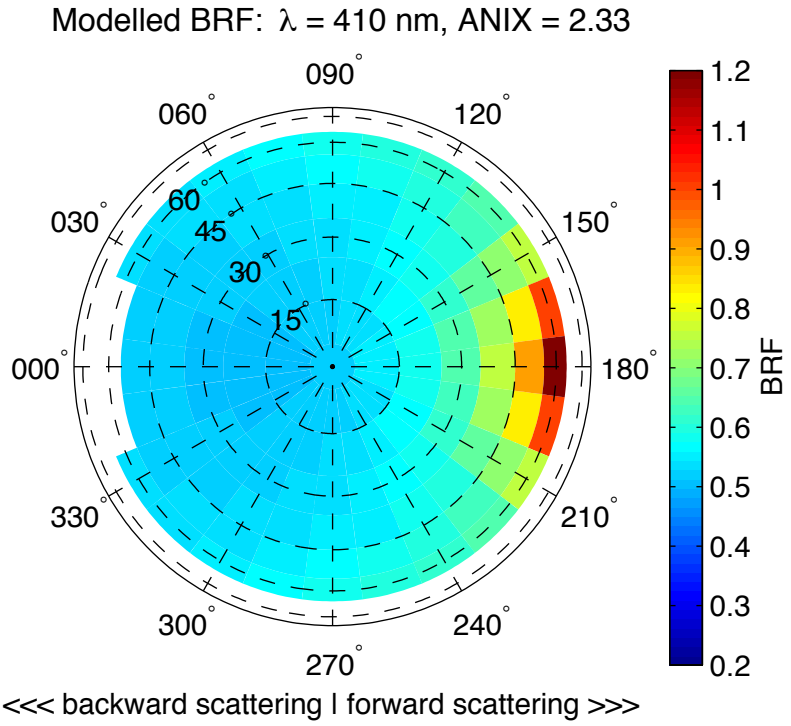

Figure 3.58. Quad-averaged modeled BRF of laboratory generated sea ice with 22 cm thickness at 410 nm

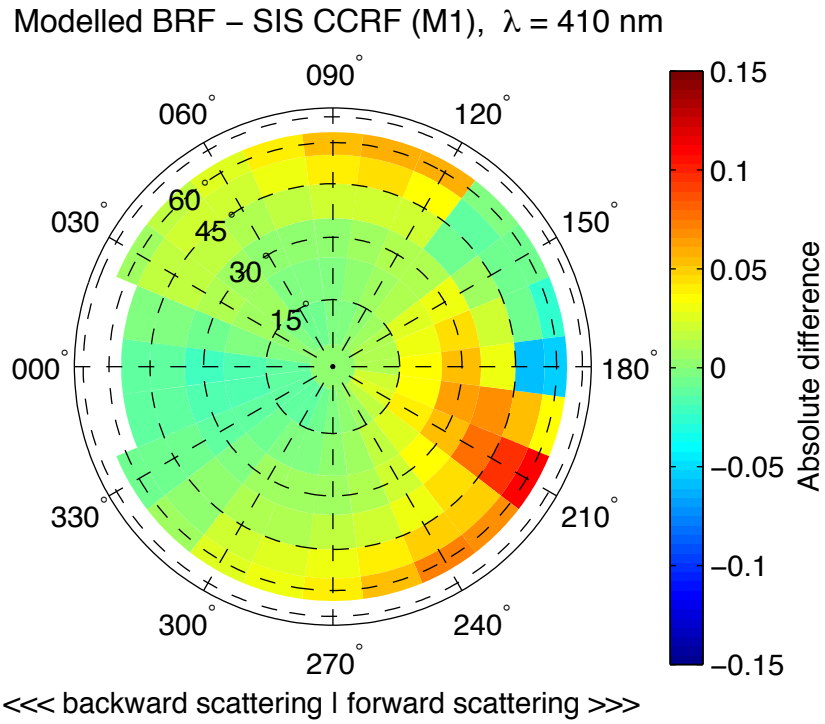

Figure 3.59. Absolute differences in modeled and measured sea ice reflectance factors at a wavelength of 410 nm

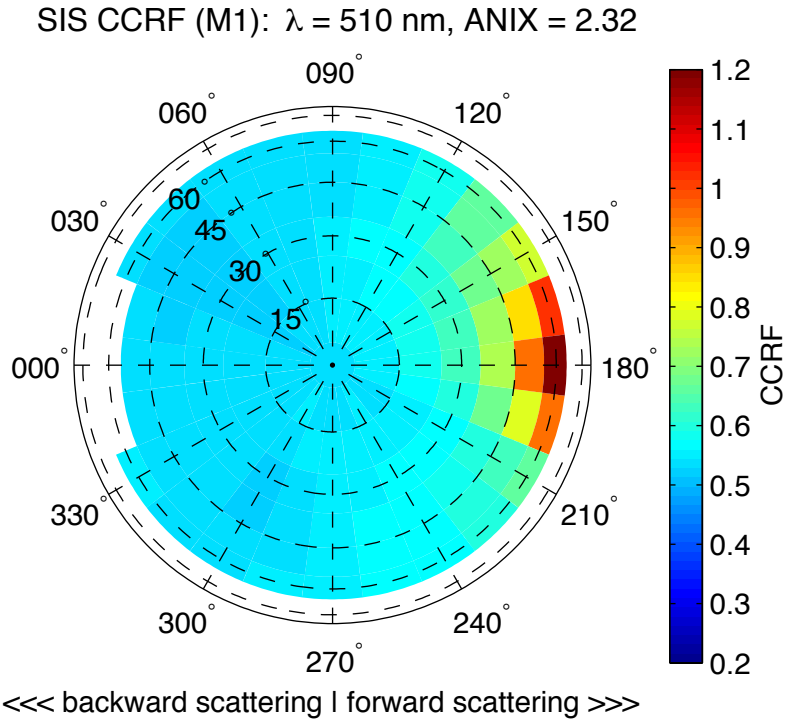

Figure 3.60. Quad-averaged CCRF measurements (M1) of laboratory generated sea ice with 22 cm thickness at 510 nm

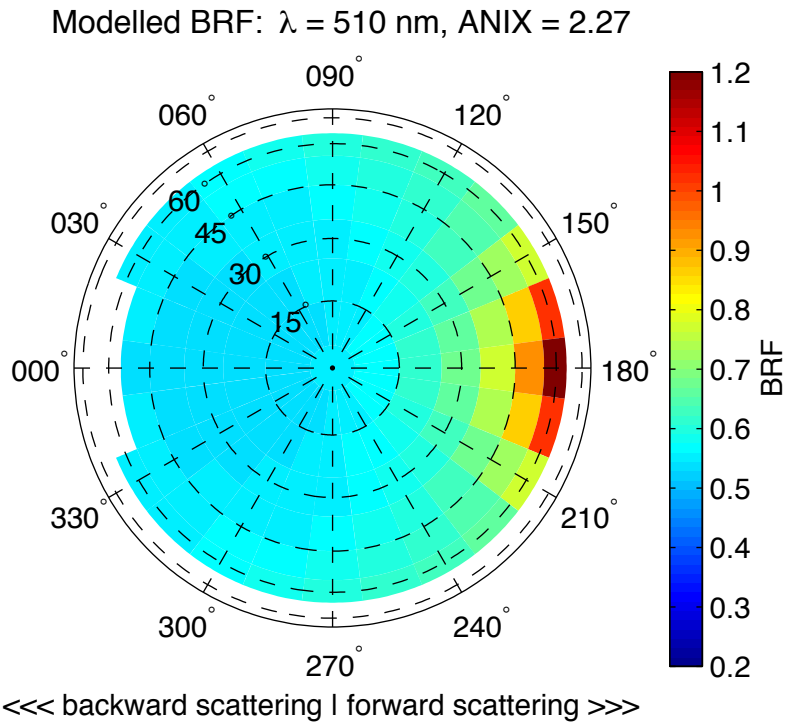

Figure 3.61. Quad-averaged modeled BRF of laboratory generated sea ice with 22 cm thickness at 510 nm

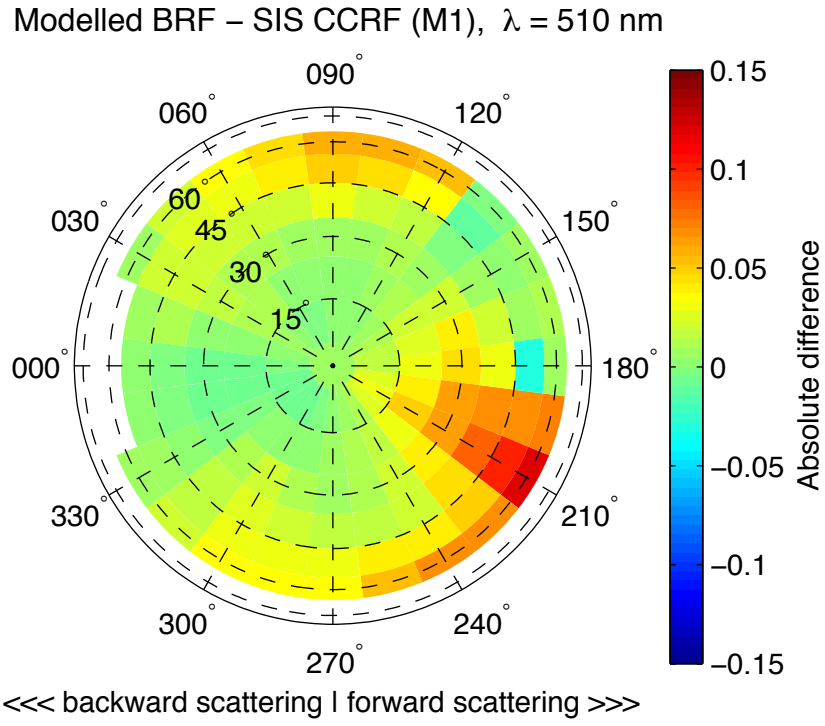

Figure 3.62. Absolute differences in modeled and measured sea ice reflectance factors at a wavelength of 510 nm

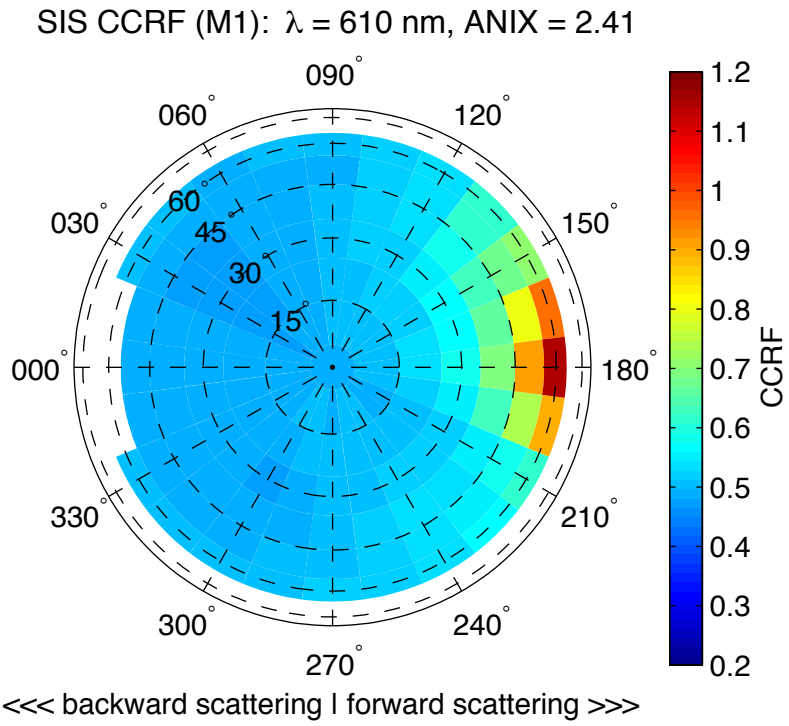

Figure 3.63. Quad-averaged CCRF measurements (M1) of laboratory generated sea ice with 22 cm thickness at 610 nm

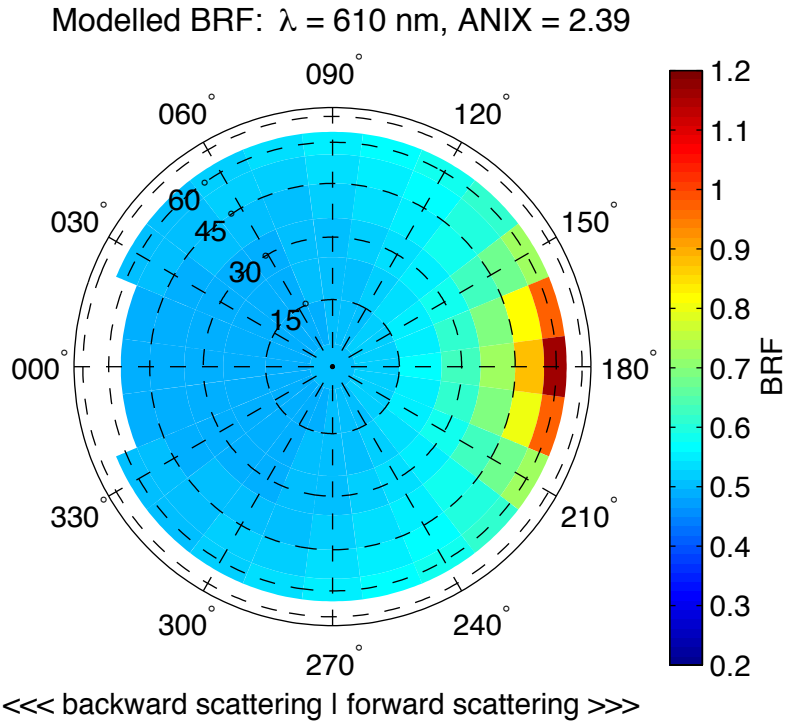

Figure 3.64. Quad-averaged modeled BRF of laboratory generated sea ice with 22 cm thickness at 610 nm

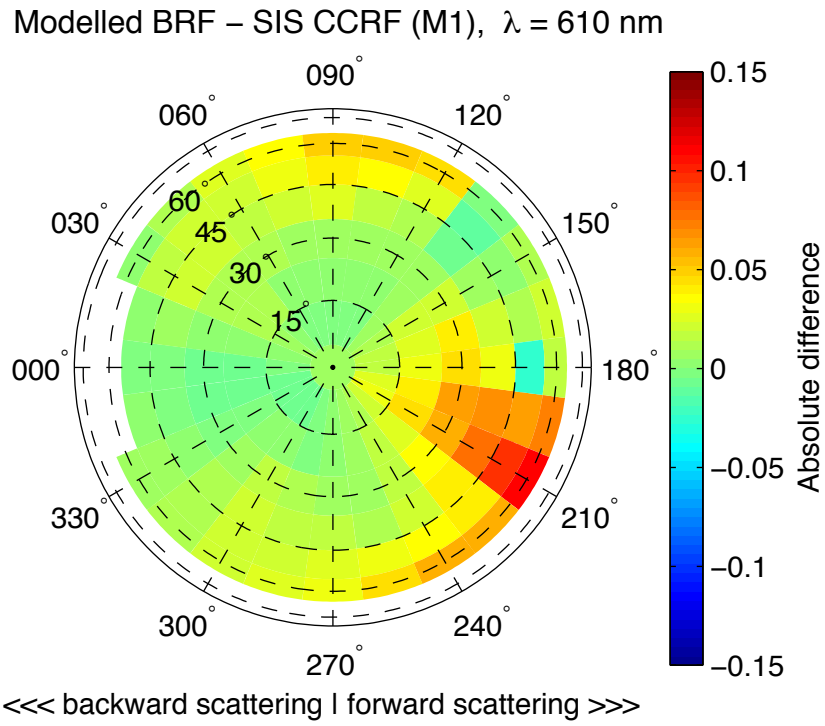

Figure 3.65. Absolute differences in modeled and measured sea ice reflectance factors at a wavelength of 610 nm

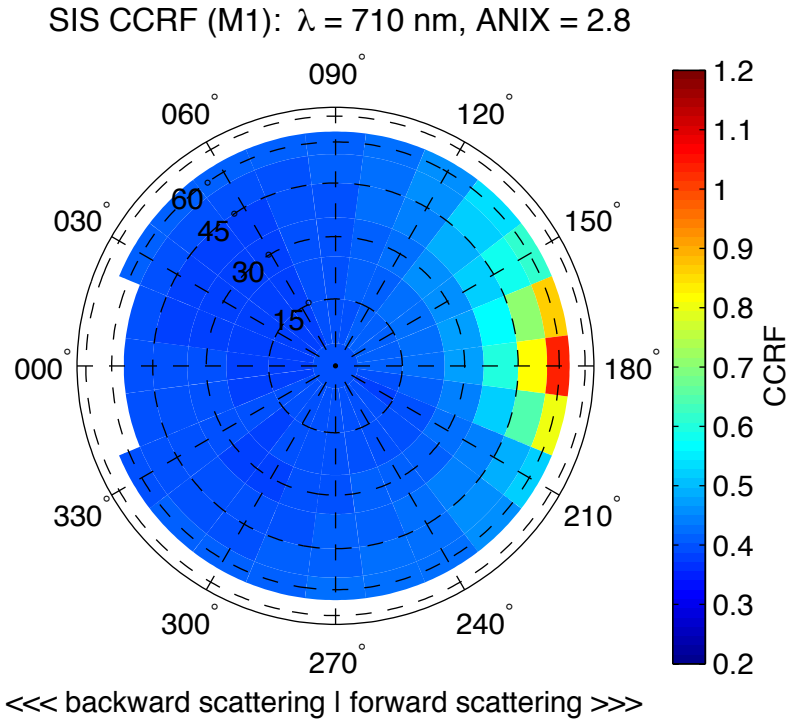

Figure 3.66. Quad-averaged CCRF measurements (M1) of laboratory generated sea ice with 22 cm thickness at 710 nm

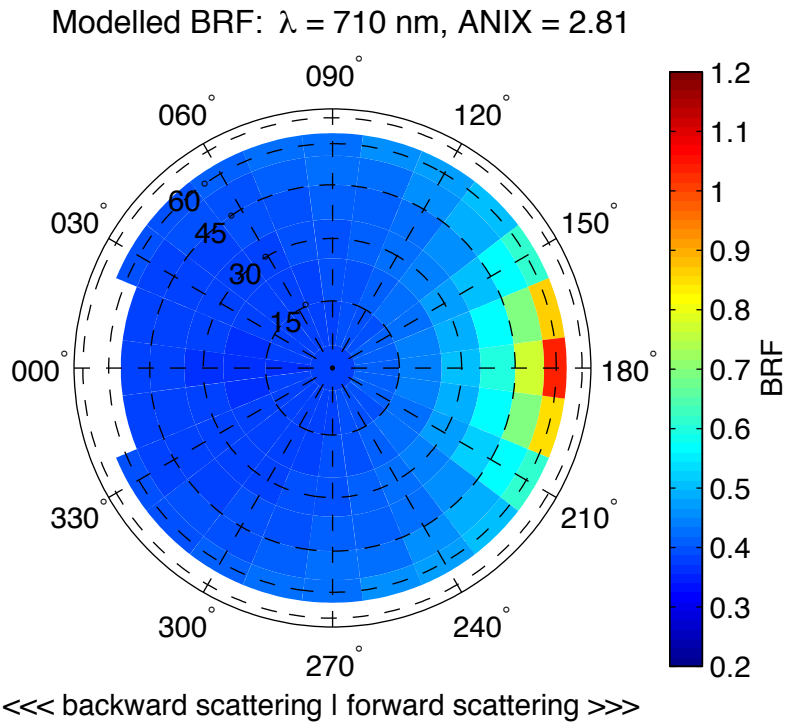

Figure 3.67. Quad-averaged modeled BRF of laboratory generated sea ice with 22 cm thickness at 710 nm

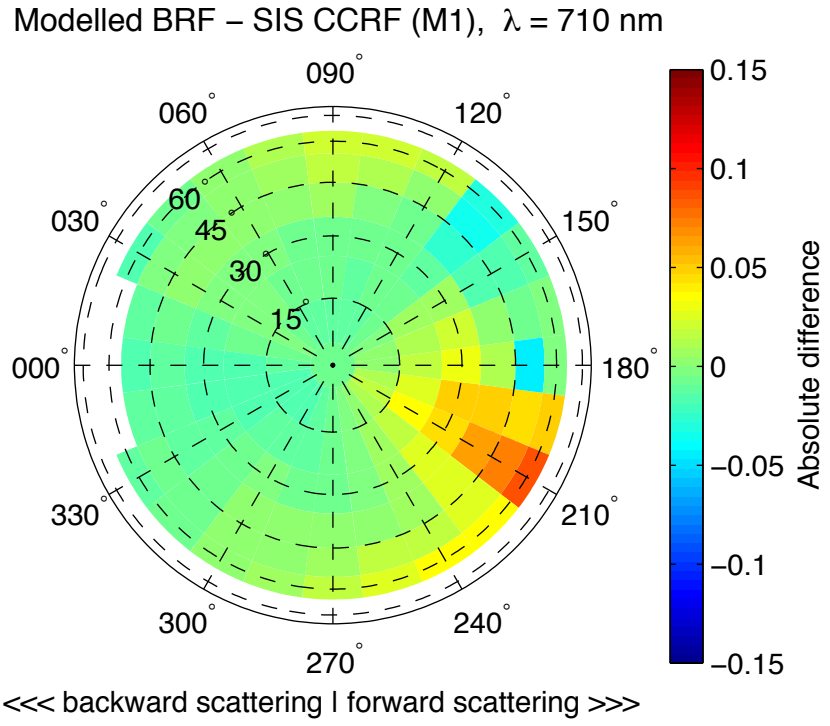

Figure 3.68. Absolute differences in modeled and measured sea ice reflectance factors at a wavelength of 710 nm

The measured and modeled reflectance factors show a strong forward scattering peak, which is strongest in the specular direction of 60° zenith angle and 180° azimuth angle. The reflectance factor for the quad centered at 60° zenith angle and 180° azimuth angle was greatest at 510 nm, and had a value of 1.21 for the measured CCRF, and a value of 1.20 for the modeled BRF. The forward peak was weakest at 710 nm with a reflectance factor value of 1.04 for both the measured CCRF and modeled BRF. Despite the forward peak being weakest at longer wavelengths, both measured and modeled reflectance factors have an ANIX values that increase with wavelength up to a maximum value of 2.9 at 730 nm. In general, the angular dependence to the reflectance factors over the hemisphere is minimal for viewing angles in the backward direction and for viewing angles less than 15° in the forward direction for both the measured and modeled reflectance factors over the wavelength range measured. The laboratory measured reflectance factors are near symmetric over the solar principal plane, whereas the modeled reflectance factors are perfectly symmetric. The measured and modeled reflectance factors for sea ice generally agree very well for most of the quads, with absolute differences typically around ± 0.02. The maximum difference between and measured and modeled reflectance factors was 0.12 for the quad centered at the viewing angle of 60° and an azimuth angle of 210° for a wavelength of 530 nm. The averaged difference between the quads was quantified by the CV(RMSE) and was typically around 5 %, and showed a negligible wavelength dependence of less than 1 % for the M1 acquisition. The maximum CV(RMSE) for the M1 acquisition was 5.4 % at 550 nm.

3.5.1.2 M1: reflectance factors at the nadir view angle with wavelength

Nadir reflectance of the laboratory generated sea ice as a function of wavelength is given in Figure 3.69 along with the output from the PlanarRad radiative transfer model. The uncertainty bars of the laboratory measurements are 2 standard deviations of 4 replicate measurements of the sea ice surface taken at different times during the CCRF acquisition.

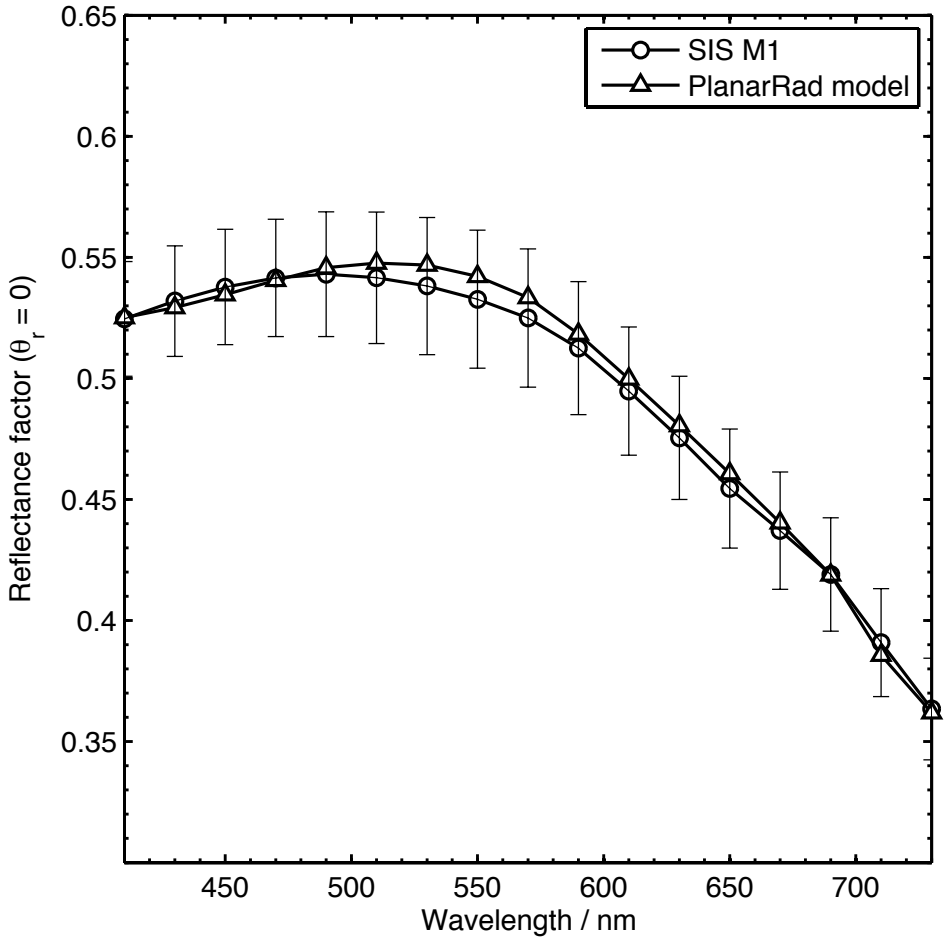

Figure 3.69. Measured and modeled nadir reflectance factors with wavelength for sea ice with thickness of 22 cm. Uncertainty bars are given to 2 standard deviations of the replicate nadir measurements

The nadir reflectivity of the sea ice decreased with wavelength for the wavelength range 490 nm to 730 nm by approximately 0.18, but increased with wavelength from 410 nm to 490 nm by approximately 0.02. Despite a smaller absorption coefficient at 410 nm the model reproduced the general shape of the

nadir reflectance spectra, but with a slight difference in the peak of reflectivity, which was 530 nm for the model and 490 nm for the measured results, the minor differences between the modeled and measured nadir reflectance factors were well within the uncertainty of the laboratory measurements and was typically less than 0.02.

3.5.1.3 M1: reflectance factors in the solar principal plane

Measured and modeled reflectance factors in the solar principal plane for the M1 acquisition are presented in Figure 3.70.

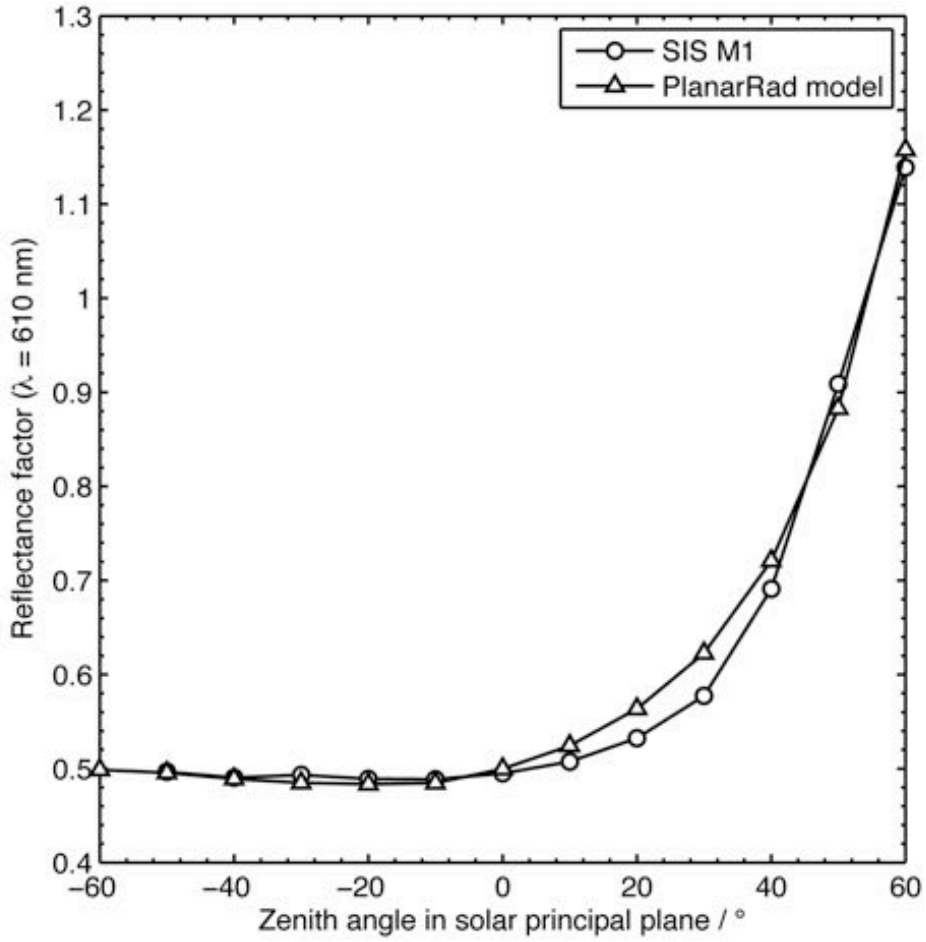

Figure 3.70. Measured and modeled reflectance factors in the solar principal plane of sea ice with a thickness of 22 cm

The measured reflectance factors for the M1 acquisition increased by 0.64 over the viewing angle range 0° to 60° zenith in the forward direction in the solar

principal plane. The modeled reflectance factors show a very similar shape to the measured reflectance curve, and are typically within 0.02 of the measured values in the solar principal plane. The increase in the modeled reflectance factor was 0.66 from 0° to 60° zenith angle in the forward direction. Both the measured and modeled results show negligible angular dependence in the solar principal plane for viewing angles 0° to 60° in the backward direction.

3.5.1.4 M1: CV(RMSE) with wavelength

The coefficient of variation of the RMSE between the measured and modeled reflectance factors is presented in Figure 3.71.

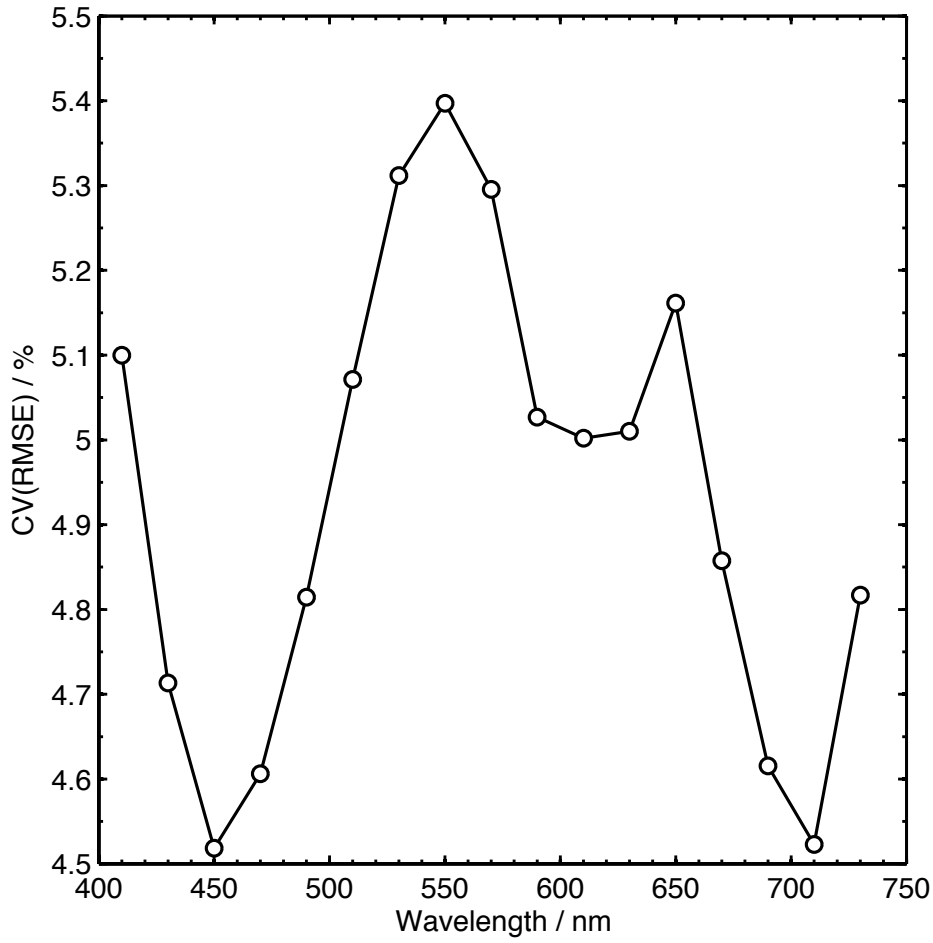

Figure 3.71. Coefficient of variation of the root mean squared error (RMSE) between the measured and modeled reflectance factors as a function of wavelength

The CV(RMSE) was typically 5 % for the M1 acquisition, and was greatest at 550 nm, but has a wavelength dependence of less than ± 0.5 %.

3.5.1.5 M1: anisotropy index (ANIX) with wavelength

Anisotropy in the reflectance factors over the hemisphere was quantified by the ANIX value, and is given as the function of wavelength in Figure 3.72 for both the measured and modeled quantities.

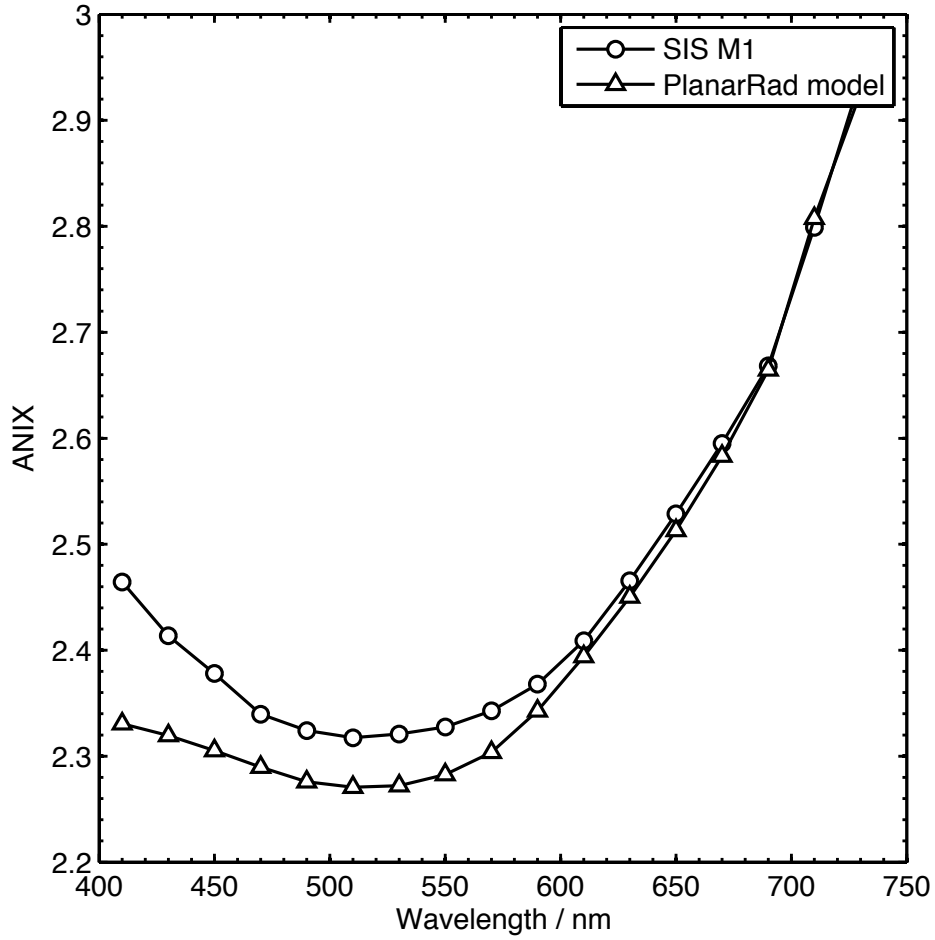

Figure 3.72. Anistropy index (ANIX) as a function of wavelength for the measured and modeled reflectance factors for 22 cm thick laboratory generated sea ice

The anisotropy was weakest at 510 nm for both the modeled and measured reflectance factors; at 510 nm the ANIX value was 2.27 and 2.32 for the modeled and measured reflectance factors respectively. The measured ANIX

values decreased from 410 nm to 510 nm and increased to a maximum of 2.94 at 730 nm. The model reproduced the same general shape to the ANIX curve, but had an ANIX value that was 0.13 lower than the measured ANIX value at 410 nm, indicating that the model underestimated the anisotropy in the sea ice reflectance more strongly at shorter wavelengths. The model closely matched the measured ANIX values for longer wavelengths, and had a maximum ANIX value of 2.93 at 730 nm, which is within 0.01 of the measured value.

3.5.2 M2 acquisition

The M2 CCRF acquisition was carried out with same batch of sea ice as the M1 acquisition, but 75L of seawater was added on top of the M1 sea ice layer increasing its thickness for the M2 acquisition by 5 cm. Modeled and measured reflectance factors for M2 acquisition are presented in this section.

3.5.2.1 M2: CCRF and BRF over the hemisphere

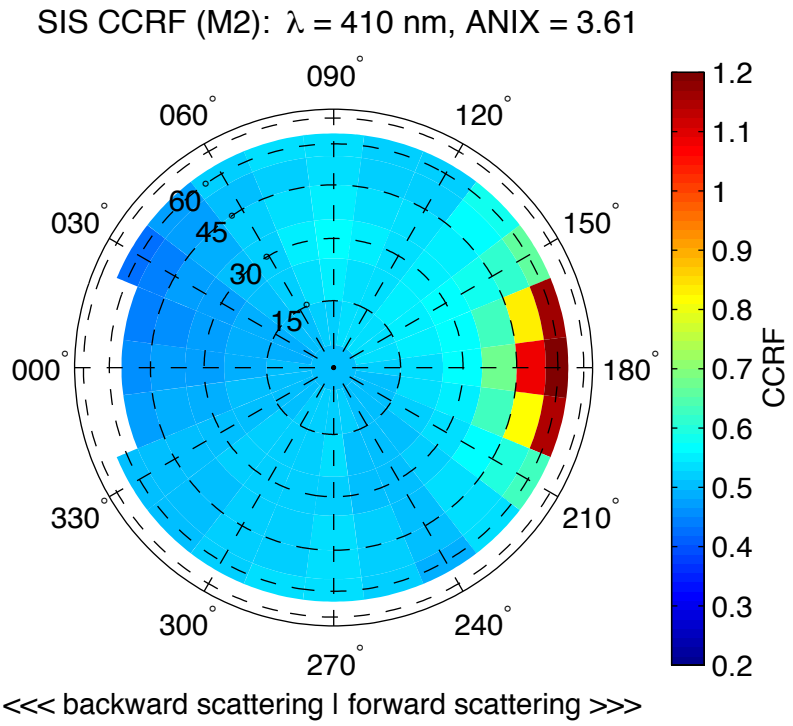

Figure 3.73. Quad-averaged CCRF measurements (M2) of laboratory generated sea ice with 27 cm thickness at 410 nm

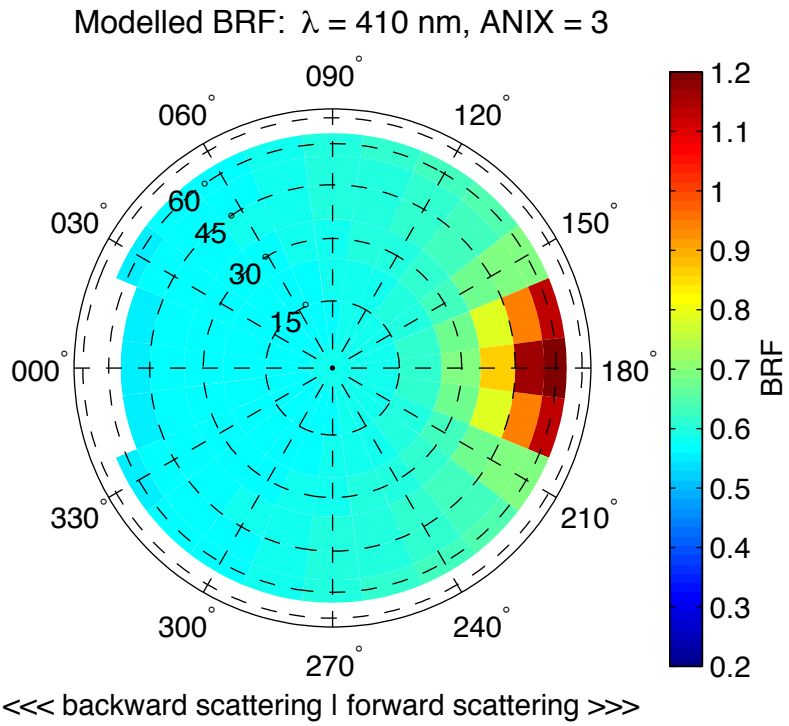

Figure 3.74. Quad-averaged modeled BRF of laboratory generated sea ice with 27 cm thickness at 410 nm

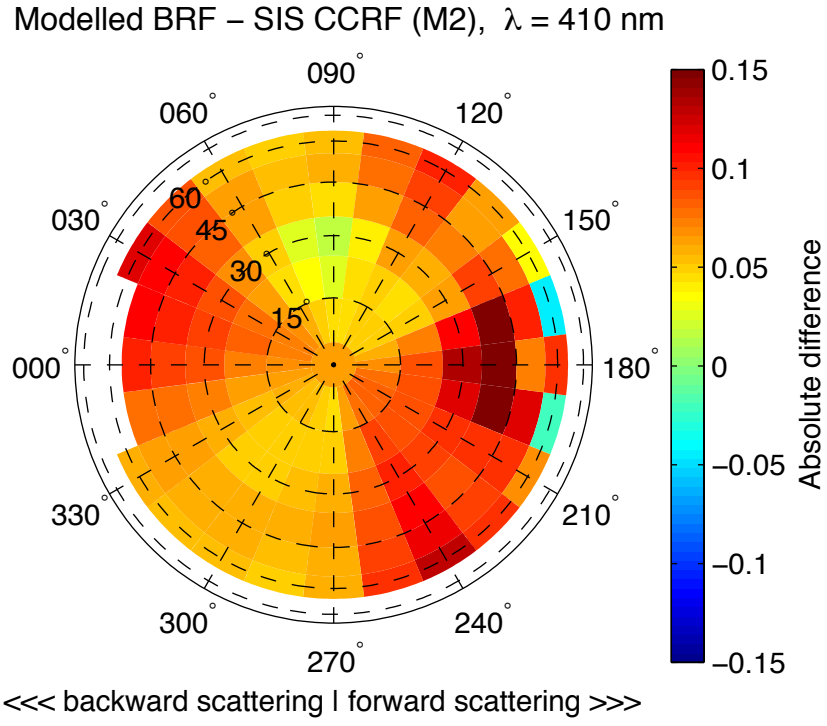

Figure 3.75. Absolute differences in modeled and measured sea ice reflectance factors at a wavelength of 410 nm

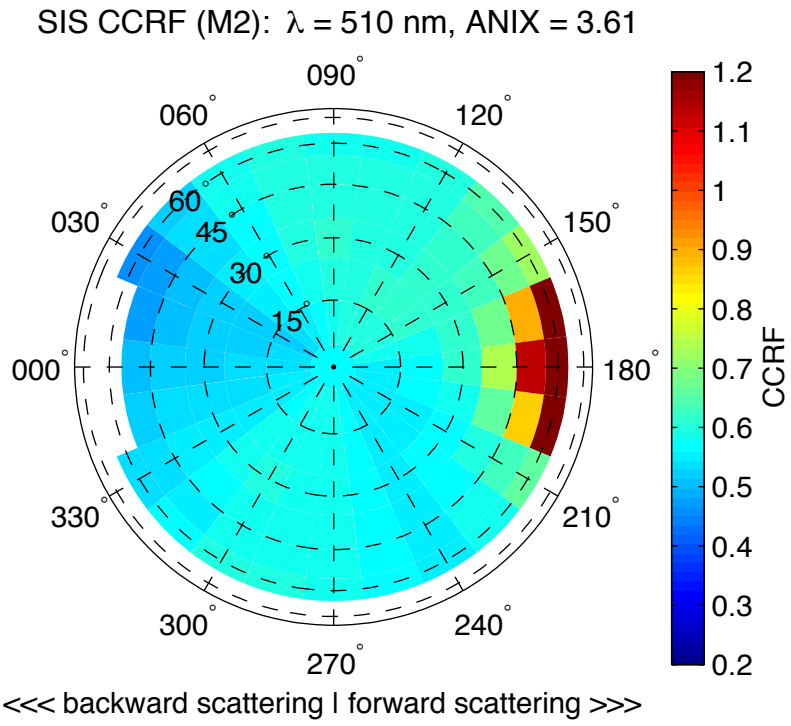

Figure 3.76. Quad-averaged CCRF measurements (M2) of laboratory generated sea ice with 27 cm thickness at 510 nm

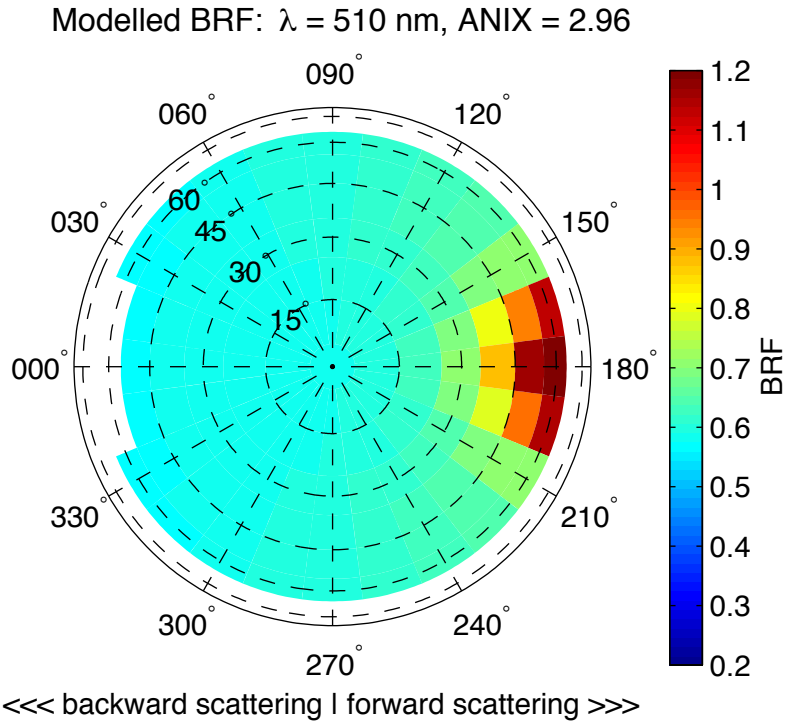

Figure 3.77. Quad-averaged modeled BRF of laboratory generated sea ice with 27 cm thickness at 510 nm

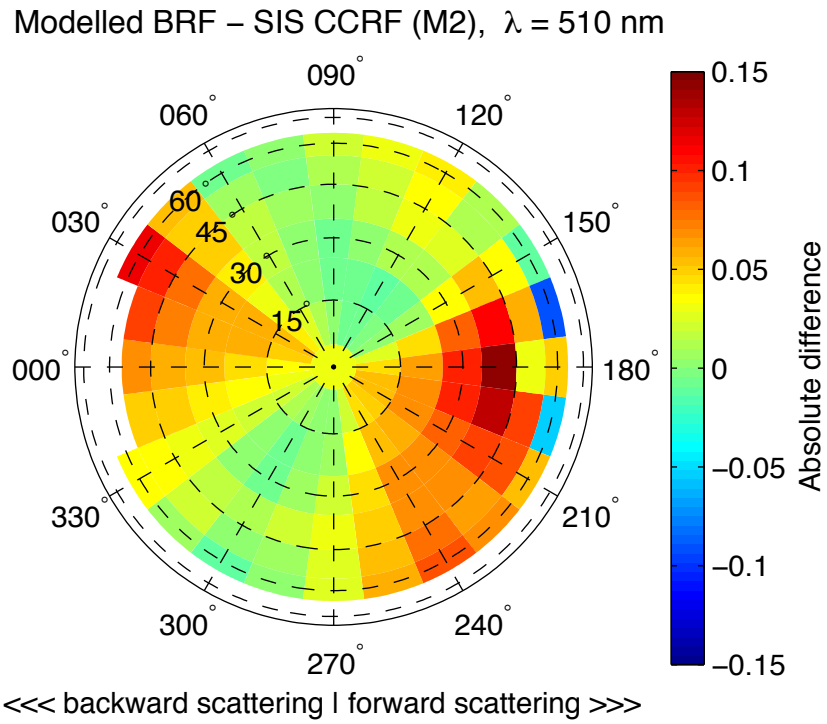

Figure 3.78. Absolute differences in modeled and measured sea ice reflectance factors at a wavelength of 510 nm

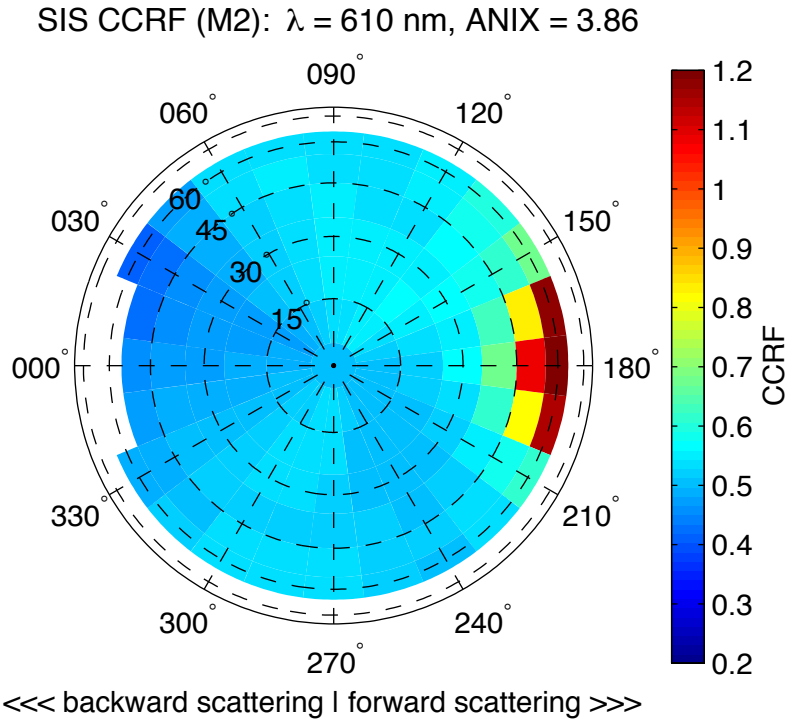

Figure 3.79. Quad-averaged CCRF measurements (M2) of laboratory generated sea ice with 27 cm thickness at 610 nm

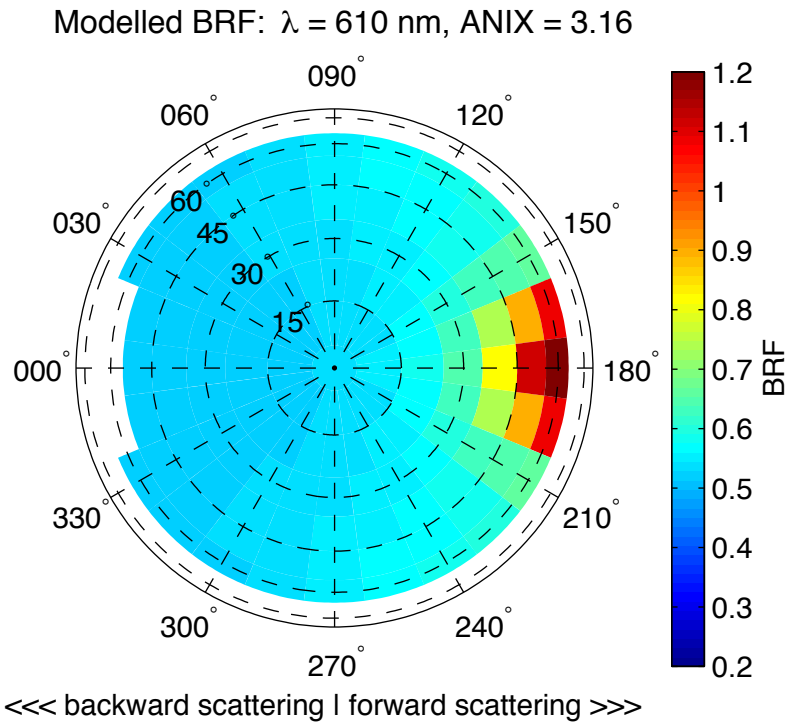

Figure 3.80. Quad-averaged modeled BRF of laboratory generated sea ice with 27 cm thickness at 610 nm

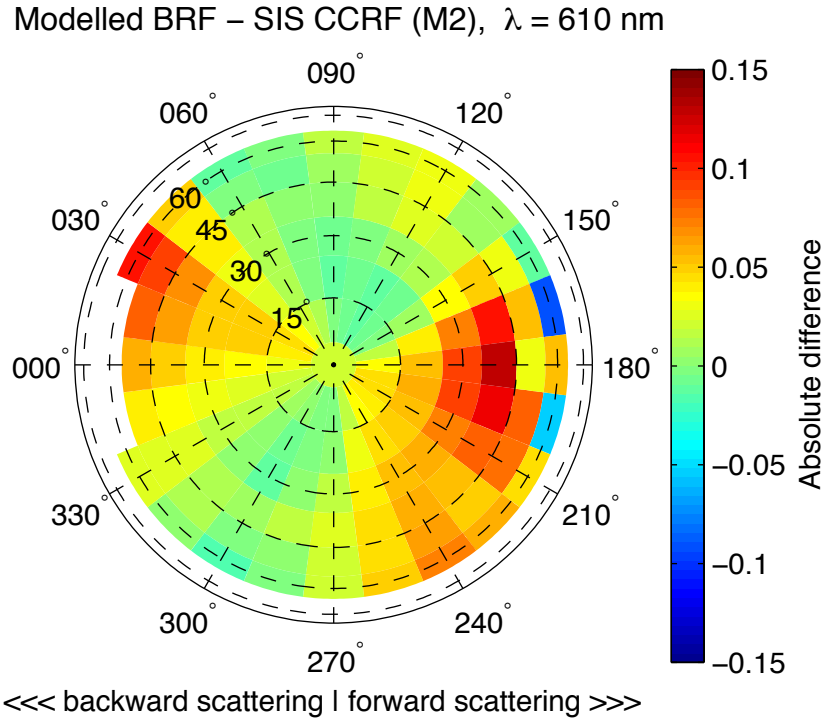

Figure 3.81. Absolute differences in modeled and measured sea ice reflectance factors at a wavelength of 610 nm

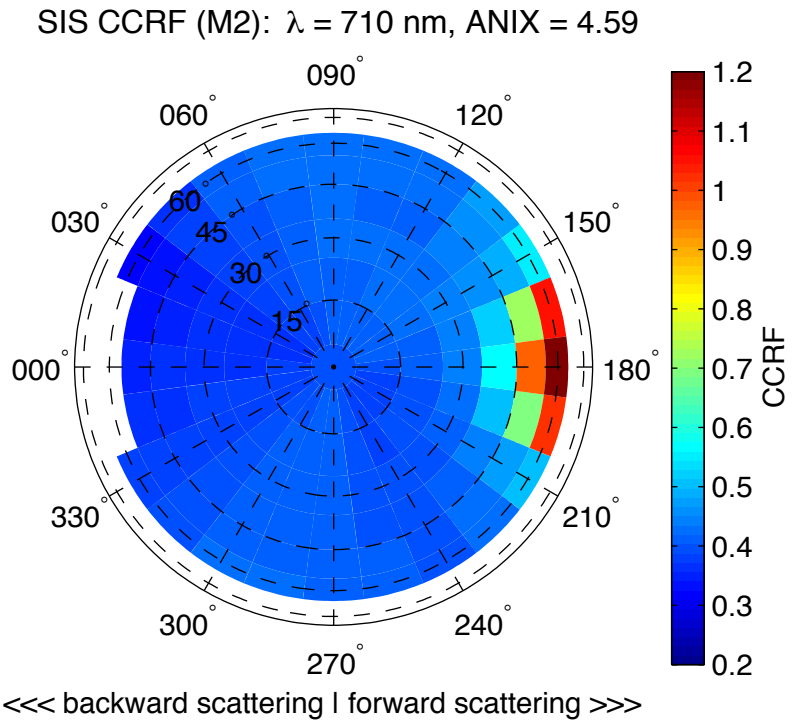

Figure 3.82. Quad-averaged CCRF measurements (M2) of laboratory generated sea ice with 27 cm thickness at 710 nm

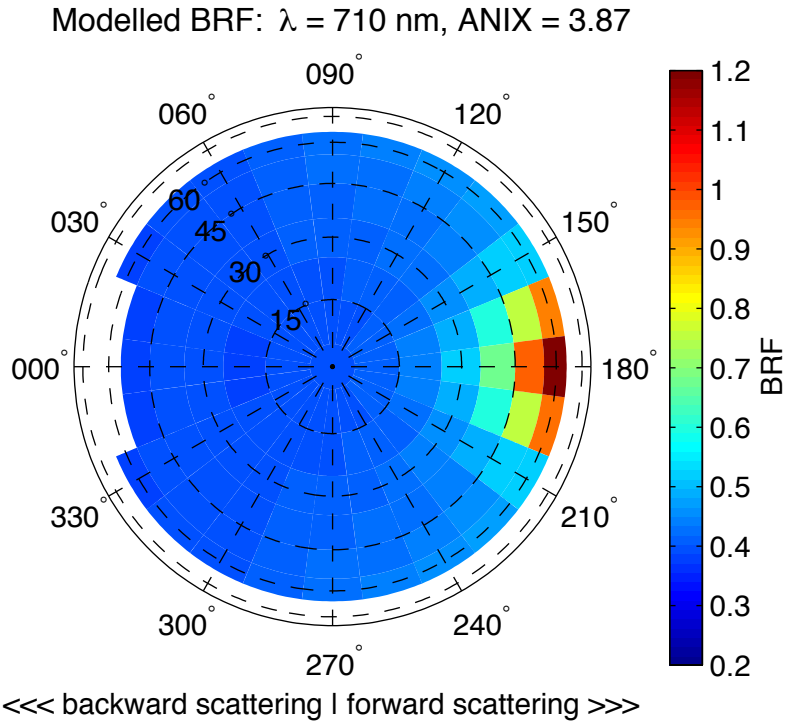

Figure 3.83. Quad-averaged modeled BRF of laboratory generated sea ice with 27 cm thickness at 710 nm

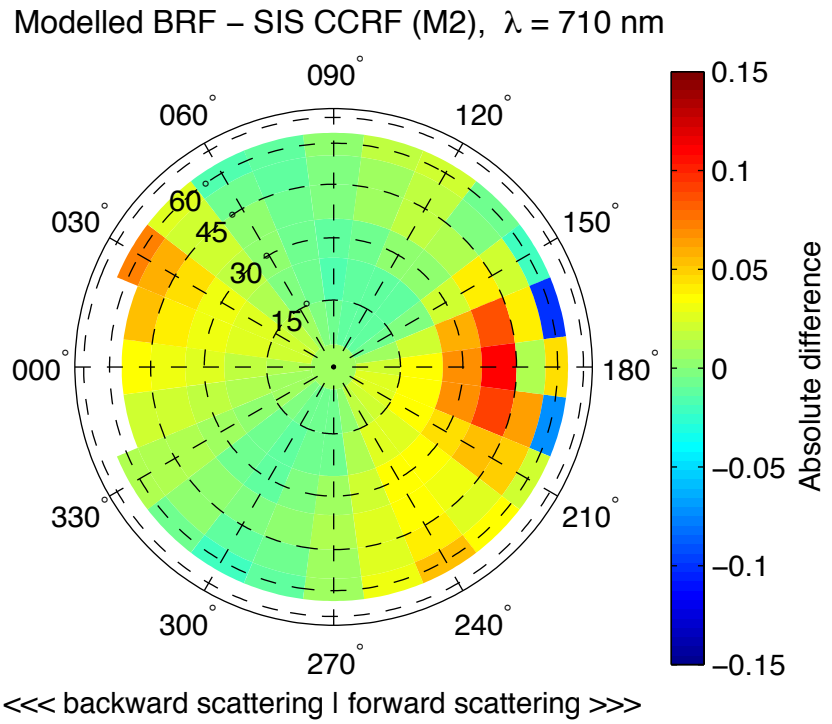

Figure 3.84. Absolute differences in modeled and measured sea ice reflectance factors at a wavelength of 710 nm

The M2 measured and modeled reflectance factors show a strong forward scattering peak and the shape over the hemisphere was similar to the M1 acquisition, with the greatest reflectance factor at the same viewing angle as the M1 measurement (60° zenith angle and 180° azimuth angle). However, the M2 measurement had a much stronger forward scattering peak with a maximum of 1.63 at 510 nm, compared to a reflectance factor of 1.20 for the M1 measurement at 510 nm. The stronger forward peak in the M2 measurement is evident in the ANIX values, which increased to a maximum of 4.59 at 710 nm, compared to maximum of 2.80 for the M1 acquisition at 710 nm. Despite the increase in anisotropy with wavelength the forward peak was weakest at 710 nm in the M2 acquisition, with a reflectance factor of 1.45 for the measured CCRF and 1.49 for the modeled BRF. Indicating that both the M1 and M2 acquisitions generally had the same wavelength dependence to the anisotropy and the strength of the forward peak. Angular dependence to the reflectance

factors over the hemisphere for the M2 acquisition also generally followed the same pattern as observed for the M1 acquisition, with minimal effects for viewing angles in the backward direction and for viewing angles less than 15° in the forward direction for both the measured and modeled reflectance factors. The laboratory measured reflectance factors are near symmetric over the solar principal plane for the M2 acquisition, whereas the modeled reflectance factors are perfectly symmetric, as was observed for the M1 acquisition.

The measured and modeled reflectance factors for the M2 acquisition generally agree well for wavelengths equal or greater than 490 nm, but show much greater differences below 490 nm, an effect that was not observed in the M1 acquisition. The absolute differences between the modeled and measured reflectance factors over the hemisphere for the M2 acquisition were typically around ± 0.03, with a CV(RMSE) of around 7.5 %, which is a small increase of approximately 2.5 % in the CV(RMSE) observed for the M1 measurements. However, the differences between the modeled and the measured reflectance factors were much greater at wavelengths below 490 nm for the M2 acquisition over all viewing angles, with a CV(RMSE) of up to 12.3 % for a wavelength of 410 nm. The maximum difference between the measured and the modeled results was 0.18 at 410 nm for the M2 acquisition. The quad with the maximum difference had a viewing angle in the solar principal plane of 40° zenith angle and 180° azimuth angle.

3.5.2.2 M2: reflectance factors at the nadir view angle with wavelength

Nadir reflectance of the laboratory-generated sea ice as a function of wavelength is given for the M2 acquisition in Figure 3.85.

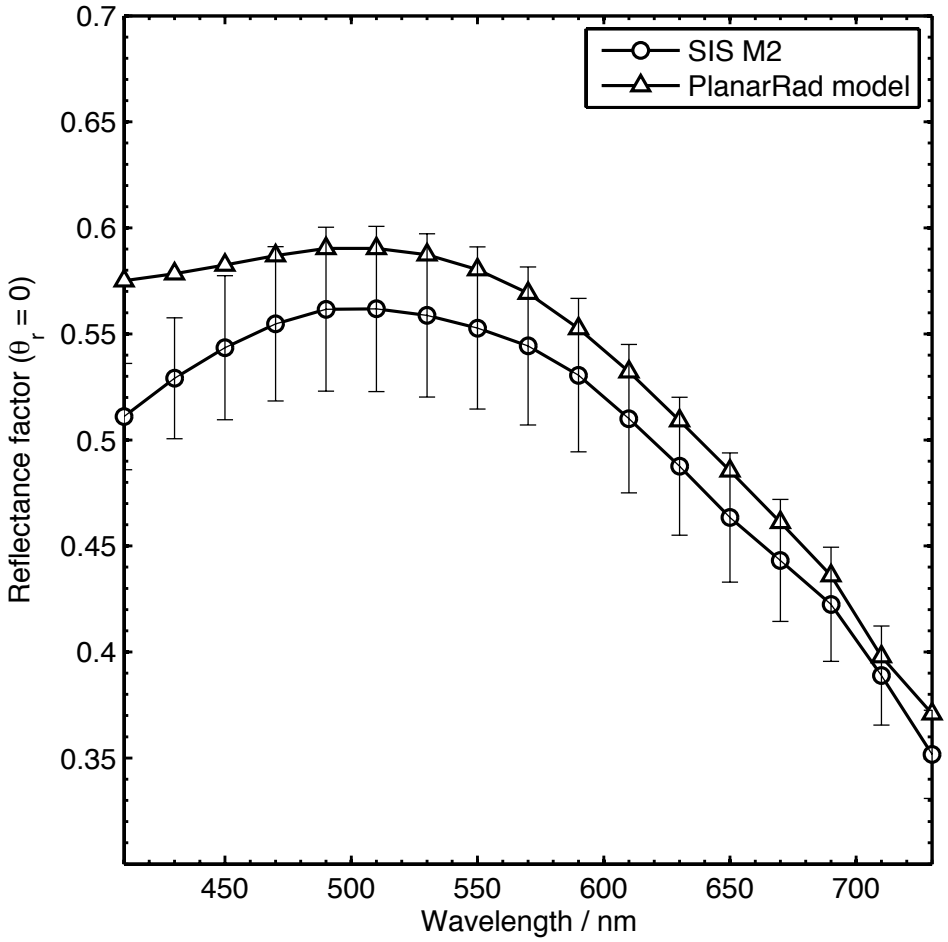

Figure 3.85. Measured and modeled nadir reflectance factors with wavelength for sea ice with thickness of 27 cm. Uncertainty bars are given to 2 standard deviations of the replicate nadir measurements

The modeled nadir reflectance factors are reproduced by the model to within the uncertainty of the laboratory measurements for wavelengths equal or greater than 470 nm, but differences between the model and the measured nadir reflectance factors is slightly greater than it was for the M1 acquisition, with the modeled nadir reflectance typical greater than the measured value by around 0.04 for the M2 acquisition, and around 0.01 for the M1 acquisition. The modeled and measured reflectance factors decrease with wavelength for wavelengths greater than 510 nm and increase with wavelength between 410 nm and 510 nm, indicating that the model reproduces the general shape of the nadir reflectance curve for the M2 measurement. However, there is a much

greater difference of approximately 0.06 between the measured and modeled values at 410 nm, where the measured reflectance factors are reduced relative to the modeled values and cause the modeled values to fall outside the range of uncertainty in the laboratory measurements.

3.5.2.3 M2: reflectance factors in the solar principal plane

Measured and modeled reflectance factors in the solar principal plane for the M2 acquisition are presented in Figure 3.86.

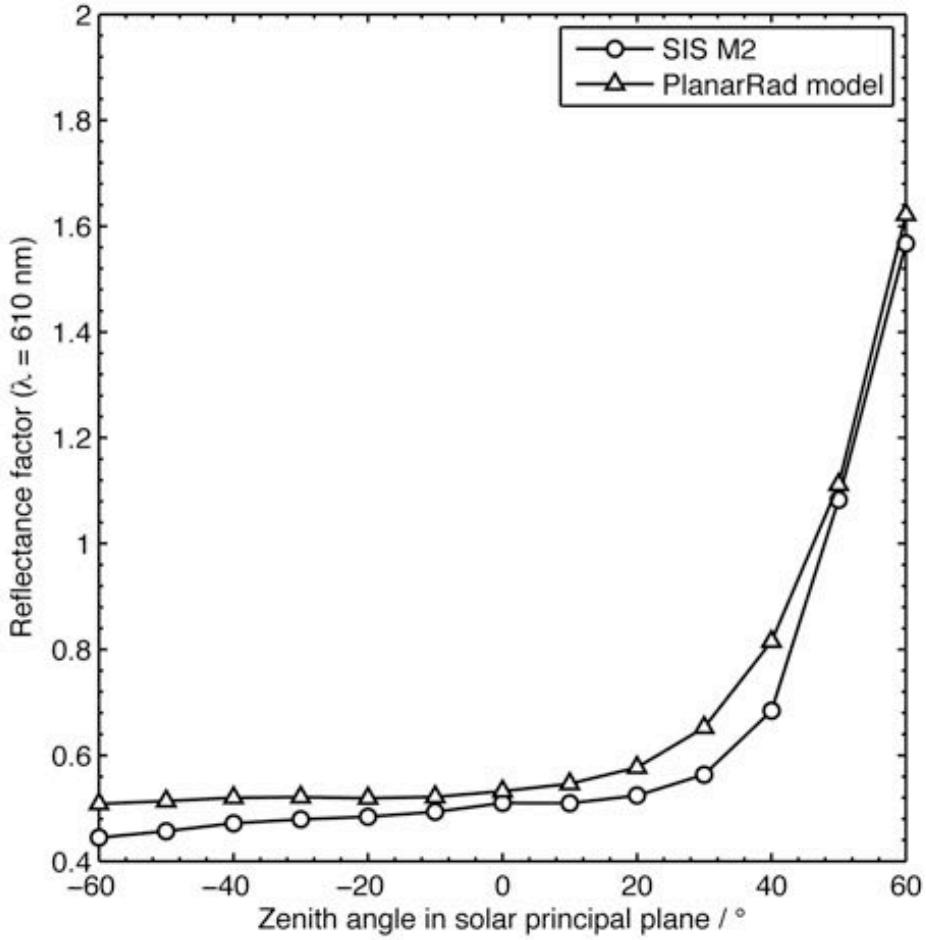

Figure 3.86. Measured and modeled reflectance factors in the solar principal plane of sea ice with a thickness of 27 cm

The measured reflectance factors for the M2 acquisition increased by 1.06 over the viewing angle range 0° to 60° zenith in the forward direction in the solar principal plane. The modeled reflectance factors show a similar shape to the

measured reflectance curve, and were typically within 0.05 of the measured values in the solar principal plane. The increase in the modeled reflectance factors was 1.09 over the viewing angle range 0° to 60° zenith angle in the forward direction. Both the measured and modeled results show a relatively weak angular dependence in the solar principal plane for viewing angles 0° to 60° in the backward direction, although the measure values show a slight decrease of around 0.05 for a viewing angle of 50° in the backward direction.

3.5.2.4 M2: CV(RMSE) with wavelength

The CV(RMSE) for the M2 acquisition is presented in Figure 3.87.

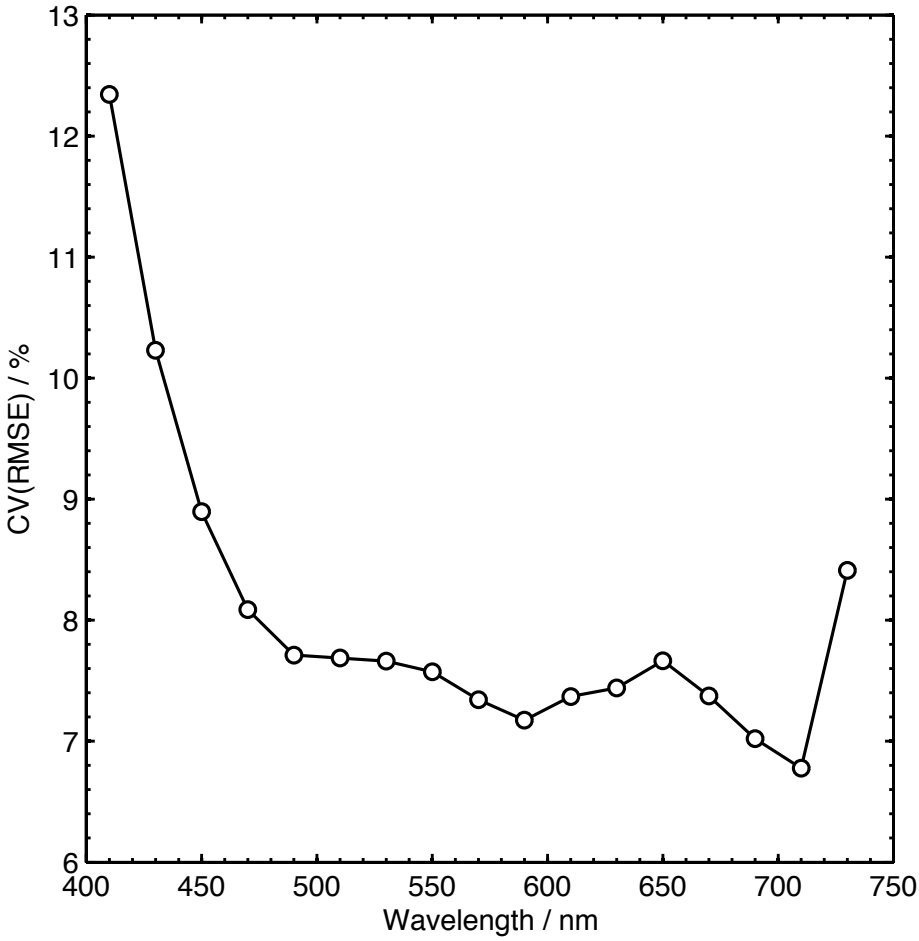

Figure 3.87. Coefficient of variation of the root mean squared error (RMSE) between the measured and modeled reflectance factors as a function of wavelength

The CV(RMSE) for the M2 acquisition was typically around 7.5 % for wavelengths equal or greater than 490 nm, which is approximately 2.5 % greater than for the M1 acquisition. The CV(RMSE) increased inversely with wavelength for wavelengths below 490 nm to a maximum value of 12.3 % at 410 nm, indicating that agreement between the model and the measurements decreased inversely with wavelength for wavelengths below 490 nm.

3.5.2.5 M2: anisotropy index (ANIX) with wavelength (M2)

The ANIX value is given as the function of wavelength in Figure 3.88 for both the measured and modeled quantities for the M2 acquisition.

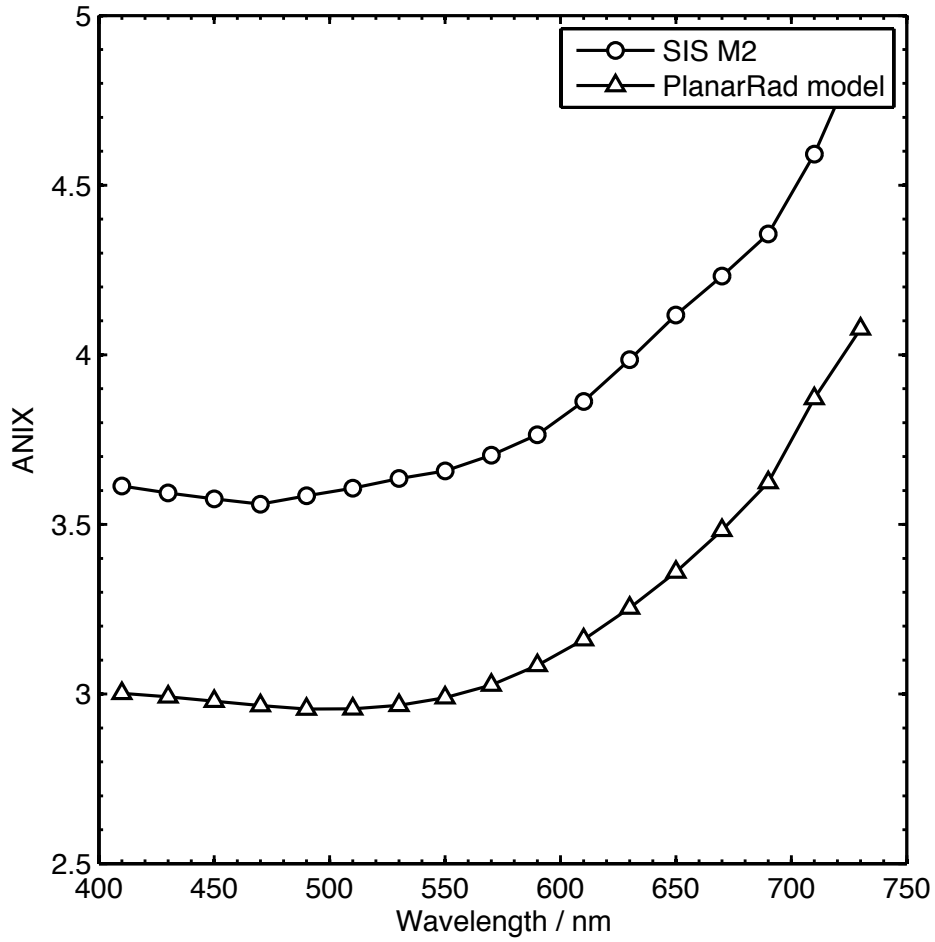

Figure 3.88. Anistropy index (ANIX) as a function of wavelength for the measured and modeled reflectance factors for 27 cm thick laboratory generated sea ice.

As was observed for the M1 acquisition, the anisotropy is weaker at shorter wavelengths for the M2 acquisition, and increases with wavelength strongly beyond 550 nm. The ANIX values for the M2 acquisition are approximately a factor of 1.7 greater than the M1 acquisition at 730 nm. The greatest ANIX value for the M1 measurement was 2.9 at 730 nm, compared to 4.9 for the M2 measurement at 730 nm. The model reproduced the same general shape to the ANIX curve for the M2 acquisition, but had an ANIX value that was typically 0.7 lower than the measured ANIX values.

3.6 Discussion

The CCRF of the laboratory-generated sea ice was strongly forward scattering for both the M1 acquisition and the M2 acquisition. The thicker laboratory-generated sea ice exhibited greater reflectivity, with the nadir reflectance increasing by approximately 3.8 % at 510 nm, and the forward scattering peak increasing by nearly 40 % at 510 nm. The increased strength of the forward peak with ice thickness is unexpected because thicker ice will generally increase the number of scattering events an average photon will undergo, which will increase the diffusely reflected portion of reflected radiation, relative to the portion of specularly reflected radiation. But rather the opposite was observed when comparing the M1 and M2 acquisitions, with a substantial increase in reflectance anisotropy for the thicker ice sea for the M2 acquisition. The effect is explained by a difference in the surface roughness scale parameter between the M1 and M2 acquisitions. An agreement with the model output that was within the uncertainty of the M2 measurement was obtained by decreasing the surface roughness scale parameter by 31 %, while keeping all the other parameters constant. As discussed in Section 3.4.4.2, the strength of the forward scattering peak is very sensitive to the scale of the surface roughness elements, while the

nadir reflectance is relatively insensitive to changes in the scale of the surface roughness elements. Interestingly, there was also a decrease in reflectance of up to 7.9 % in backward scattering direction for the M2 measurement, for the viewing angle of 50° in the solar principal plane. Given a decrease in surface roughness scale for the M2 acquisition, a decrease in backward scattering is expected, and is evident in the results.

The nadir reflectance of the laboratory-generated sea ice decreased with wavelength, for wavelengths beyond 510 nm for both the M1 and M2 acquisition, but increased from 410 nm to 510 nm for both acquisitions. There is a strong negative correlation between absorption and reflectance, with a correlation coefficient of -0.99 for the nadir reflectance and sea ice absorption coefficients for the M1 acquisition; and a correlation coefficient of -0.97 for the M2 acquisition; indicating that the reflectance spectrum is strongly influenced by the absorption spectrum for sea ice, which increases nearly 3 orders of magnitude over the wavelength range 410 nm to 730 nm. However, absorption coefficients by sea ice strongly increased between 410 nm and 510 nm, but the nadir reflectance also increased over this wavelength range for both the M1 and M2 acquisitions. The observation is explained by the influence of the lower boundary, which increases in hemispherical reflectance by approximately a factor of 3 over the wavelength range 410 nm to 510 nm, resulting in greater absorption of radiation at shorter wavelengths. A positive correlation of 0.71 for the M1 measurement, and 0.79 for the M2 measurement, was observed between the lower boundary reflectance and the nadir reflectance of the laboratory-generated sea ice for the wavelength range 410 nm to 730 nm; suggesting that the lower boundary influences the reflectance of the laboratory-generated sea ice. In addition, the sensitivity tests in Section 3.4.4.2 indicated

that the lower boundary reflectance influences the reflectance factors of the laboratory generated sea ice over the whole wavelength range studied, but the influence was approximately an order of magnitude less at 730 nm compared to the influence of the lower boundary at 410 nm.

The reflectance of the laboratory-generated sea ice typically increased with thickness, with a 3.8 % increase in the nadir reflectance at 510 nm for a 5 cm increase in thickness. The increase in reflectivity is probably the net result of an increased numbered of scattering events in the medium, which causes a greater number of photons to be scattered back towards the upper boundary. However, the change in reflectivity with thickness had wavelength dependence, and was negative at 730 nm and at 410 nm. A decrease in nadir reflectance of 3.2 % was observed at 730 nm for a 5 cm increase in the thickness of the ice, which is probably the net result of increased absorption by the sea ice, which is more than an order of magnitude greater at 730 nm compared to 510 nm; indicating that increased absorption by sea ice – owing to the thicker ice layer – is a more dominant process affecting reflectivity for longer wavelengths than the increased proportion of photons scattered back towards the surface. The reason for a decrease of 2.6 % in nadir reflectivity with increased thickness at 410 nm is less obvious, because at this wavelength absorption is much weaker and the thicker ice was expected to reduce the amount of radiation absorbed by the lower boundary, resulting in an overall increase in reflectance at the surface; but rather the opposite effect was observed for wavelengths below 490 nm. The observed effect is explained by light absorbing impurities in the 5 cm layer of sea ice that was added for the M2 acquisition in order to increase the ice thickness. Algae has a similar absorption spectrum to humic-like substances (HULIS), having a absorption spectrum that strongly increases inversely with

wavelength for wavelengths below 510 nm (France et al., 2012). An absorption spectrum for HULIS given by France et al. (2012) was combined with the absorption spectrum for sea ice in order to test whether the observed increase in absorption at shorter wavelengths could be explained by the presence of algae in the sea ice for the M2 acquisition. The model simulation was run for a range of realistic concentrations of HULIS within the sea ice; the absorption coefficients for sea ice with a mass ratio of HULIS of 1.5 μg g^{-1}, 0.5 μg g^{-1} and 0 μg g^{-1} were calculated and the results from the PlanarRad radiative-transfer model are given in Figure 3.89.

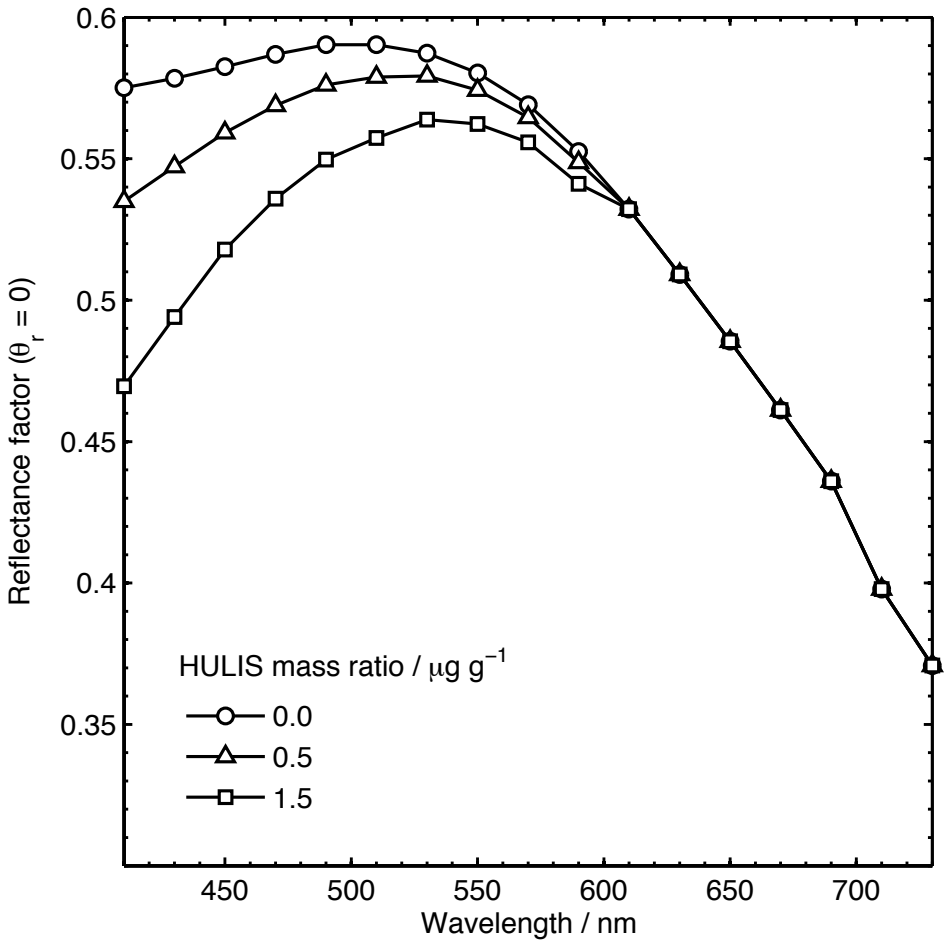

Figure 3.89 Nadir reflectance factors as a function of wavelength with varying mass ratios of HULIS in sea ice

A concentration of 0.7 μg g^{-1} of HULIS was found to be sufficient to reduce the absorption at wavelengths below 510 nm so that the modeled reflectance factors were well within the uncertainty of the measured reflectance factors, the results of the simulation with HULIS are given in Figure 3.90, Figure 3.91 and Figure 3.92.

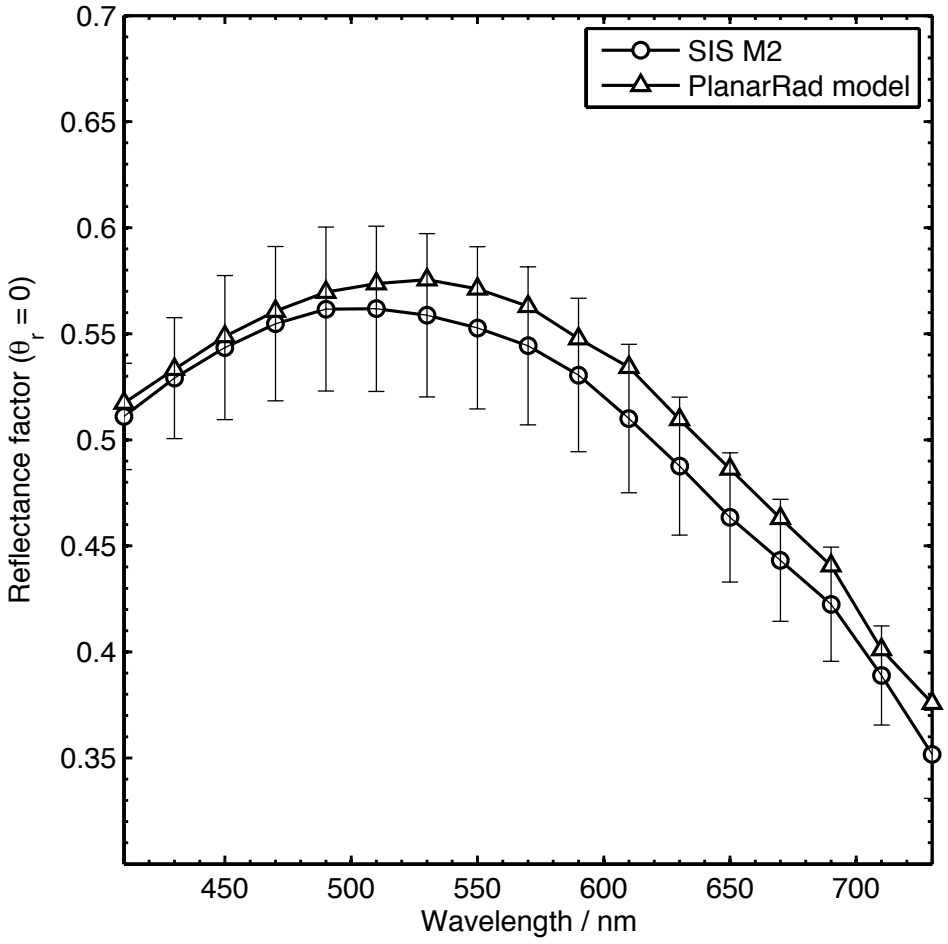

Figure 3.90. Nadir reflectance factors as a function of wavelength for the M2 acquisition when modeled using an absorption spectrum combined for sea ice and HULIS. Uncertainty bars are given to 2 standard deviations of the replicate nadir measurements

The CV(RMSE) for the M2 acquisition and the model simulation was calculated when the HULIS absorber was used in the model and is presented in Figure 3.91.

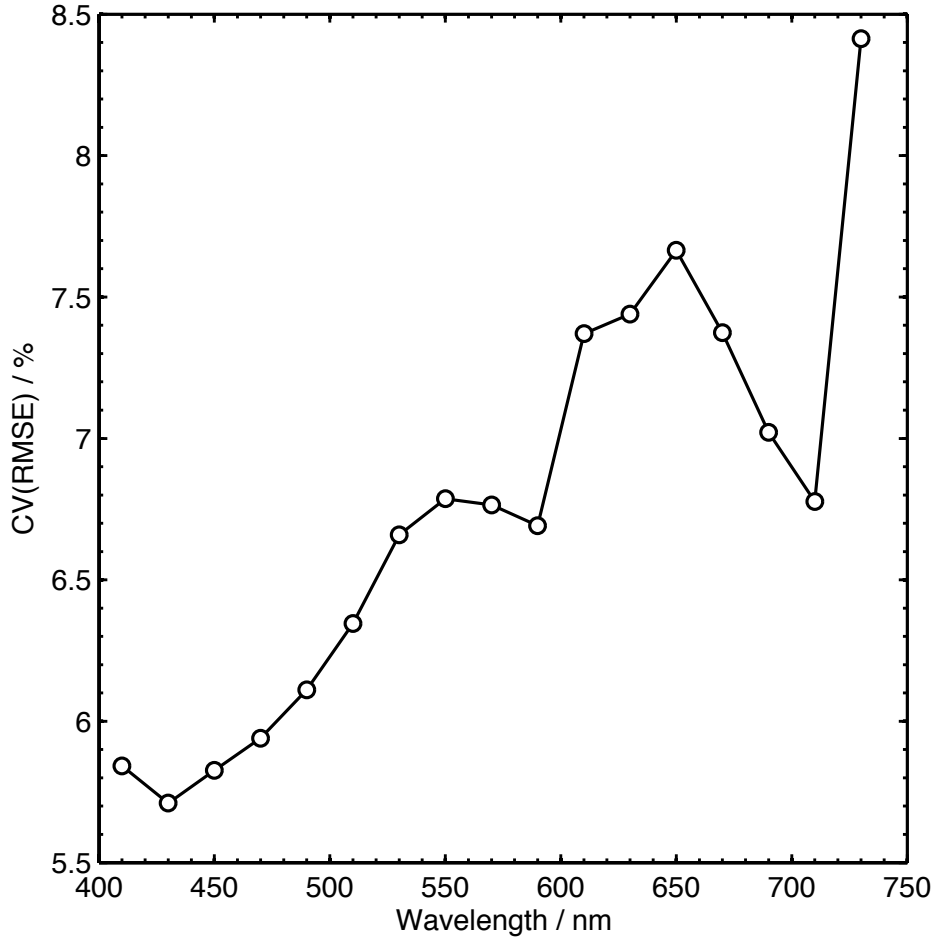

Figure 3.91 Coefficient of variation of the root mean squared error (RMSE) between the measured and modeled reflectance factors when a HULIS absorber was used in the model

When the absorption spectrum for HULIS was combined with that of sea ice, the CV(RMSE) for the M2 acquisition was reduced from 12.5 % to less than 7 % for wavelengths below 510 nm, indicating that absorption by HULIS can account for the larger differences between the modeled and measured reflectance factors at shorter wavelengths for all viewing angles in the upward facing hemisphere for the M2 acquisition. The ANIX values as a function of wavelength when the HULIS absorber was used in the model is presented in Figure 3.92.

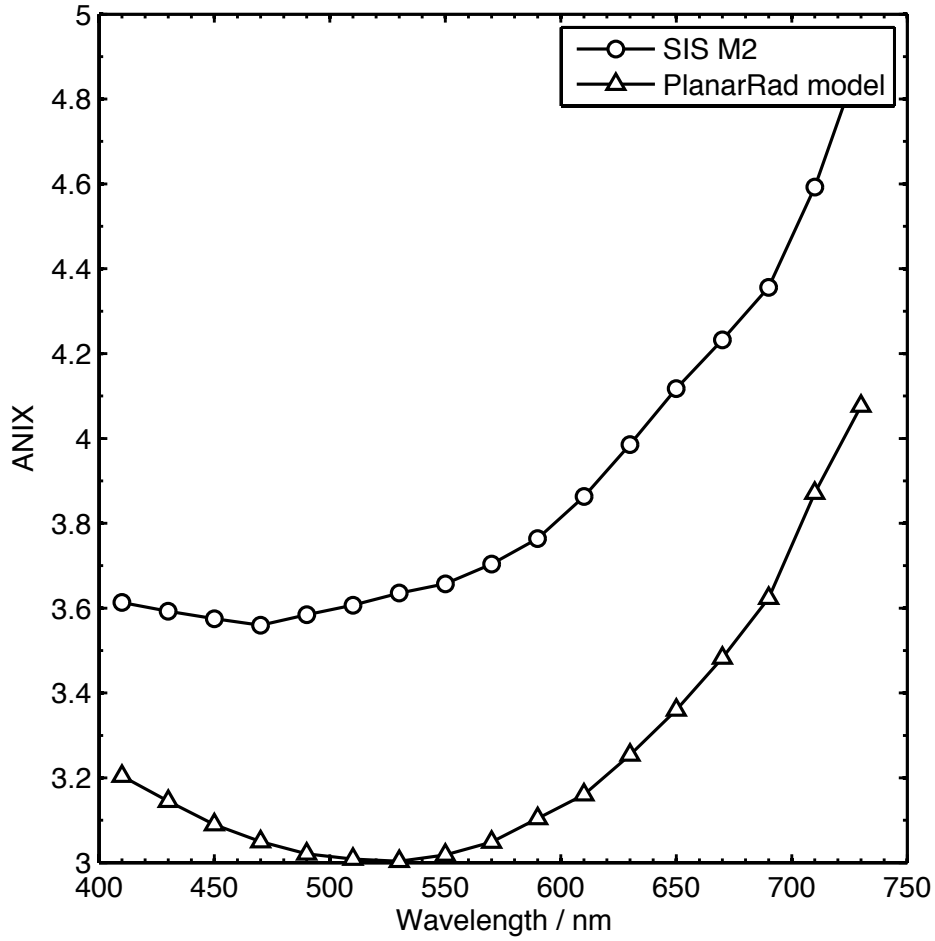

Figure 3.92 Anistropy index (ANIX) as a function of wavelength for the measured and modeled reflectance factors when a HULIS absorber is added to the model

Anisotropy of the sea ice with wavelength is positively correlated with absorption for wavelengths beyond 500 nm for both the M1 and M2 acquisitions, with anisotropy increasing most strongly beyond 550 nm. There was an increase in anisotropy with wavelength despite an overall decrease in the strength of the forward scattering peak for both the M1 and M2 acquisitions; indicating that the portion of diffusely reflected light decreases at a faster rate than the portion of specularly reflected light as the wavelength of incident light increases. The observation can be explained by enhanced absorption of photons by the sea ice owing to multiple scatting. The majority of photons reflected into the specular direction will undergo fewer extinction events as they generally penetrate less

deeply into the sea ice, whereas diffusely reflected photons tend to penetrate much deeper and will undergo many more extinction and scattering events. Thus, as absorption increases with wavelength, the diffusely reflected photons have a greater probability of absorption compared to photons reflected into the specular direction. A similar explanation is given by Warren and Wiscombe (1980) for increasing anisotropy for the directional reflectance of snow with wavelength.

There is a slight increase in anisotropy for wavelengths less than 500 nm for both the modeled and measured M1 and M2 acquisitions, the negative correlation with wavelength is stronger for the M1 acquisition. The effect is explained by absorption by the lower boundary, which has greatest reflectivity around 550 nm. The lower boundary is a Lambertian reflector and acts as a diffuser for light that reaches the base of the tank. The reflectance of the lower boundary was measured and decreases in hemispherical reflectance by more than a factor of 3 between 500 nm and 410 nm, thus its influence as a diffuser also decreases inversely with wavelengths below 550 nm. As a result, the anisotropy at the surface is slightly greater at 410 nm compared to 500 nm. It follows, that the effect is weaker for thicker ice, as is observed in the ANIX values for the M2 acquisition for the same wavelength range.

Overall, there was generally very good agreement between the modeled and measured reflectance factors over the hemisphere, with a CV(RMSE) of less than 6 % for all wavelengths for the M1 measurement, and a CV(RMSE) of less than 13 % for the M2 measurement for all wavelengths, which decreases to less than 9 % after accounting for absorption by HULIS in the model. In addition to changing the absorption coefficient of sea ice for wavelengths shorter than

550 nm, the surface roughness parameter also had to be adjusted to obtain a fit between the model output and the measured reflectance factors, but all other input parameters apart from the ice thickness were held constant; indicating that the asymmetry parameter, *g*, could be calculated through model inversion if the surface roughness parameter, *hsd*, was known.

The modeled reflectance factors were perfectly symmetric over the solar principal plane, but there was some asymmetry in the measured CCRF for both the M1 and the M2 measurement. The small amount of asymmetry in the measured results is likely to be the combined effect of errors related to the contribution of diffuse irradiance, shadowing of the sampling area by the goniometer's arm, and irregularly shaped roughness elements that were not azimuthally symmetric.

The reflectance factors of the laboratory-generated sea ice were measured for only a single incidence angle of 60°. To further test the agreement between the model and the measured reflectance factors, the CCRF measurements need to be carried out over a wide range of incidence angles. The PlanarRad radiative-transfer model has the potential to be used in a predictive capacity upon further testing of the agreement between the model and the laboratory measurements. In addition, with an improved characterization of the scale of surface roughness elements for each CCRF acquisition, the measured CCRF could be used in conjunction with the PlanarRad radiative-transfer model to derive the optical properties of the sea ice such as the asymmetry parameter, *g*, through model inversion.

3.6.1 Implications for current state-of-the-art

Increased absorption of solar radiation by the Arctic Ocean owing to decreased albedo and the resulting amplification of global warming (ice-albedo feedback) has been widely hypothesized and is of critical importance for forecasting global climate change (Serreze et al., 2011; Flanner et al., 2011; Perovich, 2007; Winton, 2006; Curry et al., 1995). In recent years, radiometers aboard Earth observing satellites such as MODIS, AVHRR and CERES have enabled measurements of the surface radiation budget of the Arctic over large spatial and temporal resolution. These observations have enabled the verification of the hypothesized ice-albedo feedback through direct observations of the Arctic (Pistone et al., 2014; Kato et al., 2006; Wang et al., 2005). Derivation of surface albedo through the use of BRDF/albedo retrieval algorithms has thus become an essential tool to detect change in the Earth's radiation budget. For example, Pistone et al. (2014) recently estimated though the use of satellite sensor data from the period 1979 to 2011 a decrease in Arctic planetary albedo of 0.04, which is equivalent to a forcing 25% as large as the forcing owing to the change in the CO_2, for the same period. In order to ensure high accuracy estimates of surface albedo from satellite sensors, it is critical that the radiative-transfer models used in the derivation of these properties are validated (Jin and Simpson, 2001); failure to include important parameters such as surface roughness in these models has been shown to result in order of magnitude errors in the derivation of surface properties (Kuchiki et al., 2011). Development of ground-based laboratory techniques for the validation of radiative-transfer models, such as the methodology described in this study, offer the unique opportunity to test the accuracy of satellite sensor BRDF/albedo retrieval algorithms and radiative-transfer models under controlled and repeatable

conditions. Repeatable results cannot be achieved under field conditions owing to variability in atmospheric conditions, the movement of the sun in the sky and diffuse irradiance reflected from the surrounding terrain. This study demonstrates a new method for generating laboratory sea ice and characterizing its bidirectional reflectance under controlled laboratory conditions at high spectral resolution. The results were compared with the radiative-transfer model PlanarRad, which was able to reproduce the measured CCRF of sea ice with an RMSE of less than 9 %. The distribution of reflected radiation was particularly sensitive to the surface roughness scale and the surface roughness parameter had to be adjusted within a realistic range to obtain a fit for both sets of CCRF measurements. Going forward, further development of the techniques described in this study will enable the validation of radiative-transfer models used for the derivation of surface albedo from satellite sensors; assisting in the development of BRDF models for sea ice, and increasing the accuracy of satellite sensor measurements of surface albedo in the Arctic, which is critical for verifying the effects of a warming Arctic through direct observation on a large spatial scale, and ultimately improving forecasts of global climate change.

3.7 Conclusion

CCRF acquisitions of laboratory generated sea ice had a strong forward scattering peak that was greatest in the specular direction of 60° viewing zenith angle, and which increased up to a maximum reflectance factor of 1.63 at 510 nm. The reflectance factors over the hemisphere had an anisotropy that was strongly wavelength dependent, with a maximum ratio of maximum to minimum reflectance factors of 4.9 at 730 nm. The anisotropy in the CCRF was greatest at longer wavelengths, despite a weakening of the forward scattering peak with wavelength; indicating that the diffuse component to the reflectance

decreased more strongly with wavelength. Angular effects on the reflected distribution were minimal for viewing angles in the backward direction and for viewing angles less than 15° in the forward direction for both the measured and modeled reflectance factors, for both the M1 and M2 acquisitions.

An increase in sea ice thickness of 5 cm resulted in a small increase of around 4 % reflectance for wavelengths between 450 nm and 690 nm, but decreased the reflectance for wavelengths greater than 690 nm by up to 3.2 %, owing to increased absorption at longer wavelengths. The wavelength dependence to the reflectance of sea ice was dominated by the absorption coefficient of sea ice, but the reflectance of the lower boundary was shown to influence the reflectance at the surface. The hemispherical reflectance of the lower boundary influenced the reflectance of the ice in both the measured and the modeled results, and caused a decrease in anisotropy at the wavelengths for which the lower boundary was most reflective, but had an order of magnitude less influence at 730 nm than at 410 nm, owing to the reduced penetration depth of radiation at longer wavelengths.

The reflectance factors over the hemisphere were modeled with the radiative transfer model PlanarRad, and the input parameters were determined from the literature and physical measurements of the laboratory generated-sea ice where possible. In order to obtain a fit within the uncertainty of the CCRF measurements, the surface roughness parameter had to be adjusted within a realistic range for both the M1 and M2 acquisitions. The modeled reflectance factors generally agreed well with the measured CCRF once the surface roughness parameter was adjusted, having a coefficient of variation of the RMSE of less than 6 % over all wavelengths for the M1 acquisition, and less

than 9 % for the M2 acquisition, when a HULIS absorber was included in the model. The model was able to reproduce the general shape of the CCRF over the hemisphere and its wavelength dependence, with differences in the reflectance factors typically less than 0.05.

3.8 References

Aoki, T., and Aoki, T., 2000, Effects of snow physical parameters on spectral albedo and: Journal of Geophysical Research, v. 105, p. 10219–10236.

Arnold, G.T., Tsay, S.C., King, M.D., Li, J.Y., and Soulen, P.F., 2002, Airborne spectral measurements of surface-atmosphere anisotropy for arctic sea ice and tundra: International Journal of Remote Sensing, v. 23, no. 18, p. 3763–3781.

Bourgeois, C.S., Calanca, P., and Ohmura, A., 2006, A field study of the hemispherical directional reflectance factor and spectral albedo of dry snow: Journal of Geophysical Research, v. 111, p. D20108.

Bourgeois, C.S., Ohmura, A., Schroff, K., Frei, H.-J., and Calanca, P., 2006b, IAC ETH goniospectrometer: A tool for hyperspectral HDRF measurements: Journal of Atmospheric and Oceanic Technology, v. 23, p. 573–584.

Boyer, T.P., Antonov, J.I., Baranova, O.K., Coleman, C., Garcia, H.E., Grodsky, A., Johnson, D.R., Locarnini, R.A., Mishonov, A.V., O'Brian, T.D., Paver, C.R., Reagan, J.R., Siedov, D., Smolyar, I.V., et al., 2013, World Ocean Database 2013: NOAA Atlas NESDIS 72.

Brissaud, O., Schmitt, B., Bonnefoy, N., Doute, S., Rabou, P., Grundy, W., and Fily, M., 2004, Spectrogonio radiometer for the study of the bidirectional reflectance and polarization functions of planetary surfaces. 1. Design and tests: Applied Optics, v. 43, p. 1926–1937.

Comiso, J.C., 2012, Large decadal decline of the Arctic multiyear ice cover: Journal of Climate, v. 25, p. 1176–1193.

Curry, J.A., Schramm, J.L., Ebert, E.E., 1995, Sea ice-albedo climate feedback mechanism: Journal of Climate, 8, no. 2.

Dangel, S., Kneubuhler, M., Kohler, R., Schaepman, M., Schopfer, J., Schaepman-Strub, G., and Itten, K., 2003, Combined field and laboratory goniometer system- FIGOS and LAGOS: IEEE Proceedings Geoscience and Remote Sensing Symposium, v. 7, p. 4428–4430.

de Berg, M., Cheong, O., Kreveld, M., and Overmars, M., 2008, Computational Geometry: Algorithms & Applications: Springer-Verlag.

Dumont, M., Brissaud, O., Picard, G., Schmitt, B., Gallet, J.C., and Arnaud, Y., 2010, High-accuracy measurements of snow Bidirectional Reflectance Distribution Function at visible and NIR wavelengths – comparison with modelling results: Atmospheric Chemistry and Physics, v. 10, p. 2507–2520.

Flanner, M.G., Zender, C.S., Randerson, J.T., and Rasch, P.J., 2007, Present-day climate forcing and response from black carbon in snow: Journal of Geophysical Research, v. 112 p. D11202.

France, J.L., Reay, H.J., King, M.D., Voisin, D., Jacobi, H.W., Domine, F.,

Beine, H., Anastasio, C., MacArthur, A., and Lee-Taylor, J., 2012, Hydroxyl radical and NO xproduction rates, black carbon concentrations and light-absorbing impurities in snow from field measurements of light penetration and nadir reflectivity of onshore and offshore coastal Alaskan snow: Journal of geophysical research, v. 117, p. D00R12.

Grenfell, T.C., Warren, S.G., and Mullen, P.C., 1994, Reflection of solar radiation by the Antarctic snow surface at ultraviolet, visible, and near-infrared wavelengths: Journal of Geophysical Research, v. 99, p. 18669.

Hall, D.K., Foster, J.L., and Chang, A.T.C., 1992, Reflectance of snow measured in situ and from space in sub-Arctic areas in Canada and Alaska: IEEE Transactions on Geoscience and Remote Sensing, v. 30, p. 634–637.

Hudson, S.R., Warren, S.G., Brandt, R.E., Grenfell, T.C., and Six, D., 2006, Spectral bidirectional reflectance of Antarctic snow: Measurements and parameterization: Journal of Geophysical Research, v. 111, p. D18106.

Jin, Z., and Simpson, J., 2001, Anisotropic reflectance of snow observed from space over the Arctic and its effect on solar energy balance: Remote Sensing of Environment, v. 75, p. 63–75.

Kato, S., Loeb, N. G., Minnis, P., Francis, J. A., Charlock, T. P., Rutan, D. A., Sun-Mack, S., 2006, Seasonal and interannual variations of top-of-atmosphere irradiance and cloud cover over polar regions derived from the CERES data set: Geophysical Research Letters, 33, no. 19.

Kuhn, M., 1985, Bidirectional reflectance of polar and alpine snow surfaces: Annals Glaciology, v. 6, p. 164–167.

Li, S., and Zhou, X., 2004, Modelling and measuring the spectral bidirectional reflectance factor of snow-covered sea ice: an intercomparison study: Hydrological Processes, v. 18, p. 3559–3581.

Lindsay, R.W., and Rothrock, D.A., 1994, Arctic sea ice albedo from AVHRR: Journal of Climate, v. 7, p. 1737–1749.

Marks, A.A, 2014. Sea ice response to anthrapogenic pollution: an experiment and modeling study: PhD thesis, Royal Holloway University of London.

Marks, A.A., and King, M.D., 2013, The effects of additional black carbon on the albedo of Arctic sea ice: variation with sea ice type and snow cover: The Cryosphere, v. 7, p. 1193–1204.

Markus, T., Stroeve, J.C., and Miller, J., 2009, Recent changes in Arctic sea ice melt onset, freezeup, and melt season length: Journal of Geophysical Research, v. 114, p. C12024.

Martin, S., Drucker, R., and Fort, M., 1995, A laboratory study of frost flower growth on the surface of young sea ice: Journal of Geophysical Research, v. 100, p. 7027.

Maslanik, J., Stroeve, J., Fowler, C., and Emery, W., 2011, Distribution and trends in Arctic sea ice age through spring 2011: Geophysical Research

Letters, v. 38.

Maykut, G.A., 1978, Energy exchange over young sea ice in the central Arctic: Journal of Geophysical Research: Atmospheres, v. 83, p. 3646–3658.

Mobley, C., 1994, Light and water, radiative transfer in natural waters: Academic Press Inc.

Mobley, C.D., Cota, G.F., Grenfell, T.C., Maffione, R.A., Pegau, W.S., and Perovich, D.K., 1998, Modeling light propagation in sea ice: Geoscience and Remote Sensing, IEEE Transactions on, v. 36, no. 5, p. 1743–1749.

Nicodemus, F.E., Richmond, J.C., Hsia, J.J., Ginsberg, I.W., and Limperis, T., 1977, Geometrical considerations and nomenclature for reflectance: United States National Bureau of Standards.

Painter, T.H., 2004, Measurements of the hemispherical-directional reflectance of snow at fine spectral and angular resolution: Journal of Geophysical Research, v. 109, p. D18115.

Painter, T.H., Paden, B., and Dozier, J., 2003, Automated spectro-goniometer: A spherical robot for the field measurement of the directional reflectance of snow: Review of Scientific Instruments, v. 74, p. 5179.

Pegrum, H., Fox, N., Chapman, M., and Milton, E., 2006, Design and testing a new instrument to measure the angular reflectance of terrestrial surfaces, IEEE Geoscience and Remote Sensing Symposium, 2006. p. 1119–1122.

Peltoniemi, J.I., Kaasalainen, S., Naranen, J., Matikainen, L., and Piironen, J., 2005, Measurement of directional and spectral signatures of light reflectance by snow: Geoscience and Remote Sensing, IEEE Transactions on, v. 43, p. 2294–2304.

Perovich, D.K., 2003, Complex yet translucent: the optical properties of sea ice: Physica B, v. 338, p. 107–114.

Perovich, D.K., 1994, Light reflected from sea ice during the onset of melt: Journal of Geophysical, v. 99, p. 3351–3359.

Perovich, D.K., 2002, Seasonal evolution of the albedo of multiyear Arctic sea ice: Journal of Geophysical Research, v. 107, p. 8044.

Perovich, D.K., 1996, The optical properties of sea ice: US Army Corps of Engineers CRREL, p. 1–24.

Perovich, D.K., 1999, SHEBA: The surface heat budget of the Arctic Ocean: US Army Corps of Engineers CRREL, p. 1–24.

Perovich, D.K., and Polashenski, C., 2012, Albedo evolution of seasonal Arctic sea ice: Geophysical Research Letters, v. 39.

Perovich, D.K., Richter Menge, J.A., Jones, K.F., and Light, B., 2008, Sunlight, water, and ice: Extreme Arctic sea ice melt during the summer of 2007: Geophysical Research Letters, v. 35, p. L11501.

Pistone, K., Eisenman I., Ramanathan V., 2014. Observational determination of albedo decrease caused by vanishing Arctic sea ice: Proceedings of the National Academy of Sciences, no. 9, p. 3322-3326.

Rees, W.G., 2006, Remote sensing of snow and ice: CRC Press.

Sandmeier, S., Müller, C., Hosgood, B., and Andreoli, G., 1998, Sensitivity analysis and quality assessment of laboratory BRDF data: Remote Sensing of Environment, v. 64, p. 176–191.

Sandmeier, S.R., and Strahler, A.H., 2000, BRDF laboratory measurements: Remote Sensing Reviews, v. 18, p. 481–502.

Schaepman-Strub, G., Schaepman, M.E., Painter, T.H., Dangel, S., and Martonchik, J.V., 2006, Reflectance quantities in optical remote sensing—definitions and case studies: Remote Sensing of Environment, v. 103, p. 27–42.

Schlosser, E., 1988, Optical studies of Antarctic sea ice: Cold Regions Science and Technology, v. 15, p. 289–293.

Schopfer, J., Dangel, S., Kneubühler, M., and Itten, K.I., 2008, The improved dual-view field goniometer system FIGOS: Sensors, v. 8, p. 5120–5140.

Serreze, C.M., Roger B.G., 2011, Processes and impacts of Arctic amplification: A research synthesis: Global and Planetary Change, p. 85-96.

Wang, X., Key, J. R., 2005. Arctic surface, cloud, and radiation properties based on the AVHRR Polar Pathfinder dataset. Part I: Spatial and temporal characteristics: Journal of Climate, no. 14, p. 2558-2574.

Walsh, J.E., and Chapman, W.L., 2001, 20th-century sea-ice variations from observational data: Annals of Glaciology, v. 33, p. 444–448.

Warren, S.G., 2013, Can black carbon in snow be detected by remote sensing?: Journal of Geophysical Research: Atmospheres, v. 118, p. 779–786.

Weeks, W.F., 2010, On sea ice: University of Alaska Press.

Winton, M., 2006 Does the Arctic sea ice have a tipping point? Geophysical Research Letters, 33, no. 23.

Wiscombe, W.J., and Warren, S.G., 1980, A model for the spectral albedo of snow. I: Pure snow: Journal of the Atmospheric Sciences, v. 37, p. 2712–2733.

Zhonghai Jin, and Simpson, J.J., 2000, Bidirectional anisotropic reflectance of snow and sea ice in AVHRR channel 1 and channel 2 spectral regions. II. Correction applied to imagery of snow on sea ice: IEEE Transactions on Geoscience and Remote Sensing, v. 38, p. 999–1015.

Chapter 4

Effect of the phase transition at 19°C on PTFE Spectralon reference standards for reflectance

4.1 Abstract

Sintered polytetrafluroethylene (PTFE) is strongly reflective and is widely used as a reference standard and as an optical diffuser in remote sensing, radiometry and spectroscopy. PTFE has a room temperature phase transition at 19 °C, the effect of the phase transition was investigated on: (a) the transmittance of Spectralon diffusers, and (b) the reflectance of Spectralon reference standards (Ball et al., 2013). There was considerable uncertainty in the transmittance measurements owing to the measurement technique used, and a change in transmittance was not detected above the level of uncertainty in the measurements over the temperature range 12.5 °C to 20 °C. However, the average of 16 repeat measurements showed a change of around 1.6 % at 350 nm, and 1.3 % at 600 nm. The measured and averaged change in

transmittance agreed well with similar experiments by McKenzie et al. (2005) and Ylianttila and Schreder (2005), both of whom attribute the measured change in transmittance to the PTFE phase transition at 19 °C. The relative change reflectance over the phase transition temperature was determined for a wavelength of 633 nm by measuring the change in output flux from a Spectralon integrating sphere. The measured change in output flux from the integrating sphere was 1.82 ± 0.21 %, which corresponds with a small change of 0.09 ± 0.02 % in the total hemispherical reflectance of Spectralon. For the majority of users, this very small change measured in total hemispherical reflectance is unlikely to impact significantly the accuracy of PTFE flat panel reflectors used as reference standards. However, owing to the multiple reflections that occur inside an integrating sphere cavity the effect is multiplied, and remedial action should be applied, either via a mathematical correction or though temperature stabilisation of the integrating sphere when high accuracy measurements of flux, irradiance or radiance are required from PTFE based integrating spheres at temperatures close to the phase transition at 19 °C.

4.2 Aims of the study

Initially the investigation aims to confirm the impact of the phase transition on the transmittance of PTFE diffusers, first reported by Yliantilla and Schreder (2005) and McKenzie et al. (2005). However, the overarching aim was to quantify the potential impact of the phase transition on the reflectance of PTFE reference standards for reflectance, which are widely used in remote sensing, radiometry and spectroscopy. A Spectralon PTFE reference standard was used for the measurements presented in Chapter 2 and Chapter 3. The measurements were conducted at ambient temperatures below the phase transition temperature, but the panel was calibrated at a temperature above the

phase transition temperature, as a result, the investigation described here has potentially important implications for the wider results presented in this thesis.

4.3 Introduction

Sintered polytetrafluoroethylene (PTFE), which is also known under the trade names Spectralon from Labsphere, and OP.DI.MA from Gigahertz-Optik, is widely used in terrestrial remote sensing, spectroscopy and radiometry as a primary reference standard for reflectance (e.g. Xiong and Barnes, 2006; Bourgeois et al., 2006; France et al., 2011; Sandmeier and Itten, 1999; Susaki et al., 2004; Negi and Kokhanovsky, 2011). PTFE is also used in integrating spheres for the spatial integration of irradiance (e.g. Perovich, 2002; Tschudi et al., 2008) and as a uniform radiance source for the calibration of remote sensing systems (e.g. Pegrum et al., 2004). PTFE has wide application in the remote sensing community because it exhibits approximately Lambertian reflectance over the UV-VIS-NIR region of the spectrum, it is chemically inert, washable and extremely hydrophobic (Springsteen, 1999; Weidner and Hsia, 1981), making it ideal for field use.

As an optical diffuser, the optical transmittance of PTFE has been shown to change by up to 3 % between the temperatures of 13 °C and 22 °C (Ylianttila and Schreder, 2005). The authors ascribe these changes in transmittance to a phase transition that results in a change in the crystalline structure of PTFE at 19 °C. The phase transition may represent a particular problem because its temperature is close to common field operating conditions in temperate climates. For example, McKenzie et al. (2005) reported a significant impact on the accuracy of measured UV irradiances (~ 2 %) when using PTFE diffusers in

the field at ambient temperatures that straddle the phase transition temperature at 19 °C.

PTFE is known to undergo phase transitions at both 19 °C and 30 °C (Quinn et al., 1951; Kirby, 1956; Clark, 1999). Studies involving X-ray diffraction have shown that these phase transitions result from an uncoiling of the helical structure of fluorine atoms around a central carbon backbone (Yamamoto and Hara, 1986). In combination, the transitions at 19 °C and 30 °C result in a reversible change of ~ 1 % in the volume of PTFE (Quinn et al., 1951; Kirby, 1956). The transition at 19 °C accounts for the majority (~ 85 %) of the total volumetric change (Quinn et al., 1951).

The reflectance of pressed PTFE is known to depend on its density (Weidner and Hsia, 1981), and given the widespread use of PTFE as a reference standard for reflectance, the observed changes in transmittance of visible light (McKenzie et al., 2005; Ylianttila and Schreder, 2005) and the known structural changes at 19 °C (Quinn et al., 1951; Kirby, 1956; Yamamoto and Hara, 1986; Clark, 1999) it is pertinent to assess whether the phase transition affects the reflectance of PTFE. The investigation described here used a temperature controlled sintered PTFE (Spectralon) integrating sphere, making use of the amplifying nature of the multiple internal reflections in the sphere cavity to study the signal produced by a change in reflectance of the PTFE coating with temperature. A Spectralon integrating sphere was used because sintered PTFE is more widely used in integrating spheres and as flat panel reflectors. Pressed PTFE and sintered PTFE exhibit slightly different properties in reflectance (Tsai et al., 2008), although they are based on the same raw material.

The work carried out in this thesis chapter has been published in the peer-reviewed journal: Applied Optics (AO), by Ball et al. (2013). The coauthors (A.P. Levick, E.R. Wooliams, P.D. Green, M.R. Dury, R. Winkler, A.J. Deadman, N.P. Fox and M.D. King) provided advice and guidance to the first author of the publication (C.P. Ball) on various aspects of the work in a supervisory fashion. A.P. Levick provided the derivation for Equation 4.28 and recommended the use of an integrating sphere to enhance the sensitivity of the measurement.

4.4 Methodology

The methodology will be divided into two main sections, describing the PTFE transmittance experiments, and the PTFE reflectance experiments respectively.

4.4.1 PTFE transmittance experiments

The transmittance of a 210 μm thick PTFE diffuser was recorded using a Cary 5000 UV-VIS spectrophotometer over the temperature range -10 °C to 40 °C, and the average change in transmittance of the diffuser from the reference temperature of 12.5 °C was calculated. The experiments were carried out in a temperature-controlled laboratory at the National Physical Laboratory (NPL). Two samples of the PTFE diffuser were cut to shape and fitted inside aluminium cuvettes, and were held within a multicell block, which regulated the temperature of the samples using a water bath during the transmittance measurements. Transmittance measurements were made for the wavelength range 350 nm to 600 nm at a bandwidth of 5 nm, for the temperature range -10 °C to 40 °C at 5 °C increments in temperature. Within the area of specific interest near to the 19 °C phase transition (between 10 °C and 30 °C) increments in temperature were 2.5 °C. The spectrophotometer was left to

warm up for an hour before any measurements are carried out. Once the multicell block reached the required temperature for each step in temperature, a temperature stabilization period of 20 minutes was used to ensure the samples reached the same temperature as the multicell block. A metal on silica (MOS) filter with no known temperature response was used as a control on transmittance throughout the experiment; and an MOS filter with 3 % transmittance was used to set the baseline of the spectrophotometer. Dark measurements were taken at each temperature step and a dark signal correction was applied to the transmittance measurements. The transmittance measurements were repeated 8-times at each temperature step for each Spectralon sample, and the average transmittance of both samples was taken. A photograph of the Cary 5000 UV-VIS spectrophotometer is given in Figure 4.1, and a photograph of the multicell block used to regulate the temperature of the samples is given in Figure 4.2.

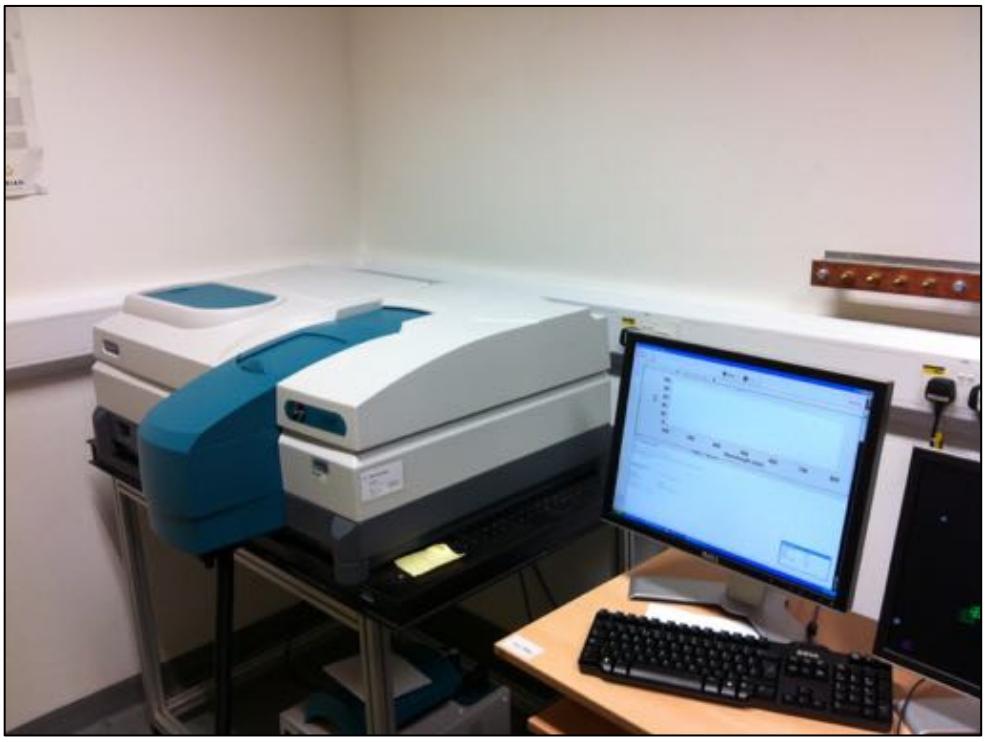

Figure 4.1. Cary 5000 UV-VIS spectrophotometer used for PTFE transmittance experiments

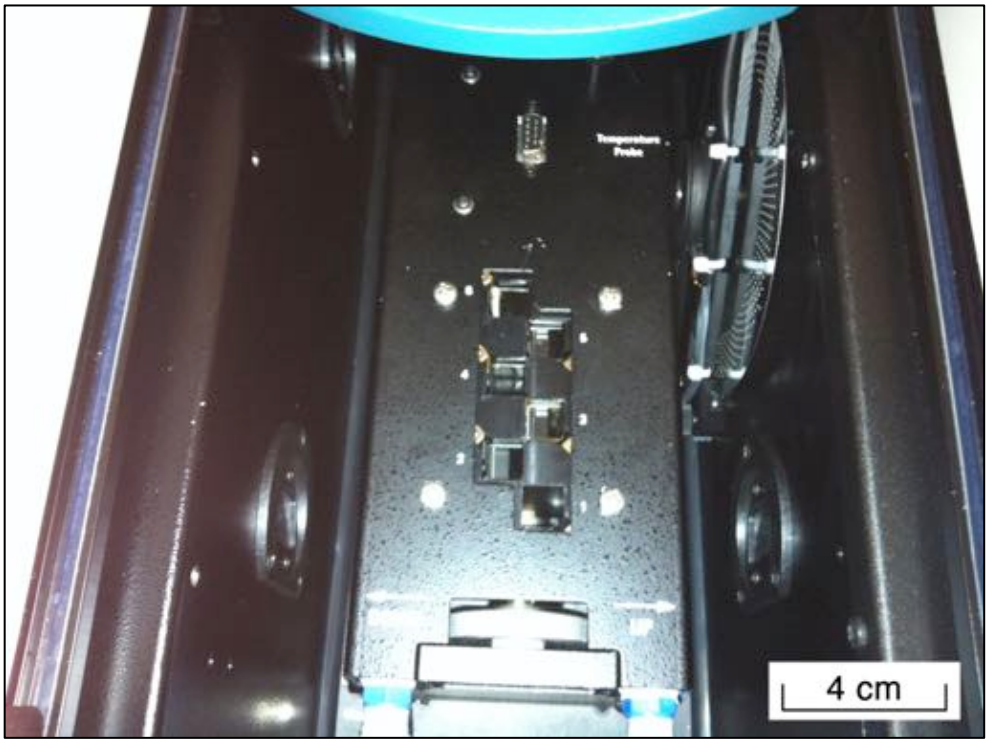

Figure 4.2. Multicell block used to regulate the temperature of the PTFE samples during the PTFE transmittance experiments

The transmittance of the MOS control filter as a function of temperature is presented in Figure 4.3.

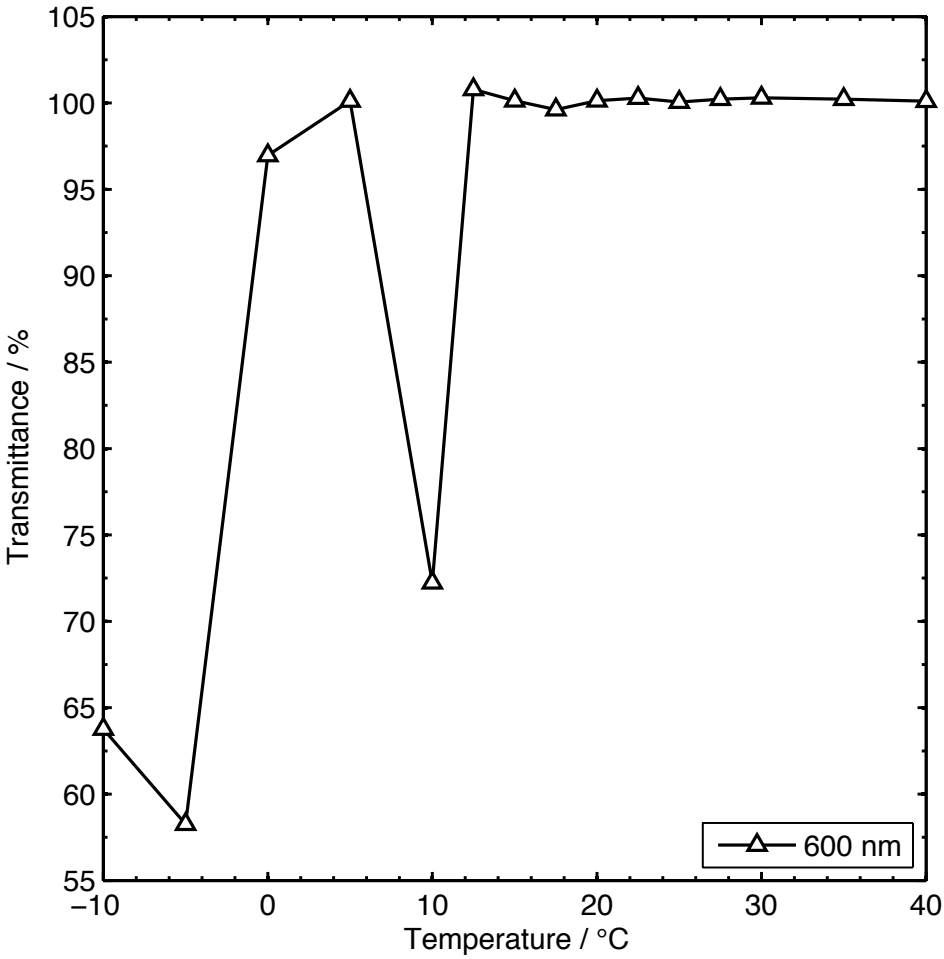

Figure 4.3. Transmittance of the MOS filter over the temperature range -10° C to 40 °C

The transmittance of the control filter decreased by up to 42 % from the transmittance at 12.5 °C for temperatures below 12.5 °C, which was the result of condensation or ice forming on the filter. There was also a decrease of around 38 % at 10 °C. The transmittance at 10 °C was taken approximately 20 minutes after the transmittance at -10 °C, and was affected by droplets of melted ice on the filter that had not evaporated. As a result, all transmittance measurements made for temperatures below 12.5 °C were omitted from the final analysis. The control filter was stable in transmittance to ± 0.5 % for temperatures greater than 10 °C.

4.4.2 PTFE reflectance experiments

A description of the methodology for the PTFE reflectance measurements is given in the following section.

4.4.2.1 Effective temperature control of PTFE

PTFE is a poor thermal conductor, and as a result the experiment needed to provide a stable ambient air temperature surrounding the PTFE, in order to minimize thermal gradients across the PTFE material. Any such thermal gradient could affect the results by causing the monitoring thermocouple to provide an inaccurate measurement of the temperature of the PTFE at the surface, where the measurement of reflectance is made. Initial testing of different methodologies to temperature control a flat panel reflector involved fixing a block of Spectralon to a copper plate, and temperature controlling the copper plate by circulating water from a chiller water bath. To test for thermal gradients in the PTFE material, the temperature across the PTFE slab was measured using a thermal camera when the temperature of the water bath of set to 15 °C and 40 °C, a 30-minute temperature stabilization period between each temperature step was used prior to capturing the thermal images. The thermal images are given in Figure 4.4 and Figure 4.5.

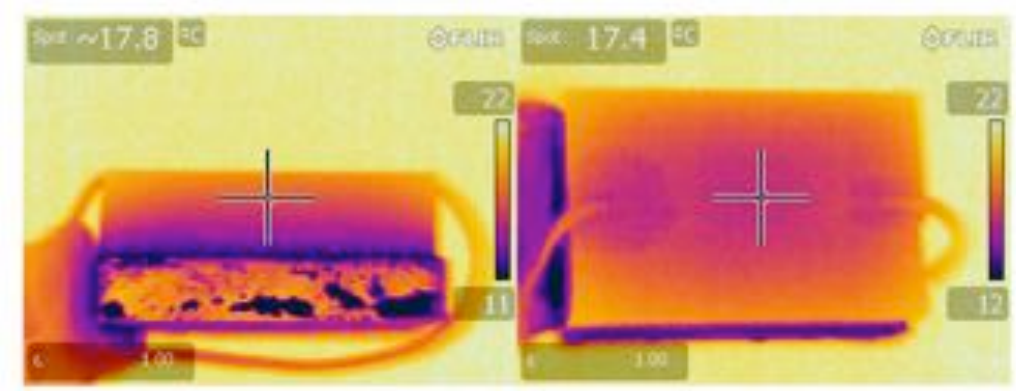

Figure 4.4 Thermal images of a ~ 1 cm thick PTFE slab on top of copper plate with circulating water with a temperature of 15 °C. The colour bars have units of degrees Celsius

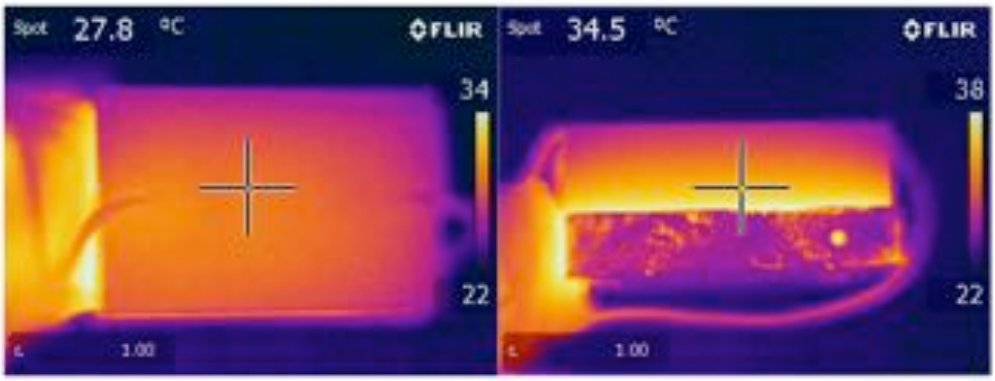

Figure 4.5 Thermal images of a ~ 1 cm thick PTFE slab on top of copper plate with circulating water with a temperature of 40 °C. The colour bars have units of degrees Celsius

Visual inspection of the thermal images in Figure 4.4 and Figure 4.5 show considerable thermal gradients across the PTFE material. As a result, an alternative experiment had to be designed, which involved the use of a thermally insulated chamber, and a PTFE integrating sphere, the experiment setup is described in detail in Section 4.4.2.2.

4.4.2.2 Experiment set-up

The change in total hemispherical reflectance (hereafter referred to as reflectance) of PTFE, over the temperature range 14 °C to 28 °C was measured relative to the measured reflectance at a reference temperature of 14 °C, using a temperature controlled PTFE integrating sphere in a thermally insulated chamber. The output flux from the exit port of a temperature controlled PTFE integrating sphere was measured with an input flux of stabilised monochromatic light. The use of an integrating sphere for this application was apt because the calculated flux from the sphere's exit port is very sensitive to changes in the reflectance of the PTFE sphere due to the multiple reflections that occur inside the sphere's cavity. The use of an integrating sphere rather than a flat panel reflector also allowed the PTFE to be heated and cooled uniformly because the

integrating sphere's aluminium casing provided good thermal conductance around the PTFE material, which was relatively thick (~ 1 cm), and a poor thermal conductor, as discussed in Section 4.4.2.1.

The experiment was carried out in a temperature-controlled laboratory at the National Physical Laboratory (NPL). The integrating sphere was placed in contact with a copper plate inside the thermally insulated chamber, the copper plate was temperature controlled by circulating water from a chiller water bath as shown in Figure 4.6. The chamber was insulated sufficiently so that the ambient air temperature within the chamber was stable to within 0.1 °C (1σ) (tested over a 12-hour period).

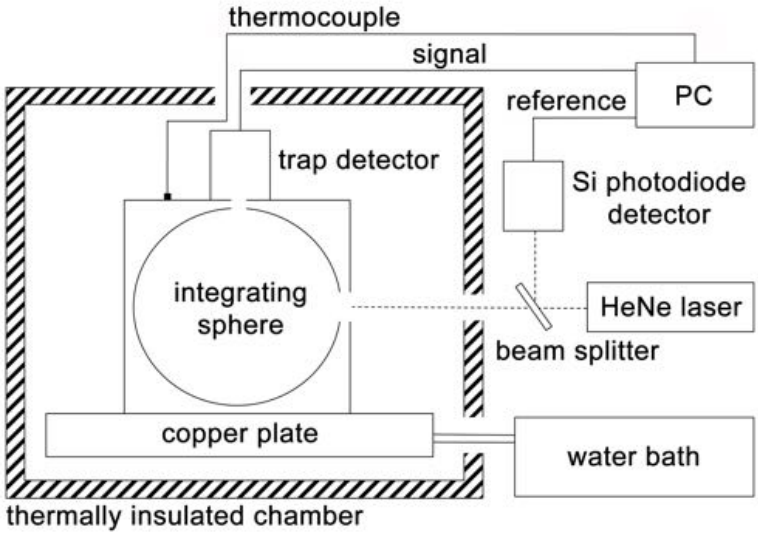

Figure 4.6. Schematic of the experiment set-up, from Ball et al. (2013).

A 5 mW intensity-stabilised HeNe laser with a wavelength of 633 nm was directed via a beam splitter into the integrating sphere input port. The flux from the exit port of the PTFE integrating sphere was measured using a reflectance trap detector over a period of 18 hours as the temperature of the sphere was incrementally increased. The light in the trap detector undergoes a total of 5 internal reflections between 3 Hamamatsu S1337 PN photodiode detectors and

the photo-current from all 3 detectors are summed to produce the measured output current. The multiple reflections in the trap detector result in almost no net reflectance (less than 0.25 %), leading to a response that is relatively insensitive to external factors such as ambient humidity (Zalewski and Duda, 1983). The second beam from the beam splitter was a reference beam, and a silicon photodiode detector was used to monitor its intensity. The signal from each detector was logged to a PC with an integration time of 5 seconds.

Quinn et al. (1951) found that a minimum of 2 hours was required for PTFE to reach a steady state volume after heating through part of the transition temperature. For this reason, the temperature of the water bath was incremented at 3 hour intervals allowing stabilisation at temperatures of 14 °C, 17 °C, 21 °C, 24 °C and 28 °C. The temperature of the integrating sphere was monitored with a type-T thermocouple attached to the aluminium casing of the sphere and the data was logged to the PC. Silica beads were used to reduce the humidity within the chamber and to prevent condensation, a problem that was identified from the transmittance experiments.

The flux from the integrating sphere's exit port was corrected for drifts in the incident laser radiant power during the experiment by taking the quotient of the signal from the trap detector and the signal from the reference beam. A correction for the temperature response of the trap detector was not applied because the effect was considered negligible (the temperature coefficient at a wavelength of 633 nm over the temperature range studied for the Hamamatsu silicon photodiode detectors is less than – 0.01 % $°C^{-1}$). No dark current correction was applied to the measurement of exit port flux because the ratio of signal to dark current was found to be in excess of 3×10^4 and therefore the

temperature sensitivity of the dark current has a negligible uncertainty contribution. A photograph of the experiment set-up is given in Figure 4.7. A photograph of the inside of the thermally insulated chamber is given in Figure 4.8, and a schematic is given in Figure 4.6.

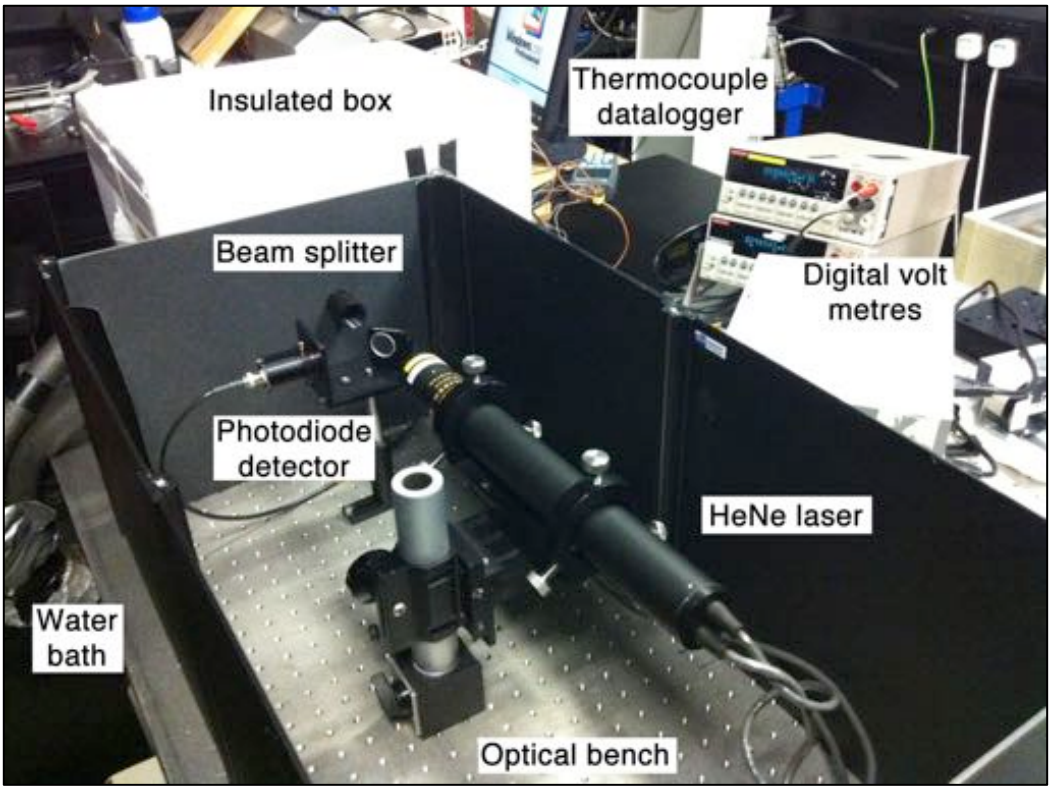

Figure 4.7. Photograph of the experiment set-up in the laboratory at NPL

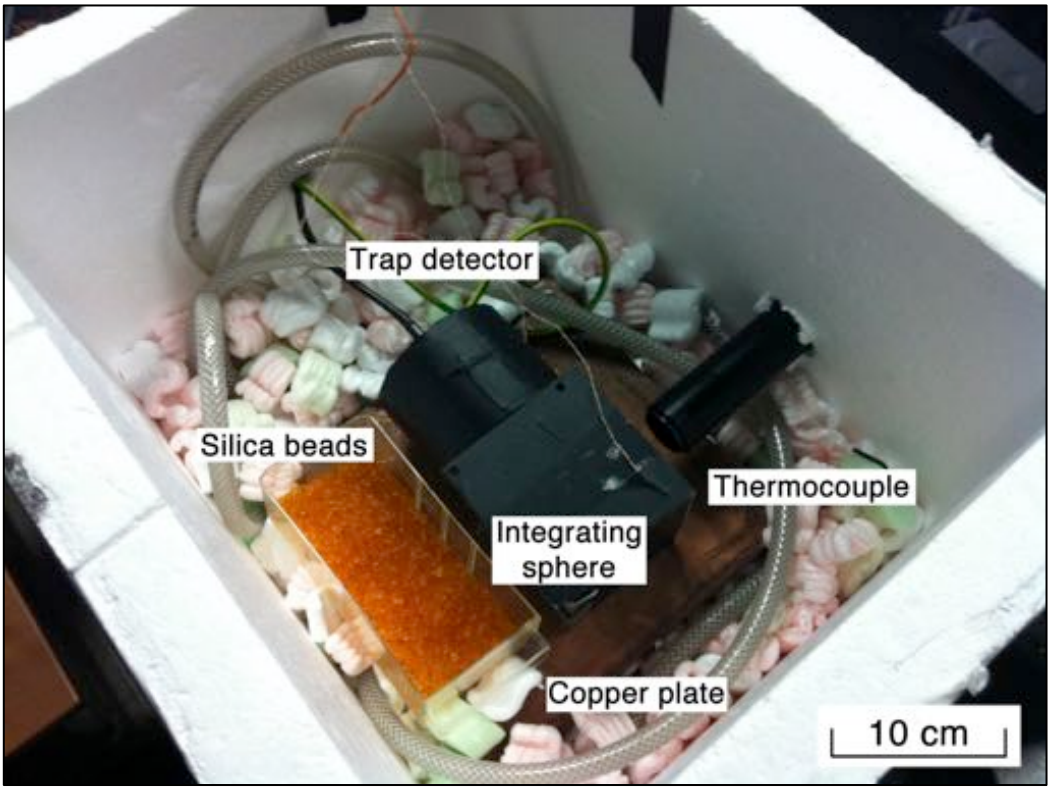

Figure 4.8. Photograph of the inside of the insulated chamber

To test that the observed change in output flux was not due to the temperature response of the detector, or other factors related to the experiment setup, the experiment was repeated by substituting the PTFE integrating sphere with a barium sulphate coated integrating sphere (that has no known temperature sensitivities over the temperature range studied), which showed no detectable change in signal (± 0.03 %) (1σ) over the temperature range of interest.

4.4.2.3 Sphere radiance, output flux, thermal expansion and reflectance

The integrating sphere radiance is the photon flux density per unit solid angle of light emitted from the surface of the sphere and is a function of input flux, sphere radius, reflectance and port fraction and is given by (Carr, 1997)

$$L = \frac{\Phi_i}{\pi A_s} \frac{\rho}{1-\rho(1-f)}, \qquad \text{Eq. 4.1}$$

where L is the integrating sphere radiance, Φ_i is the input flux, A_s is the surface area of the integrating sphere, ρ is the reflectance of the PTFE sphere and f is the sphere port fraction. The port fraction is the ratio of the surface area of the sphere's ports to the surface area of the sphere (Carr, 1997). A schematic of the integrating sphere is given in Figure 4.9.

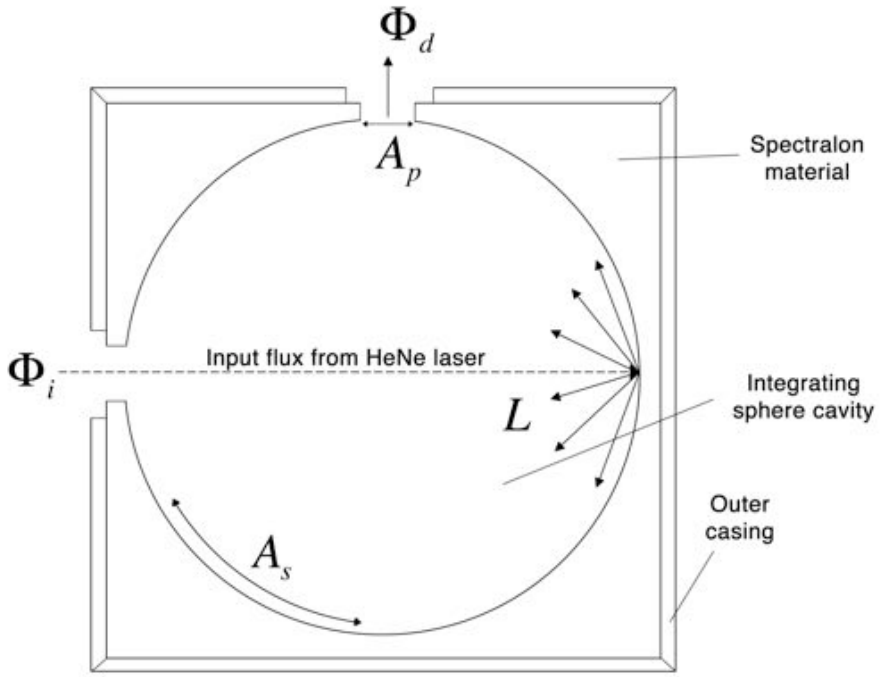

Figure 4.9 Schematic of the Spectralon integrating sphere

The measurement system (given in Figure 4.6, Figure 4.8 and Figure 4.9) has a detector mounted externally to the integrating sphere at a short distance from the sphere exit port. There are no additional apertures and therefore the PTFE integrating sphere exit port and the detector size define the radiometric measurement configuration. The radiometric flux onto the detector Φ_d is given by (Carr, 1997)

$$\Phi_d = A_p \Omega_{det-p} L \qquad \text{Eq. 4.2}$$

A_p is the area of the exit port, $\Omega_{\det-p}$ is the solid angle subtended by the detector from the exit port. Combining Eq. 4.1 and Eq. 2.2 gives

$$\Phi_d = A_p \Omega_{\det - p} \frac{\Phi_i}{\pi A_s} \frac{\rho}{1-\rho(1-f)}, \qquad \text{Eq. 4.3}$$

The solid angle subtended by the detector Ω_{det-p}, the input flux Φ_i, and the port fraction f, in Eq. 4.3, all remain constant with temperature. The sphere surface area and the exit port area change with temperature owing to thermal expansion of the sphere. The change in detector signal $\delta\Phi_d$ is given by the partial differentiation of Φ_d with respect to the exit port radius r_p, the sphere radius r_s, and the reflectance ρ, which may be written as follows

$$\delta\Phi_d = \left(\frac{\partial\Phi_d}{\partial r_p}\right)\delta r_p + \left(\frac{\partial\Phi_d}{\partial r_s}\right)\delta r_s + \left(\frac{\partial\Phi_d}{\partial\rho}\right)\delta\rho \,. \qquad \text{Eq. 4.4}$$

The partial derivatives in Eq. 4.4 will each be considered in turn to assess their contribution to the total change in detector signal, the resulting equation can then be used to derive the change in reflectance for a known change in detector signal, exit port radius, and sphere radius.

4.4.2.3.1 Exit port radius

The relative change in flux onto the detector owing to thermal expansion of the exit port is given by the partial differentiation of Φ_d in Eq. 4.3 with respect to A_p. The exit port area depends on the exit port radius

$$A_p = \pi r_p^2 \,. \qquad \text{Eq. 4.5}$$

Combining Eq. 4.3 with Eq. 4.5 gives

$$\Phi_d = \pi r_p^2 \Omega_{\det - p} \frac{\Phi_i}{\pi A_s} \frac{\rho}{1-\rho(1-f)}, \qquad \text{Eq. 4.6}$$

and partial differentiation of Φ_d with respect to r_p yields

$$\frac{\delta\Phi_d}{\delta r_p} = 2 r_p k \,, \qquad \text{Eq. 4.7}$$

where k is the constants in Eq. 4.6, and is defined as

$$k = \pi\Omega_{\det-p}\frac{\Phi_i}{\pi A_s}\frac{\rho}{1-\rho(1-f)}, \qquad \text{Eq. 4.8}$$

k is related to Φ_d from Eq. 4.6 as follows

$$\Phi_d = kr_p^2. \qquad \text{Eq. 4.9}$$

Rearranging Eq. 4.9 for k,

$$k = \frac{\Phi_d}{r_p^2}, \qquad \text{Eq. 4.10}$$

and substitution of Eq. 4.10 into Eq. 4.7 gives

$$\frac{\delta\Phi_d}{\delta r_p} = \frac{2r_p\Phi_d}{r_p^2} = \frac{2\Phi_d}{r_p}. \qquad \text{Eq. 4.11}$$

Dividing through by Φ_d in Eq. 4.11 gives

$$\frac{\delta\Phi_d}{\delta r_p\Phi_d} = \frac{2}{r_p}, \qquad \text{Eq. 4.12}$$

and then multiplying both sides by δr_p gives

$$\frac{\delta\Phi_d}{\Phi_d} = \frac{2\delta r_p}{r_p}. \qquad \text{Eq. 4.13}$$

Eq. 4.13 is the relative change in flux on the detector owing to a change in exit port radius, or exit port surface area. The relative change in flux onto the detector Φ_d is twice the relative change in the exit port radius r_p.

4.4.2.3.2 Sphere radius

The relative change in flux onto the detector owing to thermal expansion of the PTFE sphere is given by the partial derivative of Φ_d in Eq. 4.3 with respect the sphere surface area A_s. The sphere surface area depends on the radius of the sphere

$$A_s = 4\pi r_s^2. \qquad \text{Eq. 4.14}$$

Combing equation Eq. 4.3 and Eq. 4.14,

$$\Phi_d = A_p \Omega_{\det - p} \frac{\Phi_i}{\pi^2 4 r_s^2} \frac{\rho}{1-\rho(1-f)}, \quad \text{Eq. 4.15}$$

and differentiating Eq. 4.15 with respect to r_s yields

$$\frac{\delta \Phi_d}{\delta r_s} = -2 r_s^{-3} q = \frac{-2q}{r_s^3}, \quad \text{Eq. 4.16}$$

where q is the constants in Eq. 4.3, and is defined as

$$q = A_p \Omega_{\det - p} \frac{\Phi_i}{4\pi^2} \frac{\rho}{1-\rho(1-f)}, \quad \text{Eq. 4.17}$$

q is related to Eq. 4.15 as follows

$$\Phi_d = \frac{q}{r_s^2}. \quad \text{Eq. 4.18}$$

Rearranging Eq. 4.18 for q

$$q = \Phi_d r_s^2, \quad \text{Eq. 4.19}$$

and substituting into Eq. 4.16

$$\frac{\delta \Phi_d}{\delta r_s} = \frac{-2\Phi_d r_s^2}{r_s^3} = \frac{-2\Phi_d}{r_s}. \quad \text{Eq. 4.20}$$

Dividing Eq. 4.20 by Φ_d gives

$$\frac{\delta \Phi_d}{\delta r_s \Phi_d} = \frac{-2}{r_s}, \quad \text{Eq. 4.21}$$

and then multiplying by δr_s gives

$$\frac{\delta \Phi_d}{\Phi_d} = \frac{-2\delta r_s}{r_s}. \quad \text{Eq. 4.22}$$

Eq. 4.22 is the relative change in flux on the detector owing to a change in the radius of the integrating sphere, or sphere surface area. The relative change in flux onto the detector Φ_d is inversely proportional to the change in sphere radius r_s, and is twice the relative change in the sphere radius.

4.4.2.3.3 Reflectivity of the sphere

The relative change in flux onto the detector owing to a change in reflectivity of the sphere is given by the partial derivative of Φ_d in Eq. 4.3 with respect to the sphere reflectance ρ . Using the quotient rule, the derivative of Φ_d with respect to ρ is as follows

$$\frac{\delta\Phi_d}{\delta\rho} = \frac{1-\rho(1-f)+\rho(1-f)}{\left(1-\rho(1-f)\right)^2} = \frac{1}{\left(1-\rho(1-f)\right)^2} \quad \text{Eq. 4.23}$$

The differentiation leading to the derivation to Eq. 4.23 is given in Appendix 4.

Dividing Eq. 4.23 by Eq. 4.3 gives

$$\frac{\delta\Phi_d}{\delta\rho\Phi_d} = \frac{1-\rho(1-f)}{\rho\left(1-\rho(1-f)\right)^2} = \frac{1}{\rho\left(1-\rho(1-f)\right)} \quad \text{Eq. 4.24}$$

and then multiplying Eq. 4.24 by $\delta\rho$ gives the relative change in flux on to the detector owing to a change in reflectance of the sphere, as follows

$$\frac{\delta\Phi_d}{\Phi_d} = \frac{\delta\rho}{\rho}\frac{1}{\left(1-\rho(1-f)\right)} \quad \text{Eq. 4.25}$$

Finally, combing Eq. 4.13, Eq. 4.22, and Eq. 4.25, and substituting into Eq. 4.4 gives

$$\frac{\delta\Phi_d}{\Phi_d} = \frac{2\delta r_p}{r_p} - \frac{2\delta r_s}{r_s} + \frac{\delta\rho}{\rho}\frac{1}{\left(1-\rho(1-f)\right)}, \quad \text{Eq. 4.26}$$

which is the total relative change in flux onto the detector owing to a change in the reflectivity of the sphere, and thermal expansion of the sphere and its exit port.

The port aperture is formed from the PTFE sphere, thus the relative change in radius of the port owing to thermal expansion is equivalent to the relative change in radius of the sphere (i.e. $\delta r_p / r_p = \delta r_s / r_s$) (assuming isotropic linear

expansion) and the first and second terms in Eq. 4.26 cancel, and Eq. 4.26 simplifies to

$$\frac{\delta\Phi_d}{\Phi_d} = \frac{\delta\rho}{\rho}\frac{1}{\left(1-\rho\left(1-f\right)\right)}, \qquad \text{Eq. 4.27}$$

Therefore, for the experiment described, where the sphere exit port is one of the radiance defining apertures, the change in flux with temperature depends solely on the change in the reflectivity of the PTFE sphere. Thus the relative change in reflectance $\delta\rho/\rho$ can be determined without accurate knowledge of the PTFE expansion coefficient or other geometrical information, by rearranging Eq. 4.27 as follows

$$\frac{\delta\rho}{\rho} = \frac{\delta\Phi_d}{\Phi_d}\left(1-\rho\left(1-f\right)\right). \qquad \text{Eq. 4.28}$$

Eq. 4.28 gives the relationship between the relative change in reflectance of the sphere and the change in the flux onto the detector at the spheres exit port; and can be used to calculate the change in reflectivity of the sphere, for a given change in flux onto the detector. Eq. 4.28 is an elegant solution to the problem of calculating a very small change in the hemispherical reflectivity of a material. The multiplicative term, $1/\left(1-\rho\left(1-f\right)\right)$ in Eq. 4.27 represents the gain in sensitivity to reflectance due to the multiple reflections within an integrating sphere compared to a flat panel. Given the large reflectivity of PTFE $\left(\rho = 0.99\right)$ and the small port fraction used here $\left(f = 0.04\right)$, the sphere multiplier for the PTFE used in this experiment, and the magnitude of the enhanced sensitivity, is of the order of 20.

4.4.2.4 System stability

Prior to undertaking the experiment, the stability of the illumination source was measured by monitoring the flux from the PTFE sphere for a 12-hour period at a

constant temperature of 14 °C. The results are shown in Figure 4.10 and Figure 4.11. No change in flux was observed and the relative standard deviation of the signal, $\delta\Phi_d/\Phi_d$, was $\sim 5 \times 10^{-4}$.

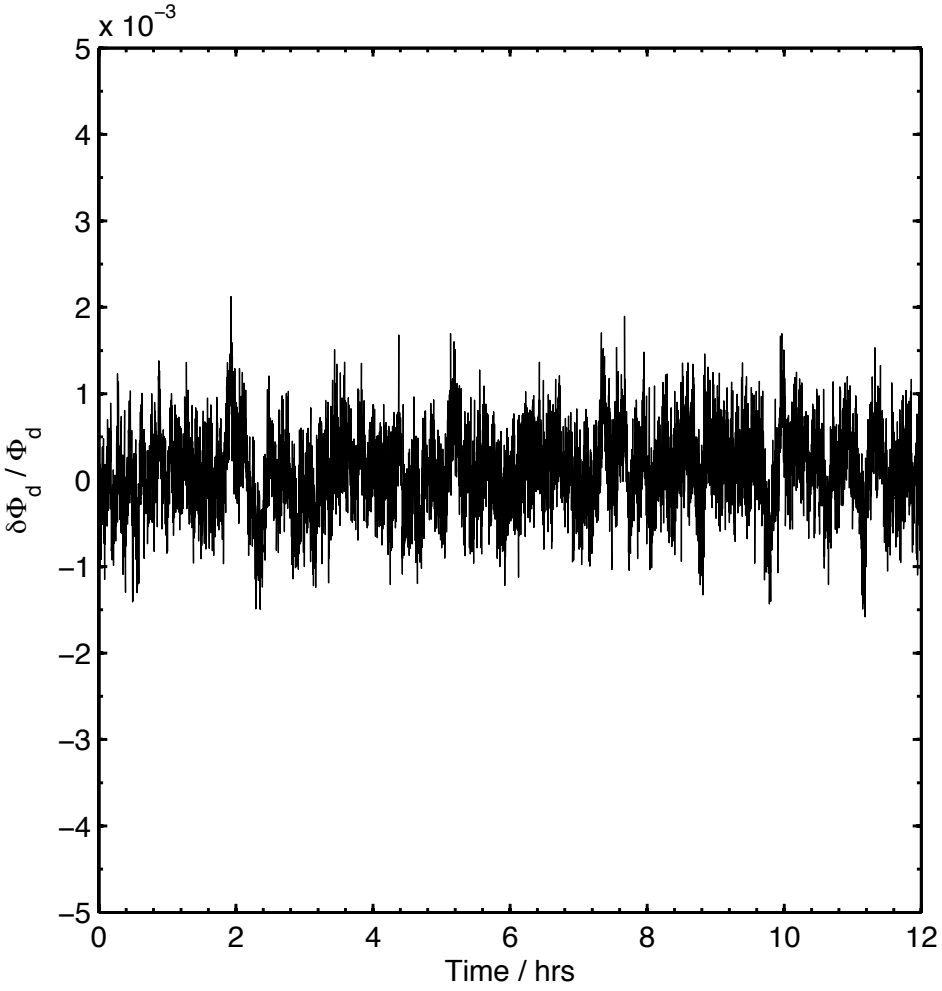

Figure 4.10. Relative change in flux over a 12-hour period for the PTFE integrating sphere, demonstrating the stability of the measurement set-up

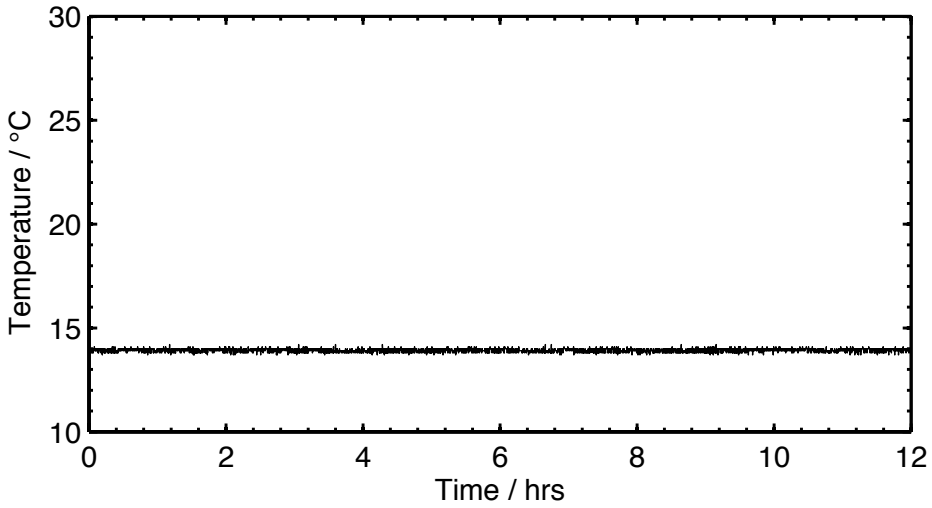

Figure 4.11. Temperature over a 12-hour period during the stability test for the PTFE integrating sphere

4.5 Experiment results

The results section will be divided into sections presenting the results of the transmittance experiments and the results of the reflectance experiments separately.

4.5.1 Transmittance experiments

The averaged transmittance for 16 measurements as a function of temperature is given for the PTFE diffuser at 400 nm in Figure 4.12, and at 600 nm in Figure 4.13.

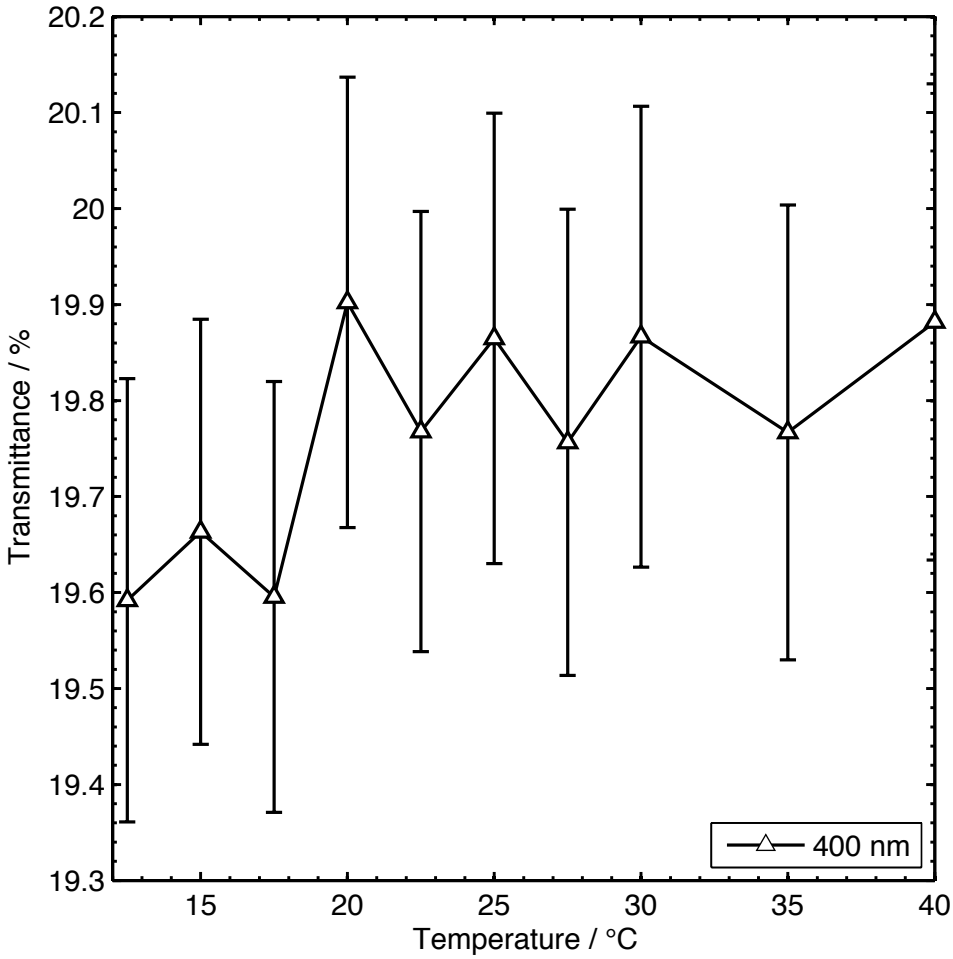

Figure 4.12. Percentage transmittance as a function of temperature for the PTFE diffuser at a wavelength of 400 nm. The uncertainty bars are one standard deviation of the 16 averaged measurements

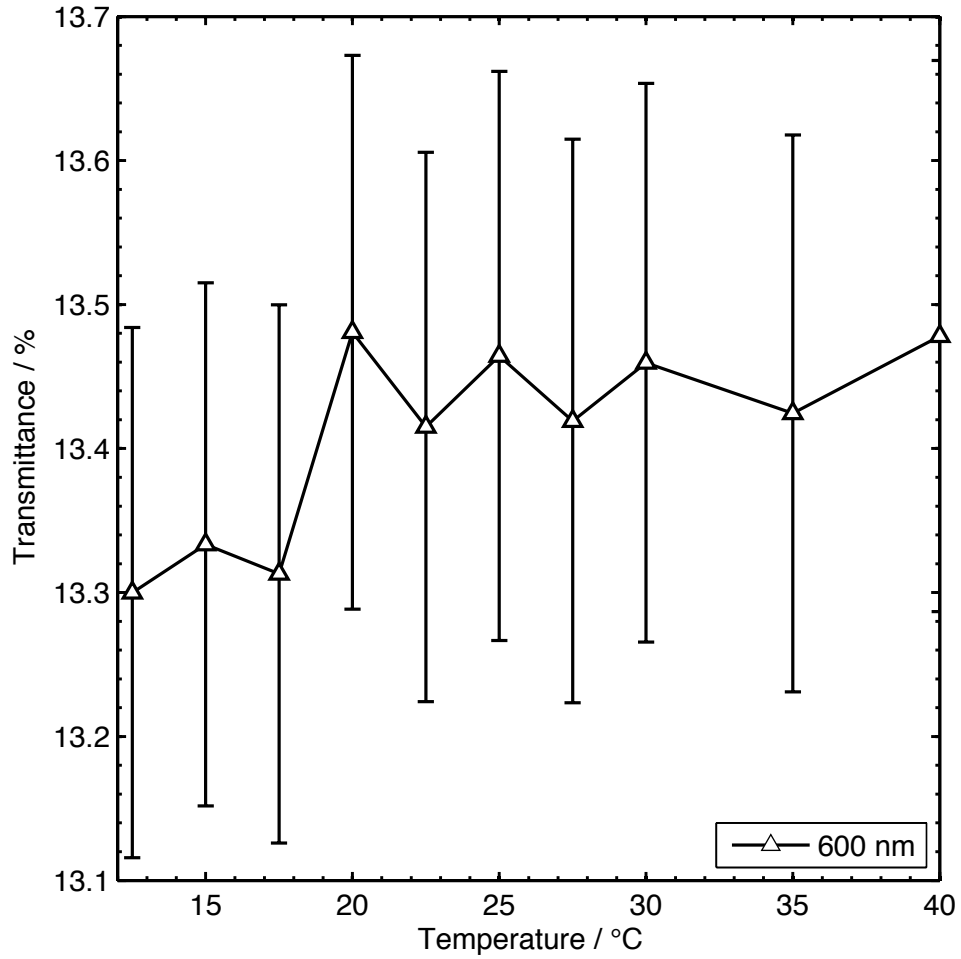

Figure 4.13. Percentage transmittance as a function of temperature for the PTFE diffuser at a wavelength of 600 nm. The uncertainty bars are one standard deviation of the 16 averaged measurements

There was considerable variance in the averaged measurements with a maximum standard deviation of 0.29. There was no detectable change above the level of uncertainty in the averaged measurements, but there was a notable increase in transmittance between 17.5 °C and 20 °C of 0.3 % at 400 nm, with an increase of 0.2 % in transmittance at 600 nm. The greatest increase was observed between the temperature steps that correlates with the position of the 19 °C PTFE phase transition, where PTFE undergoes a first order phase change from phase II to phase IV (Clark, 1999).

The relative change in transmittance $\delta T/T$ was calculated as follows

$$\frac{\delta T}{T} = \frac{T - T_0}{T_0} \quad \text{Eq. 4.29}$$

where T is the transmittance and T_0 is the transmittance at the reference temperature of 12.5 °C. The uncertainty in $\delta T/T$ was calculated by propagating the uncertainty given by one standard deviation of the averaged transmittance measurements presented in Figure 4.12 and Figure 4.13. The uncertainty was propagated given a function of the form

$$y = \frac{x - x_0}{x_0} \quad \text{Eq. 4.30}$$

as in Eq. 4.29, and with uncertainty in both x and x_0. The variables y, x and x_0 in Eq. 4.30, are equal to $\delta T/T$, T and T_0 in Eq. 4.29 respectively. The uncertainty in y, or $\delta T/T$, is given by the error propagation equation (Bevington and Robinson, 2003):

$$\sigma_y^2 \simeq \sigma_x^2 \left(\frac{\partial y}{\partial x}\right)^2 + \sigma_{x_0}^2 \left(\frac{\partial y}{\partial x_0}\right)^2 \quad \text{Eq. 4.31}$$

where σ_y^2 is the uncertainty in y. Partial differentiation of y with respect to x in Eq. 4.30 gives

$$\frac{\partial y}{\partial x} = \frac{1}{x_0} \quad \text{Eq. 4.32}$$

and partial differentiation of y with respect to x_0 in Eq. 4.30 gives

$$\frac{\partial y}{\partial x_0} = \frac{-x}{x_0^2} \quad \text{Eq. 4.33}$$

Substitution of Eq. 4.32 and Eq. 4.33 into Eq. 4.31 gives

$$\sigma_y^2 \simeq \frac{\sigma_x^2}{x_0^2} + \frac{x^2 \sigma_{x_0}^2}{x_0^4} \quad \text{Eq. 4.34}$$

Given that $x \sim x_0$, Eq. 4.34 can be simplified to

$$\sigma_y^2 \simeq \frac{2\sigma_x^2}{x^2} \quad \text{Eq. 4.35}$$

and thus,

$$\sigma_y \simeq \frac{\sqrt{2}\sigma_x}{x} \quad \text{Eq. 4.36}$$

The relative change in transmittance as a function of temperature for the averaged measurements is given in Figure 4.14 at 400 nm, and in Figure 4.15 at 600 nm.

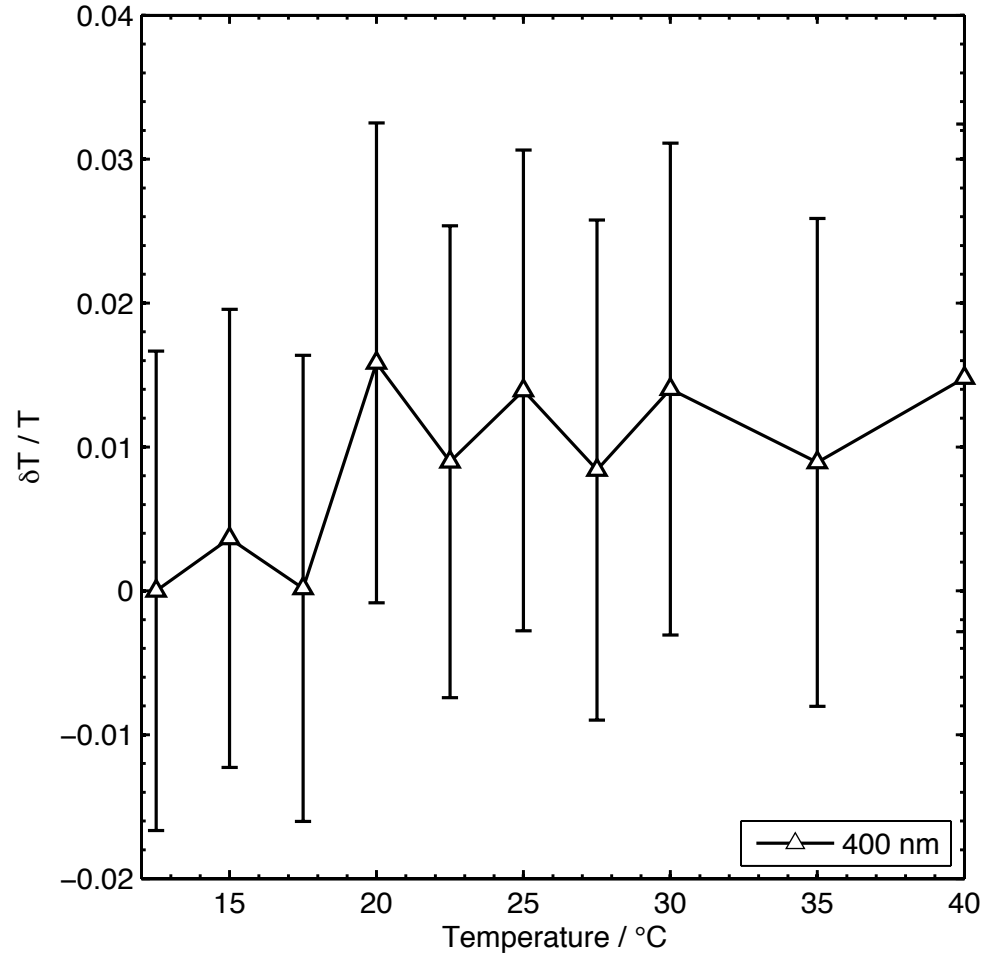

Figure 4.14. Relative change in the averaged transmittance of Spectralon as a function of temperature at 400 nm. Uncertainty bars were propagated from one standard deviation of the averaged transmittance measurements

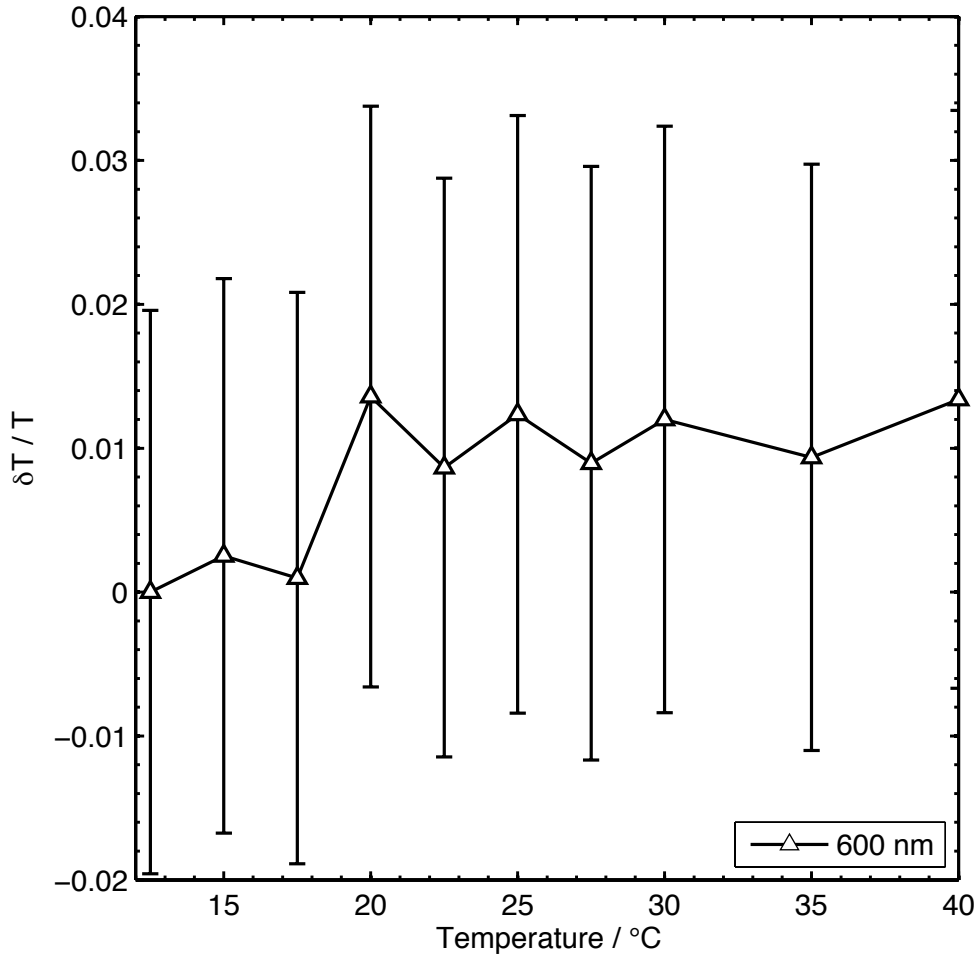

Figure 4.15. Relative change in the averaged transmittance of Spectralon as a function of temperature at 600 nm. Uncertainty bars were propagated from one standard deviation of the averaged transmittance measurements

The relative change for the averaged measurements between 12.5 °C and 20 °C was 1.6 % at 400 nm, and was 1.4 % at 600 nm. The relative change in the transmittance was greatest at the temperature step 17.5 °C to 20 °C, which correlates with the 19 °C phase transition temperature. However, there is low confidence in the measured change in transmittance because of the large variance in the repeat measurements. The transmittance as a function of wavelength at 15 °C, and at 20 °C, is given in Figure 4.16, and the relative change in transmittance $\delta T/T$ as a function of wavelength is given in Figure 4.17.

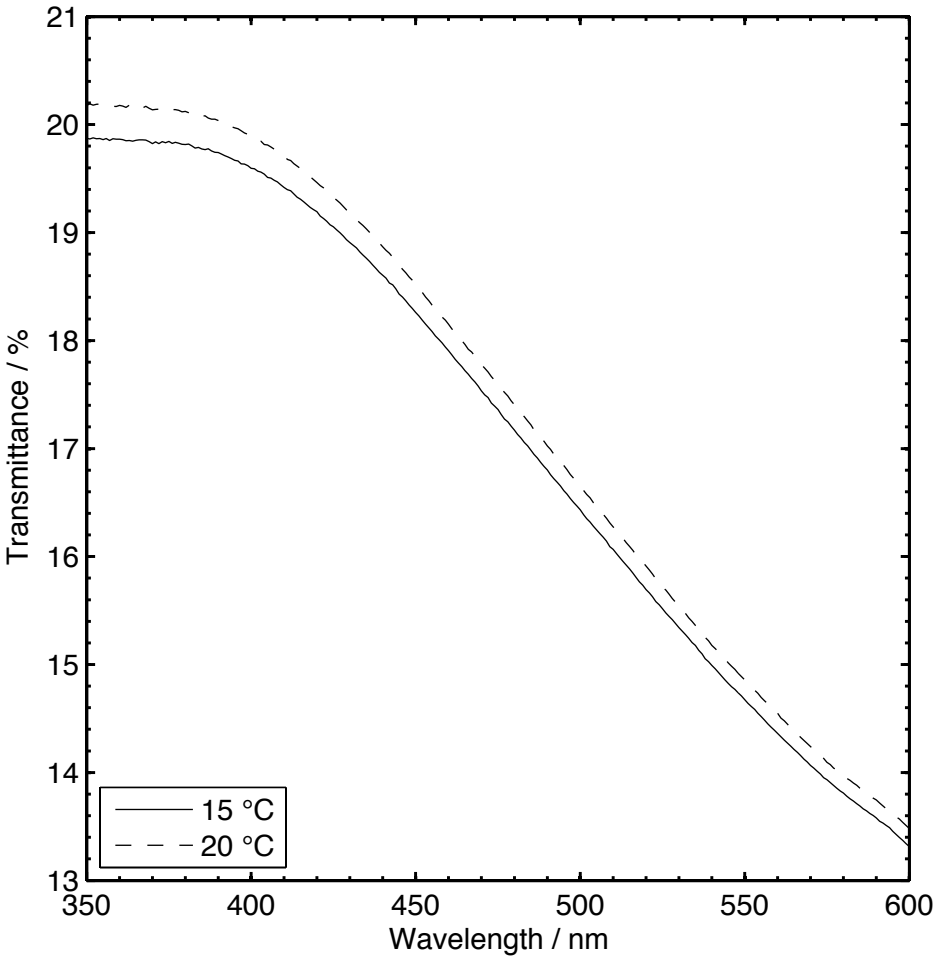

Figure 4.16. Transmittance of Spectralon as a function of wavelength at temperatures that straddle the phase transition temperature

The effect of the phase change appears to have a small wavelength dependence of around 0.3 %, with the relative change in transmittance between the transmittance at 12.5°C and at 20 °C increasing inversely with wavelength to a maximum of 1.7 % around 350 nm; although the measured change in transmittance is within the uncertainty of the averaged measurements.

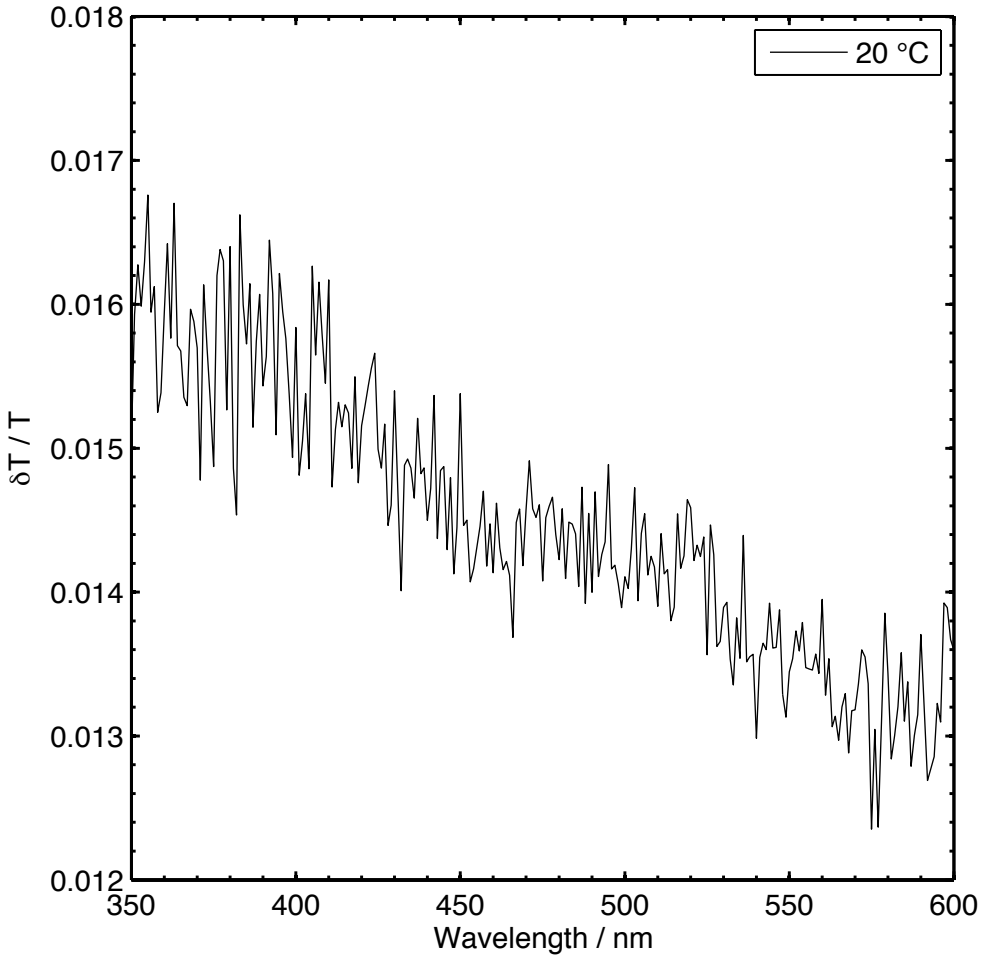

Figure 4.17. Relative change in transmittance from the reference temperature of 12.5 °C as a function of wavelength for a temperature of 20 °C

4.5.2 Reflectance experiments

The relative change in integrating sphere output flux with time is presented in Figure 4.18 for the PTFE sphere, and the temperature of the PTFE sphere is given in Figure 4.19. The relative change in output flux with time is presented in Figure 4.20 for the barium sulphate sphere, and the temperature of the barium sulphate sphere is given in Figure 4.21. The output flux from each integrating sphere was averaged over the final 30-minute period of each temperature step and the data are presented in Figure 4.22 The uncertainty bars in Figure 4.22 represent two standard deviations of the averaged measurements of output flux.

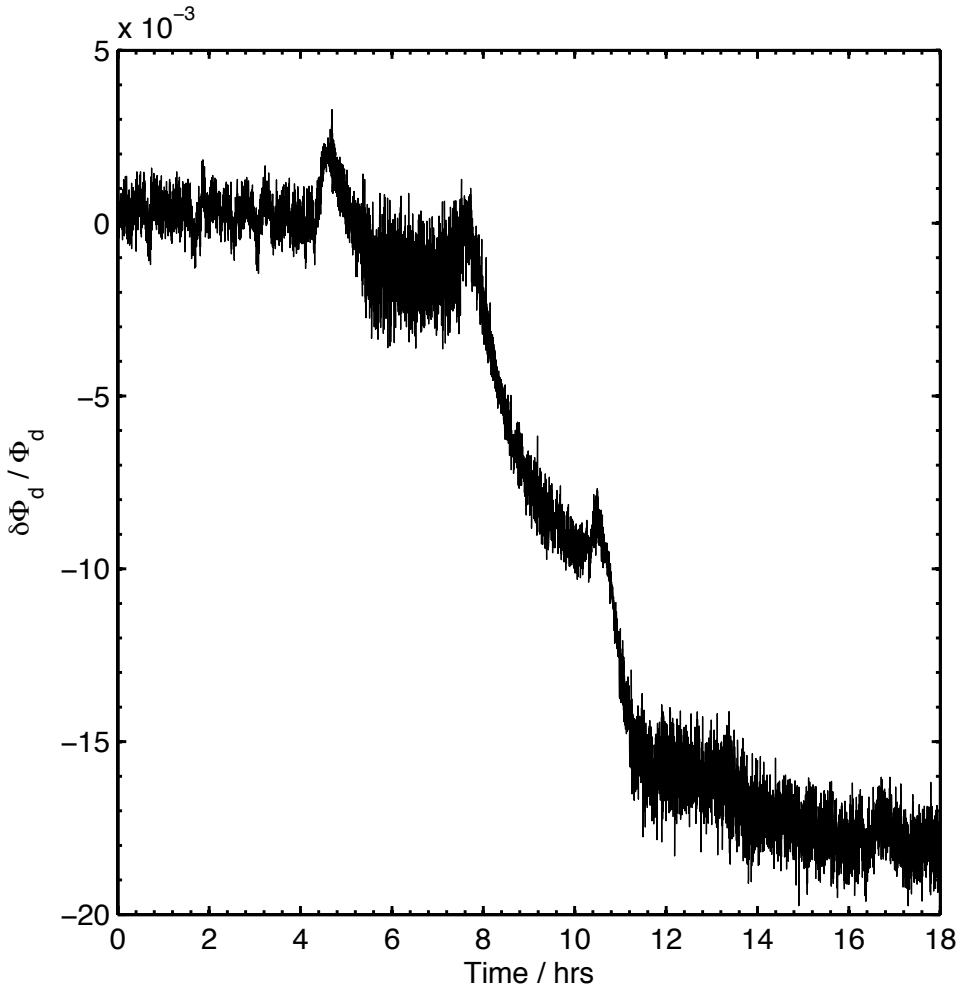

Figure 4.18. Relative change in flux from the exit port of the PTFE integrating sphere, when the temperature is increased in a stepwise fashion

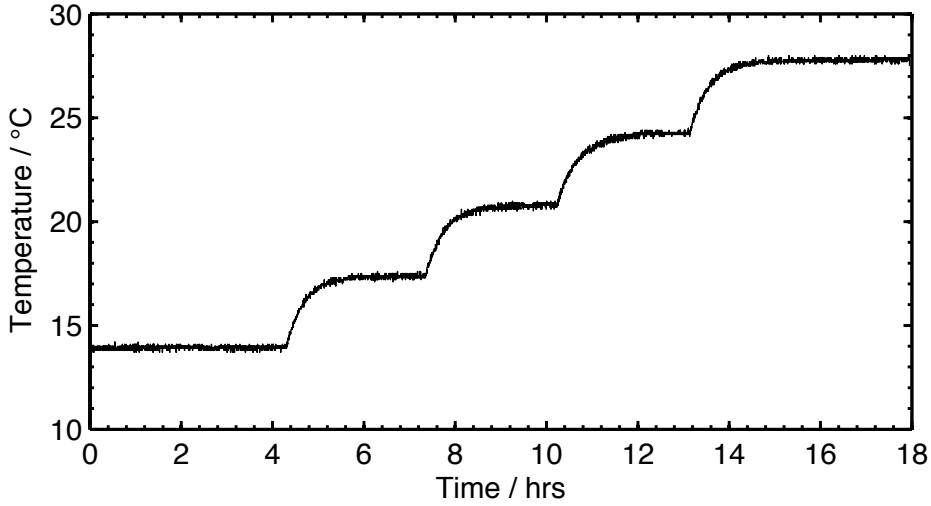

Figure 4.19. Measured change in temperature of the PTFE integrating sphere

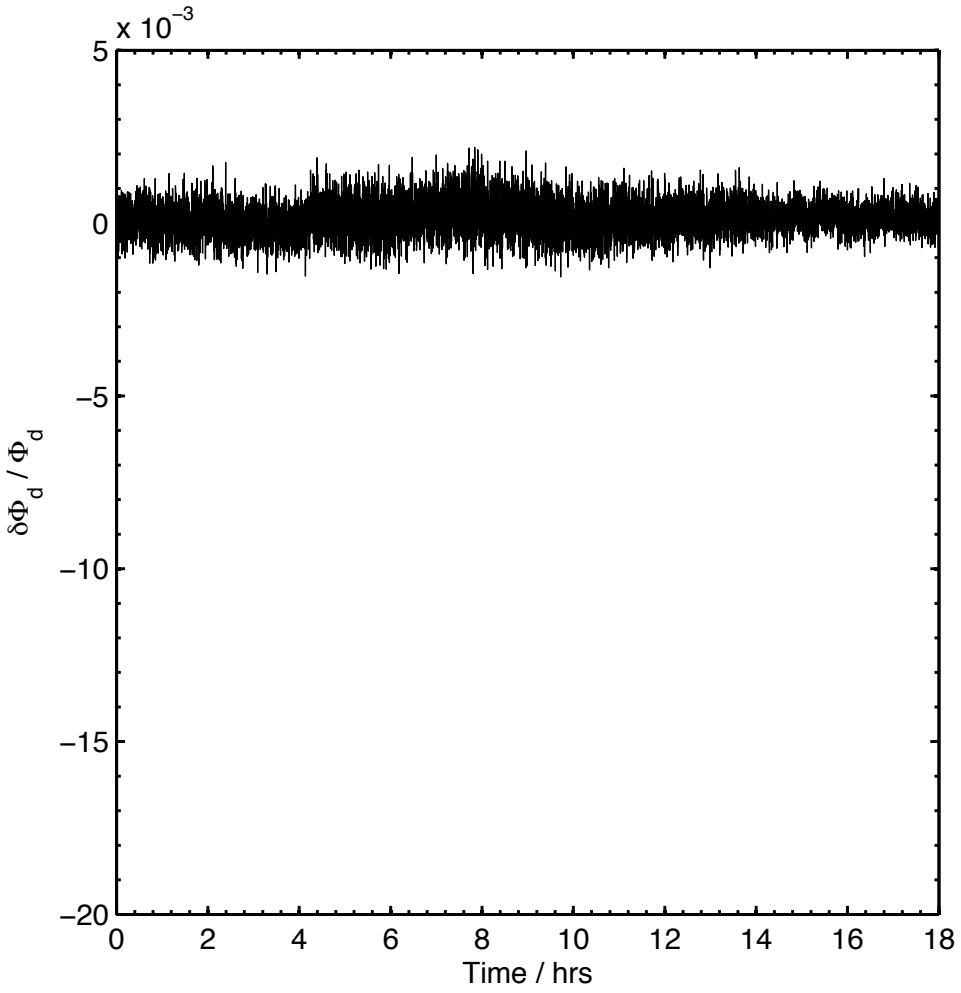

Figure 4.20. Relative change in flux from the exit port of the barium sulfate integrating sphere, when the temperature is increased in a stepwise fashion

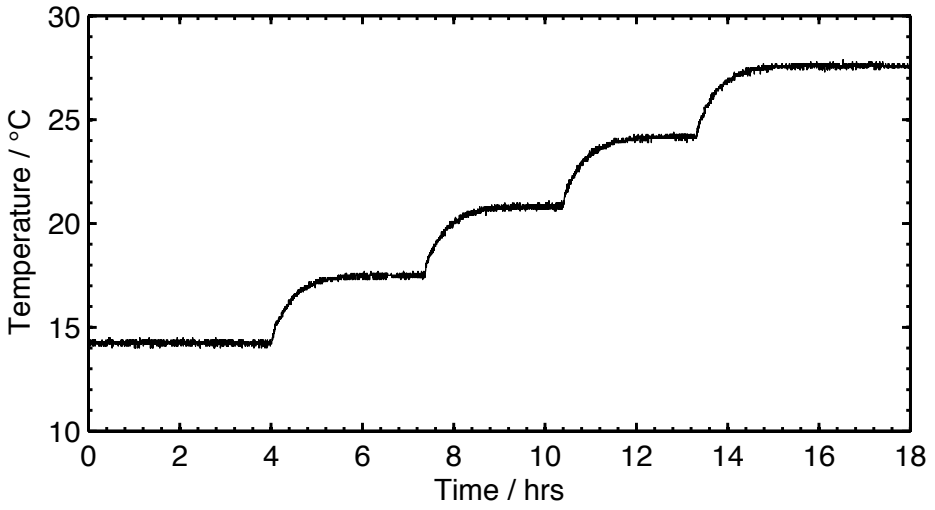

Figure 4.21. Measured change in temperature of the barium sulphate integrating sphere

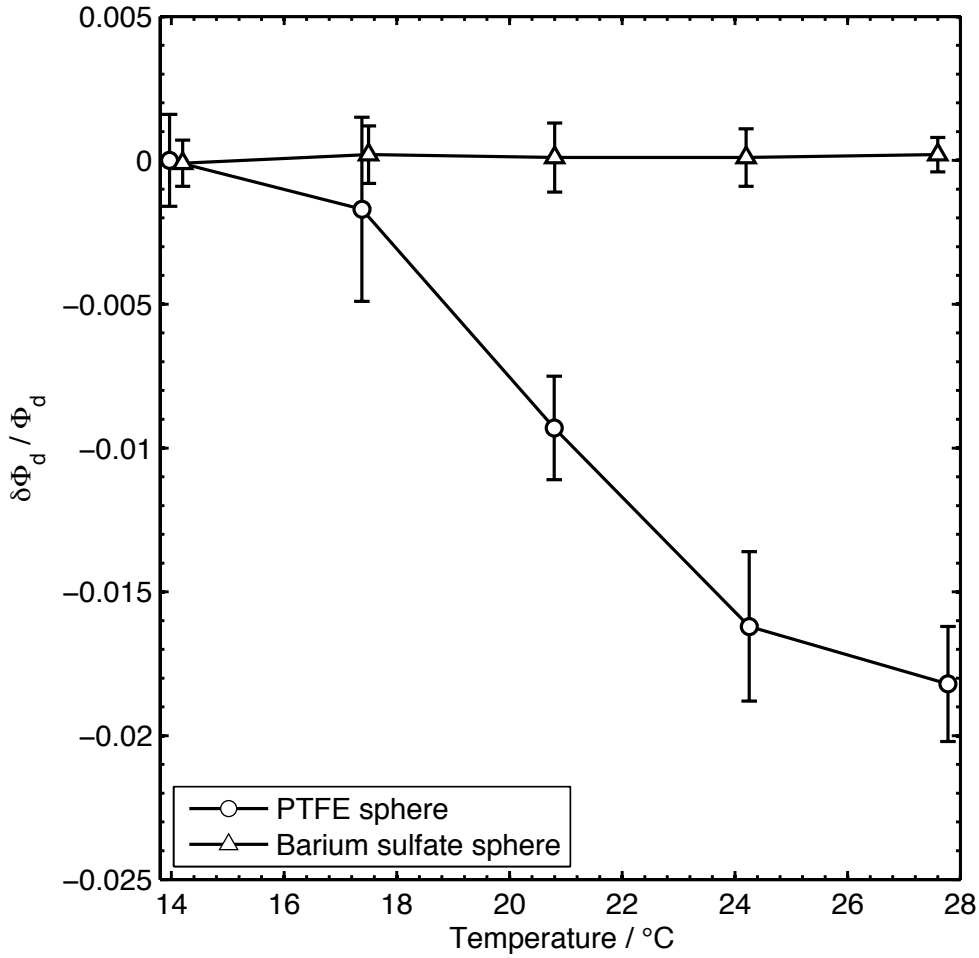

Figure 4.22. Relative change in output flux with temperature for the PTFE sphere and the barium sulphate sphere. Uncertainty bars are given to two standard deviations

Inspection of Figure 4.18 and Figure 4.19 demonstrates that the output flux from the PTFE integrating sphere decreased with each increment in the temperature, leading to a total decrease of 1.82 ± 0.21 % in output flux between 14 °C and 28 °C. Within the measurement uncertainty, there was no detectable change in the output flux from the barium sulphate sphere over the same temperature range; indicating that the change in output flux with temperature in Figure 4.18 is related to the phase transition in PTFE, and not an artefact of the measurement system. The magnitude of the decrease in output flux with temperature from the PTFE sphere is largest in the temperature steps from 17 °C to 21 °C (~ 0.75 % of magnitude); compared to a decrease in output flux between 14 °C and 17 °C of approximately 0.17 % and between 24 °C and 28 °C of approximately 0.20 %

of the total observed magnitude change. The position of greatest change in output flux correlates with the position of the 19 °C phase transition, where PTFE undergoes a first order phase change (Clark, 1999). The relative change in reflectance of the PTFE coating over the temperature range 14 °C to 28 °C from the reference temperature at 14 °C has been calculated using Eq. 4.28 and is presented in Figure 4.23.

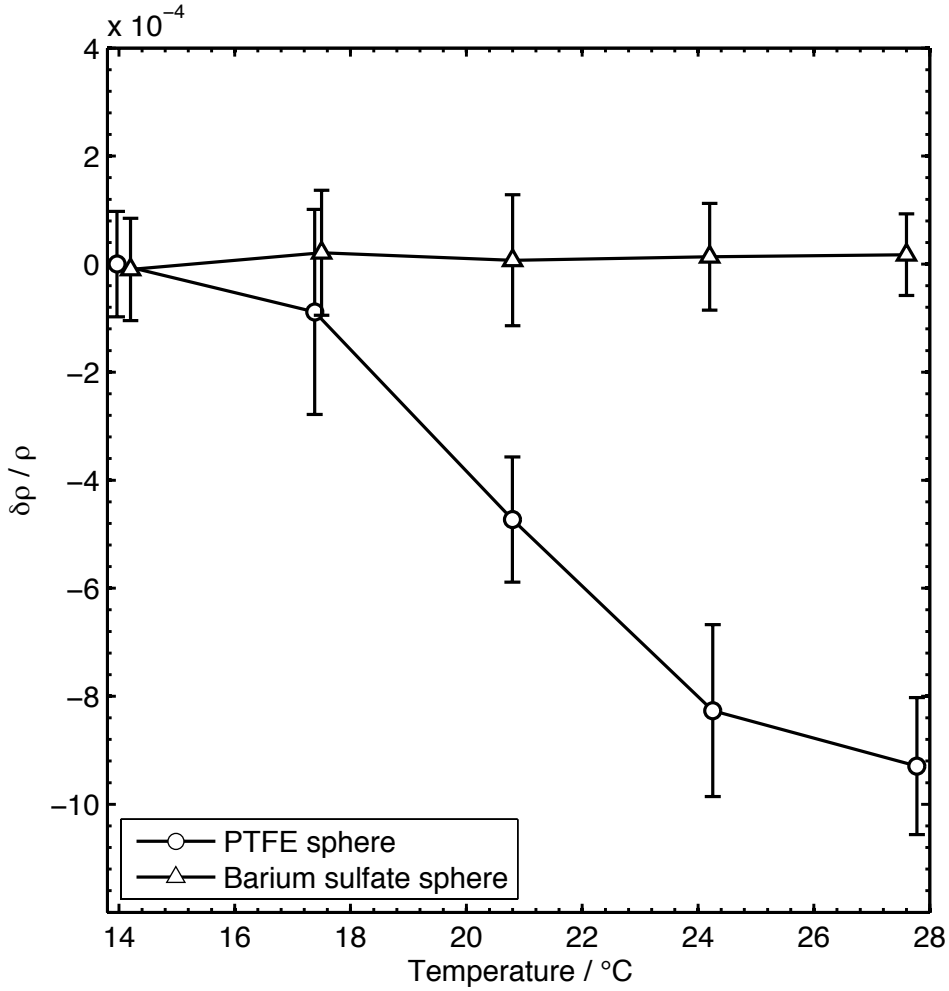

Figure 4.23. Relative change in reflectance with temperature from 14 °C to 28 °C for the PTFE sphere and the barium sulfate sphere. Uncertainty bars are two standard deviations of the averaged measurements with an additional uncertainty term of 20% owing to uncertainty associated with the sphere multiplier

The total decrease in reflectance over temperature range 14 °C to 28 °C is 0.09 ± 0.02 %. The uncertainty associated with the calculated reflectance is dominated by the limited knowledge of the sphere multiplier. The relative

change in reflectivity is calculated from the sphere reflectance and the port fraction, itself a function of the sphere and port areas. Since these terms are only known approximately, a conservative estimate of 20 % is given to the uncertainty associated with the sphere multiplier.

4.6 Discussion

The discussion section will be divided into separate sections presenting the results of the transmittance experiments and the results of the reflectance experiments.

4.6.1 Transmittance experiments

The experiments showed an increase in transmittance of up to 1.7 % at 350 nm between 12.5 °C and 20 °C, corresponding with the position of the phase change identified in the literature at 19 °C (McKenzie et al., 2005; Ylianttila and Schreder, 2005). The change in transmittance had a small wavelength dependence of around 0.3 %. There was however, considerable variance in the averaged measurements owing to the combined effect of differences in the thickness of the PTFE samples used, the short temperature stabilization period, and the small amount of radiation transmitted by the samples. Transmission through the filters used in this study was very small (less than 3 %) and as a result, the control filter had instability in its transmittance of up to ± 0.5 %, and the dark signal was up to 0.45 % of the measured transmittance; indicating that the spectrophotometer is close to its limit of detection. As a result, there was considerable uncertainty associated with the results while trying to resolve differences in transmittance of less than 0.5 %. Averaging multiple measurements helped to reduce the variance in the results, and in general, the averaged results agreed well with previous studies by McKenzie et al. (2005)

and Ylianttila and Schreder (2005), that measured a 2 %, and a 1 % to 3 %, increase in transmittance of PTFE diffusers owing to the 19 °C phase change respectively. In order to improve the transmittance experiments in this study, thinner samples of PTFE should be used and an improved characterization of the thickness of the samples should be undertaken. In future experiments a spectrophotometer with an integrating sphere should to used to capture all radiation transmitted through the sample.

4.6.2 Reflectance experiments

The discussion leading to the derivation of Eq. 4.28 associates all the observed change in output flux with the PTFE reflectance, for this particular experimental set-up. The use of an integrating sphere increased the sensitivity of the measurement set-up by approximately a factor of 20, compared to an experiment monitoring reflected flux from a flat panel. The temperature at which the greatest change in output flux from the PTFE sphere was observed corresponds with the position of the phase change identified in the literature at 19 °C. A control experiment with a barium sulphate sphere has confirmed that the output flux changes observed are not a consequence of the experimental design.

Eq. 4.28 assumes isotropic linear expansion of the PTFE material, whereby the relative change in the sphere and exit port radii as a function of thermal expansion are equivalent. The integrating sphere is contained within an aluminium box, which could potentially restrict the free expansion of the sphere. However, the cancellation of terms in Eq. 4.28 does not require a detailed knowledge of the internal strain, only that the forces acting on the sphere are isotropic. Through the analysis of the construction of the apparatus (i.e.

dismantling of the sphere casing) no realistic mechanism that could produce significant anisotropic behavior was apparent. There is, however, some temporal smearing of the effect across the temperature range. The temporal smearing suggests that the full phase transition is not contained solely in the 17 °C to 21 °C temperature range, but extends above 21 °C. The rapid flattening of the curve beyond 11 hours in Figure 4.18 suggests that there is little effect above 24 °C. The observed width of the transition is likely to be widened by temperature gradients across the sphere exacerbated by the low thermal conductivity of the PTFE material. Further studies could be performed to better understand this behavior with measurements over narrower temperature steps and longer stabilization periods between these steps. However, the observations presented here suggest that researchers using PTFE as a reflectance medium anywhere in the 17 °C to 24 °C temperature range should consider the effect of the material phase transition, and also consider the likely magnitude of any temperature gradients that may exist in the experimental set-up.

An approximate 1 % change in the density of PTFE across the 19 °C phase transition temperature is predicted for pressed PTFE (Quinn et al., 1951; Kirby, 1956; Clark, 1999), the reflectance of which is known to be dependent on its density (Weidner and Hsia, 1981). Given this prior knowledge, a change in reflectance of PTFE owing to a change in the density of the PTFE caused by the phase transition at 19 °C is a likely explanation for the observed change in output flux from the PTFE sphere. Owing to the amplifying effect of the sphere multiplier, a change of 1.82 ± 0.21 % in output flux represents only a small change (0.09 ± 0.02 %) in the reflectance of the PTFE sphere. For the majority of applications using a PTFE flat panel reflector as a reference standard, and

particularly in field studies, this small change is unlikely to be a significant contribution to the uncertainty budget.

The effect on output flux from a PTFE integrating sphere is significantly larger. Therefore, neglecting to correct for, or adequately stabilise the temperature when operating in this temperature regime, would introduce a significant source of error for measurements of flux, irradiance or radiance made from PTFE integrating spheres. From Eq. 4.1, the magnitude of the effect observed is dependent on the specific dimensions of the integrating sphere. For example, the effect will be magnified with decreasing port fraction.

The experiment required a very stable collimated beam, hence a He-Ne laser was used, and thus the study presented here investigated the change in reflectance at a single wavelength of 633 nm. The reflectance of PTFE across the UV-VIS wavelengths is effectively constant, and the temperature-dependent phase change is a bulk material mechanism, so a wavelength dependence in the temperature induced reflectance change is considered very unlikely. The phase transition of PTFE may have a small effect on the bidirectional reflectance (BRDF) of the PTFE material. The use of an integrating sphere prevents the investigation of this effect. However, investigation of the BRDF over the PTFE phase transition may be important for flat panel reflectors, and is worthy of investigation.

The phase transition of PTFE at a temperature of 19 °C (with smeared effect to a few degrees each side of this temperature) is of particular importance as typical operating temperature for both field studies in many temperate zones of the planet and laboratory studies. Depending on the configuration,

environmental challenges and uncertainty requirements of the measurement the optimal strategy will be one of temperature monitoring and application of a correction algorithm and/or active temperature stabilisation. To the author's knowledge, no other such measurement of the change in reflectivity of PTFE over the 19 °C phase transition exist.

4.7 Conclusion

A relative change in transmittance of up to 1.7 % was measured for a 210 μm thick Spectralon diffuser, confirming the effect of the 19 °C phase change identified by McKenzie et al. (2005) and Ylianttila and Schreder (2005) on the optical transmittance of PTFE diffusers. The relative change in the reflectance of Spectralon over the 19 °C phase change was investigated by controlling the temperature of a PTFE integrating sphere and monitoring the output flux from the sphere's exit port. The output flux from the sphere's exit port at 633 nm over the room temperature phase transition of PTFE at 19 °C was measured as 1.82 ± 0.21 % for a change in temperature from 14 °C to 28 °C. The change in flux from the integrating sphere is related to the PTFE phase transition at 19 °C as a result of a change in density of the PTFE, and was explained by a small change of 0.09 ± 0.02 % in total hemispherical reflectance of the Spectralon material. The results from the PTFE reflectance experiment have implications for both field and laboratory studies that make use of PTFE as a flat panel reflector or within an integrating sphere in room temperature conditions. In addition, the magnitude of effect observed is strongly dependent on the measurement configuration, and may vary for pressed PTFE. The maximum effect of the phase change is observed when PTFE is employed in a multiple reflection scenario, such as in an integrating sphere.

4.8 References

Ball, C.P., Levick, A.P., Woolliams, E.R., Green, P.D., Dury, M.R., Winkler, R., Deadman, A.J., Fox, N.P., and King, M.D., 2013, Effect of polytetrafluoroethylene (PTFE) phase transition at 19°C on the use of Spectralon as a reference standard for reflectance: Applied Optics, v. 52, p. 4806–4812.

Bourgeois, C.S., Calanca, P., and Ohmura, A., 2006, A field study of the hemispherical directional reflectance factor and spectral albedo of dry snow: Journal of Geophysical Research, v. 111, p. 1984–2012.

Carr, K.F., 1997, Integrating sphere theory and applications part 1: Integrating sphere theory and design: Surface Coatings International, v. 80, p. 380–385.

Clark, E.S., 1999, The molecular conformations of polytetrafluoroethylene: forms II and IV: Polymer, v. 40, p. 4659–4665.

France, J.L., King, M.D., Frey, M.M., Erbland, J., Picard, G., Preunkert, S., MacArthur, A., and Savarino, J., 2011, Snow optical properties at Dome C (Concordia), Antarctica; implications for snow emissions and snow chemistry of reactive nitrogen: Atmospheric Chemistry and Physics, v. 11, p. 9787–9801.

Kirby, R.K., 1956, Thermal expansion of polytetrafluoroethylene (teflon) from -190° to +300° C: Journal of Research of the National Bureau of Standards, v. 57, p. 91–94.

McKenzie, R., Badosa, J., Kotkamp, M., and Johnston, P., 2005, Effects of the temperature dependence in PTFE diffusers on observed UV irradiances: Geophysical Research Letters, v. 32, p. L06808.

Negi, H.S., and Kokhanovsky, A., 2011, Retrieval of snow albedo and grain size using reflectance measurements in Himalayan basin: The Cryosphere, p. 203–217.

Pegrum, H.M., Woolliams, E.R., Fox, N.P., van Riel, L., Otter, G., and Kowalewski, M., 2004, Calibration of the NPL transfer standard absolute radiance source (TSARS) and its use with GOME 2-FM3 spectral radiance measurements, Proceedings SPIE, v. 5570 p. 503–514.

Perovich, D.K., 2002, Seasonal evolution of the albedo of multiyear Arctic sea ice: Journal of Geophysical Research, v. 107, 8044.

Quinn, F.A., Roberts, D.E., and Work, R.N., 1951, Volume-temperature relationships for the room temperature transition in teflon: Journal of Applied Physics, v. 22, p. 1085.

Sandmeier, S.R., and Itten, K.I., 1999, A field goniometer system (FIGOS) for acquisition of hyperspectral BRDF data: Geoscience and Remote Sensing, IEEE Transactions on, v. 37, p. 978–986.

Springsteen, A., 1999, Standards for the measurement of diffuse reflectance – an overview of available materials and measurement laboratories: Analytica Chimica Acta, v. 380, p. 379–390.

Susaki, J., Hara, K., JongGeol Park, Yasuda, Y., Kajiwara, K., and Honda, Y., 2004, Validation of temporal BRDFs of paddy fields estimated from MODIS reflectance data: IEEE Transactions on Geoscience and Remote Sensing, v. 42, p. 1262–1270.

Tsai, B.K., Allen, D.W., Hanssen, L.M., Wilthan, B., and Zeng, J., 2008, A comparison of optical properties between solid PTFE (teflon) and (low density) sintered PTFE: Proceedings SPIE, v. 7065, p. 70650Y.

Tschudi, M.A., Maslanik, J.A., and Perovich, D.K., 2008, Derivation of melt pond coverage on Arctic sea ice using MODIS observations: Remote Sensing of Environment, v. 112, p. 2605–2614.

Weidner, V.R., and Hsia, J.J., 1981, Reflection properties of pressed polytetrafluoroethylene powder: JOSA, v. 71, p. 856–861.

Xiong, X., and Barnes, W., 2006, An overview of MODIS radiometric calibration and characterization: Advances in Atmospheric Sciences, v. 23, p. 69–79.

Yamamoto, T., and Hara, T., 1986, X-ray and Monte Carlo studies on the 19° C transition of poly (tetrafluoroethylene): Polymer, v. 27, p. 986–992.

Ylianttila, L., and Schreder, J., 2005, Temperature effects of PTFE diffusers: Optical Materials, v. 27, p. 1811–1814.

Zalewski, E.F., and Duda, C.R., 1983, Silicon photodiode device with 100% external quantum efficiency: Applied Optics, v. 22, p. 2867–2873.

Chapter 5

Conclusion of thesis

5.1 Introduction

The overarching aim of the thesis was to measure the bidirectional reflectance of snow and sea ice in order to improve the understanding of the directional reflectance of the cyrosphere, and to improve the methodologies used to determine these properties. The thesis focused on 3 core areas of research: (1) field measurements of Arctic snow HCRF (2) laboratory measurements of sea ice CCRF and (3) temperature effects on PTFE reference standards for reflectance. This chapter will summarise the key findings from each of the 3 core areas of study, provide concluding remarks relevant to the complete thesis, and will make recommendations for future research.

5.2 Individual studies

Key findings from each of the 3 core areas of research within this thesis are presented in this section.

5.2.1 Arctic snow HCRF study

Chapter 2 focused on HCRF measurements of Arctic snow covered tundra, undertaken during the Spring 2013 field campaign in Ny-Ålesund, Svalbard. The main conclusions from the study are summarized below:

- The GonioRAdiometric Spectrometer System (GRASS) was tested for mechanical accuracy in the laboratory at Royal Holloway University of London (RHUL) by tracing the ground instantaneous field of view (GIFOV) for 6 of the goniometer's foreoptics while rotating the arms through 3-part rotations of 90° in azimuth. The pointing accuracy of the goniometer was found to be ± 20.5 cm, and the circular sampling area was approximately 0.4 m^2 for the 8° (full angle) foreoptics; the sampling area was not sampled fully or equally.
- Optical stability of the GRASS system upon rotation of the goniometer's arms was tested in the laboratory at RHUL. The relative standard deviation of the radiances recorded by each of the 16-GRASS foreoptics while viewing a stabilised integrating sphere source was less than 5 % (1σ) for 8 replicate measurements over the wavelength range 450 nm to 1600 nm, and was typically around 2 %.
- Snow surfaces at the field sites in Ny-Ålesund showed considerable variability in the scale of roughness elements and the snowpack depth, with snow depths ranging from 9 cm to 57 cm, and surface roughness elements ranging in height from 1 cm to 6 cm, and wavelength (spacing between the crests) from 5 cm to 30 cm.
- The HCRF measurements reflected the variability in the snow surfaces, and the site with the largest roughness elements had no forward peak and a strong asymmetry over the solar principal plane. However, the

HCRF measurements showed good agreement between sites where the snow surface was smooth and the snowpack depth was greater than 40 cm, with a relative standard deviation of less than 10 % for backward and near nadir viewing angles. The averaged HCRF showed good symmetry with respect to the solar principal plane, and exhibited a forward scattering peak that was strongly wavelength dependent, with a greater than a factor of 2 increase in the anisotropy index over the wavelength range 400 nm to 1300 nm, for viewing angles 0° to 50°.

- The averaged sites agreed with similar measurements by Painter and Dozier (2004) at a different location for infrared wavelengths, but showed differences of up to 0.24 in the HCRF for the visible wavelength range. Differences in the HCRF were attributed to large mass ratios of black carbon in the snowpack owing to the proximity of the field sites to the Ny-Ålesund research base. Mass ratios of up to 299 ± 72 ng g^{-1} of black carbon in the top 10 cm of the snowpack were recorded at the site closest to the research station, which was much larger than typical background levels measured in Svalbard.
- Given the limited footprint size and the scale of the roughness elements there was considerable uncertainty in the measured HCRF at the site with the largest roughness elements. The ratio of shaded to sunlit areas within the nadir foreoptic footprint was modeled using a Monte Carlo method for 100 different viewing positions that were varied according to the pointing accuracy of the goniometer. The ratio of sunlit to shaded area had a relative standard deviation of 24.5 % for a footprint with diameter of 0.28 m; indicating that sampling precision was limited

primarily by the size of the footprint area relative to the size of the surface roughness elements.

- An improved pointing accuracy and a larger footprint area was required to reduce sampling uncertainty related to the roughness elements and to enable a full explanation for the observed effect of macroscale surface roughness. In addition, an improved characterization of grain size in the upper surface layer is required to rule out potential effects of snow grain size in the infrared region of the spectrum. However, the measurements show the potential influence of snow surface roughness on the HCRF at large solar zenith angles, and highlight the importance of sampling multiple surface types to obtain measurements of HCRF that are representative at the larger spatial scale.

Given the logistical and technical challenges associated with conducting the HCRF measurements with the GRASS instrument, the short period of time available to undertake the measurements, and the very limited budget, the field campaign was generally regarded as very successful.

5.2.2 Sea ice CCRF study

Chapter 3 focused on the CCRF measurements of sea ice grown in the laboratory at RHUL, which were undertaken using a specially designed sea ice laboratory goniometer and the Royal Holloway Sea Ice Simulator. The main conclusions from the study are summarized below:

- A methodology was developed to characterize the biconical reflectance (CCRF) of laboratory generated sea ice with two different ice thicknesses. The angular distribution of reflected radiance had a strong forward scattering peak with a maximum CCRF of 1.63, and showed good symmetry over the solar principal plane.

- The CCRF had an anisotropy that was strongly wavelength dependent, with a maximum anisotropy index of 4.9 at 730 nm. Anisotropy generally increased with wavelength despite a weakening of the forward scattering peak with wavelength; indicating that the diffuse component of the reflectance decreased more strongly with wavelength than the specular component.
- The CCRF between 450 nm and 690 nm increased by up to 4 % for an increase in thickness of 5 cm, but the CCRF decreased by up to 3.2 % for wavelengths greater than 690 nm, owing to increased absorption at longer wavelengths. The wavelength dependence to the CCRF of sea ice appeared to be dominated by the absorption coefficient of sea ice, but the hemispherical reflectance of the lower boundary influenced the CCRF for both the measured and the modeled results. The reflectivity of the lower boundary (i.e. the bottom of the tank) had approximately an order of magnitude less influence at 730 nm than at 410 nm, owing to the reduced penetration depth of radiation at longer wavelengths.
- The radiative-transfer model was able to reproduce the general shape of the CCRF over the hemisphere and its wavelength dependence, with differences in the reflectance factors typically less than 0.05. However, in order to obtain a fit within the uncertainty of the CCRF measurements and the radiative-transfer model the surface roughness parameter had to be adjusted within a realistic range of 0.05 mm to 0.17 mm; the surface roughness parameter was defined as the standard deviation of vertex heights in a cosine wave fitted to the measured amplitude to wavelength of the sea ice roughness elements. Upon adjustment of the surface roughness parameter the coefficient of variation of the RMSE between

the measured and modeled reflectance factors was less than 9 % for both acquisitions, although a HULIS absorber had to be included in the model for the M2 measurement owing to the growth of algae in the seawater. An absorption spectrum for HULIS was obtained from the literature (France et al. 2012) and the model was run for a range of HULIS mass ratios in the sea ice. A HULIS mass ratio of 0.7 μg g^{-1} was found to reduce the CCRF for wavelengths below 510 nm sufficiently so that the modeled reflectance factors were well within the uncertainty of the measured reflectance factors.

5.2.3 Effect of PTFE phase change on transmittance and reflectance

Chapter 4 focused on an investigation into the 19 °C phase change in PTFE and its effect on: (1) the optical transmittance of Spectraon diffusers, and (2) the reflectance of Spectralon reference standards for reflectance. The main conclusions from the study are summarized below:

- The relative change in the optical transmittance of a 210 μm thick Spectralon diffuser over the PTFE phase transition temperature at 19 °C for a wavelength of 350 nm to 600 nm was measured as approximately 1.6 % at 600 nm and 1.3 % at 350 nm, confirming the effect of the phase change identified by McKenzie et al. (2005) and Ylianttila and Schreder (2005).
- The relative change in the reflectance of Spectralon over the 19 °C phase change was measured at 633 nm by controlling the temperature of a PTFE integrating sphere. The output flux from the sphere's exit port over the phase transition of PTFE at 19 °C was 1.82 ± 0.21 %. The change in flux from the integrating sphere is related to the PTFE phase transition at 19 °C as a result of a change in density of the PTFE, and

was explained by a small change of 0.09 ± 0.02 % in total hemispherical reflectance of the Spectralon material.

- The results indicate that PTFE phase transition does affect the reflectance of Spectralon. Consequently, temperature stabilisation or monitoring and implementation of a correction algorithm should be considered when using PTFE based integrating spheres or flat panel reflectors. In addition, the magnitude of effect observed is strongly dependent on the measurement configuration, with the maximum effect when PTFE is employed in a multiple reflection scenario, such as in an integrating sphere.

5.3 Summary of thesis

Methodologies were developed to enable the characterization of the bidirectional reflectance of snow and sea ice using a field and laboratory goniometer respectively. The bidirectional reflectance was strongly forward scattering and had strong wavelength dependence to the anisotropy index for both snow and sea ice. The bidirectional reflectance of laboratory generated sea ice was calculated using the radiative-transfer model PlanarRad, and the variation of the RMSE between the measured and modeled reflectance factors was less than 9 % for both acquisitions when the scattering coefficient and the surface roughness parameter was varied within a realistic range. A HULIS absorber was added to the model for the second acquisition in order to obtain a fit for wavelengths shorter than 490 nm, owing to growth of algae in the laboratory seawater. Both the laboratory and field measurements highlighted the influence of surface roughness on the bidirectional reflectance of snow and sea ice. The largest snow surface roughness elements caused a strong asymmetry over the solar principal plane and a reduction in forward scattering. There was

considerable uncertainty in the measurements for snow surface roughness owing to the large size of the roughness elements relative to the size of the foreoptics footprint; indicating that an accurate characterization of the surface roughness effects on the bidirectional reflectance requires careful consideration of sampling biases owing to surface heterogeneity. An investigation into the reflectance of Spectralon (which was used as a reference standard for reflectance) at temperatures below the room temperature phase transition showed that the reflectance of Spectralon changed by less than 0.1 % over the phase transition at 19 °C. As a result, no correction to the calibration of the Spectralon panel at room temperature was required when using the panel at polar temperatures. However, owing to the multiple reflections that occur inside an integrating sphere cavity the effect is multiplied, resulting in a change in output flux from the sphere of the sphere by 1.82 ± 0.21 % over the phase transition. Hence users of PTFE integrating spheres should consider the effect of the PTFE phase transition when high accuracy measurements of flux, irradiance or radiance are required from PTFE based integrating spheres at temperatures close to the phase transition temperature at 19°C.

5.4 Recommendations for future research

In order to improve future research on subjects within this thesis, a number of recommendations – based on the outcome of this study – are given:

- When considering the effects of surface roughness for heavily windblown snowpack, an improved characterization of grain size in the upper surface layer is required to rule out potential effects of snow grain size for infrared wavelengths owing to gravitation sorting. In addition, an improved characterization of the geometry of surface roughness

elements is required to fully understand the effects of windblown surface roughness on snow bidirectional reflectance.

- When measuring the HCRF of heterogeneous targets the total acquisition time of the GRASS instrument should be reduced in order to limit geometric perturbations in the reflected distribution associated with changes in solar azimuth angle, mainly because a correction cannot be implemented for the change in solar azimuth angle for heterogeneous targets without detailed knowledge of the surface geometry.
- An improved consideration of errors related to the leveling of the GRASS instrument should be given for future field measurements, especially for HCRF acquisitions under large solar zenith angles for rough surfaces.
- The PlanarRad radiative-transfer model has the potential to be used in a predictive capacity to derive sea ice optical properties through model inversion. However, the agreement between the model and measured bidirectional reflectance needs to be tested over a wider range of incidence angles, and an improved characterization of the scale of the surface roughness elements needs to be carried out in future experiments.
- Future laboratory CCRF experiments should consider in more detail the effect of using a highly non-parallel beam as the illumination source in order to estimate the bidirectional reflectance of a surface.
- The magnitude of the effect of the PTFE phase transition at 19 °C on the optical transmittance of PTFE diffusers had a wavelength dependence of around 0.3 %. The change in reflectance was calculated for a monochromatic wavelength and it was assumed there was no

wavelength dependence to change in reflectance; this should be confirmed by future experiments.

5.5 References

France, J.L., Reay, H.J., King, M.D., Voisin, D., Jacobi, H.W., Domine, F., Beine, H., Anastasio, C., MacArthur, A., and Lee-Taylor, J., 2012, Hydroxyl radical and NO xproduction rates, black carbon concentrations and light-absorbing impurities in snow from field measurements of light penetration and nadir reflectivity of onshore and offshore coastal Alaskan snow: Journal of Geophysical Research, v. 117, p. D00R12.

McKenzie, R., Badosa, J., Kotkamp, M., and Johnston, P., 2005, Effects of the temperature dependence in PTFE diffusers on observed UV irradiances: Geophysical Research Letters, v. 32, p. L06808.

Painter, T.H., 2004, Measurements of the hemispherical-directional reflectance of snow at fine spectral and angular resolution: Journal of Geophysical Research, v. 109, p. D18115.

Ylianttila, L., and Schreder, J., 2005, Temperature effects of PTFE diffusers: Optical Materials, v. 27, p. 1811–1814.

Appendix 1

A1.1 MATLAB code for Monte Carlo simulation in Figure 1.15

```
%% 2-D Monte Carlo simulation for calculating multiple scattering in an absorbing
medium

clear all; close all

%% Input variables:
n_p = 100; % number of incident photons
u = 0; % incidence angle from surface normal [°]
z = 0.30; % medium thickness [m]

k = 250; % extinction coefficient [m-1]
w = 0.99; % single scattering albedo
g = 0.95; % asymmetry parameter (controls  proportion of forward and backward
scattering)
n_s = 10^3; % maximum number of loop iterations

%% Calculate optical properties:
tau = k*z; % optical depth
mu = 1/k; % mean free path
dir_0 = u*(pi/180); % incident angle [radians]
t = exp(-tau/cosd(u)); % direct transmittance

pstart_x = zeros(1,n_p); % xcoordiante for all incident photons
pstart_y = zeros(1,n_p); % ycoordinate for all incident photons
pstart_x(1,:) = z/100;

%% Generate a probability density for scattering from hg phase function:
[pf, theta] = hg_pf(g); % builds probability density function
theta_rad = theta*(pi/180);
pf = [flip(pf) pf];
theta_rad = [flip(theta_rad) , -theta_rad];
s_prob = pf./sum(pf); % sums to unity

f1 = figure(1);
plot(theta_rad, s_prob) % plots probability density
title('Sattering angle probability density', 'FontSize', 14)

%% Generate a probability density for free path length:
d_range = 0:mu*0.01:mu*2;
d_std = mu*0.25;
df = normpdf(d_range, mu, d_std); % builds probability density function
d_prob = df./sum(df); % sums to unity

f2 = figure(2);
plot(d_range, d_prob) % plots probability density
title('Free path length probability density','FontSize', 14)

%% First extinction event
timerV = tic;
% Calculate number of photons absorbed
r = rand(1,n_p);
abs_1 = r<(1-w); % logical index 1 == absorbed

% Calculate first scatter direction for all photons
r = rand(1,n_p);
[~,dir] = histc(r, cumsum([0, s_prob]));
dir_1 = theta_rad(1,dir);
dir_1 = dir_1+dir_0;
dir_prev(1,:) = dir_1;

f3 = figure(3);
hist(dir_1,n_p/2) % plots histrograms of scattering angles
title('Scattering angles [rad]: first extinction event', 'FontSize', 14)

% Calculate first path length (free path) for all photons
r = rand(1,n_p);
[~,dist] = histc(r, cumsum([0, d_prob]));
dist_1 = d_range(1,dist);
```

```
f4 = figure(4);
hist(dist_1,n_p/2) % plots histrograms of free paths
title('Free path lengths [m]: first extinction event', 'FontSize', 14)

% Calculate coordinates of the new photon positions based on their starting
position,
% scattered angle and distance traveled.
p1_x = pstart_x + cos(dir_1).*dist_1;
p1_y = pstart_y + sin(dir_1).*dist_1;
n_rho = sum(p1_x(1,:) < 0); % number of reflected photons
n_t = sum((p1_x(1,:) > z));
p1_x(p1_x < 0 | p1_x > z ) = NaN; % Photons that go outside the boundary become
NaNs
p1_y(p1_x < 0 | p1_x > z ) = NaN;
dir_1(abs_1) = NaN; % Absorbed photons become NaNs
% Plot the new positions and the draw path
f5 = figure(5);
scatter(p1_x, p1_y, 'kx')
title('up <<<<<       Photon paths       >>>>> down', 'FontSize', 16)
grid on
for i = 1:n_p
line([pstart_x p1_x(i)], [pstart_y p1_y(i)], 'Color', 'k')
end

% Draw boundaries and definie axis limits
ws_x = [-0.1 0.4];
ws_y = [-0.25 0.25];

line([0,0],[-z*10, z*10], 'LineWidth', 2, 'Color', 'k') % Top surface
line([z,z],[-z*10, z*10], 'LineWidth', 2, 'Color', 'k') % Bottom surface

xlim(ws_x)
ylim(ws_y)
set(gcf, 'Position', [50 50 800 800])
hold on

%% Multiple scattering: Calculate n_s extinction events for n_p photons
% Initialise variables used in loop
multi_p_x = zeros(n_s+1, n_p);
multi_p_y = zeros(n_s+1, n_p);
multi_dir = zeros(n_s+1, n_p);
multi_dist = zeros(n_s+1, n_p);
multi_abs = zeros(n_s+1, n_p);
% Set variables with outcome of the first extinction event
multi_p_x(1,:) = p1_x; % x coord
multi_p_y(1,:) = p1_y; % y coord
multi_dir(1,:) = dir_1; % direction
multi_dist(1,:) = dist_1; % distance
multi_abs(1,:) = abs_1; % absorbed

for s = 1:n_s       %%%% Each loop is an extinction event %%%%
    % Calculate number of photons absorbed
    r = rand(1,n_p);
    multi_abs(s+1,:) = r<(1-w); % logical index 1 == absorbed
    % Calculate scattering angles
    r = rand(1,n_p);
    [~,dir_2] = histc(r, cumsum([0, s_prob]));
    multi_dir(s+1,:) = theta_rad(1,dir_2);
    multi_dir(s+1,:) = multi_dir(s+1,:)+multi_dir(s,:);
    % Calculate path lengths
    r = rand(1,n_p);
    [~,dist_2] = histc(r, cumsum([0, d_prob]));
    multi_dist(s+1,:) = d_range(1,dist_2);
    % Coordinates for the new points
    multi_p_x(s+1,:) = multi_p_x(s,:) + cos(multi_dir(s+1,:)).*multi_dist(s+1,:);
    multi_p_y(s+1,:) = multi_p_y(s,:) + sin(multi_dir(s+1,:)).*multi_dist(s+1,:);
    % Count diffusely reflected and transmitted photons
    n_rho = [n_rho sum(multi_p_x(s+1,:) < 0)];
    n_t = [n_t sum(multi_p_x(s+1,:) > z)];
    multi_dir(logical(multi_abs)) = NaN; % Absorbed photons become NaNs
    % Plot positions for remaining photons
    for ph = 1:n_p
    scatter(multi_p_x(s+1, ph), multi_p_y(s+1, ph), 'kx')
    line([multi_p_x(s, ph) multi_p_x(s+1, ph)], [multi_p_y(s, ph) multi_p_y(s+1,
ph)], 'Color', 'k')
    end
```

```
    % Stop tracking the photons that are scatter outside medium
    multi_p_x(multi_p_x < 0 | multi_p_x > z ) = NaN;
    multi_p_y(multi_p_x < 0 | multi_p_x > z ) = NaN;
    n_ext = sum(sum(multi_p_x>0));
    n_rem = n_p - sum(isnan(multi_p_x(s,:)));
    fprintf('Number of photons remaining: %0.0f \nCumulative number of extinction
events: %0.0f \n', n_rem, n_ext)
    disp('-------------------------------------------------')
    pause(0.01);
    if sum(isnan(multi_p_x(s,:)))== n_p;
        n_cyc = s;
        break;
    end
end

n_abs = n_p-sum(n_rho)-sum(n_t); % number of photons absorbed
elapsed_time = toc(timerV);

disp('----------------Model setup--------------------')
fprintf('Number of photons: %0.0f \n', n_p)
fprintf('Initial incidence angle (°): %0.1f \n', u)
fprintf('Layer thickness (m): %0.1f \n', z)

disp('----------------IOPs--------------------')
fprintf('Extinction coefficient (m-1): %0.0f \n', k)
fprintf('Optical depth: %0.2f \n', tau)
fprintf('Single scattering albedo: %0.2f \n', w)
fprintf('Asymmetry parameter: %0.2f \n', g)

disp('----------------Output variables--------------------')
fprintf('Photons absorbed (%%): %0.0f \n', n_abs/n_p*100)
fprintf('Photons diffusely reflected (%%): %0.0f \n', sum(n_rho)/n_p*100)
fprintf('Photons diffusely transmitted (%%): %0.0f \n', sum(n_t)/n_p*100)
fprintf('Photons directly transmitted (%%): %0.0f \n', t)
fprintf('Total number of extinction events: %0.0f \n', n_ext)

disp('----------------Model info--------------------')
fprintf('Number of cycles in loop before break: %0.0f \n', n_cyc)
fprintf('Time taken (min): %0.1f \n', elapsed_time/60)

cd('/Users/chrisball/Desktop')
hgexport(f5,'MonteCarloOutput.eps')
```

Appendix 2

Bidirectional reflectance of windblown Arctic snow

A1.1 MATLAB code for modeling sunlit vs. shaded areas

```
%% Monte Carlo model to calculate ratio of shaded/sunlit area within a randomly
positioned foreoptic footprint with a view zenith angle of 0°

clear all; close all

%% Input variables
sun_zen=81; % Sun zenith angle [°]
sas_h = 0.015; % Sastrugi height [m]
sas_d = 0.125; % Distance between sastrugi ridges [m]
sun_sasn_azi = 70; % azimuth angle between sun and sastrugi normal (0 when sas
are perpendicular to sun direction)
sensor_r=0.01:0.01:0.50; % footprint radius [m]\
sensor_y=(y_max-y_min).*rand(100,1)+y_min; % range of sensor positions (y
coordinate)
sensor_x=(x_max-x_min).*rand(100,1)+x_min; % range of sensor positions (x
coordinate)
x_min=0.55;
x_max=0.95;
y_min=0.555;
y_max=0.95;

%% Calculate shadowed area vs sunlit areas
num_sas=1.5/sas_d+1; % number of shadow polygons in the plot
sh_l = sas_h*tand(sun_zen)*abs(cosd(sun_sasn_azi)); % shadow length

% Calculate coordinates for shadow polygons
xcoord=[0 0 1.5 1.5];
ycoord=[0 0 0 0];
poly_ycoords=zeros(length(num_sas),4);

for i=1:num_sas
poly_ycoords(i,:)= ycoord+sas_d*(i-1);
end

poly_ycoords(:,1)=poly_ycoords(:,1)+sh_l;
poly_ycoords(:,4)=poly_ycoords(:,4)+sh_l;
poly_xcoords=repmat(xcoord,round(num_sas), 1);

%Initialise variables
sensor_a=zeros(length(sensor_r),1);
shaded_a=zeros(length(sensor_r),length(sensor_y));
sunlit_a=zeros(length(sensor_r),length(sensor_y));
ratio=zeros(length(sensor_r),length(sensor_y));
diff=zeros(length(sensor_r),1);
overlap=zeros(1,10); %Shaded area within footprint

for k=1:length(sensor_y)

    for j=1:length(sensor_r)

    close all
    sensor_a(j,1)= pi*(sensor_r(j))^2; %footprint area

    % Plot shadows
    f1 = figure(1);
    hold on

        for i=1:num_sas
        fill(poly_xcoords(i,:), poly_ycoords(i,:),[0.4 0.4 0.4])
        end

    %Plot the sensor footprint
    N=256; % points in the circle
    t=(0:N)*2*pi/N;
    x=sensor_r(j)*cos(t)+sensor_y(k);
    y=sensor_r(j)*sin(t)+sensor_x(k);
    plot(x,y,'k','LineStyle', '-');

        % Calculate overlap/shadowed area viwed by the sensor
        for i=1:num_sas
        [xa,
ya]=polybool('intersection',x,y,poly_xcoords(i,:),poly_ycoords(i,:));
        fill(xa,ya,'r')
        overlap(i)= polyarea(xa,ya);
```

```
        % pause(0.1)
        end

    shaded_a(j,k)= sum(overlap);
    sunlit_a(j,k)= sensor_a(j)-shaded_a(j,k);
    ratio(j,k)= shaded_a(j,k)/sunlit_a(j,k);

        if j==14
        xlim([0 1.5])
        ylim([0 1.5])
        xlabel('distance / m')
        ylabel('distance / m')
        set(gca,'LineWidth',1.1)
        set(gcf,'PaperPositionMode','auto', 'Units', 'centimeters')
        set(gca, 'FontSize', 11, 'xMinorTick', 'on', 'yMinorTick', 'on')
        set(f1, 'Position', [2 2 5 5]);
        title(['loop iteration: ', num2str(k)])
        daspect('manual');
        daspect([1,1,1]);
        hold on
        cd('/Users/chrisball/Documents/PhD Work/Thesis chapters/Chapter
3/Figures')
        hgexport(f1, ['SRmodel_00', num2str(k), '.eps'])
        end
    end
% pause(0.1)
diff(k,1)= (ratio(sensor_r==0.5,k)-
ratio(sensor_r==0.14,k))/ratio(sensor_r==0.5,k)*100; % relative difference in the
ratio
% disp(['loop iteration: ', num2str(k)])
end

f2 = figure(2);
plot(sensor_r, ratio)
xlabel('Sensor footprint radius / m', 'FontSize', 11)
ylabel('Shaded to sunlit area ratio', 'FontSize', 11)
xlim([0 0.50])
ylim([0 3])
set(gca,'XMinorTick', 'on')
set(gca, 'YMinorTick', 'on')
set(gca,'LineWidth',1.1)
set(gcf,'PaperPositionMode','auto', 'Units', 'centimeters')
set(gca, 'FontSize', 11, 'xMinorTick', 'on', 'yMinorTick', 'on')
set(f2, 'Position', [2 2 14 14]);

cd('/Users/chrisball/Documents/PhD Work/Thesis chapters/Chapter 3/Figures')
hgexport(f2, 'SRmodel.eps')

mean_diff=mean(abs(diff));
std=std(ratio(sensor_r==0.14,:))/mean(ratio(sensor_r==0.14,:))*100;
```

Appendix 3

Bidirectional reflectance of laboratory-generated sea ice

A3.1 MATLAB code for generating PlanarRad quads

```
% Converts spherical coordinates of points surrounding each segment/quad in
% planarrad to cartesian coordiantes and builds polygons that represents the
% segments/quads in 2D.

% Define the azimuth and zeinth coordinates for the lines separating the
% segments

azi_interval = 15; % units seprating great circles [degrees]
zen_interval = 10; % units separating lines of latitude [degrees]

poly_start_azi = 7.5:azi_interval:345; % Azimuth lines at the start of each
segment
poly_end_azi = 22.5:15:360; % Azimtuh lines at the end of each segment
poly_centre_azi = 0:15:345;
poly_start_zen = 5:zen_interval:75; % Zenith lines at the start of each segment
poly_end_zen = 15:zen_interval:90; % Zenith lines at the end of the each segment
poly_centre_zen = 10:10:80;

num_sectors = 360/15; % nunber of sectors in the cirlce
num_segments_in_sector = length(poly_end_zen); % number of segments in each
sector
num_segments_total = num_segments_in_sector*num_sectors; % total number of
segments

%% Create 3D arrays containing lists of points in spherical coordinates for each
segment.

% The circle has been spilt into 24 sectors each containing 8 segments/quads
(polygons).
% Poly_points_zen and poly_points_azi are 3d arrays containing lists of zenith
% or azimuth coordinates for each segment (polygon) in each sector of the circle.
% Each layer in Poly_points_zen and poly_points_azi is a different sector of the
ciricle.
% Each row in a layer is a list of coordinates for points that make up a segment
in that sector.

for i = 1:num_segments_in_sector
    for k = 1:num_sectors-1
        poly_points_zen(i,:,k) =
[flip(poly_start_zen(i):poly_end_zen(i)),repmat(poly_start_zen(i),1,15),...
            flip(poly_start_zen(i):poly_end_zen(i)),
repmat(poly_end_zen(i),1,16)];
        poly_points_azi(i,:,k) = [repmat(poly_start_azi(k),1, poly_end_zen(i)-
poly_start_zen(i)),...
            poly_start_azi(k):poly_end_azi(k),repmat(poly_end_azi(k),1,
poly_end_zen(i)-poly_start_zen(i)+1),...
            flip(poly_start_azi(k):poly_end_azi(k))];
    end
end

%% Convert from spherical to cartesian coordinates
r = 0.5; % Define the radius of the circle

% Calculate the distance of each point from nadir
for i = 1:num_segments_in_sector
    for k = 1:num_sectors-1
        d_nadir(i,:,k)=sind(poly_points_zen(i,:,k)).*r;
    end
end

% Calculate the x and y coordinates for each point and draw each polygon
for i = 1:num_segments_in_sector
    for k = 1:num_sectors-1
        x_coord(i,:,k) = (cosd(poly_points_azi(i,:,k)).*d_nadir(i,:,k))+0.5;
        y_coord(i,:,k) = 0.5-(sind(poly_points_azi(i,:,k)).*d_nadir(i,:,k));
    end
end

% Flip sector 12 to fill missing sector 24
x_coord(:,:,24)=1-x_coord(:,:,12);
y_coord(:,:,24)=y_coord(:,:,12);
```

A3.2 MATLAB code for plotting from PlanarRad report.txt file

```
%% Script to plot planarrad output

close all; clear all

%% Run Plot_Segments script to obtain segment polygons
cd('/Users/chrisball/Documents/PhD Work/BRDF Modelling/PLOT_PlanarRad')
run('Plot_Segments.m')

%% Request user input and set up input variables
filename = input('Enter the name of the PlanarRad output folder:', 's');
working_dir = strcat('/Users/chrisball/Documents/PhD Work/BRDF
Modelling/PlanarRad_ouput_thesis/PlanarRad_output_M1andM2/', filename);
output_dir = '/Users/chrisball/Documents/PhD Work/BRDF
Modelling/PLOT_PlanarRad/PlannarRad_Plots/PlanarRadPlots_Thesis ';
num_bands = 17; % number of wavelength bands in plannarad output
interval = 22; % Specify number of rows between bands in file
pp_colorbar_min = 0.2;
pp_colorbar_max = 1.2;
g_ylimits = [0.2 1.8];
g_legend_pos = 'northwest';

% Move all polygon coordinates to a 2d array
for k = 1:num_sectors
    for i = 1:num_segments_in_sector
        if k > 1
        p_x_coord(8*(k-1)+i,:) = x_coord(i,:,k);
        p_y_coord(8*(k-1)+i,:) = y_coord(i,:,k);
        else
        p_x_coord(k+(i-1),:) = x_coord(i,:,k);
        p_y_coord(k+(i-1),:) = y_coord(i,:,k);
        end
    end
end

%% Import, process and segment averaged radiances from PlanarRad report.txt
cd(working_dir)

% Find row number of "L_a_band 1", "theta_table" and "phi_table" in report.txt
and import data
fid=fopen('report.txt','r'); % Open file for reading
C=textscan(fid, '%s','Delimiter','\n'); % Reads each line as a string
C=C{:};

% Logical indexing to find matching text
L_a_band_1=strcmp(C,'L_a band 1');
theta_table=strcmp(C,'# Quad solid angle mean point theta table (rows are
horizontal, columns are vertical):');
phi_table=strcmp(C,'# Quad solid angle mean point phi table (rows are horizontal,
columns are vertical):');

%Extract row numbers
index=1:length(C);
i_band_1=index(L_a_band_1);
i_theta_table=index(theta_table);
i_phi_table=index(phi_table);

% Calculate row numbers for all bands based on the interval size and number of
bands
i_all_bands=i_band_1:interval:(i_band_1+interval*(num_bands-1));

% Read in upwelling radiances for all 17 bands
L_up=zeros(9,24,num_bands);
L_up_nadir=zeros(1,num_bands);

for i=1:length(i_all_bands)
L_up(:,:,i)=dlmread('report.txt', ',', [i_all_bands(i)+10, 0, i_all_bands(i)+18,
23]);
% L_up(4,1,i)=mean([L_up(3,1,i);L_up(5,1,i); L_up(7,2,i); L_up(6,24,i)]); %
removes specular peak
L_up_nadir(i)=dlmread('report.txt','\t',[i_all_bands(i)+19, 0, i_all_bands(i)+19,
0]);
```

```
end

band_centres=dlmread('report.txt', ',', 'C5..S5');
BRDF=L_up; % sr-1
PlanarRad_BRF=L_up*pi; % unitless, Schaepman-Strub, 2006, Eq. 6
BRF_nadir = L_up_nadir*pi;

% Import segment averaged zenith angles
L_up_zenith=dlmread('report.txt', ',', [i_theta_table+10, 0, i_theta_table+18,
23]); % Reads from file
L_up_zenith=90-(L_up_zenith-90); % Convert zenith angles from spherical to
hemispherical

% Import segment averaged azimuth angles
L_up_azimuth=dlmread('report.txt', ',', [i_phi_table+10, 0, i_phi_table+18, 23]);

% Calculate zenith angle distance from nadir
r=0.5;
L_d_nadir=sind(L_up_zenith).*r;

% Calcualte centre position of segment/quad in cartesian coordinates
L_x_coord=(cosd(L_up_azimuth).*L_d_nadir)+0.5;
L_y_coord=0.5-(sind(L_up_azimuth).*L_d_nadir);

%% Draw and fill all polygon segments

% Plot segment centres
% plot(L_x_coord, L_y_coord, 'r*')

% Find the points inside polygons
L_poly_value= [];
L_poly_centre_coord = [];

for p = 1:num_segments_total
    for b = 1:num_bands
                in = inpolygon(L_x_coord, L_y_coord, p_x_coord(p,:),
p_y_coord(p,:));
                in = repmat(in,1,1,num_bands);
                L_poly_value(p,:) = PlanarRad_BRF(in);
    end
end

%Import NaN row numbers file from SIS output
cd('/Users/chrisball/Documents/PhD Work/BRDF
Modelling/PlanarRad_ouput_thesis/PlanarRad_output_M1andM2')
row_nums = load('nan_row_nums.mat');

% Delete polygons referenced in row_nums
PlanarRad_BRF = L_poly_value; % make a copy
PlanarRad_BRF(row_nums.row_nums,:) = [];
p_x_coord(row_nums.row_nums,:) = [];
p_y_coord(row_nums.row_nums,:) = [];

% Calculate ANIX
for i = 1:num_bands
PlanarRad_ANIX(i) = max(PlanarRad_BRF(:,i))./min(PlanarRad_BRF(:,i));
end

% Get rgb colors
c_min = pp_colorbar_min; % keep constant if possible, but if not use this:
% round((min(min(L_poly_value))-0.01)*10)/10; % set minimum value in colorbar
c_max = pp_colorbar_max; % keep constant if possible, but if not use this:
% round((max(L_poly_value(L_poly_value<min(L_poly_value(190,:))))+0.01)*10)/10; %
set max value in colorbar
L_poly_colors = mat2gray(PlanarRad_BRF,[c_min c_max]);
for i=1:num_bands
    L_poly_nadir_color(i) = mat2gray(BRF_nadir(i),[c_min c_max]);
end
cm = colormap(jet);
for i = 1 : length(PlanarRad_BRF)
    for b = 1:num_bands
        colorID(i,b) = max(1, sum(L_poly_colors(i,b) > [0:1/length(cm(:,1)):1]));
        myColor(i,b,:) = cm(colorID(i,b), :);
    end
end
for b = 1:num_bands
```

```
    colorID_nadir(b) = max(1, sum(L_poly_nadir_color(b) >
[0:1/length(cm(:,1)):1]));
    myColor_nadir(b,:) = cm(colorID_nadir(b), :);
end

%% Plot polgons and fill with colors corresponding to the radiance values and
ouput to file

cd(output_dir)
mkdir(filename) % make new directory

% Set coordinates for nadir segment
ang = 0:0.01:2*pi;
xp = sind(2.5)*cos(ang)+0.5;
yp = sind(2.5)*sin(ang)+0.5;

%Set up scattering labelc coordinates and text
x_scat_label = 0.5;
y_scat_label = -0.15;
str_text_scat_label = '<<< backward scattering | forward scattering >>>   ';

% Set up coordinates for azimuth lines
x=[cosd(0:30:330)*(sind(90)*r)+r;ones(1,12)*r];
y=[sind(0:30:330)*(sind(90)*r)+r;ones(1,12)*r];

%Creat coordinates for azi labels
    x_text_azi_labels=cosd(0:30:330)*(sind(90)*(r+0.07))+r+0.004;
    y_text_azi_labels=sind(0:30:330)*(sind(90)*(r+0.07))+r+0.004;

%Creat coordinates for zenith labels
    x_text_zen_labels=cosd(130)*(sind(15:15:60)*r)+r;
    y_text_zen_labels=sind(130)*(sind(15:15:60)*r)+r;

% Assign text for azi labels
    str_text_azi_labels = {'180^{\circ}', '150^{\circ}', '120^{\circ}',
'090^{\circ}',...
        '060^{\circ}','030^{\circ}','000^{\circ}','330^{\circ}','300^{\circ}',...
        '270^{\circ}','240^{\circ}','210^{\circ}'};
%Assign text for zen labels
    str_text_zen_labels = {'15^{\circ}', '30^{\circ}', '45^{\circ}',
'60^{\circ}'};

for band = 1:num_bands

    figure(band);
    xlim([-0.1 1.1]);
    ylim([-0.1 1.1]);
    hold on

    for i = 1:length(PlanarRad_BRF)
        h_polygon = fill(p_x_coord(i,:), p_y_coord(i,:), [myColor(i,band,1)
myColor(i,band,2) myColor(i,band,3)]);
        set(h_polygon, 'EdgeColor', 'none')
        hold on
    end

    % fill nadir segment
    fill(xp, yp, myColor_nadir(band,:), 'EdgeColor', 'none')

    % set colorbar and axis
    cb = colorbar;
    x1=get(gca,'position');
    x_cb=get(cb,'position');
    x_cb(3)= x_cb(3)*1;
    x_cb(4)= x_cb(4)*0.8;
    x_cb(2) = x_cb(2)*1.75;
    x_cb(1) = x_cb(1)*1;
    set(cb,'FontSize',11)
    caxis([c_min c_max])
    set(cb,'position',x_cb)
    set(gca,'position',x1)
    set(cb, 'ytick', 0.2:0.1:1.2, 'yticklabel', {'0.2', '0.3', '0.4', '0.5',
'0.6', '0.7', '0.8', '0.9', '1', '1.1', '1.2'})
    hold on

    title(['  Modelled BRF:  ','\lambda = ', int2str(band_centres(band)),' nm, ',
'ANIX = ' sprintf('%0.3g',PlanarRad_ANIX(band))], 'FontSize', 12)
```

```
    axis off

    % create label for forward and backward scattering
    text(x_scat_label, y_scat_label, str_text_scat_label,...
            'HorizontalAlignment','center','VerticalAlignment',
'middle','FontSize', 11)

    % create label for colorbar
    h = text(1.35, 0.5, 'CCRF',...
            'HorizontalAlignment','center','VerticalAlignment',
'middle','FontSize', 11);
    set(h, 'rotation', 90)

    %% Draw lines and labels

    % Draw azimuth angles
    line(x,y, 'color', [0 0 0],'LineStyle', '--')

    % Draw circles for 15° zenith intervals
    PlotCircle(r,r,((sind(15))*r),360,'k');
    PlotCircle(r,r,((sind(30))*r),360,'k');
    PlotCircle(r,r,((sind(45))*r),360,'k');
    PlotCircle(r,r,((sind(60))*r),360,'k');
    PlotCircle(r,r,((sind(75))*r),360,'k');
    PlotCircle_2(r,r,((sind(90))*r),360,'k');

    % Plot azi labels
    for i = 1:length(x_text_azi_labels)
        text(x_text_azi_labels(i), y_text_azi_labels(i),
str_text_azi_labels(i),...
            'HorizontalAlignment','center','VerticalAlignment',
'middle','FontSize', 11)
    end

    % Plot zen labels
    for i = 1:length(x_text_zen_labels)
        text(x_text_zen_labels(i), y_text_zen_labels(i),
str_text_zen_labels(i),...
            'HorizontalAlignment','center','VerticalAlignment',
'middle','FontSize', 11)
    end

    %% Export figure to .eps

    daspect('manual')
    daspect([1, 1, 1])
    set(gcf,'PaperPositionMode','auto', 'Units', 'centimeters')
    set(gcf, 'Position', [2 2 12 12]);


    cd(output_dir)
    cd(filename)
    saveas(gca,
strcat(filename,'_',int2str(band_centres(band)),'nm','.eps'),'epsc');
end

%% Plot BRF spectra

% Generate legend labels
theta_spp = -80:10:80;
legend_text = '\theta = ';
legend_text = repmat(legend_text,length(theta_spp),1);
for i = 1:length(theta_spp)
    legend_text_all{i,1} = [legend_text(i,:) int2str(theta_spp(i)) '°'];
end

% Get values in spp
poly_row_num_forward = 185:192; % Define row numbers for polygons of interest
poly_row_num_backward = 89:96; % Define row numbers for polygons of interest
L_forward = L_poly_value(poly_row_num_forward,:); % Get data
L_backward = L_poly_value(poly_row_num_backward,:); % Get data
PlanarRad_L_spp = cat(1,flip(L_backward), BRF_nadir, L_forward);

theta_spp = theta_spp(3:15);
PlanarRad_L_spp = PlanarRad_L_spp(3:15, :);
legend_text_all = legend_text_all(3:15,:);
```

```
%% Plot BRF with wavelength

spp_theta_row_num = [7 10 13]; % row numbers for view angle to plot

figure(num_bands+2)
plot(band_centres, PlanarRad_L_spp(spp_theta_row_num(1),:), '-ko',...
    band_centres, PlanarRad_L_spp(spp_theta_row_num(2),:), '-ks',...
    band_centres, PlanarRad_L_spp(spp_theta_row_num(3),:), '-k^',...
    'LineWidth', 1.2, 'MarkerSize', 6, 'MarkerFaceColor', 'w',...
    'MarkerEdgeColor', 'k')
xlim([410 730])
ylim(g_ylimits)
xlabel('Wavelength / nm', 'FontSize', 11)
ylabel('BRF', 'FontSize',11)
legend(legend_text_all(spp_theta_row_num), 'Location', g_legend_pos,'FontSize',
11)
set(gca, 'XMinorTick','on', 'YMinorTick','on','FontSize',11,'Linewidth',1.1)
set(gcf,'PaperPositionMode','auto', 'Units', 'centimeters')
set(gcf, 'Position', [2 2 14 14]);

cd(output_dir)
cd(filename)
saveas(gca,
strcat('Wvl_',filename,'_',int2str(band_centres(band)),'nm','.eps'),'epsc');

%% Plot BRF in principle plane

spp_band_row_num = [1 6 11 16]; % row numbers for bands to plot

figure(num_bands+3)
plot(theta_spp, PlanarRad_L_spp(:,spp_band_row_num(1)),'-ko',theta_spp,
PlanarRad_L_spp(:,spp_band_row_num(2)),'-ks',...
    theta_spp, PlanarRad_L_spp(:,spp_band_row_num(3)),'-kd',theta_spp,
PlanarRad_L_spp(:,spp_band_row_num(4)),'-k^',...
    'LineWidth', 1.2, 'MarkerSize', 6, 'MarkerFaceColor', 'w', 'MarkerEdgeColor',
'k')
for i = 1:length(band_centres)
    legend_band_centres{i,1} = [int2str(band_centres(i)) ' nm'];
end
legend_theta_spp = legend_band_centres(spp_band_row_num);
ylim(g_ylimits)
xlim([-60 60])
legend(legend_theta_spp, 'Location', g_legend_pos, 'FontSize', 11)
xlabel('Zenith angle in solar principle plane / °', 'FontSize', 11)
ylabel('BRF', 'FontSize',11)
set(gca, 'XMinorTick','on', 'YMinorTick','on', 'FontSize',11, 'Linewidth',1.1)
set(gcf,'PaperPositionMode','auto', 'Units', 'centimeters')
set(gcf, 'Position', [2 2 14 14]);

cd(output_dir)
cd(filename)
saveas(gca,
strcat('SPP_',filename,'_',int2str(band_centres(band)),'nm','.eps'),'epsc');

disp(['Plannarrad output saved: ', output_dir,'/' filename])

%% Plot ANIX

figure(num_bands+4)
plot(band_centres, PlanarRad_ANIX, '-k','LineWidth', 1.2);
hold on
plot(band_centres, PlanarRad_ANIX, 'ok',...
    'LineWidth', 1.2, 'MarkerSize', 6, 'MarkerFaceColor', 'w', 'MarkerEdgeColor',
'k');
xlabel('Wavelength / nm', 'FontSize', 11)
ylabel('ANIX', 'FontSize',11)
xlim([410, 730])
set(gca, 'XMinorTick','on', 'YMinorTick','on', 'FontSize',11, 'Linewidth',1.1)
set(gcf,'PaperPositionMode','auto', 'Units', 'centimeters')
set(gcf, 'Position', [2 2 14 14]);

cd(output_dir)
cd(filename)
saveas(gca,
strcat('ANIX_',filename,'_',int2str(band_centres(band)),'nm','.eps'),'epsc');

disp(['Plannarrad output saved: ', output_dir,'/' filename(1:2)])
```

```
%% Save plot data to structure

cd('/Users/chrisball/Documents/PhD Work/BRDF Modelling/PlanarRad_ouput_thesis')

% Build structure with plot data, taking only wavelengths 410 to 730 (17
% bands, and only -60 to 60 view angles in spp)

PlanarRad_plot_data.(filename) = struct('hemi_brf', PlanarRad_BRF,
'hemi_brf_poly_xcoord', p_x_coord, 'hemi_brf_poly_ycoord', p_y_coord,...
    'nadir_brf_wvl', [band_centres',
PlanarRad_L_spp(spp_theta_row_num(1),:)'],...
    'brf_wvl_30fwrd', [band_centres',
PlanarRad_L_spp(spp_theta_row_num(2),:)'],...
    'brf_wvl_60fwrd', [band_centres',
PlanarRad_L_spp(spp_theta_row_num(3),:)'],...
    'brf_spp_410nm', [theta_spp', PlanarRad_L_spp(:,spp_band_row_num(1))],...
    'brf_spp_510nm', [theta_spp', PlanarRad_L_spp(:,spp_band_row_num(2))],...
    'brf_spp_610nm', [theta_spp', PlanarRad_L_spp(:,spp_band_row_num(3))],...
    'brf_spp_710nm', [theta_spp', PlanarRad_L_spp(:,spp_band_row_num(4))],...
    'ANIX', [band_centres(1:17)', PlanarRad_ANIX(1:17)']);

save(strcat('PlanarRad_plot_data_',filename), 'PlanarRad_plot_data')
```

Appendix 4

Effect of the phase transition at 19°C on PTFE Spectralon reference standards for reflectance

A4.1 Derivation of Eq. 4.23

The radiometric flux onto the detector Φ_d at the spheres exit port is given by

$$\Phi_d = \frac{A_p \Omega_{\det-p} \Phi_i}{\pi A_s} \times \frac{\rho}{1-\rho(1-f)}, \quad \text{Eq.A4.1}$$

where A_p is the area of the exit port, $\Omega_{\det-p}$ is the solid angle subtended by the detector from the exit port, Φ_i is the input flux, A_s is the surface area of the integrating sphere, ρ is the reflectance of the PTFE sphere and f is the sphere port fraction.

Given an equation of the form

$$y = \frac{Ax}{1-Bx}, \quad \text{Eq.A4.2}$$

where y, x, A and B are terms in Eq. A4.1, as follows

$$y = \Phi_d, \quad \text{Eq.A4.3}$$

$$x = \rho, \quad \text{Eq.A4.4}$$

$$A = \frac{A_p \Omega_{\det-p} \Phi_i}{\pi A_s}, \quad \text{Eq.A4.5}$$

$$B = (1-f). \quad \text{Eq.A4.6}$$

Differentiation of y with respect to x in Eq.A4.2 requires the quotient rule

$$f(x) = \frac{g(x)}{h(x)}, \quad \text{Eq.A4.7}$$

$$\frac{\delta y}{\delta x} = f'(x) = \frac{g'(x)h(x) - g(x)h'(x)}{(h(x))^2}, \quad \text{Eq.A4.8}$$

where

$$g(x) = Ax, \quad \text{Eq.A4.9}$$

$$h(x) = 1 - Bx \,. \qquad \text{Eq.A4.10}$$

Differentiation of Eq.A4.9 and Eq.A4.10 yields

$$g'(x) = A \,, \qquad \text{Eq.A4.11}$$

$$h'(x) = -B \,. \qquad \text{Eq.A4.12}$$

Substitution of Eq.A4.9, Eq.A4.10, Eq.A4.11 and Eq.A4.12 into Eq.A4.8 gives

$$\begin{aligned} \frac{\delta y}{\delta x} &= \frac{A(1-Bx)+ABx}{(1-Bx)^2} \,, \\ &= \frac{A(1-Bx+Bx)}{(1-Bx)^2} \,, \\ &= \frac{A}{(1-Bx)^2} \,. \end{aligned} \qquad \text{Eq.A4.13}$$

Substituting in the terms from Eq.A4.3, Eq.A4.4, Eq.A4.5, and Eq.A4.6 for y, x, A and B into Eq.A4.13 gives

$$\begin{aligned} \frac{\delta\Phi_d}{\delta\rho} &= \frac{\frac{A_p\Omega_{\det-p}\Phi_i}{\pi A_s}}{(1-\rho(1-f))^2} \,, \\ &= \frac{A_p\Omega_{\det-p}\Phi_i}{\pi A_s} \times \frac{1}{(1-\rho(1-f))^2} \,. \end{aligned} \qquad \text{Eq.A4.14}$$

Dividing Eq.A4.14 by Eq.A4.1 gives

$$\begin{aligned} \frac{1}{\Phi_d} \times \frac{\delta\Phi_d}{\delta\rho} &= \frac{A_p\Omega_{\det-p}\Phi_i}{\pi A_s} \times \frac{1}{(1-\rho(1-f))^2} \cdots \\ &\times \frac{\pi A_s}{A_p\Omega_{\det-p}\Phi_i} \times \frac{1-\rho(1-f)}{\rho} \,, \\ &= \frac{1-\rho(1-f)}{(1-\rho(1-f))^2} = \frac{1}{1-\rho(1-f)} \,. \end{aligned} \qquad \text{Eq.A4.15}$$

Multiplying Eq.A4.15 by $\delta\rho$ gives

$$\frac{\delta\Phi_d}{\Phi_d} = \frac{\delta\rho}{\rho(1-\rho(1-f))} \,, \qquad \text{Eq.A4.16}$$

$$= \frac{\delta\rho}{\rho} \times \frac{1}{1-\rho(1-f)},$$

which is the relative change in flux owing to the change in reflectivity of the sphere. Rearranging Eq.A4.16 to find the change in reflectivity of the sphere gives

$$\frac{\delta\rho}{\rho} = \frac{\frac{\delta\Phi_d}{\Phi_d}}{\frac{1}{1-\rho(1-f)}} \qquad \text{Eq.A4.17}$$

$$= \frac{\delta\Phi_d(1-\rho(1-f))}{\Phi_d}.$$